Tampere University

OLLI OJA

Correlation between the Microstructure and Mechanical Properties of Intercritically Annealed Advanced High-Strength Steels

Tampere University Dissertations 623

Tampere University Dissertations 623

OLLI OJA

Correlation between the Microstructure and Mechanical Properties of Intercritically Annealed Advanced High-Strength Steels

ACADEMIC DISSERTATION
To be presented, with the permission of
the Faculty of Engineering and Natural Sciences
of Tampere University,
for public discussion in the auditorium K1702
of the Konetalo building, Korkeakoulunkatu 6, Tampere,
on 12 August 2022, at 12 o'clock.

ACADEMIC DISSERTATION
Tampere University, Faculty of Engineering and Natural Sciences
Finland

Responsible supervisor and Custos	Professor Pasi Peura Tampere University Finland	
Supervisors	Dr Tuomo Nyyssönen Swerim AB Sweden	
Pre-examiners	Professor Michael Ferry UNSW Sydney Australia	Professor Esa Vuorinen Luleå University of Technology Sweden
Opponents	Professor Esa Vuorinen Luleå University of Technology Sweden	Professor Jari Larkiola University of Oulu Finland

The originality of this thesis has been checked using the Turnitin OriginalityCheck service.

Cover design: Roihu Inc.

ISBN 978-952-03-2454-4 (print)
ISBN 978-952-03-2455-1 (pdf)
ISSN 2489-9860 (print)
ISSN 2490-0028 (pdf)
http://urn.fi/URN:ISBN:978-952-03-2455-1

PunaMusta Oy – Yliopistopaino
Joensuu 2022

ACKNOWLEDGEMENTS

The work presented here was carried out at the Department of Materials Science and Environmental Engineering of Tampere University and the Hämeenlinna R&D department of SSAB during 2015 - 2021. The research was mainly funded by SSAB Europe Oy under the Business Finland "Intelligent Steels and Applications" programme. The work received grants from Häme Foundation for Professorial Higher Education and Research and the Finnish Deep-Drawing Research Group. SSAB Europe Oy receives my gratitude for giving me the opportunity to study for a doctorate in addition to my responsibilities as a product development engineer.

The work was mainly supervised by Professor Pasi Peura and Dr Tuomo Nyyssönen. I would like to thank them both for all their advice on this research. I also want to thank my co-supervisor and colleague Dr Petri Jussila at SSAB for mentoring my research over the years. The work would have not been possible without the guidance and valuable help from all of my supervisors. I would also like to express my thanks to pre-examiners Professor Esa Vuorinen at Luleå University of Technology, Sweden and Professor Michael Ferry at UNSW Sydney, Australia.

I would also like to express my gratitude to Dr Mari Honkanen, Mr Shahroz Ahmed and Mr Madan Patnamsetty in Tampere University and special thanks go to Dr Vahid Javaheri at the University of Oulu as well as Dr Ari Saastamoinen at Valmet. You provided important resources without which the research would not have been possible. My thanks also to Mr Jussi Paavola and Mr Juha Uusitalo at the University of Oulu, Mr Johan Lönnqvist and Mr Christer Eggertson at Swerim, and Ms Soile Kela at SSAB for providing the experimental material for the work. I also wish to express my gratitude to all my colleagues at SSAB Raahe and Hämeenlinna Works, because the industrial trials would not have been possible without you.

Finally, my special gratitude goes to family and friends. Thank you for your everlasting understanding, patience and support for my endeavour.

Hämeenlinna, April 2022

Olli Oja

ABSTRACT

Automotive steels are undergoing constant research and development. The automotive industry has inspired the development of advanced high strength steels in recent decades by targeting a reduction in automotive body weight. In order to develop novel high-strength and formable steels for this purpose, the present work investigates the metallurgy and properties of silicon- and aluminium-alloyed, niobium- and vanadium-microalloyed steels by performing intercritical annealing and austempering as well as quenching and partitioning heat treatment. Materials were characterized by studying the microstructure and mechanical properties with the emphasis on local ductility.

The heat treatments investigated herein produced microstructures containing ferrite, bainitic ferrite and martensite with various amounts of metastable retained austenite, which led to differences in material properties. The retained austenite morphologies were investigated using electron backscatter diffraction (the EBSD method). As a novel feature, retained austenite was found in steel containing low carbon (0.08 – 0.10 wt.%) that had been processed by quenching and partitioning.

The present work investigated ten different chemical compositions which were utilized to produce four concepts for a 980 – 1180 MPa class steel. Depending on the heat treatment and processing, the strength-elongation combination showed local or global formability type mechanical properties. The local-global formability was studied by performing fracture strain measurements on the tensile test specimens. As a summary, this work defines the formability diagram of a large number of differently treated experimental steels.

The results showed that intercritical quenching and partitioning heat treatment typically led to a microstructure with local formability properties, while intercritical annealing and austempering produced more of a global type of formability. By adjusting the chemical composition and heat treatment, it was also possible to achieve a combination of these formability properties, which is useful in an advanced high strength and formable steel. These combined properties are especially required when automotive industry utilizes modern steels for more energy-efficient vehicles.

TIIVISTELMÄ

Uusien lujien ja hyvin muovattavien terästen kehitystä ajaa eteenpäin autoteollisuuden tarve keventää ajoneuvojen massaa ja siten parantaa energiatehokkuutta ilman että kolariturvallisuus samalla heikkenisi. Koska lujuuden kasvattaminen voi johtaa muovattavuuden heikkenemiseen, on tärkeää optimoida teräksen mikrorakenne muovattavuuden kannalta. Tässä tutkimuksessa pyrittiin tähän tavoitteeseen selvittämällä erilaisten lämpökäsittelyjen vaikutuksia pii- ja alumiiniseostettujen sekä niobi- ja vanadiinimikroseostettujen terästen ominaisuuksiin. Materiaaliominaisuudet selvitettiin mikrorakennetutkimuksilla ja mekaanisella aineenkoetuksella keskittyen erityisesti paikalliseen muodonmuutoskykyyn. Muovattavuutta arvioitiin mittaamalla paikallinen venymä vetosauvojen murtopinnoista. Mikrorakenteiden tarkka karakterisointi tehtiin elektronimikroskopian avulla käyttäen EBSD-menetelmää (takaisin sironneiden elektronien diffraktio).

Tutkimuksiin valittiin kymmenen eri koostumusta kirjallisuuden ja teoreettisen tarkastelun perusteella. Tavoitteena oli 980 – 1180 MPa murtolujuusluokan nykyaikaisten monifaasiterästen kehittäminen. Kaksifaasialueella tehdyn hehkutuksen yhdistäminen austemperointiin tai Quenching & Partitioning –käsittelyyn saivat aikaan mikrorakenteita, jotka sisälsivät vaihtelevia määriä jäännösausteniittia ja muita faaseja erilaisina morfologioina. Lämpökäsittelystä ja koostumuksesta riippuen, myös terästen muodonmuutoskyvyn havaittiin vaihtelevan ja vastaavan joko paikallista tai laajaa muovattavuustyyppiä. Tulosten perusteella laadittiin muovattavuuskartta, jossa tulokset osoittivat havainnollisesti lämpökäsittelyn ja mikrorakenteen morfologian vaikutuksen muovattavuuteen. Quenching & Partitioning –käsittely johti paikalliseen muovattavuustyyppiin, kun kaksifaasialueen hehkutus ja austemperointi puolestaan sai aikaa laajan muovattavuuden. Lisäksi pystyttiin osoittamaan matalahiilisten terästen (0.08 – 0.10 % C) sisältävän jäännösausteniittia Quenching & Partitioning –käsittelyn jälkeen.

Tulokset osoittivat, että lämpökäsittelyä ja koostumusta optimoimalla on mahdollista aikaansaada paikallisen ja laajan muovattavuustyypin yhdistelmä. Juuri näillä tasapainotetuilla muovattavuus- ja lujuusominaisuuksilla terästeollisuus pystyy vastaamaan tulevaisuuden ajoneuvoterästen tiukkeneviin ominaisuus- ja muovattavuusvaatimuksiin.

CONTENTS

LIST OF SYMBOLS AND ABBREVIATIONS

Greek symbols

α	Ferrite
α_t	Time-dependent constant
β_t	Time-dependent constant
α'	Martensite
α_γ	Lattice parameter of austenite
ε	Strain
ε_u	True uniform strain
ε_{3f}	Third principle strain (true strain at fracture)
γ	Austenite
ϱ_N	Number density

Latin symbols

A_0	Initial cross-sectional area of the tensile specimen
A_{25}	Total elongation that is measured using 25 mm gauge length
A_{c1}	Ferrite to austenite transformation start temperature (°C) during heating
A_{c3}	Ferrite to austenite transformation finish temperature (°C) during heating
A_{e3}	Ferrite to austenite equilibrium transformation finish temperature (°C)
A_f	Cross-sectional area of the tensile specimen at fracture
A_g	Uniform elongation
B_s	Bainite start temperature (°C)
C_{alloy}	Carbon content of steel alloy
C_γ	Carbon content of austenite
f_γ^0	Original retained austenite volume fraction
f_γ	Austenite volume fraction
$f_{\gamma IA}$	Intercritical austenite fraction
f_{eq}	Maximum austenite fraction at intercritical temperature

f_m	Martensite volume fraction
G_α	Free energy of ferrite
G_γ	Free energy of austenite
$\Delta G_{Ms}^{\gamma\alpha}$	Free energy difference required for martensite transformation
k_p	Constant related to mechanical stability of austenite
M_s	Martensite start temperature (°C)
M^{σ}_s	Temperature above which martensitic transformation can occur only due to plastic deformation (°C)
M_d	Temperature above which austenite is stable and no strain-induced martensite is formed (°C)
M_f	Martensite finish temperature (°C)
p	Autocatalytic factor of austenite
R_m	Tensile strength
$R_{p0.2}$	Yield strength
T	Temperature
t_0	Initial sheet thickness
$t_{1,3}$	Maximum thicknesses of the fracture surface (at the borders of the fracture surface)
t_2	Minimum thickness of the fracture surface (at the centre of the fracture surface)
t_f	Sheet thickness at fracture
t	Time
T_0	Thermodynamic end-point of the bainitic transformation during austempering
U	Mechanical driving force of martensite transformation
W_f	Fracture width perpendicular to the loading direction

Abbreviations

AHSS	Advanced high-strength steel
bcc	Body-centered cubic crystal structure
CE_{IIW}	Carbon equivalent according to the International Institute of Welding
CGL	Continuous galvanizing line
CP	Complex-phase
CH	Complex-phase high-formability
CPE	Constrained carbon paraequilibrium
CSP	Cross-section polisher

DH	Dual-phase high-formability
DP	Dual-phase
dp	Dew point
DARA	Dislocation absorption by retained austenite effect
DIMT	Deformation induced martensite transformation
DIPT	Deformation induced phase transformation
EBSD	Electron back-scatter diffraction
fcc	Face-centered cubic crystal structure
FESEM	Field emission scanning electron microscope
GI	Hot-dip galvanized
HE	Hydrogen embrittlement
HSLA	High-strength low-alloy
IA	Intercritical annealing
IBT	Isothermal bainitic transformation
IPF	Inverse pole figure
JMA	Johnson-Mehl-Avrami
JMAK	Johnson-Mehl-Avrami-Kolmogrov
K-M	Koistinen-Marburger
MA	Martensite-austenite island (also as M/A)
pcm	Critical metal parameter
PT	Partitioning temperature
PHS	Press hardening steel
PQM	Pattern quality map
TBF	TRIP-assisted bainitic ferritic
TFS	True fracture strain
TEM	Transmission electron microscope
TM	Tempered martensite
TRIP	Transformation induced plasticity
TTT	Time-temperature transformation
TWIP	Twinning induced plasticity
Q&P	Quenching and partitioning (also as QP)
QPT	Quenching, partitioning and tempering
QT	Quenching stop temperature
RA	Retained austenite
RT	Room temperature
SAM	Scanning Auger electron microscope

SEM	Scanning electron microscope
STEM	Scanning transmission electron microscope
Vol.%	Volume percent
wt.%	Weight percent
XRD	X-ray diffraction

AUTHOR'S CONTRIBUTION

In this thesis, the author carried out the theoretical framework, selected experimental methods and designed the experiments regarding the chemical compositions and heat treatments of the investigated materials. The contribution of other participating parties is described below.

Dr Tuomo Nyyssönen, Madan Patnamsetty, MSc, and Shahroz Ahmed, MSc, at Tampere University assisted on analysing the XRD specimens. TEM analysis was conducted by Dr Mari Honkanen, Dr Ari Saastamoinen and Shahroz Ahmed, MSc, together with the author. Dr Vahid Javaheri at the University of Oulu carried out Thermo-Calc analysis of the experimental compositions.

The interpretation of the experimental results and their discussion was performed by the author under the guidance of the responsible supervisors Professor Pasi Peura and Dr Tuomo Nyyssönen. The conclusions were prepared by the author.

1 INTRODUCTION

In the last two decades, the automotive industry has promoted the development of advanced high-strength steels (AHSS) in order to reduce the body weight of passenger cars. Usually, by increasing the strength of the steel, it is possible to decrease the amount of material needed for the same load carrying capacity. For this purpose, the automotive industry currently uses AHSS, such as dual-phase (DP), complex phase (CP), martensitic press hardening steels (PHS), twinning induced plasticity (TWIP) and transformation induced plasticity steels (TRIP) [1]. The ductile steels, including DP, CP, TRIP and TWIP, are utilized in automobile crash protection structures for energy absorption (the crumple zones), while ultra-high strength PHS are suitable for structural elements of the passenger compartment (the safety cage) [1]. These steels belong to 1st and 2nd generation AHSS categories and are used in typical automotive body-in-white, as presented in Figure 1.

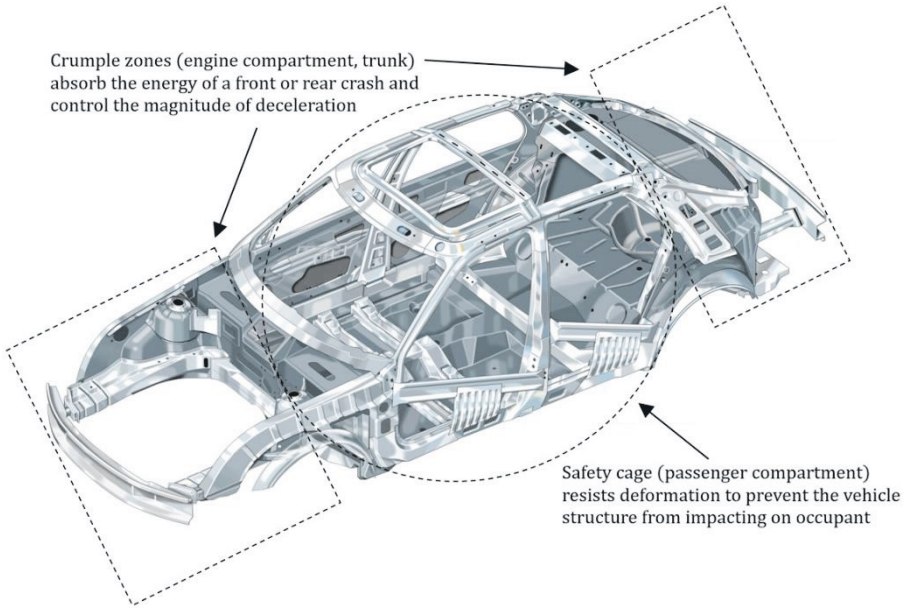

Figure 1. Crash protection in a typical passenger vehicle, adapted from [2], courtesy of SSAB.

In recent years, the global and European standards for vehicle safety and fuel economy have set new ambitious targets for the automotive industry [3], [4]. For example, the European Union fleet-wide average emission target for new internal combustion engine passenger cars is 95 g CO_2/km from 2021 [5]. The strict demand for emission control has led to increased funding for the research and development of novel materials and new designs for even lighter, more energy efficient combustion engine vehicles as well as electric vehicles. To achieve these goals, the utilization of AHSS in light-weight electric vehicle structures has already been demonstrated in FutureSteelVehicle project of WorldAutoSteel in 2011 [6].

In order to reach the new economic and safety requirements, the development of the 3rd generation AHSS is currently ongoing [7]. The aim is to produce novel steels with an enhanced combination of the strength and ductility needed in crash reinforcements, which leads to reducing the car body mass without compromising passenger safety. In this context, the new steel generation includes TRIP-assisted DP, TRIP-assisted bainitic-ferritic (TBF), and quenching & partitioning steels (Q&P) [7], [8]. The commercial TRIP-assisted DP steels are referred to as dual-phase steels with improved formability (DH) in the material specification VDA 239-100 [9] frequently used by the industry when this steel type is produced.

The production of cold-rolled steel strip involves heat treatment, which in the case of TRIP-assisted steels is austenitization or intercritical annealing before the subsequent controlled cooling and isothermal holding step [10], termed in this study TRIP heat treatment. A similar annealing step is also included in Q&P processing, but the processing also includes interrupted quenching and reheating to the holding step, which is called partitioning [8]. Whereas in TRIP heat treatment the steel is quenched rapidly from the annealing temperature to the bainite transformation temperature, Q&P processed steel is quenched from the annealing temperature to below martensite transformation start temperature. In other words, the quenching is interrupted at a point where only part of the austenite has transformed into martensite. By controlling these methods, it is possible to produce microstructures containing metastable retained austenite that have varying mechanical properties.

The motivation for the present study arises from the open questions regarding the link between the microstructure and the mechanical properties of TRIP-assisted and Q&P steels following three design principles: multi-phase, multiscale, and metastable (M^3). For instance, the mechanisms, morphology and the fraction of metastable retained austenite in TRIP-assisted steels have been studied for many decades, but open questions still exist on the ductility of these materials. The

approach of the study is to investigate the microstructural morphology and the influence of the TRIP effect on the local ductility of these steels.

The TRIP effect is a unique metallurgical phenomenon possessed by retained austenite containing steels. It is the strain-induced transformation of retained austenite to martensite during plastic deformation, which increases both strength and elongation [11], [12]. This means that the work-hardening rate of a steel that benefits from the TRIP effect persists at higher strains when that of DP steel or typical high-strength low-alloy (HSLA) steel would begin to decrease [1]. The phenomenon can be utilized in a wide range of steel types with the possibility to reach strength-elongation combination of between 25 000 and 40 000 MPa%, which is the typical target for 3rd generation AHSS [13].

The ductility of the steels can be estimated by studying the strength-elongation combination (MPa%) from the standard tensile test, but comprehension of their formability, toughness and ductility requires further examination. For instance, the local ductility of the material can be investigated [14]-[16], which allows the estimation of damage tolerance, edge-crack sensitivity, fracture toughness, and bendability of high-strength multi-phase steels. These properties are interconnected to the microstructure of the steels; thus the ductility origin can be better understood. This also allows the correlation of different microstructural characteristics and morphologies with the mechanical properties in order to study the properties of 3rd generation AHSS.

1.1 Research questions

The objective of the present study is to observe and characterize the phenomena that occur during heat treatment as well as the properties during straining and forming at room temperature of TRIP heat treated and Q&P processed 3rd generation multi-phase steels containing retained austenite. The aim is to understand the effect of microstructural constituents, such as ferrite, martensite and retained austenite on ductility and formability properties. The technological target is 1180 MPa tensile strength with improved ductility compared to the current AHSS concepts.

The main phenomenon that links the heat treatment and the final microstructure of the investigated steels is the suppression of cementite formation, which allows enrichment of carbon in retained austenite [10], [17]. The first hypothesis of the present investigation is that the rate of bainitic reaction varies at different isothermal

temperatures during TRIP heat treatment, thus affecting the stabilization of retained austenite.

The second hypothesis is that the local ductility of multi-phase steels varies, depending on the morphology and the phases present in the microstructure. The type of heat treatment affects the mechanical properties via morphological changes as well as the phases present in the final microstructure.

The present study concentrates on the 0.08 – 0.10 wt.% carbon-containing alloys, designated as "low-carbon" steel, while previous studies [18]-[23] have mainly investigated silicon and aluminium alloying in 0.20 – 0.40 wt.% carbon-containing steels. The present work also addresses the use of the microalloying elements titanium, niobium and vanadium in 0.20 wt.% carbon containing, "typical carbon" alloys. The effects of titanium and niobium on TRIP-assisted steels have been studied [24]-[28], but to the best of the author's knowledge, only a few publications on the effects of vanadium microalloying can be found [29], [30]. Extensive studies on the effect of vanadium have been performed, for example, with high-carbon forged steels [31] and HSLA steels [32]. The present study widens the understanding on the effect of microalloying additions on the properties of multi-phase steels.

With these objectives in mind, the research questions of the thesis are summarized as follows:

1. *How does the isothermal bainitic transformation holding temperature affect the stabilization of retained austenite in silicon and aluminium alloyed steels in the case of intercritical TRIP heat treatment?*

2. *Can lower carbon containing steels (0.08 – 0.10 wt.%) be utilized to produce TRIP-assisted or Q&P steels with metastable retained austenite intermixed in a dual-phase or multi-phase microstructure which is predominately ferritic and has a tensile strength of 980 MPa and above?*

3. *How does vanadium compare to the more commonly utilized niobium microalloying in the metallurgical response of TRIP and Q&P processed silicon- and aluminium-alloyed steels?*

4. *What is the main origin of ductility and the effectiveness of the TRIP effect in multi-phase TRIP heat treated and Q&P processed steels?*

In order to achieve the objectives of the present thesis, a wide literature survey was performed and a broad experimental plan was executed. Chapter 2 addresses the following topics: austenite to martensite transformation, carbon partitioning during isothermal processes, and the effect of different alloying additions in steels that benefit from the TRIP effect. Chapter 3 summarizes the experimental materials and methods utilized to answer the research questions and to reach the technological target. Chapter 4 describes the experimental results from material characterization, while the findings are discussed in Chapter 5 by reflecting them to the research questions. As a conclusion, Chapter 6 readdresses the research questions and draws remarks on the discussion. Finally, future research of certain topics left unanswered after the present study is proposed in Chapter 7. The structure of the thesis and interconnections between the hypothesis and research questions is presented in Figure 2.

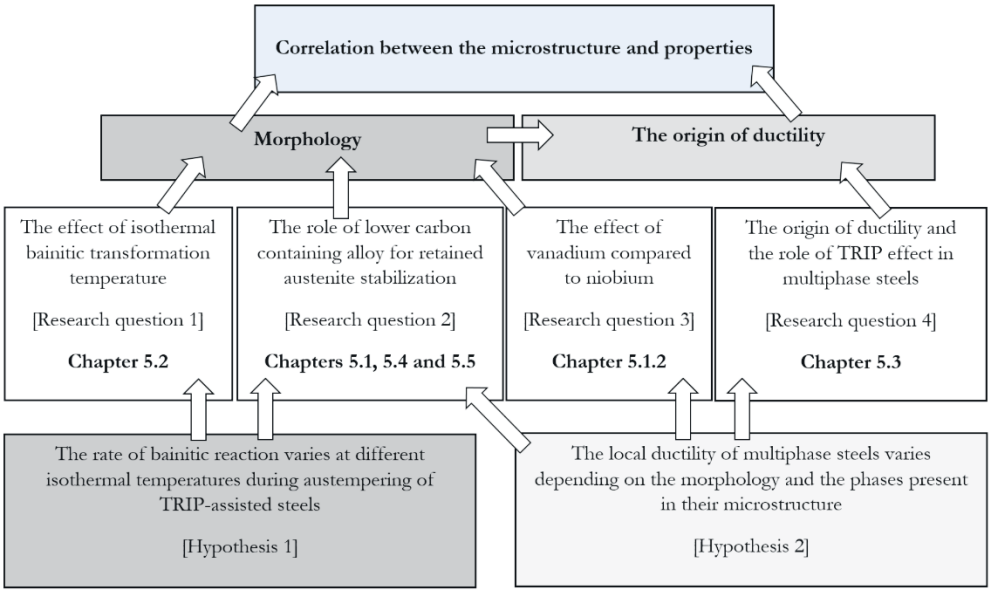

Figure 2. Structure of the present thesis.

1.2 Novel features

The present study introduces the following novel scientific contributions:

- The intercritical quenching and partitioning of low-carbon containing steels led to local formability type of material properties, while global formability was achieved by intercritical TRIP heat treatment.

- The stabilization of the retained austenite in 0.08 – 0.10 wt.% carbon containing steel was possible using intercritical annealing and the Q&P process.

- The properties of TRIP-assisted DP type microstructure were enhanced by utilizing quenching & partitioning process. This was attributed to partitioned martensite in the final microstructure, which is useful when a higher yield strength is required.

- The effect of vanadium microalloying on TRIP-assisted steels was analysed by implementing both vanadium and vanadium-niobium microalloying and comparing them to titanium microalloyed steel. The use of vanadium-microalloying decreased the retained austenite content of TRIP-assisted DP steels.

2 THEORETICAL FRAMEWORK

An overview of the literature on retained austenite containing steels is presented in this chapter. Typical characteristics of these steels are first presented by explaining the TRIP effect and the reasons for its importance regarding the properties of TRIP-assisted steels. Secondly, this chapter covers aspects behind the alloy design of these types of steels.

2.1 Characteristics of steels with TRIP effect

Conventionally, TRIP steels have been referred to as the steel type belonging to the 1st generation AHSS. However, in broader terms it can be said that TRIP steels consist of all the steels which benefit from the TRIP effect. For instance, TRIP-assisted steels usually refer to the novel TRIP steels in the 3rd generation AHSS, which differ noticeably from earlier steels. The earlier TRIP steels typically had a high silicon content (1.5 wt.%), which led to the deterioration of the hot-dip zinc galvanizing capacity (galvanizability) of the steel, because Si creates a tough oxide layer on the hot-rolled steel which is difficult to remove even in pickling [33], [34]. From a production point of view, this meant that composition modifications are needed in order to secure sufficient galvanizability. Since galvanizability is important for the additional corrosion protection of carbon steels, Al alloying with the addition of P has been proposed for hot-dip galvanized TRIP steels [10].

Modern dual-phase high-formability, TRIP-assisted bainitic-ferritic and quenching & partitioning steels are produced with numerous alloying concepts, including low-silicon or silicon-free chemical compositions with Cu, Al, Mo & P alloying additions instead of silicon to suppress carbide precipitation. Microalloying elements such as Nb, Ti & V are used to increase the strength of the material by carbide precipitation and solid solution strengthening when the carbon content has to be limited.

Before the above-mentioned modern steels were developed, the first findings of microstructural effects similar to the TRIP effect were reported by Scheil in 1930s

[35], [36] in an observation of the shear-activated formation of martensite needles in Fe-Ni alloys.

Even though the first observation of the TRIP effect dates back 90 years, it was not utilized to increase formability until the 1960s and 1970s in Fe-Cr-Ni austenitic stainless steels by Zackay et al. [37] and Bhandarkar et al. [38]. They were the first to use the famous acronym TRIP when they connected the phase transformation during straining to the observed excellent strength-ductility ratio of the steel [39].

Two decades later, the effect was discovered in certain retained austenite containing low-alloy carbon steels, which laid the groundwork for future automotive steel development. Matsumura et al. [19] and Jha et al. [40] have studied the effect of retained austenite on the properties of commercially produced dual-phase steels, later to become known as TRIP-assisted DP steels. These steels were studied by several researchers during the 1990s, mainly in the Nippon Steel Corporation [41]-[45]. Thereafter, several research institutes both in academia and in the industry have performed investigations on the subject [46]-[48].

The commercial TRIP-assisted DP steels developed in the 1990s suffered from delayed fracture, which had a negative effect on their usability. Since then, the phenomena in commercial grades have been studied [49]-[50]. The presence of hydrogen leads to the degradation of mechanical properties which may cause premature failure of the material, known as hydrogen embrittlement (HE) [51]. The advanced high strength steels with a high tensile strength of above 780 MPa require a low impurity level in the steel, because impurities such as large inclusions and segregations act as hydrogen traps, thus working as weak points for hydrogen-induced cracking. Regarding retained austenite containing steels, several studies [52]-[55] have been performed which discuss the mechanics of HE. The risk factors of hydrogen are microstructural properties, diffusible hydrogen content from internal and outside surroundings and tensile stress, both residual and applied. If at least two of these risk factors are met, the risk of hydrogen-induced failure is increased.

2.1.1 Austenite to martensite transformation

The TRIP phenomenon implies that the local transformation of metastable (retained) austenite to martensite hardens a portion of the microstructure, thus preventing further strain localization in those areas. Martensite transformation can occur spontaneously and athermally below the M_s temperature during quenching. When this is the case, the transformation is time-independent and the transformation

is driven by the difference in Gibbs free energy between the austenite and ferrite phase, which increases as the temperature drops.

In contrast to athermal transformation, martensite transformation can also occur as a function of either stress [56] or strain [57] at a static temperature. For stress-assisted transformation to occur, a mechanical driving force is needed during the straining of material which leads to an isothermal martensite transformation above the M_s temperature. The generalization of martensite transformation in terms of both stress and strain is presented in Figure 3.

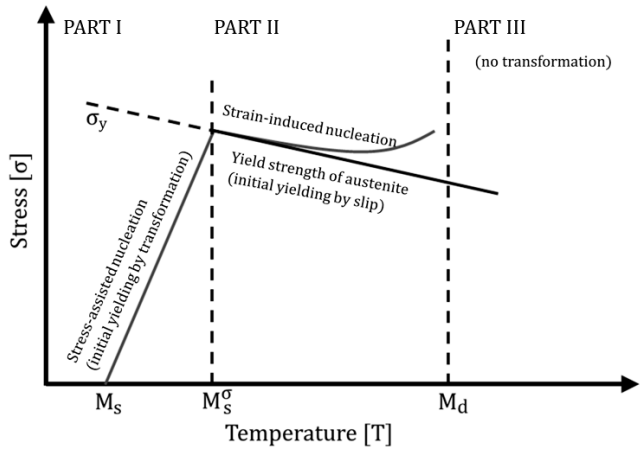

Figure 3. Schematic representation of the stress required for stress-assisted and strain-induced martensite nucleation at different temperatures, adapted from [57].

Martensite transformation can happen above the M_s temperature by stress-assisted transformation when a mechanical driving force, U, is present. In the first part of the transformation between M_s and M^{σ}_s, the temperature increases linearly with the stress up to the yield strength of austenite. The second part is the continued plastic deformation of the austenite phase above M^{σ}_s, which increases the amount of strain-induced martensite leading to subsequent nucleation of shear band intersections within the steel matrix. Because the martensite transformation happens at shear band intersections, the austenite work-hardens considerably. The transformation, however, has an upper limit temperature designated as M_d. In the condition of the third part of transformation, austenite can only deform plastically and even external mechanical loading cannot nucleate martensite.

The groundwork for modelling strain-induced transformation was performed by Olson and Cohen in the 1970s [57], [58]. They proposed an empirical model for strain-induced transformation that was based on experimental data collected a

couple of decades earlier from experiments with austenitic steels. In this model, the volume fraction of martensite is f_m, which at strain ε is obtained using Equation 2.1 [58]:

$$f_m = 1 - e^{[-\beta_t\{1-\alpha_t\varepsilon\}^n]}, \tag{2.1}$$

where n is constant and is affected by the two temperature-dependent parameters, α_t and β_t. Parameter α_t is dependent on the stacking fault energy of the steel and parameter β_t defines the probability of a shear-band intersection creation at a nucleation site, which is dependent on the chemical driving force.

The model by Olson and Cohen was formulated to describe fully austenitic steels, so later it was considered probable that steels with lower austenite content would react differently. Therefore, Sugimoto et al. [59] proposed a model for TRIP-assisted steels, presented in Equation 2.2:

$$log(f_\gamma) = log(f_\gamma^0) - k\varepsilon, \tag{2.2}$$

where f_γ^0 is the original retained austenite volume fraction and the volume fraction f_γ of the untransformed austenite at a plastic strain ε. The value k is a constant larger than zero which is derived from the experimental data, meaning that the equation has limited applicability. The model does not take into account the test temperature or chemical composition of the steel.

The limited applicability of the equation by Sugimoto et al. [59] has led to further development of the model by Sherif et al. [60] into a formula that takes into account the plastic strain, deformation temperature, original amount of retained austenite and also chemical composition. An adaptation of the formula is presented in Equation 2.3:

$$ln(f_\gamma^0) - ln(f_\gamma) = k_1\Delta G^{\alpha'\gamma}\varepsilon, \tag{2.3}$$

where f_γ^0 is the original retained austenite volume fraction and the volume fraction f_γ of the untransformed austenite at a plastic strain ε, similarly to Equation 2.2. In the equation by Sherif et al. [60], the constant k has been replaced by integrating $k_1\Delta G^{\alpha'\gamma}$ which assumes that k is proportional to the driving force $\Delta G^{\alpha'\gamma}$. The addition of the driving force into the equation means that the practical applicability of the model increases; it allows the progress of austenite transformation to be followed as a function of plastic strain, chemical composition and temperature at which the

deformation is carried out. They demonstrated that the model represented a modest experimental dataset collected from the literature with reasonable accuracy.

The mechanical driving force of martensite transformation (U) can be explained by the example presented in Figure 4, where the driving force $\Delta G^{\gamma\alpha}$ is assumed to be negative [61]. Due to the applied strain, the driving force increases and martensite transformation is possible at a higher temperature than it would otherwise be ($M_s < M^{\sigma}_s$). M^{σ}_s is the highest temperature where the stress can stimulate martensite transformation, because this is the yield strength of austenite (Fig. 3). The free energy difference ($\Delta G_{Ms}{}^{\gamma\alpha}$) required for martensite transformation increases linearly to the higher temperature up to M^{σ}_s. After this point, the required stress is lower than the stress condition.

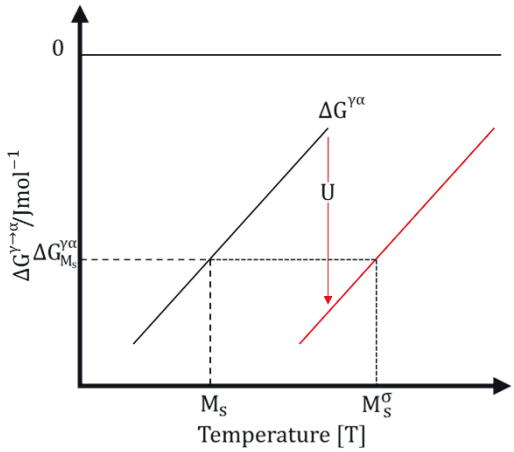

Figure 4. Schematic representation of the chemical driving force for martensitic transformation when free energy is assumed negative, adapted from [61].

In addition to the above-mentioned models, Ludwigson and Berger [62] have proposed an alternate model to describe the stability of austenite during straining. Much like the Olson and Cohen model, this relation was also developed for austenitic stainless steels, but has since been applied to carbon steels containing retained austenite [63]. The Ludwigson & Berger model is presented in Equation 2.4:

$$\frac{1}{f_\gamma} - \frac{1}{f_\gamma^0} = \frac{k_p}{p}\varepsilon^p, \tag{2.4}$$

where f_γ is the austenite fraction at true strain, $f_\gamma{}^0$ is the austenite fraction of the unstrained material, the constant k_p is related to the mechanical stability of austenite

with strain (ε), and p is the autocatalytic factor of austenite which indicates the likelihood of austenite transformation. The value p = 1 has been reported to be in good agreement with the experimental data of TRIP-assisted and Q&P steels [63].

De Moor et al. [63] have reported that lower k_p values were generally obtained for Q&P steels, suggesting higher austenite stability and less autocatalytic propagation. Autocatalytic propagation means that the formation of martensite promotes additional nucleation of more martensite. In TRIP steels, the reduction in autocatalytic propagation was observed to be connected to the introduction of secondary phases, such as intercritical ferrite or bainite laths.

According to Bhadeshia [64], the elongation contribution made by the transformation of 5 – 15 vol.% retained austenite containing steel is in the range of 0.75 – 2.25%, assuming that all of the austenite is transformed into the orientation of martensite most favourable to straining. The experimentally observed increases in elongation in steels assumed to benefit from the TRIP effect are, however, much higher than this [13]. It has been proposed that the additional work hardening imposed by strain-induced martensite transformation is in fact the most important factor behind the observed increases in elongation [65].

2.1.2 Influence of interactions between phases

Jacques et al. [65] have explained that the stability of retained austenite is not only dependent on austenite properties, but also on the properties of the other surrounding phases when austenite was the dispersed phase in a ferrite-based microstructure containing martensite. This means that in DP and TRIP-assisted steels, the strains associated with martensite formation are known to generate stresses and free dislocations in neighbouring grains of the ferrite matrix, near the ferrite-martensite interface. When the steel matrix is subjected to overall straining during, for example, a tensile test, the strain-induced phase transformation contributes to the enhancement of the dislocation formation in ferrite.

From the perspective of increased strength, the extra hardening by martensite formation is beneficial. Jacques [66] has proposed the relation of increased hardening by martensite formation, which is presented in Figure 5.

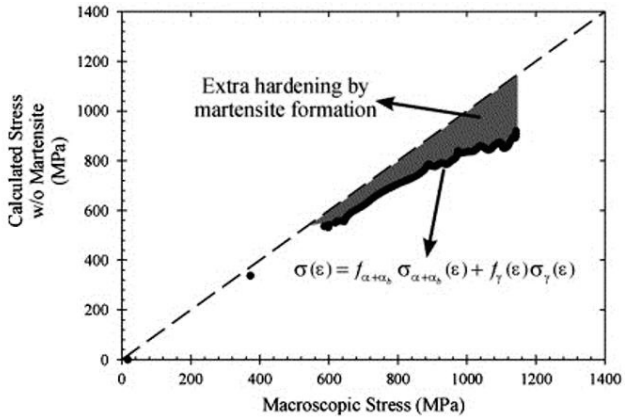

Figure 5. Macroscopic stress compared to the stress without taking the martensite phase into account [66].

Jacques [66] has postulated that the present TRIP-assisted steels contain so-called evolving composites since the proportions of austenite and martensite continuously change during straining, thus modifying stress partitioning. The shaded area in Figure 5 corresponds to the strengthening result from the progressive appearance of martensite [66].

More recently, the above-mentioned additional hardening by martensite transformation with increasing stress has been referred to as deformation-induced phase transformation (DIPT) or deformation-induced martensitic transformation (DIMT). Kim et al. [67] have explained the terminology in their research on Fe-12Mn steels. DIPT was explained as plastic deformation building up internal strain energy thus providing an additional driving force for transformation, which results in enhanced ductility with higher strength. Similarly to the model by Olson and Cohen [57], DIMT occurs in the range between M^{σ}_{s} and M_d as the strain-induced nucleation of martensite.

In an investigation of 0.2 and 0.4 mass% carbon-containing TRIP steels, Harjo et al. [68] have concluded that the different carbon content in the steel mainly affected the phase fractions of bainite and austenite, while the carbon concentration of austenite was similar in both cases (Fig. 6). They also found that the martensitic transformation started at the beginning of plastic deformation, after which it occurred continuously throughout plastic deformation, accompanied by texture evolution in the constituent phases.

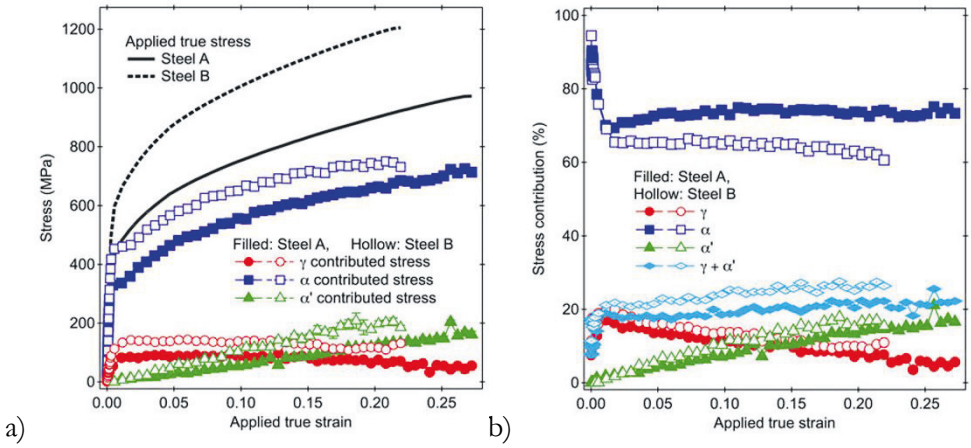

Figure 6. Contributed stresses to a) flow stress from austenite (γ), bainitic ferrite (α), and martensite (α') during deformation and b) corresponding stress contribution percentage values from these phases [68].

Harjo et al. [68] have shown that a different carbon content did not seem to affect the changes in the relative fraction of martensite transformation, which was observed as having a linear relation to strain with the same gradient even though the stress levels were different. They concluded that the phase stress, which was evaluated from phase strain according to Hooke's law using the elastic constants and Poisson's ratio, was much larger in martensite than the phase stresses of austenite and ferrite after martensite had been formed. The stress increase contribution of ferrite and austenite was almost unchanged, whereas the stress increase by martensite increased with the strain (Fig. 6b).

Transformation of austenite to martensite may be considered somewhat simple in theory, but in reality, the situation is more ambiguous. Martensite nuclei growth occurs in multislip regions by phase transformation which is stress- or strain-driven depending on the temperature. Ma et al. [69] have stated that separating the stress-assisted and the strain-induced martensite transformation mechanisms is challenging, since it is difficult to measure the austenite yield strength to estimate the chemical driving force for martensite transformation, and thereby calculate the true local stresses. Models for the phenomenological theory of martensite crystallography or physical principles of martensite transformation are therefore rarely seen in the literature. Physically-based models for microstructure-mechanical properties, however, are found for TRIP and Q&P steels [69], [70]. These constitutive models are typically semi-empirical and present the degree of martensite transformation against elongation.

Ma et al. [69] were able to develop a constitutive model based on the inverse Nishiyama-Wassermann relationship. Their model considered both strain-induced martensite nucleation and stress-assisted martensite growth at the same time. They concluded that the mechanical anisotropies of stress-assisted and strain-induced phase transformations were significantly different and the transformation of austenite grains to martensite was more rapid under tension than under compression. Their main conclusion, regarding the mechanical properties of TRIP steels, was that the TRIP effect in fact enhanced the work-hardening rate, hence being beneficial for improving the strength-ductility of steels.

Seo et al. [70] have approached constitutive modelling by examining Q&P processed medium Mn steels, which contained carbon-rich retained austenite and various amounts of tempered martensite. They proposed equations for primary, secondary, and mechanically induced martensite formation and calculated the dislocation density in martensite during deformation. As a result, they reliably modelled the work hardening rate against the true strain.

In addition to the TRIP phenomenon, Zhang et al. [71] have proposed another phenomenon contributing to the ductility increase of steels containing retained austenite: dislocation absorption by the retained austenite effect (DARA). Based on the evidence from transmission electron microscopy (TEM) and X-ray diffraction (XRD) studies, they suggested that the so called DARA effect might have had a role in the work-hardening capacity of quenching, partitioning and tempering (QPT) steels. Supposedly, austenite can continuously absorb dislocations from martensite during deformation which, at first, leads to a decreasing average dislocation density in martensite laths. After the initial decrease, the dislocation density increases slightly due to the competition between the DARA effect and dislocation multiplication. This dislocation movement to neighbouring retained austenite was indirectly verified by TEM observations. They claimed that such an effect would intensify the deformation capability of the martensite phase.

In a continuation research study with QPT steels, Zhang et al. [72] have calculated that the martensite transformation induced strain increase due to retained austenite in 0.2 and 0.4 wt.% carbon-containing steels, would be 1.56% and 3.84% respectively, following the calculations of Bhadeshia [64]. The true-stress true-strain curves of the steels in question, presented in Figure 7, shows maximum strains (Fig. 7a) and work-hardening performance (Fig. 7b). The work-hardening increase due to higher carbon content was in line with the findings by Harjo et al. [68] (Fig. 6).

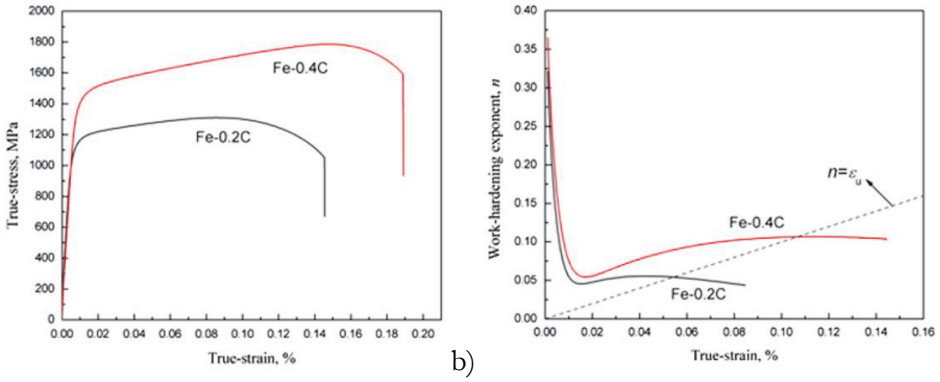

Figure 7. a) True stress-strain curves and b) work-hardening exponent as a function of true strain of Fe-0.2C and Fe-0.4C of QPT steel [72].

Zhang et al. [72] were unable to verify the DARA effect definitively because their investigations were indirect. However, they were able to explain that the flake-like retained austenite laths (also known as retained austenite films) located between the martensite laths could have effectively enhanced ductility by both the DARA and TRIP effects.

2.1.3 Stability of retained austenite

Due to the difficulties in the constitutive and theoretical material modelling of retained austenite containing steels, far more common methods are material characterization by tensile or formability testing and microstructural investigations via scanning electron microscopy (SEM) and electron back-scatter diffraction (EBSD).

The stability of retained austenite is of key importance in enhancing the TRIP effect during straining of the material. The stability is affected by the carbon content of austenite [68] and the surrounding phases [65] as well as the morphology of the surrounding phases in connection to retained austenite [73]. On the last mentioned factor, Sugimoto et al. [73] have proposed that if the retained austenite is surrounded by a hard microstructure, e.g. martensite or bainite laths, volume expansion during strain-induced martensite transformation is constrained due to hydrostatic pressure, which increases the stability of retained austenite by decreasing its M_s temperature.

Wang et al. [74] have concluded that the effect of retained austenite grain size on stability and transformation capacity in TRIP steels is two-fold: grains smaller than 0.01 μm are ineffective because they will not transform into martensite and grains

larger than 1 μm transform immediately during cooling or at the first stages of straining thus being ineffective.

The shape aspect of the retained austenite mechanical stability has been investigated by Park et al. [75] using tensile straining and EBSD measurements. Their measurements revealed that the granular retained austenite, located in ferrite boundaries, fully transformed into martensite when the tensile strain was gradually increased from 0% to 15% (Fig. 8). Film-type retained austenite, on the other hand, remained untransformed even with 26% of nominal strain. They estimated that film-type retained austenite exists between ferrite laths in the bainitic microstructure. A similar effect has been found in a study of moderately high carbon TRIP steels by Varshney et al. [76] and more recently in a study on Q&P steels by Tan et al. [77].

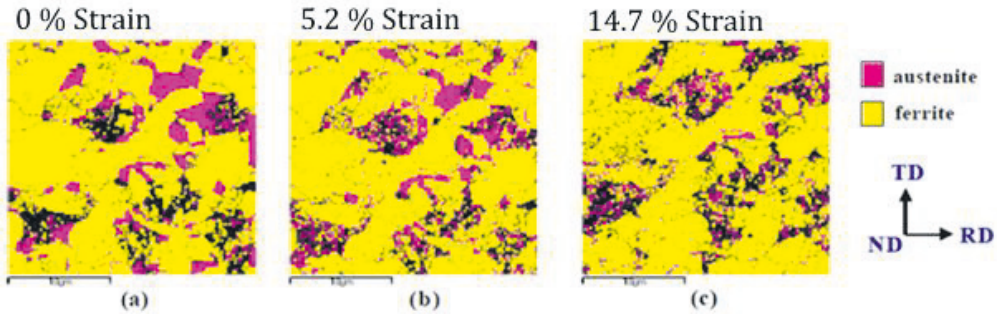

Figure 8. Strain-induced transformation of retained austenite into martensite as EBSD phase maps representing the following strains and retained austenite fractions: a) strain 0%, RA 14.9 vol.%; b) strain 5.2%, RA 10.9 vol.%; and c) strain 14.7%, RA 5.9 vol.% [75].

Tirumalasetty et al. [78] have studied a similar effect on TRIP-assisted 800 MPa strength class steel, in which they found that the retained austenite grains at the surface of the steel were the first to transform, whereas the grains in the bulk of the material had a lower tendency to transform. Examples of their findings are presented in Figure 9, which shows the EBSD phase identification maps from the transformation of retained austenite grains at ferrite triple junctions (the square areas), while those containing twin faults (the hexagons) have twin boundaries indicated in blue.

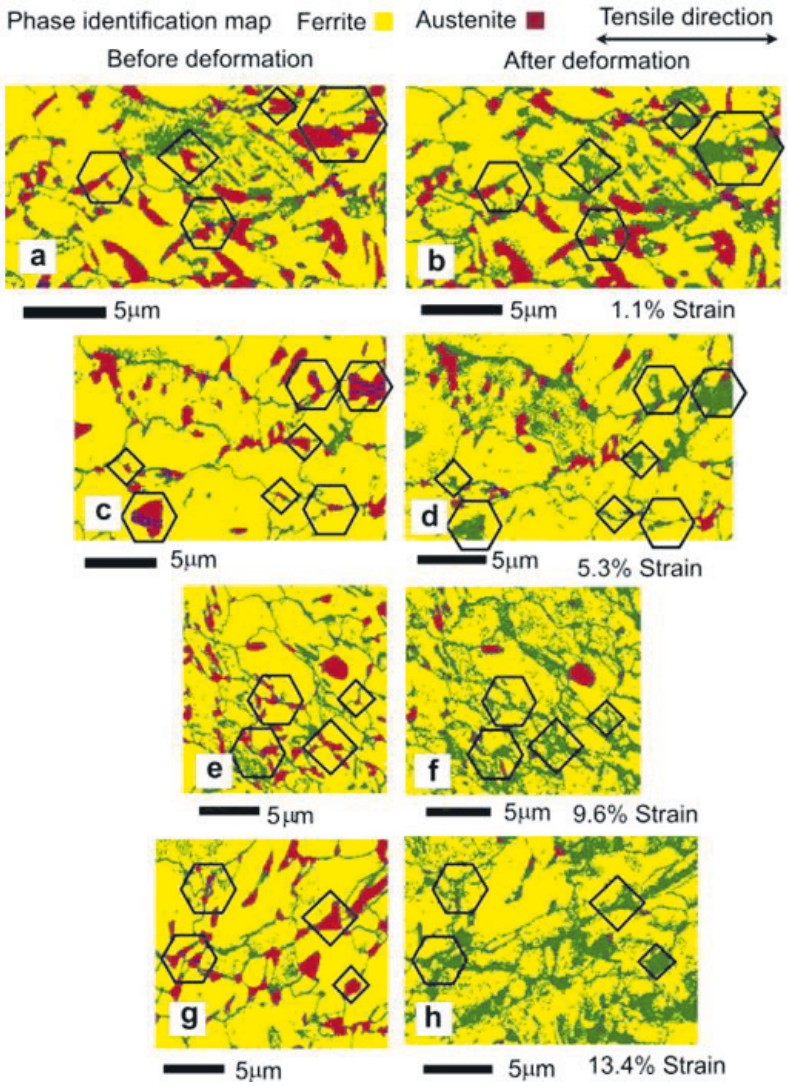

Figure 9. EBSD phase maps representing the strain-induced transformation of austenite to martensite at 1.1% to 13.4% strain [78].

Tirumalasetty et al. [78] have also found that local defects near the retained austenite grains, such as twins, lowered the stability of retained austenite leading to transformation at an earlier stage. They identified that austenite grains, which resided at the grain boundaries between multiple ferrite grains, were amongst the first to transform, while austenite grains fully embedded in larger ferrite grains might undergo rotations. In addition, they concluded that the differences in strain-induced

behaviour was likely to be associated with different stress states and grain rotation capabilities exhibited by the austenite grains upon deformation.

2.1.4 Austenite formation during intercritical annealing

During the heat treatment of TRIP-assisted steels, the introduction of the austenite phase is significant because austenite transforms into other phases during subsequent cooling. The evolution of austenite transformation at elevated temperatures is studied using the Avrami-type phase transformation. For example, the experimental data from a dilatometer test can be fitted to an equation called the Johnson-Mehl-Avrami (JMA) equation to calculate the fraction of intercritical austenite transformed at the desired temperature. The intercritical austenite fraction ($f_{\gamma IA}$) can be obtained from Equation 2.5 [79]:

$$f_{\gamma IA} = 1 - e^{-kt^n}, \tag{2.5}$$

where n is a numerical exponent whose value can vary from 1 – 4. Assuming that there is no change in the nucleation mechanism, n is independent of temperature, whereas k on the other hand is dependent on time t.

De Meyer et al. [80] have presented an empirical method for evaluating both the intercritical annealing and bainite transformation of TRIP-assisted steels using the JMA equation. They proposed that, when the evolution of ferrite to austenite follows the JMA equation, a plot of $\ln\{\ln[1/(1-f_{\gamma IA})]\}$ versus ln(t) should yield a straight line which has a slope equal to n and an intersection with the y axis equal to ln(k). Figure 10 presents plots of $\ln\{\ln[1/(1-f_{\gamma IA})]\}$ from a study with Si- and Al-alloyed TRIP-assisted steel at annealing temperatures of 780 °C and 840 °C.

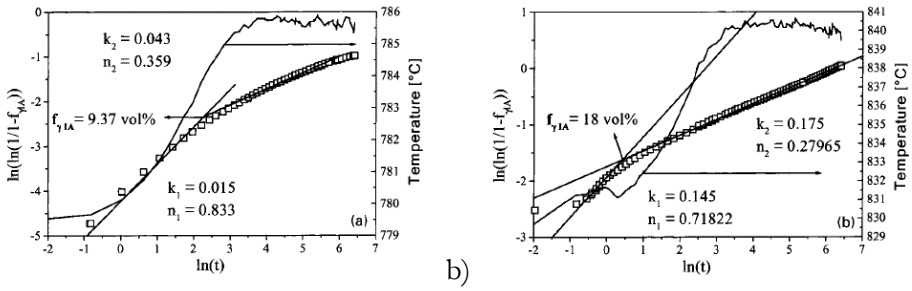

a) b)

Figure 10. Plots of $\ln\{\ln[1/(1-f_{\gamma IA})]\}$ for intercritical annealing temperatures of (a) 780 °C and (b) 840 °C of CMnAlSi TRIP steels [80].

Figure 11 presents the dilatometer results of the same experimental steel by DeMeyer et al. [80]. The A_{c3} increasing effect of Al can clearly be observed in the dilatometer curves when CMnSi is compared to CMnAlSi.

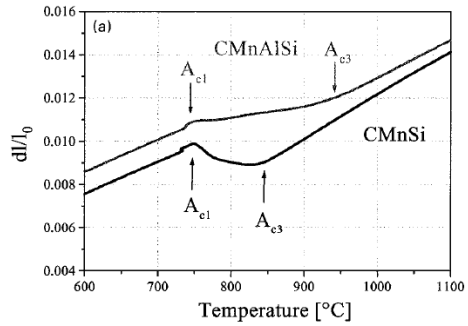

Figure 11. Dilatometer measurement of intercritical annealing of Si- and AlSi-alloyed TRIP-assisted steels [80].

Oh et al. [81] have utilized a variation of the JMA equation in the dilatometric analysis of low carbon TRIP steels: the Johnson-Mehl-Avrami-Kolmogrov equation (JMAK). In contrast to JMA, the novel variation takes into account the maximum austenite fraction at the intercritical temperature (f_{eq}). In this case, $f_{\gamma IA}$ is expressed as Equation 2.6:

$$f_{\gamma IA} = f_{eq}(1 - e^{-kt^n}) \tag{2.6}$$

Oh et al. [81] found that the effect of carbon enrichment during intercritical annealing can be effectively taken into account in this analysis. They concluded that this variation describes the annealing effect of TRIP-assisted steels more accurately than Equation 2.5.

2.1.5 Isothermal bainitic transformation

In TRIP-assisted steels, the retention of the austenite phase from its high temperature state to room temperature, and below, is possible through an isothermal bainite transformation which is also referred to as austempering [10], [82]. The bainitic transformation temperature region resides below the range where pearlite is formed in cooperation with ferrite and cementite, but above the displacive, diffusionless transformation of austenite to martensite. This intermediate temperature range, which forms maybe the most complex microstructural

constituent, bainite, can also be used for austenite stabilization. However, carbide precipitation must be hindered by alloying elements in order to have a sufficient amount of free carbon for retained austenite stabilization.

De Cooman [10] has reviewed the structure-properties relationships in intercritically annealed cold-rolled TRIP-assisted steels. Figure 12 shows a schematic representation of a continuous annealing cycle (left), and a pseudo-binary Fe-C diagram for Fe-1.5%Mn showing the changes in C content of the austenite (middle), which includes the corresponding phase diagram indicating the position of T_0 where the free energy of ferrite equals the free energy of austenite ($G_\alpha = G_\gamma$). When this condition is reported as carbon content vs. temperature (right), T_0 indicates the end-point for the bainitic transformation during austempering.

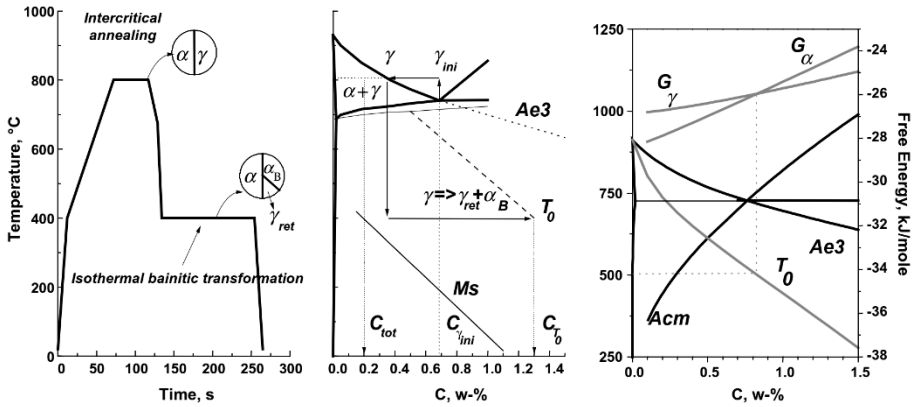

Figure 12. Schematic representation of a typical continuous annealing cycle and the carbon enrichment of retained austenite during austempering, adapted from [10].

From the conditions presented in Figure 12, it follows that the absence of cementite precipitation makes retained austenite enrichment possible during isothermal bainitic transformation. Simultaneously, bainitic ferrite platelets nucleate and grow from the austenite, which has an increasing carbon content. This reaction continues until it reaches the point dictated by thermodynamics, T_0. After this point, the carbon content of the retained austenite no longer increases, which means that the holding period will not lead to additional growth of the platelets. Longer times would lead to the decomposition of austenite into ferrite and carbides [10], [80], [82], [83]. The austempering effect on the properties of TRIP-assisted DP steels has been investigated in several studies [11], [34], [84], [85].

Sugimoto et al. [86] have concluded that the increased formability was the result of a uniform, fine lath structure matrix and film-like, stable retained austenite. To

determine formability, they used hole expansion tests and concluded that the film-like retained austenite decreased the edge-damage of hole punching on the material, thus developing an uninterrupted plastic flow. This led to an increasing hole expansion ratio via the suppressed crack propagation due to the TRIP effect of retained austenite. In contrast to the effect of retained austenite, they noted that the blocky initial martensite might increase the surface damage, thus contributing to crack propagation as stress concentration sites. They concluded that the final microstructure contained blocky martensite especially when austempering was performed above M_s [87].

Hausmann et al. [88] have demonstrated the possibility to adjust the mechanical properties of 1.0 wt.% Si-containing TRIP-assisted bainitic-ferritic steel by implementing over-ageing in different parts of the temperature range from 350 °C to 475 °C. They proposed that the yield ratio, when the maximum strength was 1180 MPa, could be controlled by utilizing the lower or upper part of the range. At the lower end, the yield ratio was 0.80, while the upper end resulted in 0.60, because the yield strength was lower in that case. In contrast, the middle range, which was from 400 °C to 425 °C, led to the highest total elongations, but in that case the tensile strength was approximately 1000 MPa. They concluded that it was possible to produce TRIP-aided bainitic-ferritic type steel by using the lower temperature range of the bainitic transformation region, which was near the M_s temperature of the steel. In this case, however, when temperatures below the bainite nose are used, the holding times should be long enough for isothermal bainite transformation to proceed to the increased ranges. Due to the decreased bainite transformation rate, the carbon partitioning into retained austenite takes longer.

2.1.6 Carbon movement during quenching and partitioning

Steels produced using the quenching & partitioning (Q&P) process are promising candidates for the 3rd generation AHSS, because they combine high strength with increased formability, unlike many other steels of a similar strength level. The conventional Q&P method aims at producing tempered martensitic steel containing some amount of retained austenite. Similarly to TRIP steels, Q&P steels also contain retained austenite which assists in inducing increased ductility properties in the final product. In addition to TRIP heat treatment, the Q&P concept introduces an intermediate quenching step which is of key importance, because the method relies on carbon enrichment from martensite to austenite during the subsequent

partitioning step. The partitioning step is comparable to austempering in TRIP heat treatment. The schematic presentation shown in Figure 13 compares these heat treatment types.

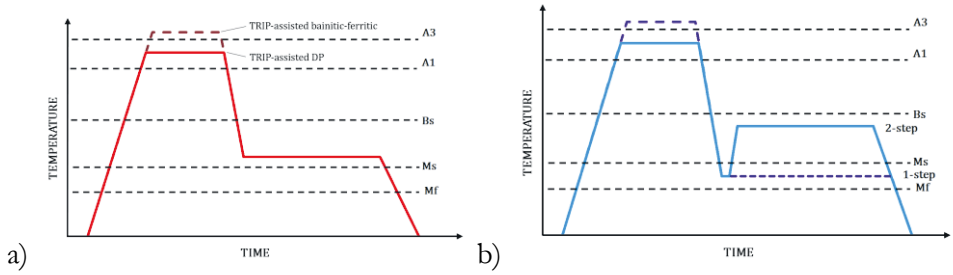

Figure 13. Comparison of heat treatment cycles aiming at retained austenite containing steels: a) intercritically annealed TRIP-assisted DP cycle and fully austenitized TBF cycle, and b) intercritical or fully austenitized Q&P cycles with 1-step or 2-step partitioning.

The Q&P concept, which was proposed by Speer et al. in 2003 [89] and further investigated by Streicher et al. in 2004 [90], has since attracted interest from academia and the steel industry [91]-[94]. Although the industrial implementation of Q&P is still sparse, the automotive industry has shown great interest in it [95]-[96] due to the formability of Q&P steels. For example, the yield strength and hole expansion ratio may reach values beyond those of DP steels. In an ideal case, the microstructure of the steel is predominantly martensite, rather than ferrite or bainitic ferrite, leading to the higher strength levels required in many automotive safety applications [97].

For continuously annealed and galvanized steels, two basic variants of Q&P heat treatment exist: 1-step and 2-step Q&P processes (Fig. 13b). In the first variant, carbon partitioning is achieved by a holding step at the initial quenching temperature (QT) before final cooling to ambient temperature. In the second variant, partitioning is achieved by reheating the steel to a higher temperature, called the partitioning temperature (PT).

In both variants, the austenitized microstructure or intercritically annealed austenite-ferrite mixture is then rapidly cooled below the M_s temperature in order to transform some of the austenite into martensite. The quenching end temperature is controlled and stopped before the martensite transformation finish temperature (M_f), because some amount of austenite should be left untransformed for the partitioning of carbon into untransformed austenite. The Koistinen-Marburger (K-M) equation (Eq. 2.7) [98], which calculates the fraction of martensite (f_m) in cooling below the M_s temperature, can be utilized to optimize the quenching temperature:

$$f_m = 1 - e^{-K(M_s - QT)}, \quad (2.7)$$

where M_s is the martensite transformation start temperature of the material, QT is the quenching temperature and K is the fitting constant. It is typically assumed that all the competing transformations are avoided, thus all the carbon remains free to partition into retained austenite [89]. The QT can be estimated by calculating the new M_s temperature from the composition of austenite after the above mentioned prediction.

The M_s temperature can be predicted using physical or empirical models. Typically, the empirical models assume a linear relationship between the alloying content and M_s. An example of such a linear relationship is Equation 2.8 proposed by Stuhlmann [99]:

$$M_s(°C) = 550 - 350C - 40Mn - 20Cr - 10Mo - 17Ni - 8W - 35V - 10Cu + 15Co + 30Al \quad (2.8)$$

After the quenching stage, the initial austenite fraction is $1 - f_m$. Due to the assumption that all the carbon remains free to partition into retained austenite without carbide precipitation for example, the carbon content of austenite after the partitioning C_γ step can be calculated by using Equation 2.9 [100]:

$$C_\gamma = \frac{C_{alloy}}{1 - f_m}, \quad (2.9)$$

where C_{alloy} is the carbon content of the steel. The optimal QT is selected in order to produce the highest possible phase fraction of retained austenite in the final microstructure. The selection of QT and optimization of the Q&P process can be performed by utilizing the theory of constrained carbon paraequilibrium (CPE). CPE is the metastable condition representing the completion of carbon partitioning between martensite and austenite. In contrast to the paraequilibrium conditions in which the Fe/X ratios (X = carbon, for example) are fixed and the carbon potentials are equal in phases, CPE represents a complete absence of iron and substitutional atom movements. The carbon atoms, however, are free to migrate if needed. [89]

The most significant property of CPE is that there is an infinite set of possible ferrite and austenite composition variations that satisfies the general thermodynamic condition [89]. Conventionally, these thermodynamic conditions are represented as a tangent intercept of $\mu_c^{\alpha-1} = \mu_c^{\gamma-1}$. The conditions are illustrated in Figure 14, which represents the schematic molar Gibbs free energy (G) against the composition

diagram of metastable equilibrium at a certain temperature between ferrite (α) and austenite (γ) and offers two possible CPE conditions (designated as I and II).

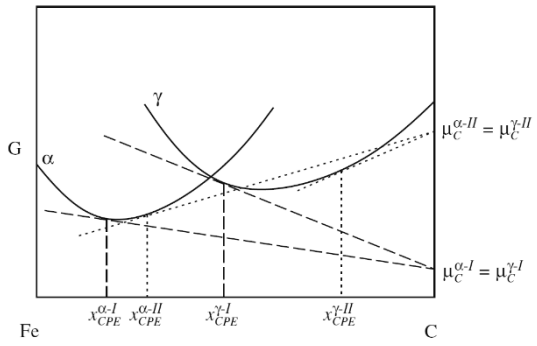

Figure 14. Schematic molar Gibbs free energy against ferrite and austenite composition diagrams [101].

In order to estimate the quench condition needed for the highest possible retained austenite at room temperature, the phase fraction can be calculated using the K-M relationship (Equation 2.7). The resulting carbon content and final retained austenite content are plotted against QT [97].

Figure 15a presents an example of an ideal QT for a Fe-C binary system, whereas Figure 15b presents the effect of carbon content on the ideal QT between 0.2 – 1.0 wt.% carbon. Clearly, the binary system is idealized and further examination of other composition variations is needed in practice. For binary alloys, the chemical composition of phases at an intercritical equilibrium is obtained from phase diagrams by the lever rule. When multicomponent alloys are in question, the common practice is to utilize kinetic and thermodynamic calculation software and suitable thermodynamic databases, such as JMatPro® and Thermo-Calc [102], [103]. When using JMatPro®, for instance, it is possible to construct a phase-fraction-temperature diagram predicting the desired temperature range of the phase fractions and compositions. The Q&P methodology, combined with the above-mentioned assumption of the M_s temperature, gives a basic understanding of the potential microstructures and properties.

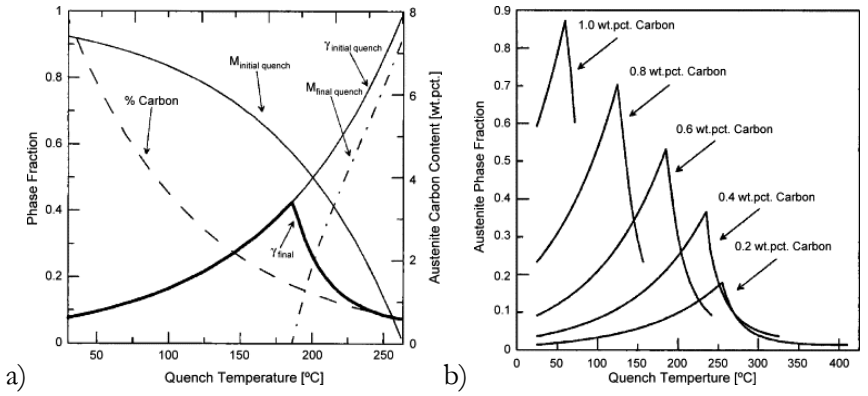

Figure 15. K-M relation used to estimate a) the ideal QT for the Fe-C binary system and b) the effect of carbon on the ideal QT [97].

Nyyssönen et al. [93] have presented findings on the Q&P response of high aluminium steels. They concluded that when it comes to austenitization and quenching, the behaviour of the steels could be estimated using dilatometry. The stability of the austenite, on the other hand, was heavily dependent on the retained austenite morphology. It appeared that the stabilization of small finer grains was more rapid compared to blocky coarse austenite grains. In addition, De Meyer et al. [80] have reported that the martensite transformation occurs earlier in Al-alloyed steels compared to Si-alloyed steels, which is visible in Figure 16.

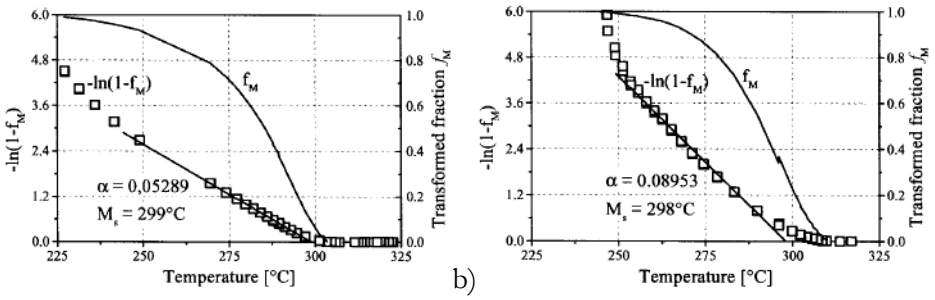

Figure 16. Martensite transformation during quenching of a) CMnSi- and b) CMnAlSi-alloyed TRIP-assisted steels [80].

Nyyssönen et al. [104] have further demonstrated that the successful quenching and partitioning response of an intercritically annealed steel seems to dependent on the state of austenite prior to quenching. Sufficient carbon content and a small austenite grain size gives the robust behaviour required regarding the heat treatment where

the martensite transformation is controlled by varying the quench stop temperature. Also, the amount of retained austenite has been shown to correlate with both the quench temperature as well as the elongation in tensile testing [105].

2.1.7 Microstructural morphology

The microstructure of steels utilizing the TRIP effect varies greatly between different heat treatments and chemical compositions, although similarities between differently processed steels also exist. The conventional heat treatment of cold-rolled TRIP-assisted steel, which is typically hot-dip galvanized or electrogalvanized for additional corrosion protection, consists of two steps: intercritical annealing between the ferrite to austenite transformation temperatures A_{c1} and A_{c3} in the ferrite-austenite dual-phase region, and rapid quenching to a specific isothermal holding temperature in the bainitic transformation temperature range [10]. This approach leads to a multi-phase microstructure consisting of several microstructural constituents and phases. Mainly, the microstructure consists of varying amounts of allotriomorphic ferrite, bainite, martensite and metastable retained austenite [106]. Depending on the alloying additions, alloy carbides may also be present.

Bainite and martensite are formed from austenite during cooling, while the retained austenite, which is the untransformed austenite still present after the annealing step, is stabilized to room temperature by the partitioning of carbon from martensite to the retained austenite. The carbon enrichment of austenite occurs during the austempering step of the process. An example micrograph of this type of microstructure is presented in Figure 17.

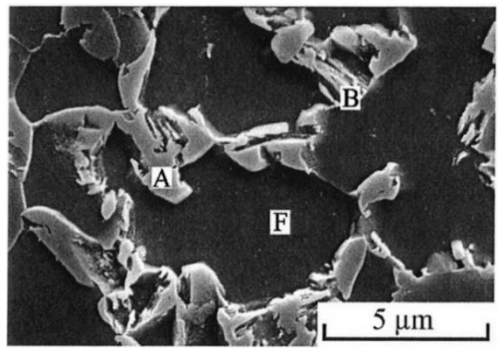

Figure 17. Electron micrograph of TRIP-assisted multi-phase steel containing bainite (B) and retained austenite (A) in a ferrite matrix (F) [106].

The carbon content of austenite during annealing itself is not sufficient to stabilize austenite to room temperature, which is why carbon enrichment via partitioning from surrounding phases is required. The partitioning of carbon between phases via diffusion is possible because the bainitic transformation takes place in paraequilibrium conditions. This means that the temperature is too low for the diffusion of substitutional alloying elements, but the interstitial carbon can still partition between the bainite and retained austenite. The low carbon bainite in TRIP steels is sometimes referred to as carbide-free bainite [10]. Carbon enrichment leads to a decrease in the M_s temperature of local retained austenite to below room temperature. Thus, this high temperature phase can be seen as islands in the room temperature microstructure.

After the heat treatment of TRIP-assisted steels, in cases where bainite is not present, the microstructure consists of martensite-austenite (MA) islands in a ferrite matrix [18]. In this type, all the intercritical austenite has transformed into martensite and carbon-enriched retained austenite (Fig. 18).

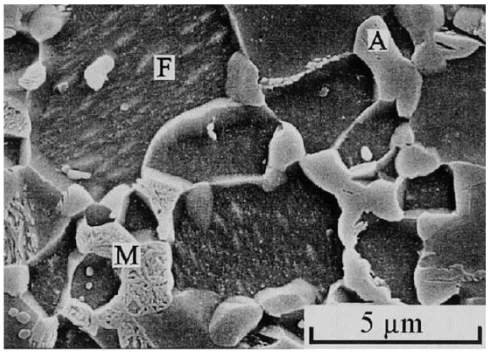

Figure 18. Electron micrograph of TRIP-assisted DP steel containing martensite (M) and retained austenite (A) in a ferrite matrix (F) [18].

In many cases, the microstructural features may be difficult to distinguish from each other based only on their morphology after the etching response. Martensite and retained austenite are especially challenging when the martensite sub-structure is not clearly visible, as it is in Figure 18. Also, the determination of bainitic ferrite and ferrite causes difficulty. To meet the challenge, Girault et al. [107] have proposed metallographic characterization techniques to distinguish different microstructural constituents from one another. The morphology of ferrite is equiaxed, whereas bainitic ferrite is typically located as lamellae between the retained austenite and martensite. Additional tempering may also be utilized in order to form tempered

martensite, after which colour-etching may be performed to investigate the retained austenite content.

Compared to TRIP-assisted DP or DH steels, TRIP-assisted bainitic-ferritic steels (TBF) might have a larger prior austenite grain size since they are typically fully austenitized during the annealing step. By implementing microalloying additions, such as Nb, it is however possible to control the grain size [27]. The primary characteristic which separates the microstructure of TBF steel from that of DP steel is the bainitic-ferritic steel matrix. An example of 0.025 wt.% Nb-microalloyed TRIP-assisted bainitic-ferritic steel is shown in Figure 19, where bainite had formed relatively large blocks with interspersed retained austenite grains and martensite islands [27].

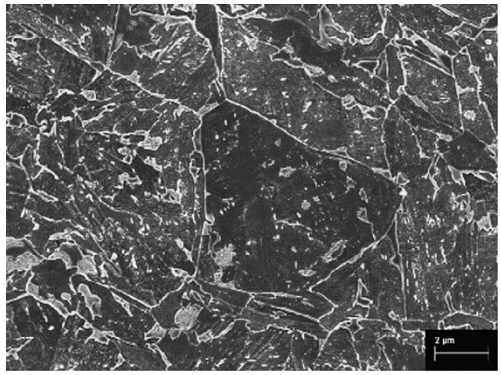

Figure 19. Electron micrograph of retained austenite containing TRIP-assisted bainitic-ferritic steel [27].

Quenching and partitioning (Q&P) steels have some characteristics similar to TRIP-assisted steels. The retained austenite content is dependent on the carbon movement during partitioning. In that sense, Q&P steels are much like TRIP steels; they depend on the degree of carbon-aided austenite stabilization. They are, however, quenched below the M_s temperature at a carefully selected quenching temperature before subsequent partitioning.

In contrast to the fully austenitized Q&P steel proposed by Speer et al. in 2003 [89], another adaptation is intercritically annealed Q&P steel [77], [90], [94], [104]. This adaptation is usually favourable in continuous annealing lines, where the annealing is performed in the ferrite-austenite dual-phase region. The volume content of retained austenite in these steels may be lower compared to fully austenitized TRIP or Q&P steels. However, the carbon content of austenite during intercritical annealing is higher, which leads to increased stabilization of the retained

austenite. In addition, the intercritical ferrite content decreases the grain size leading, to increasing formability of the steels and may impart higher ductility compared to some other TRIP and Q&P steels of similar strength. Figure 20 presents a microstructure of Si-alloyed TRIP steel after intercritical annealing at a temperature resulting in 75 vol.% austenite followed by interrupted quenching to 200 °C and subsequent partitioning at 400 °C [90].

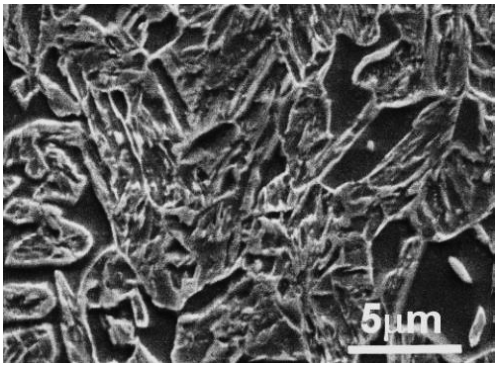

Figure 20. Electron micrograph of Si-alloyed and intercritically annealed Q&P steel [90].

Depending on the chemical composition of the steel and the annealing temperature, the intercritical Q&P heat treatment leads to a final microstructure containing tempered martensite with retained austenite needles or ferrite matrix containing martensite-austenite islands. The ductility of the final microstructure is increased by the deformation-induced transformation of austenite into martensite, which is made possible with the increased strain-hardening rate due to the carbon-enriched austenite [13].

It has been proposed by Tan et al. [77] that the ability of the retained austenite to contribute to strain hardening depends on its localization, morphology and stability. They observed that the transformation of retained austenite into martensite remains limited when the deformation occurs primarily in the ferrite phase. Also, the film-like morphology of retained austenite, which results in high mechanical stability, and the localization of the austenite away from ferrite-prior austenite interfaces will both promote unwanted mechanical stability. The carbon-rich areas of the microstructure, which contain the martensite grains and the film-like retained austenite within them, are controlled by the surrounding ferrite grains (Fig. 21).

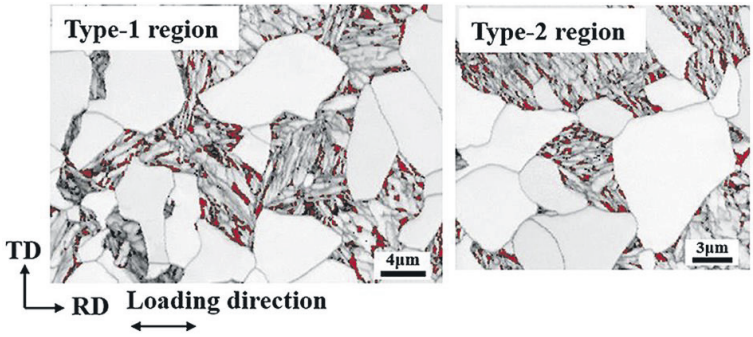

Figure 21. EBSD observations of carbon and strain partitioning in ferrite-containing Q&P steel [77].

The analysis by Tan et al. [77] proposed that the design of ferrite-containing Q&P steels should aim at four microstructural feature targets. Firstly, a martensite fraction above 50 vol.% in order to have a reduced ferrite fraction and increase the local strain carried by the martensite (Type 1 region in Figure 21). Secondly, well isolated and non-percolating ferrite regions, which should lead to decreased strain contrast at the ferrite-martensite interfaces. Thirdly, a martensite size of above 5 μm, because larger martensite dimensions experience higher deformation, thus leading to the TRIP effect due to retained austenite content inside the martensite islands. Lastly, the shape of martensite regions may also decrease the strain contrast at the ferrite-martensite interface, which is presented as convex polygonal morphology in the Type 2 region, shown in Figure 21.

2.1.8 Global and local formability

The conventional and the most widely used test method to determine the stress and strain values of AHSS is the uniaxial tensile test, where elongation values, such as the uniform elongation and total elongation, are given as the result. This is done by calculating the true stress-true strain and finding its intersection with the derivative true stress-true strain curve ($d\sigma/d\varepsilon$) [21], which shows the necking onset point. However, to comprehend the formability and damage resistance characteristics of the steel requires further tests, such as hole expansion or bending tests.

In cases where only a limited amount of test material is available, the tensile test data and test specimens can be further processed in advanced examination of the local ductility of the material. For that purpose, a global and local formability diagram can be derived as a novel designation of mechanical properties for advanced high-

strength steels [14]. The material possesses different characteristics depending on the location in the diagram.

Global formability has been described by Hance [14] and later by Heibel et al. [15] as the ability of a material to undergo plastic deformation without the formation of a localized neck, because the strain is distributed uniformly. The conventional material characteristics which indicate uniform strain distribution are the forming limit curve, the work-hardening exponent or n value, uniform elongation as well as the total elongation values. These properties increase within the x-axis of the global and local formability diagram, where dual-phase steels are typically found, as shown in Figure 22a and 22b. Heibel et al. [15] have reported that true uniform strain ε_u and the n value have a strong correlation.

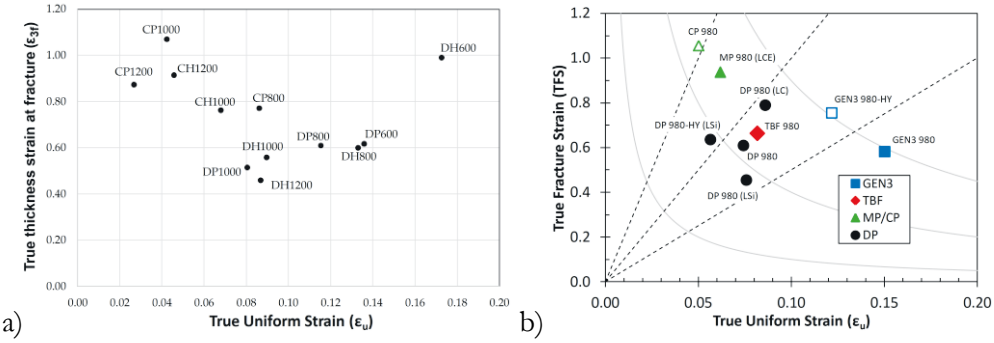

Figure 22. Global and local formability diagram presenting a) true thickness strain at fracture and b) true fracture strain as a function of true uniform strain, adapted from [14] and [15].

Complex-phase steels, on the other hand, are typically found on the y-axis, as shown in Figure 22a and 22b, where local formability and the ε_{3f} value increase. Heibel et al. [15] proposed that the measurement of true thickness strain at fracture (ε_{3f}), which is also known as the third principal strain, allows the estimation of the damage tolerance, edge-crack sensitivity, fracture toughness and bendability of high-strength multi-phase steels. True thickness strain at fracture is the local fracture thickness of the sheet, which has been reported to correlate with the hole expansion ratio [15], [16]. Gruenbaum et al. [16] have added that ε_{3f} values do not correlate with the bending angle in the three-point bending test according to the VDA 238-100 standard. Local formability is typically also linked to the stretch flangeability, hole extrusion capacity and tight-radius bendability of the material [14].

2.2 Design of retained austenite containing steels

In the previous three decades, low-alloy TRIP-assisted steels have incorporated additions of Si and Al+P in various combinations, also including the low-Si or Si-free concepts [10], [17], [33], [40], [41], [59], [108]-[112]. Alloying additions of Cr, Cu and Mo are typically utilized [20], [27], [28], [109]. Keeping in mind the galvanizability of cold-rolled strip steel, the alloying addition of Si is typically avoided and Al favoured [11], [85], [113]-[115].

Microalloying elements, such as Nb, Ti and V, are used for additional hardening and grain refinement [20], [22], [26], [30], [116]. Typically, the microalloying elements are used in combination, meaning that their interactions need to be taken into account, because they compete for the same interstitial elements of carbon and nitrogen [117].

This section presents some aspects of the alloying effects on retained austenite containing steels. For example, Si, Al and P are ferrite stabilizers, whereas C, Mn, Cu and Ni, for instance, are austenite stabilizers. The alloy design is a key aspect in material performance and usability as well as on the heat treatment response.

2.2.1 Common elements

Carbon (C): Steels are Fe-C systems where carbon is the main alloying element controlling all phase transformations. For example, carbon stabilizes austenite, leading to the retention of austenite in TRIP steels, provided a sufficient amount of alloying elements that hinder carbide precipitation is present. Carbon content in retained austenite containing steels varies from 0.05 to 0.40 wt.%, but welding requirements usually limit the carbon contents to 0.20 wt.% or below. [47], [118]

Carbon fundamentally affects all the microstructural constituents and phases that form during both the cooling and isothermal holding of the steel. In retained austenite containing steels, the effect of carbon is paramount in the controlling of the austenite stabilization during partitioning. Despite the diffusionless martensite formation from austenite, which can be considered instant in the conceivable timescale, transformations are hardly ever spontaneous. For instance, bainite formation and saturation of carbon into carbon-rich and carbon-poor regions depends on carbon movement during heat treatment. [61]

Carbon is the most powerful austenite-stabilizing element, which means it significantly enlarges the austenite region in the Fe-C phase diagram, resulting in a

reduction of austenite to ferrite transformations when the carbon content is increased. Consequently, additions of carbon lead to the deceleration of transformations and lowering of the free energy. [10], [61], [83]

Manganese (Mn): Mn is utilized as an austenite-stabilizing element, because it lowers the austenite transformation temperature and enhances the possibility of carbon enrichment by increasing the carbon solubility in the austenite. It also extends the applicable cooling rate ranges because it delays pearlite formation. Manganese increases the steel strength by solid solution hardening. [118] Mn also increases the stability of austenite by lowering the M_s temperature [38].

In steel making, manganese is used both as a deoxidizer and an alloying element [119]. In the latter case, the maximum manganese content is typically below 2.2 wt.% in low-carbon TRIP steels, whereas Q&P steels may contain up to 3.0 wt.% of manganese [13]. However, in studies of Q&P steels, higher Mn additions up to 5.0 wt.% have also been included. The high Mn additions are close to the alloying region of the so-called medium Mn steels, and have in some cases led to mechanical properties typical to those of 3rd generation AHSS [91], [120].

Regarding TRIP and Q&P steels, Hausmann [28] has studied the alloying effects of manganese in the 980 and 1180 MPa tensile strength classes. She found that relatively small changes in manganese content, 0.2 wt.%, had a significant effect on the phase transformation kinetics, microstructure as well as on the mechanical properties. The content of manganese demonstrated a significant deceleration of phase transformations during continuous cooling and bainite formation during over-ageing. An example of these findings is presented in Figure 23, which presents the deceleration of bainite formation during cooling.

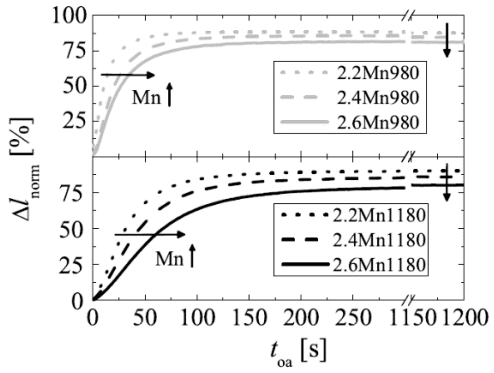

Figure 23. Normalized dilatometry sample length (Δl_{norm}%) of Mn alloyed TRIP-assisted steels variants during over-ageing at 400 °C, where t_{oa} denotes over-aging time in seconds [28].

Hausmann [28] further made two main observations. Firstly, the effect of manganese was more pronounced in the 1180 MPa than in the 980 MPa grade. Secondly, the final transformed phase fraction after 1200 s over-ageing period was lower for the higher manganese content. In addition, it is visible in Figure 23 that the bainite transformation did not stop within the initial 1200 s of over-ageing. The latter is indicated by the slight slope in the curve at the end of the over-ageing step. According to these observations, Hausmann concluded that the effect of decelerated phase transformation due to manganese addition was two-fold. It led to a larger retained austenite grain size at a low over-ageing temperature, but also to larger MA islands at a high over-ageing temperature.

Takahashi and Bhadeshia [121] have proposed that the carbon concentrations of retained austenite and austenite are equal because of the identical free energies due to the same chemical composition at T_0. According to their theory, it is probable that addition of manganese lowers the A_{e3} and T_0, which results in a relative reduction in carbon concentration although the volume fraction of retained austenite increases. This might lead to unexpected observation regarding the microstructure of TRIP-assisted steels, because the excess additions of Mn may lower T_0 so much that bainite transformation begins before the partitioning of carbon into austenite during the isothermal transformation. Thus, at a certain degree of Mn alloying, the volume fraction and carbon concentration of retained austenite may be reduced and bainite, on the other hand, increased. This phenomenon has been reported by Sugimoto et al. [59] for example, who concluded that, even though the addition of Mn increased the initial retained austenite volume fraction, the carbon concentration was decreased in 2.5 wt.% Mn-containing steel. With regard to silicon, however, the theory is not applicable because the influence of Si to T_0 is minuscule.

Chromium (Cr) and molybdenum (Mo): Chromium is a strong carbide former together with other elements, such as titanium, vanadium, niobium and molybdenum [61]. The metallic carbides formed by these elements will replace the cementite in a steel microstructure, often with a relatively low alloy content. While microalloying the elements Ti, V and Nb are typically used in concentrations of less than 0.1 wt.% [61], alloying with Cr and Mo is usually 0.1 – 0.5 wt.% for the effective strengthening of TRIP-assisted steels [27], [28]. Because the use of carbon is usually limited to a maximum of 0.2 wt.% in TRIP-assisted steels, the tensile strength level may be increased from 780 MPa up to 1180 MPa with Cr and Mo [20], [25].

Hausmann [28] concluded in the investigation of TBF steels that, in the 1180 MPa Mn variants, the yield strength decreased with increasing Cr content at over-ageing times beyond 180 s at 350 °C over-ageing temperature. On the other hand, at

the higher over-ageing temperature, which was 425 °C, the increased Cr content consistently increased the yield strength. Hausmann suspected that cementite precipitation could be successfully delayed by the addition of Cr.

In the same case, Hausmann [28] also noted that Cr does not increase the A_{e3} temperature in the same way as Al does, which is a positive side effect from a production point of view, because the fully austenitic state is then possible at lower temperatures.

2.2.2 Retained austenite stabilizing elements

Silicon (Si) and aluminium (Al): Si and Al are both ferrite stabilizers, which means that they increase the A_{e3} temperature during intercritical annealing [111], [122] and delay austenite recrystallization [123]. In the steels that benefit from the TRIP effect, Si and Al induce the partitioning of carbon into retained austenite during isothermal bainitic transformation, because both of them prevent cementite precipitation. When utilizing quenching and partitioning, Si and Al are essential for carbon removal from the primary martensite into the adjacent retained austenite.

Al additions have been studied by, for example, Jacques et al. [18] and Girault et al. [21] after the groundwork research in the field by Matsumura et al. [19]. The alloying addition of Si and Al in various combinations between 0.5 – 2.0 wt.% has been the topic of several studies on the suitable combination of intercritical annealing and austempering temperatures [22], [41], [44], [59], [124].

Wang et al. [20] have reported that the retained austenite content was promoted by smaller Si alloying (0.69 wt.%) when Al alloying of 1.0 wt.% was utilized. They concluded that by varying the isothermal bainitic temperature from 320 ºC to 480 ºC, the volume fraction of retained austenite was 6 – 10 vol.% when the carbon content of the steel was 0.20 wt.%. Their main conclusion was that at a holding temperature of 440 ºC, the volume fraction of retained austenite and the carbon concentration in the austenite phase were 10.8 vol.% and 1.05 wt.%, respectively. The microstructure resulted in high tensile strength (1080 MPa) with enhanced total elongation (23%).

Similar effects have been found by Krizan et al. [22] with Si and Al alloying of 0.6 wt.% and 0.80 wt.% respectively. They concluded that with the addition of Nb and V microalloying in 0.22 wt.% carbon-containing steel the result was a combination of ultimate tensile strength and total elongation of 16 000 MPa%. In their case, an IBT of 425 ºC led to 15 vol.% of retained austenite in the final microstructure.

When both Si and Al alloying are used, it is important to take into account their different effect on the bainitic reaction temperature. Al accelerates the bainite reaction in a range close to galvanizing temperatures (460 ºC to 480 ºC), while the rapid transformation range in Si alloyed steels is lower (400 ºC) [125]. Phase transformation temperatures are estimated via dilatometric tests or by calculations using computerized software. For example, time-temperature transformation diagrams (TTT) with JMatPro® software are useful [102], [126].

Bhadeshia [83] concluded that substitutional solute atoms are trapped in cementite when it precipitates in bainite or martensite. The free energy change associated with this paraequilibrium precipitation of cementite would be much smaller in Si-alloyed steel compared with Si-free steels. This is most probably the reason for the suppression of cementite in Si-alloyed steels.

According to the lattice constant calculations made by Jang et al. [127], additions of Si improve the coherency of ε-carbide with the martensite lattice, resulting in enhanced nucleation kinetics over cementite. Additions of Al have an inverse effect as they decrease the coherency of ε-carbide. On the other hand, and unlike Si, both Al and Mn have a thermodynamic stabilization effect on the carbides. This effect is stronger on the ε-carbide, possibly to the extent that it could replace cementite as the stable precipitate in Mn-rich steels.

Girault et al. [21] found that aluminium-containing TRIP-assisted steels exhibited a TRIP effect which was comparable to silicon-bearing grades. Silicon, however, also contributes as a solid solution strengthener of ferrite, which leads to additional strength. Consequently, Al-bearing grades had a lower strength-ductility combination when Si was fully replaced with Al. They reported that, after tensile tests, the flow stress of 1.5 wt.% Al-alloyed steel had lower true stress compared with 1.5 wt.% Si-alloyed steel (Fig. 24a). This effect was partly caused by the fact that Si, in contrast to Al, is a solid solution strengthener of the ferrite matrix. The fact that the true stress of Al-alloyed steel was lower than that of Si-alloyed steel highlights the deterioration of the strength-ductility balance.

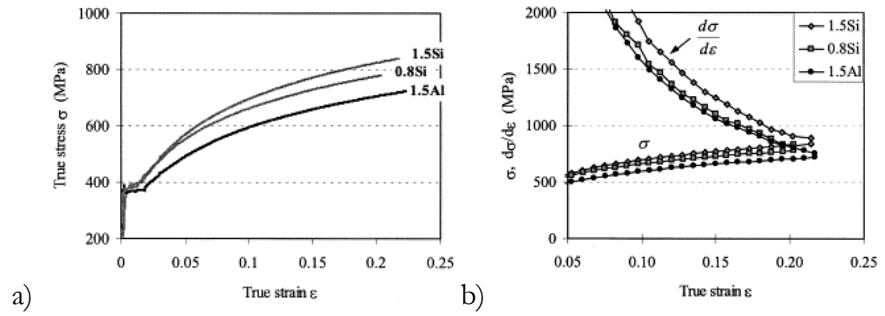

Figure 24. (a) True stress-true strain curves and (b) their corresponding dσ/dε intersections to the true strain curves of Si- and Al-alloyed TRIP-assisted steels [21].

Girault et al. [21] utilized the typical method of presenting the uniform elongation capacity of the steels. As presented in Figure 24b, the true stress-true strain curve (σ) was compared to the derivative of the true stress-true strain (dσ/dε) where their intersection presents the necking onset point and uniform elongation end-point. This means, generally, that the ductility of the material can be considered higher when this point reaches higher values.

Copper (Cu) and nickel (Ni): Cu and Ni are austenite-stabilizing alloying elements as they increase the A_{c3} temperature during intercritical annealing [59], [128], but copper is also a tramp element in steels. The average amount of Cu in steels is growing due the increasing usage of scrap in steel production which is very unlikely to decrease in the future [129]. The reason why Cu is difficult to remove from steel is because it has a lower affinity to oxygen, which means that Fe oxidizes before Cu [130].

The effect of Cu alloying on steels that benefit from the TRIP effect has been studied in a number of studies, often in combination with nickel [109], [131]. Because copper acts as an austenite stabilizer, it has a beneficial effect on the formation of retained austenite. For example, Kim et al. [109] have concluded that additions of both Cu and Cu+Ni increased the volume fraction of the retained austenite, resulting in favourable combinations of ultimate tensile strength and total elongation.

In addition to the austenite stabilization effect, Cu is considered as a solution-hardening element in ferrite grains [20]. Cu also slows the precipitation of carbides in a similar manner to Si and Al [112].

Phosphorous (P): P is known as one of the strongest solid solution strengthening elements of steels, and it is also a ferrite stabilizer that can partially replace Si and/or

Al in TRIP-assisted steels [132]. However, P is hardly ever used by itself because its effect on counteracting carbide formation is less than that of Si and Al [133]. On the other hand, P does not decrease the galvanizing capability of cold-rolled steel [134]. The downside is, however, its tendency to segregate into grain boundaries which causes deterioration in ductility [135].

Chen et al. [135] have investigated the effect of P on the formation of retained austenite and found that a P amount of 0.07 wt.% together with 0.5 wt.% Si produced a high amount of retained austenite. Phosphorus, like silicon, also inhibits the formation of carbides, leaving more carbon in solution for partitioning to austenite [136]. In some cases, an addition of P has been reported to decrease the weldability of steel due to possible embrittlement problems, but the additional benefits on the reduction in surface defects in galvanizing might be desirable [131].

2.2.3 Microalloying elements

Titanium (Ti), niobium (Nb) and vanadium (V): Microalloying elements, such as Ti, Nb and V, are strong carbide-forming elements [61]. They increase the strength of the steel by grain refinement and precipitation hardening when sufficient carbon is present. Microalloying is one of the methods for increasing the steel strength by an increase of the carbon content without deteriorating its weldability.

For example, the effect of Ti microalloying on the mechanical properties of Si- and Al-alloyed TRIP-assisted steel has been investigated by Krizan et al. [25]. One of their main conclusions was that Ti addition refined the final microstructure due to the pinning of the austenite and ferrite grain boundaries by the TiC precipitates during the heat treatment process. Secondly, they concluded that the precipitation strengthening by TiC precipitates was the main factor in controlling the yield strength of the steel.

Tang et al. [26] have studied the effects of Nb microalloying on the microstructure and mechanical properties of Si- and Al-alloyed TRIP-assisted steel. In the case of Nb, they concluded that it refined the grain size, but decreased the volume fraction of retained austenite in the final microstructure.

Hausmann et al. [27] have concluded that addition of Nb resulted in considerable grain refinement. Additionally, their Nb variant grades showed higher amounts of retained austenite due to the reduced amount of cementite that was seen in the bainitic microstructural constituent. A significant change in bainite morphology from lath-like to globular was also observed. Their TEM investigations showed

evidence of Nb content increasing the carbide size rather than the amount of carbides. In the additional experiments with 980 and 1180 MPa strength class TBF and Q&P steels, Hausmann [28] has reported that a contrast existed between the two grades. The higher carbon and manganese content of the 1180 grade, accompanied by the addition of Nb, led to the suppression of the formation of softer phases upon cooling to the over-ageing temperature.

Hausmann et al. [27] have also concluded that the grain refinement by Nb addition resulted in an increase in beneficial formability, because Nb microalloying increases the total elongation and lowers edge crack susceptibility. In their work, they observed two populations of NbC particles, consisting of coarse and fine precipitates. In the experimental variants, which had a Nb content from zero to 0.090 mass%, the density of coarse carbides increased with increasing Nb content. They also found that no further grain refinement occurred above a Nb content of 0.025 mass%.

Perrard et al. [29] have studied the effect of V microalloying on CSiMn-alloyed TRIP steels with various N contents (50 – 1550 ppm). Their TEM investigations showed that the precipitation behaviour of V(C, N) in ferrite and austenite during continuous annealing takes place inside a continuously evolving two-phase matrix, while the time-varying solubility of precipitates is due to their changing C/N ratio.

Scott et al. [30] have reported that V alloying can strengthen steel by 60 – 100 MPa while preserving good total elongation values. They also noted that V-microalloyed steels were susceptible to hot-rolling conditions and intercritical annealing temperatures.

Lagneborg et al. [117] have pointed out the importance of interactions between vanadium and other microalloying elements such as Ti and Nb, because they compete for the same interstitial elements (carbon and nitrogen). It has been suggested that vanadium carbides have higher solubility in austenite than other microalloying elements, which means they will be completely dissolved at low austenitizing temperatures.

Regarding the over-stoichiometric concentrations of nitrogen and vanadium, excess V will precipitate as carbides and carbonitrides. Lagneborg et al. [117] have calculated the chemical driving forces for VN and VC precipitation as a function of vanadium and nitrogen content ($0.06\% < V < 0.15\%$ & $0.005\% < N < 0.015\%$) in steels with a carbon content of 0.1 wt.%. They concluded that the increased precipitation driving force of VN and VC increases the precipitation in ferrite. In this case, it was found that V did not influence the retained austenite or its carbon

content. They proposed that strength evolution was entirely related to precipitation hardening.

2.2.4 Galvanizing of Si- and Al-alloyed steels

The most convenient and cost-effective method of corrosion prevention for the steels that benefit from the TRIP effect is hot dip galvanizing, but due to alloying additions they are not always compatible with continuous annealing. The selective oxidation of alloying elements on the steel surface prior to galvanizing leads to poor reactive wetting of Zn and can cause bare spots on the coating.

Investigations on the alloying of these steels have considered the possibility of using low Si alloying and replacing some Si with Al in order to enhance wetting during the galvanizing operation. For example, Jacques et al. [17] have concluded that despite low Si content (0.38 wt.%) almost 10 vol.% of retained austenite was obtained, which led to a desirable strength-ductility combination: 810 MPa ultimate tensile stress with 18% total elongation. On the other hand, Pichler et al. [110] have suggested that a Si content of 0.6 wt.% results in insufficient prevention of carbide precipitation to obtain retained austenite for a satisfactory retained austenite content. However, the study by Wang et al. [20] has demonstrated that the retained austenite content (up to 15 vol.%) can be promoted by lesser Si alloying (0.6 - 0.7 wt.%), when they used Al alloying of 0.8 - 1.0 wt.% with optimum intercritical annealing and isothermal bainitic heat treatment conditions. These results suggest that the effect of alloying on the final amount of retained austenite is not straightforward.

Si is particularly problematic from a production point of view, but galvanizability can also be decreased by other elements. Annealing prior to galvanizing reduces the iron oxides on the surface of the sheet, but promotes the oxidation of other alloying elements, such as Mn and Al. The composition of TRIP steels is usually a complex variation of alloying elements in order to obtain the desired microstructure with the heat treatment.

Mahieu et al. [84] have concluded that 1.5 wt.% Si-containing steels are not compatible with the conventional hot-dip galvanizing process, as it appeared in their surface studies that an increase in the dew point (dp) resulted in better coating quality, but bare spots could not be fully eliminated. Reactive wetting can be adjusted by selective oxidation and controlling the dew point [85], [114]. Bellhouse et al. [114] have investigated the selective oxidation and reactive wetting of Si- and Al-alloyed TRIP-assisted steels and found that by controlling the dew point in annealing, it is

possible to achieve good reactive wetting of zinc. They observed the effect of different conditions by investigating oxides on the surface with a scanning Auger electron microscope (SAM), after which they attributed the complete reactive wetting to the oxide chemistry on the surface, as shown in Figure 25. From this observation, they concluded that the number of bare spots in the zinc overlay decreased significantly when the surface was covered with Mn-, Si- and Al-rich oxides in the case of -53 °C dew point (Fig. 25a), whereas +5 °C dew point resulted in a relatively thick MnO film, indicating insufficient aluminothermic reaction.

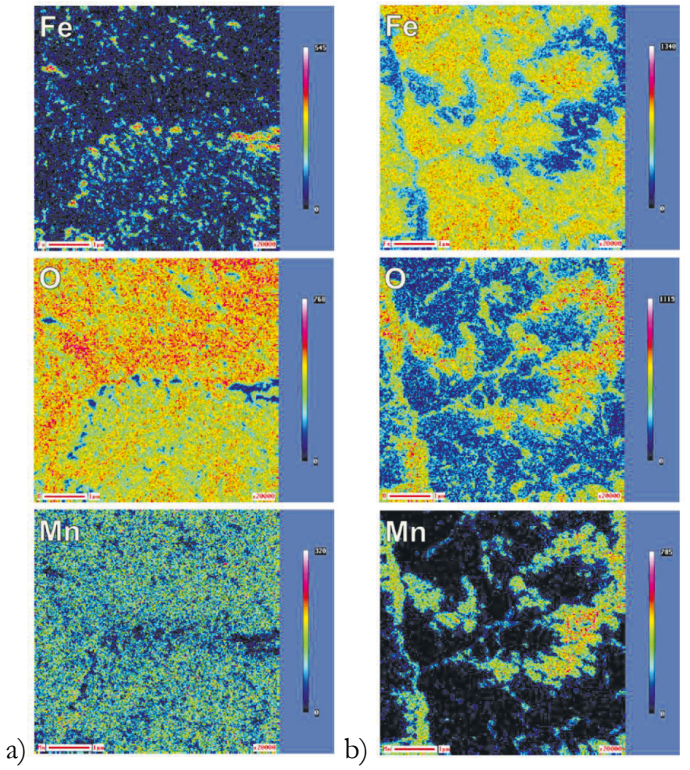

Figure 25. SAM elemental mapping of Fe, O and Mn on the surface after a) -53 °C dp and b) +5 °C dp utilized during the annealing of TRIP-assisted steel. Modified from [114].

The galvanizing of TRIP steels, both hot and cold rolled, has been studied in a programme sponsored by the International Lead Zinc Research Organization (IZA), formerly ILZRO [137] and in the RFCS (Research Fund for Coal and Steel) project in 1998 – 2002, which was aimed at enhancing hot-dip galvanizing by controlled oxidation in an annealing furnace. In the final report on the latter, Bordignon et al. [138] concluded that no pre-oxidation conditions for sufficient wettability

improvement were found for Si-alloyed TRIP steel (0.14C-1.5Mn-1.4Si). On the other hand, they found that, for a certain Al-alloyed steel (0.16C-1.5Mn-1.2Al), avoiding the galvanizing problem was possible using pre-oxidation.

2.3 State of the art

The current TRIP steels in the 3rd generation AHSS category are referred to as TRIP-assisted or TRIP-aided steels. The early TRIP steels contained large quantities of austenite-stabilizing alloying elements, making them fully austenitic at room temperature. In contrast, the alloying additions in TRIP-assisted steels are smaller, which leads to a minor austenite phase in the final microstructure.

In addition to novel TRIP steels, the 3rd generation AHSS include Q&P steels, which also benefit from the retained austenite content in the microstructure. Thus, they have a beneficial strength-ductility combination for the cold-forming applications used in the automotive industry. Compared to TRIP steels, Q&P steels typically have higher strength due to the increased martensite fraction, which makes them promising candidates for replacing martensitic steels in automotive body-in-white.

The typical heat treatment of cold-rolled TRIP-assisted steels consists of two steps: austenitization or intercritical annealing and rapid quenching to an austempering temperature in the bainitic transformation temperature range. This approach results in a multi-phase microstructure consisting of several microstructural constituents and phases: ferrite, bainite, martensite and metastable retained austenite.

TRIP-assisted steels can be multi-phase CP-type steels that have a bainitic or ferritic matrix with tempered martensite and retained austenite, or they can be DP steels with a small amount of retained austenite in martensite islands in the ferritic steel matrix. The literature survey showed that TRIP-assisted steels typically contain between 5 and 15 vol.% retained austenite and a varying amount of other phases and microstructural constituents.

The heat treatment involved in the Q&P processing makes Q&P steels different from TRIP or martensitic steels. In TRIP heat treatment, steels are quenched from the annealing temperature quickly to the bainite transformation temperature. In contrast, in Q&P processing, the steel is quenched from the annealing temperature to below the martensite transformation start temperature where the quenching is interrupted at a point where only some of the prior austenite has transformed into

martensite. In the two-step Q&P process, heat treatment also includes a subsequent reheating step to the partitioning temperature.

The industrial heat treatment of these cold-rolled steel strips is typically performed using a continuous hot-dip galvanizing line (CGL), which combines the annealing with the hot-dip coating of the strip in a corrosion protective liquid metal, which is typically zinc or zinc alloy. The use of the CGL line to produce these steels is cost-effective, but the downside is alloy limitations caused by the reactive wetting of the steel surface that is required. Si is especially problematic, which is why Si-free or low-Si compositions that use additions of Al have been developed. However, even the addition of Al does not solve all problems, because other alloying elements of the steel may promote oxidation on the steel surface. This is counteracted by controlling the dew point and adjusting the selective oxidation of the alloying elements.

The literature survey showed that development has been driven by retained austenite for implementing the TRIP effect on novel grades. In addition, the pursuit of galvanizability has raised interest in various combinations of low-Si or Si-free alloying concepts. For additional strengthening and grain size control, microalloying elements, such as Nb, Ti and V have been utilized. Many examples showed that microalloying additions have been incorporated into high-strength and increased elongation steels.

Carbon is needed for controlling the phase transformations, but, on the other hand, high levels may lead to the deterioration of the properties of the final steel product, because carbon has the tendency to form carbides with the alloying elements. From the viewpoint of alloy design, the carbon content selected is always more or less a compromise compared to some other elements which typically have a specific purpose, for example cementite precipitation preventing effect of Si and Al or the austenite stabilizing effect of Mn, Cu and Ni.

3 EXPERIMENTAL MATERIALS AND METHODS

This chapter describes the design behind the experimental materials and the methods for material characterization. Nine experimental alloys were designed for laboratory manufacturing and small-scale testing, while one alloy was designed for full-scale steel production and line trials. The laboratory heat treatments correspond to the heat treatment profiles of many continuous hot-dip galvanizing lines currently in use.

3.1 Design of the experimental alloys

The alloys were divided into reference material and two series based on the research questions of the present study (Table 1). The first test series aimed at comparing the effects of the microalloying elements Ti, Nb and V on the mechanical properties of Al- and Si-alloyed 0.20 wt.% carbon containing steel, which answered the first and third research questions. The second series aimed at investigating the effect of Mn-Al-Si alloying on the formation of retained austenite in V-microalloyed 0.08 wt.% carbon-containing steels to answer the second research question. The mechanical properties investigation of all of the experimental alloys, including the industrial alloy, which was derived from alloy 2.4 and is presented in Section 3.5, were utilized to answer the fourth research question on the ductility origin and the effectiveness of the TRIP effect. The reference material, REF, was designed on the basis of an experimental Cu- and Mo-containing 1180 MPa grade made in an earlier study [48].

Table 1. Target alloying elements (in wt.%) of the laboratory castings.

Alloy	C	Si	Mn	Al	Nb	V	Cu	Cr	Mo	N_{max}	P_{max}	S_{max}	CE_{IIW}	pcm
REF	0.15	0.45	2.3	0.03	0.015	0	0.3	0.04	0.3	0.006	0.015	0.004	0.63	0.32
1.1	0.20	0.70	1.5	1.0	0.040	0	0.5	0	0.2	0.006	0.015	0.004	0.52	0.34
1.2	0.20	0.70	1.5	1.0	0.040	0.10	0.5	0	0.2	0.006	0.015	0.004	0.54	0.35
1.3	0.20	0.70	1.5	1.0	0	0.10	0.5	0	0.2	0.006	0.015	0.004	0.54	0.35
1.4	0.20	0.70	1.5	1.0	0	0	0.5	0	0.2	0.006	0.015	0.004	0.52	0.34
2.1	0.08	0.30	2.6	0.15	0	0.10	0	0.30	0.1	0.006	0.015	0.004	0.61	0.25
2.2	0.08	0.70	2.6	0.15	0	0.10	0	0.30	0.1	0.006	0.015	0.004	0.61	0.27
2.3	0.08	0.30	2.6	1.0	0	0.10	0	0.30	0.1	0.006	0.015	0.004	0.61	0.25
2.4	0.08	0.70	2.6	1.0	0	0.10	0	0.30	0.1	0.006	0.015	0.004	0.61	0.27

$CE_{IIW} = C + Mn / 6 + (Cr + Mo + V) / 5 + (Ni + Cu) / 15$ [139]

$pcm = C + (Mn + Cr + Cu) / 20 + Si / 30 + Ni / 60 + Mo / 15 + V / 10 + 5 \cdot B$ [140]

The first series (compositions 1.1 – 1.4) were designed to have a carbon content of 0.2 wt.% and silicon content of 0.7 wt.%, which was similar to that of used in the experiments by Tang et al. [26], Wang et al. [20] and Krizan et al. [22]. Si and Al act together to suppress cementite formation in bainitic ferrite and allow carbon to partition into retained austenite during isothermal bainitic transformation. Cu was added as an austenite stabilizer. Mo was utilized to inhibit the formation of pro-eutectoid ferrite during the bainite transformation.

The second test series consisted of compositions 2.1 – 2.4. Compared to the first concept, these compositions aimed at lower carbon contents, but the carbon equivalent (CE_{IIW}) was higher due to the higher manganese content. In addition to CE_{IIW}, the critical metal parameter (pcm) was used to evaluate the spot weldability of the steel [141]. The pcm parameter was proposed by Ito et al. [140] to evaluate the weldability of steels with low carbon content [140], [141]. The first composition, 2.1, with 0.3 wt.% of Si and 0.15 wt.% of Al, was close to typical 1000 MPa grade steel with low Si and Al content. The effect of Si and Al was investigated with compositions 2.2 – 2.4.

All the concept alloys in Table 1 were designed to have a maximum total N, P and S impurity content of 60 ppm, 150 ppm and 40 ppm, respectively. The compositions were also designed to have a carbon equivalent CE_{IIW} of between 0.50 – 0.80 and a pcm of between 0.25 – 0.35.

3.2 Production of TRIP and Q&P sheets

3.2.1 Casting and chemical analysis

The investigated laboratory castings were manufactured at the Swerim (formerly SWEREA KIMAB) Research Centre in Stockholm, Sweden. Laboratory slabs were cast as 40 mm · 40 mm · 160 mm billets into a water-cooled copper die in a low-pressure casting furnace. After cooling, the chemical compositions of the slabs were measured using the optical emission spectroscopy (OES) method.

The chemical analysis of the casts is presented in Table 2, which includes all the relevant alloying elements as well as unavoidable impurities (N, P and S). The chemical analysis also contained a minuscule amount of trace elements, such as Pb, Zr, Zn and Ca which were below the detection capacity of OES (< 10 ppm) and are not presented. The rest, 95 – 96 wt.%, was iron (Fe).

Table 2. Chemical analysis (in wt.%) of the laboratory castings measured using OES.

Alloy	C	Si	Mn	Al	Nb	V	Cu	Cr	Mo	N	P	S	Ni	Ti	B
REF	0.14	0.46	2.3	0.02	0.016	0.003	0.30	0.02	0.29	0.0018	0.005	0.0031	0.02	0.021	0.0003
1.1	0.20	0.72	1.5	1.0	0.043	0.002	0.50	0.02	0.21	0.0010	0.005	0.0037	0.02	0.023	0.0004
1.2	0.20	0.71	1.5	1.0	0.041	0.098	0.50	0.02	0.21	0.0013	0.016	0.0037	0.02	0.024	0.0004
1.3	0.21	0.70	1.5	0.9	0.002	0.097	0.50	0.02	0.21	0.0045	0.017	0.0041	0.02	0.023	0.0002
1.4	0.21	0.71	1.5	1.0	0.001	0.002	0.50	0.02	0.21	0.0025	0.018	0.0042	0.02	0.024	0.0002
2.1	0.08	0.32	2.6	0.1	0.002	0.098	0.01	0.32	0.10	0.0013	0.003	0.0029	0.01	0.001	0.0003
2.2	0.08	0.71	2.6	0.1	0.001	0.100	0.02	0.30	0.10	0.0020	0.018	0.0040	0.02	0.013	0.0004
2.3	0.09	0.33	2.6	1.0	0.001	0.100	0.01	0.31	0.10	0.0020	0.015	0.0040	0.02	0.012	0.0004
2.4	0.09	0.73	2.6	1.1	0.002	0.100	0.02	0.33	0.11	0.0018	0.004	0.0035	0.01	0.002	0.0004

The actual CE_{IIW} and pcm values as well as phase transformation temperatures A_{c1}, A_{c3} and M_s are presented in Table 3. A_{c1} was calculated using the conventional equation developed by Brandis [142]. The A_{c3} equation used was designed by Park et al. [143] specifically for Al-alloyed TRIP steels. M_s was calculated according to Stuhlmann [99] as presented in Equation 2.8, in which Co and W were assumed to be zero, because their content in the alloys was negligible.

Table 3. CE_{IIW}, pcm values, and A_{c1}, A_{c3}, and M_s according to chemical analysis.

Alloy	C_{IIW}	pcm	A_{c1} [°C]	A_{c3} [°C]	M_s [°C]
REF	0.60	0.31	725	891	403
1.1	0.54	0.35	728	964	441
1.2	0.54	0.34	731	968	443
1.3	0.56	0.36	730	951	434
1.4	0.55	0.35	728	952	436
2.1	0.62	0.26	728	890	411
2.2	0.61	0.27	728	910	412
2.3	0.62	0.26	727	944	434
2.4	0.63	0.28	728	973	437

$A_{c1} = 739 - 22C - 7Mn + 2Si + 14Cr + 13Mo - 13Ni + 20V$ *[142]*

$A_{c3} = 955 - 350C - 25Mn + 51Si + 106Nb + 100Ti + 68Al - 11Cr - 33Ni - 16Cu + 67Mo$ *[143]*

$M_s = 550 - 350C - 40Mn - 20Cr - 10Mo - 17Ni - 8W - 35V - 10Cu + 15Co + 30Al$ *[99]*

The C_{IIW} values were well within the design parameters of 0.50 – 0.80. The values of pcm, varying between 0.26 – 0.36, were considered acceptable.

3.2.2 Laboratory rolling

Before hot rolling, the low-pressure cast slabs were homogenized by annealing at 1250 °C for 60 minutes. The annealed slabs were first hot rolled into 3 mm sheets with the finish rolling temperature (FRT) well above the recrystallization limit temperature. The hot rolled sheets were quenched to 600 °C followed by slow cooling by wrapping them in an insulator blanket.

After cooling to room temperature, the sheets were cold rolled into 60-mm-wide and 1-mm-thick sheets. Laboratory rolling was performed using a laboratory rolling mill available at the University of Oulu Centre for Advanced Steel Research (CASR), Finland.

3.2.3 Laboratory annealing

Laboratory heat treatments were performed using the Gleeble 3800 thermomechanical simulator (Figure 2 and 3, Appendix 3) at CASR. Duplicate specimens were prepared from each annealing experiment; the first specimen (10 mm · 60 mm) for microstructural investigations, and the second specimen (20 mm · 120 mm) for mechanical tests.

In the TRIP type heat treatments, the intercritical annealing (IA) temperatures were 830 and 900 °C and austempering (IBT) temperatures were 420, 450 and 480 °C. The heating rate for IA was 4 °C/s after which the specimens were cooled to the IBT at 10 °C/s. After 100 s at the IBT, the final cooling to below M_s was performed at approximately 10 °C/s before slow cooling (2 °C/s) to ambient temperature. Schematic presentations of the heat treatment schedules are presented in Figures 26a and 26b.

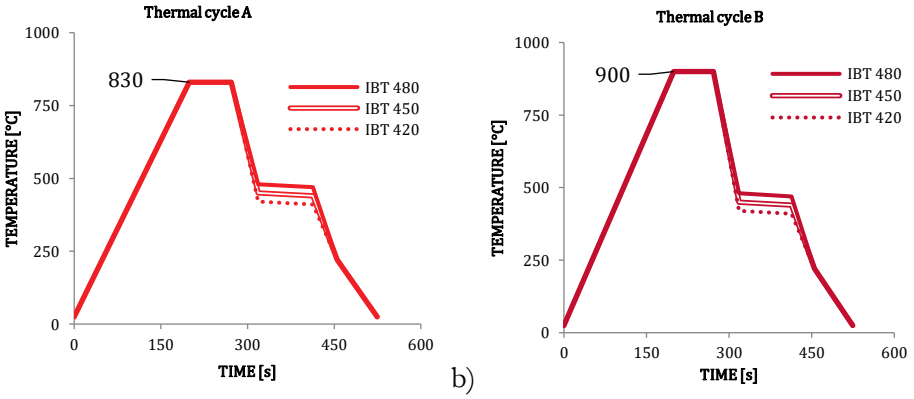

Figure 26. TRIP type heat treatment of the investigated alloys at a) IA 830 °C and b) IA 900 °C.

Thermal cycles A and B were performed on 1.1 – 1.4 and 2.1 – 2.4. For REF, only thermal cycle A was used. The heat treatment parameters for temperatures and times are presented in Table 4.

Table 4. Set parameters of temperature and time for thermal cycles A and B.

Alloy	Thermal cycle	IA [°C]	t_{IA} [s]	IBT [°C]	t_{IBT} [s]
REF	A	830	70	420, 450, 480	100
1.1	A, B	830, 900	70	420, 450, 480	100
1.2	A, B	830, 900	70	420, 450, 480	100
1.3	A, B	830, 900	70	420, 450, 480	100
1.4	A, B	830, 900	70	420, 450, 480	100
2.1	A, B	830, 900	70	420, 450, 480	100
2.2	A, B	830, 900	70	420, 450, 480	100
2.3	A, B	830, 900	70	420, 450, 480	100
2.4	A, B	830, 900	70	420, 450, 480	100

Q&P processing using thermal cycle C was performed for alloy 2.4 in which the IA was 830 or 850 °C; the quenching step temperature (QT) was varied between 200 – 350 °C and the partitioning temperature (PT) was set at 450 °C. The heat treatment profiles are presented in Figure 27 and the set parameters for temperature and time in Table 5.

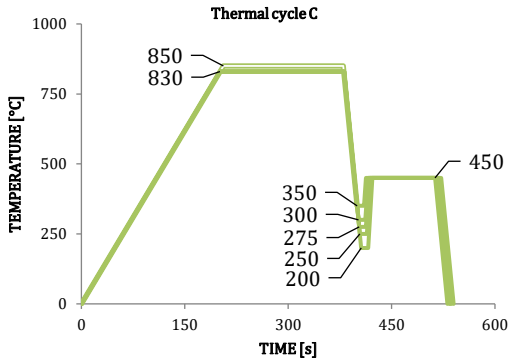

Figure 27. Q&P processing of 2.4QP specimens.

Table 5. Set of temperature and time parameters for Q&P processing of alloy 2.4.

Alloy	Thermal cycle	IA [°C]	t_{IA} [s]	QT [°C]	PT [°C]	t_{PT} [s]
2.4	C	830, 850	180	200, 250, 275, 300, 350	450	100

The heating rate to IA was 4 °C/s and cooling to QT was performed at 25 °C/s. The QT temperatures were selected after dilatometer studies (see Section 4.3.1). After interrupted quenching, the heating rate to PT was approximately 25 °C/s. After 100 s of partitioning the final quenching was done approximately at 25 °C/s. PT 450 °C was selected according to a prior study by Nyyssönen et al. [104].

3.3 Evaluation of phase transformations

3.3.1 Dilatometry

The phase transformations were studied experimentally using a Model 39018 CCT dilatometer within the Gleeble 3800 thermomechanical simulator at CASR. The dilatometer used was a linear variable differential transducer (LVDT) type designed for accurate measurements of phase transformations. It has quartz contact tips for continuous width measurement during heating, annealing and the subsequent continuous cooling.

The dilatometry specimens were prepared by water-jet cutting from 1.0-mm-thick cold-rolled sheets. The specimen length was 60 mm and the width, from which the dilatometric measurement was carried out, was 10 mm. The starting microstructure was a cold-worked highly deformed ferritic-pearlitic microstructure. Dilatometer data, which is time (s) vs. temperature (°C) vs. dilation (mm), was exported to a personal computer for further processing.

The contraction and extension curves were used for the calculations, either the austenite transformation during heating or the martensite transformation during the cooling operation. The phases were calculated from the dilatometer data using the lever rule for phases A and B. Schematic representations of dilation (ε, mm) versus temperature (°C) are shown in Figure 28.

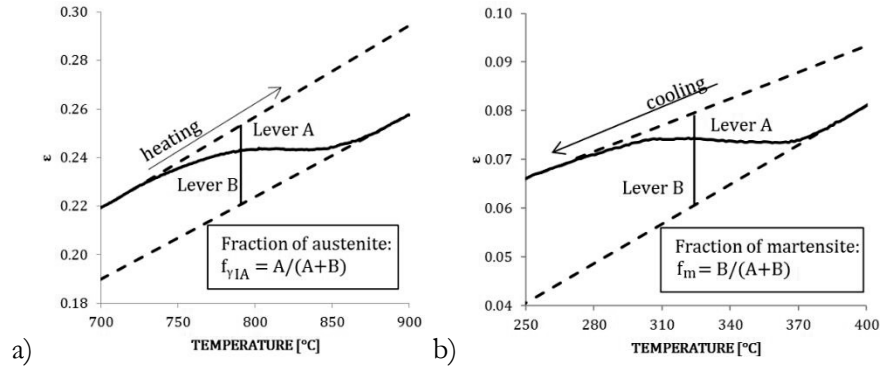

Figure 28. Portions of the dilatometer curve from which a) austenite transformation and b) martensite transformation were determined.

The specimens were subjected to computer-controlled resistance heating from room temperature into 900 °C or 1000 °C at a rate of 4 °C/s to determine the austenite

transformation temperatures during heating: A_{c1} and A_{c3}. The former temperature is the point where the austenite first starts to transform, but the ferrite phase is still present. As the heating continues, the latter temperature, A_{c3} is where all the ferrite is transformed into austenite. The evolution of austenite transformation during annealing was studied by fitting the time (t) vs. phase transformation data to the JMA formula (Equation 2.5) and finding the parameters k and n.

After annealing using a holding period of 60 s, the dilatometer test proceeded to controlled cooling at 25 °C/s with a high-pressure argon gas jet in order to investigate the decomposition of austenite. The martensite transformation range was estimated from the dilatometer curve. The martensitic starting temperature (M_s) was determined by fitting the dilatometer temperature data (T) to the K-M formula (Equation 2.7) and finding the empirical fitting constant (K).

Examples of fitting the dilatometer data into JMA (Eq. 2.5) and K-M (Eq. 2.7) equations are presented in Figure 29. JMA was utilized because the specimens were fully austenitized and fitting was performed using the solver in Microsoft Excel®, version 2010. Fitting of the K-M equation on non-linear regression to find the parameters M_s and K was done using Minitab®, version 18.1 (Minitab Inc., USA).

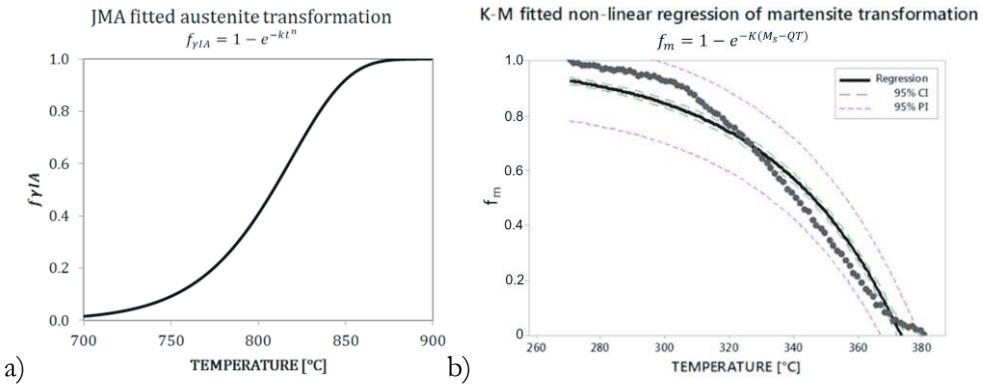

Figure 29. Example of performing the fitting of dilatometer data to a) JMA equation, in which $f_\gamma IA$ represents austenite fraction, and b) K-M equation, in which f_m represents martensite fraction.

Dilatometer test data was used in addition to the calculations in order to investigate the possible differences between previous models and the experimental materials in question. It was assumed that in many cases the chemical composition was outside the scope of the phase transformation formulae or the method did not take into account the differences in the initial microstructure (grain size, deformation state).

In order to validate the use of experimental dilatometer data in the JMA equation to investigate the ferrite to austenite transformation, the plot of $\ln\{\ln[1/(1-f_{\gamma IA})]\}$ versus ln(t) was selected. The method proposed by De Meyer et al. [80] that the relation, which has a slope equal to n and the intersection with the y axis equal to ln(k), was investigated.

3.3.2 Thermodynamic and kinetic calculations

In addition to dilatometer tests, thermodynamic and kinetic calculations of phase transformations were calculated using JMatPro® software, version 11 (Sente Software Ltd., UK). Continuous cooling transformation (CCT) and time temperature transformation (TTT) curves for each composition were calculated and compared to the dilatometry results. Calculations included the reaustenitization and quenching properties as well as the carbon content of austenite during annealing.

Thermo-Calc (Thermo-Calc Software, Sweden) was utilized in order to calculate the phase fractions and chemical composition of phases in the relevant temperature range (300 – 1400 °C). The diffusion module (DICTRA) and Precipitation module (TC-PRISMA) in the software were available for advanced investigations of carbide and nitride precipitation.

3.4 Metallography and material characterization

3.4.1 Sample preparation for electron microscopy and diffraction studies

The specimens for microstructural investigations using JEOL JSM 6100 scanning electron microscope (SEM) as well as JEOL-7000F and JEOL-7200F high-resolution field emission scanning electron microscopes (FESEM) were embedded into epoxy resin and subjected to mechanical material removal by grinding. The fine grinding step before polishing was done using a 1 μm Nap cloth with a 2 min polishing time and 20 N force. After cleaning with isopropanol and ethanol, the final polishing was performed using OP-U colloidal silica for 15 s. After rinsing with ethanol, the specimen was ultrasonically cleaned in acetone, before etching with 2% nitric acid and ethanol solution (Nital) for 5 seconds.

In addition to chemical etching, the specimens were subjected to carbon sputtering using the sputtering target in a JEOL cross-section polisher (IB-

19530CP). The carbon sputtering was done to counteract the surface charging during the electron microscope investigations using high acceleration voltages (15 – 20 kV). The sputtering was also utilized for the EBSD samples which were embedded in epoxy resin.

The secondary sample preparation method for electron microscopy was ion-milling. In this method, the sample was bombarded with an accelerated Ar-ion beam. The interaction between the surface and ion beam removed some amount of material, uncovering a deformation-free and smooth surface.

The above-mentioned JEOL IB-19530 cross-section polisher was used to prepare two types of samples for microstructural and EBSD investigations: 1) optically polished cross-section samples embedded in epoxy were subjected to surface polishing at an 80° tilt angle using an ion beam accelerating voltage of 5.0 kV and a polishing time of 10 minutes, and 2) mechanically cut cross-section samples were subjected to cross-section polishing with an ion beam accelerating voltage of 6.0 kV, a polishing time of 3 hours and an additional 45 minutes of fine-polishing with 3.0 kV for a better final result. The second method was used for selected specimens to determine the retained austenite content of the strained material (at total elongation).

EBSD studies were also performed for mechanically cut and ion-polished cross-sections of selected tensile test specimens with a size of 5 mm · 8 mm. These specimens were first cut longitudinally to the tensile test direction after which the cross-sections were subjected to ion-milling similarly to other cross-section EBSD specimens. The primary investigation location was at the crack tip of the fractured tensile specimen. The secondary location of interest was 8 mm from the crack tip, at a position where the strain was considerably lower during tensile testing.

The sample preparation method for the X-ray diffraction (XRD) measurements was electrolytical polishing of the sample surface. These samples were also used for additional EBSD investigations. In the electrolytical polishing method, a thickness of 0.2 mm was first ground from the specimen surface using SiC grinding paper with a roughness of P800. Next, the specimens were ground with progressively finer papers, ending with a roughness of P2000. The specimens were then electrolytically polished for 12 s at 40 V using a Lectropol-5 polisher with A2 electrolyte.

The microstructural specimens intended for analysis by EBSD and XRD were cut in half from the point of the thermocouple, which means that for the XRD measurements and microstructural investigations there were two samples with a size of 5 mm · 10 mm. The temperature gradient within the Gleeble specimens using the same equipment has been investigated by Nyyssönen et al. [104], who reported that

the temperature gradient within a distance of between 3 and 6 mm from the thermocouple remains below 3 – 5 °C at all stages of heat treatment. This means that the microstructural characteristics of the investigated microstructures were representative.

3.4.2 Method for XRD analysis

The microstructural specimens were subjected to XRD studies in order to calculate the retained austenite volume fraction and carbon content in the unstrained material. XRD analysis was performed using a Panalytical Empyrean X-Ray Diffractometer instrument (Malvern Panalytical Ltd, UK) available at Tampere University, Finland.

In practice, a copper and cobalt cathodes were utilized in different measurements. 2θ angle was between 40◦ and 102 – 130° and the power setup was 40 kV/45 mA. The peaks analysed for ferrite were (110), (200), (211), and (220), whereas the austenite peaks used were (111), (200), (220), and (311). The aperture size used was ¼“ with a 10 mm mask in order to confine the area of measurement. Thus, the size of the X-ray on the surface of the sample was 3.0 mm · 10 mm at the beginning of the test and 0.5 mm · 10 mm at the end of the test. The aim of this procedure was to concentrate the measurement on the area where the experimental heat treatment had been the most uniform.

The volume percent of the retained austenite was calculated using the method described in the standard SP-453 [144]. When the measured and calculated amount of retained austenite was over 2 vol.%, the measurement was duplicated. Therefore, the measured retained austenite was an average of two measurements. The accuracy of the XRD measurement was ± 2 vol.%. The retained austenite fractions V_γ (%) were calculated from the integrated intensity peaks of the X-ray analysis using the Equation 3.1:

$$V_\gamma(\%) = \frac{100 - V_c(\%)}{1 + 4.27\left(\frac{I_\alpha(200)}{I_\gamma(200) + I_\gamma(220)}\right)}, \tag{3.1}$$

where I_a (200) is the integrated intensity of the (200) peak in the ferrite, I_γ (200) and I_γ (220) are the integrated intensities of the (200) and (220) peaks in the austenite, respectively, and V_c is the percentage of cementite, which was assumed to be zero. The average room temperature carbon content of the retained austenite Cγ (in wt.%) was calculated using Equation 3.2, proposed by Dyson and Holmes [145]:

$$C\gamma = (\alpha\gamma - (3.578 + 0.00095 \times Mn\gamma + 0.0028 \times Al\gamma)) / 0.033, \quad (3.2)$$

where $\alpha\gamma$ is the lattice parameter of retained austenite in Å, and $Mn\gamma$ and $Al\gamma$ are the solute contents of Mn and Al in the retained austenite which were assumed to be equivalent to the added contents.

3.4.3 Method for EBSD analysis and phase determination

Selected specimens from the laboratory and industrial trials were subjected to back-scatter diffraction studies. The electron back-scatter diffraction (EBSD) detector used was a Bruker eFlash® FS which includes the ARGUS forward-scatter detector (FSE) imaging system. The EBSD system was fitted into a JEOL-7200F high-resolution FESEM. EBSD analysis was performed for phase contrast and orientation mapping of the specimens. The parameters for EBSD analysis were: acceleration voltage 20kV, probe current 11 – 13 nA, working distance 14 - 15 mm, tilt angle of 70° with variable pixel size (50 – 150 nm). EBSD phase mapping for each location was performed at least three times.

The post-processing of the EBSD data was performed using Esprit 2 microanalysis software (Bruker Nano GmbH, DE). Additional processing in certain cases was done using an MTEX 5.1.1 toolbox integrated into Matlab®, version R2018b (The Mathworks, Inc.) and the Parent Austenite Reconstruction algorithm developed by Nyyssönen [92].

EBSD data was presented using pattern quality maps (PQM), which is a typical EBSD data presentation mode depicting microstructural features, such as phases and grain boundaries. In this technique, the pattern quality parameter of each pixel is calculated using the information contained in the corresponding Kikuchi pattern. The information is then formatted into greyscale image where the contrast varies between pixels, thus forming a micrograph. Typically, the largest differences in contrast are given for different phases, ferrite and austenite as well as martensite in this case.

The EBSD data was processed to present the ferrite grain boundaries in yellow, austenite-ferrite boundaries in white and austenite-austenite boundaries in red. In the phase maps, ferrite (bcc) was coloured in light red and austenite (fcc) in dark blue. The other phases than retained austenite were determined from SEM and FESEM micrographs using ASTM E562 point count method with 7 · 6 grid. Phase percentages were calculated using at least 126 measurement points.

3.4.4 TEM and STEM-EDS investigations

Advanced electron microscopy was performed using a JEOL JEM-F200 transmission electron microscope (TEM) at the Tampere Microscopy Center of Tampere University. The precipitation state of the microalloying elements was studied. Carbon extraction replicas were prepared to analyse the distributions and positions of the precipitated microalloying elements, while qualitative analysis was performed using an energy dispersive spectrometer (EDS) in scanning transmission electron microscope (STEM) mode. Replicas were prepared by first coating pre-polished and Nital (4%) etched samples with carbon. The carbon coating was then cut into 1 mm · 1 mm sections and removed with Nital for precipitate analysis.

3.4.5 Mechanical testing

The duplicate specimens (20 mm · 120 mm) from heat treatments were prepared for uniaxial tensile testing. Tensile test specimen geometry was as follows: total length (L_t) 120 mm, original gauge length (L_0) 30 mm and original gauge width (L_w) 5 mm. The tensile specimens were tested using the MTS 810 material testing system (ZwickRoell GmbH, DE) to define the yield strength at 0.2% elongation ($R_{p0.2}$) and ultimate tensile strength at maximum force value (R_m). Elongations were measured using a 25 mm elongation sensor. The test data was exported to personal computer for further processing and calculating the true stress (σ, MPa) and true strain (ε, mm/mm) values. The true stress-true strain data was further utilized for the calculation of incremental strain hardening exponent (n value) and to find the necking onset point, which is also the point of uniform elongation (A_g). The incremental strain hardening (n value) was calculated with Equation 3.4:

$$n = \frac{\partial ln\sigma}{\partial ln\varepsilon} = \frac{ln\sigma_2 - ln\sigma_1}{ln\varepsilon_2 - ln\varepsilon_1} \tag{3.4}$$

The necking onset point, where the cross-section of the specimen begins to decrease, was measured from the intersection of the true stress-true strain curve σ(ε) and the derivative true stress-true strain curve (dσ/dε), for which

$$\left(\frac{d\sigma}{d\varepsilon}\right)_{\varepsilon=\varepsilon_u} = \sigma(\varepsilon_u) \tag{3.5}$$

A schematic illustration on finding the necking onset point by utilizing the true stress-true strain data is presented in Figure 30.

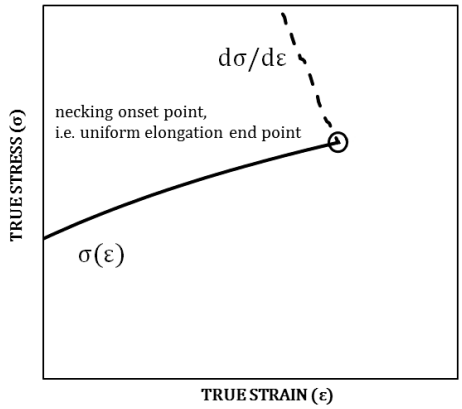

Figure 30. Schematic example of the method used to find the necking onset point by using the true stress-true strain data from tensile tests.

The true uniform strain ε_u, which is the true strain at maximum load, was also determined from the tensile test curves for each sample. This was combined with the examination of the fracture surface cross-sections of the tensile test pieces. Together they were utilized to evaluate the local ductility of the tensile specimen. In this evaluation, the reduction of area (A_f), true fracture strain (TFS), or the true thickness strain at fracture (ε_{3f}) were the main parameters of interest. These parameters are defined as follows:

$$\varepsilon_{3f} = \ln(\frac{t_0}{t_f}), \tag{3.6}$$

where t_0 is the initial sheet thickness and t_f the sheet thickness at fracture, and

$$TFS = \ln(\frac{A_0}{A_f}), \tag{3.7}$$

where A_0 is the initial cross-sectional area of the tensile specimen, and A_f is an estimation of the area at fracture (according to ASTM E8) [146]. A_f is calculated as follows:

$$A_f = W_f \cdot \frac{1}{6}(t_1 + 4t_2 + t_3), \tag{3.8}$$

where W_f is the specimen width at fracture, which is projected to the plane perpendicular to the loading direction, t_2 is the minimum thickness of the fracture surface and t_1 and t_3 are the maximum thicknesses of the fracture surface. Typically, the thinner thickness, t_2 can be measured from the centre of the sample, while the thicker parts t_1 and t_3 are at the border of the specimen, where the sample has thinned less. A schematic presentation of the fracture surface thickness measurement on a tensile test sample is given in Figure 31.

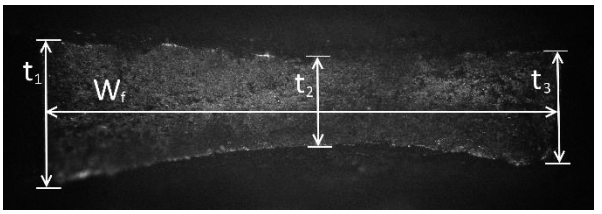

Figure 31. Example of fracture surface thickness and width measurement technique.

In order to reliably calculate the A_f value, the length of the fracture surface, W_f, was calculated using trigonometry by projecting the test direction on the plane perpendicular to the sample surface and measuring the width of test sample W and the fracture angle α_f. The procedure is illustrated in Figure 32.

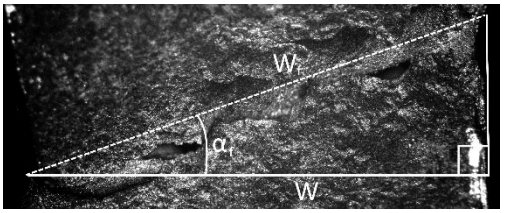

Figure 32. Example of fracture surface projected on the plane perpendicular to the fracture direction.

When α_f was below 10°, however, trigonometry could not be used to reliably determine W_f,. In this case, the value of W was used instead of W_f in Equation 3.8.

Measurements of t_1, t_2, t_3, W, and α_f were done using a Nikon optical microscope. In certain cases, where the focus length of the Nikon optical microscope was insufficient, a Nikon optical stereomicroscope was utilized instead. Both were operated using NIS Elements software (Nikon Instruments Inc.).

3.4.6 Evaluation of retained austenite stability

The mechanical stability of retained austenite was investigated from the tensile specimens of alloys 1.1 and 1.4 that contained above 2.0 vol.% of austenite in XRD measurements. The fracture end of the tensile specimen was ground with progressively finer papers up to 4000 grit. XRD measurements using a cobalt tube were performed on three areas at the distance of 2 mm, 5 mm and 8 mm from the crack tip. The length of measurement areas was 1.5 mm and their width between 4 mm to 5 mm depending on their distance from fracture tip. The presentation of the procedure is presented in Figure 33. XRD analysis was performed using the practice described in Section 3.4.2.

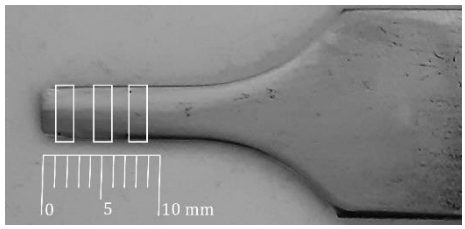

Figure 33. Example of XRD measurement of the tensile specimen.

The k_p values were determined by the Ludwigson & Berger relation by the linear relationship of austenite transformation V_γ as a function of true strain (ε) values. The retained austenite volume fraction measured by XRD from microstructural specimen was used as $V_{\gamma 0}$, and the autocatalytic factor p was 1.

The second method for evaluating the stability of retained austenite was EBSD phase mapping from the cross-section of the tensile test specimen after the tensile test. The cross-section was subjected to ion-polishing similarly to other EBSD specimens, described in Section 3.4.3. The unstrained location was 10 mm and the maximum strain 1 mm from the crack tip.

3.5 Investigations on the industrially produced Nb microalloyed sheets

The technological target of the present work was set as 1180 MPa grade improved-ductility steel which can be processed in a continuous galvanizing line. Laboratory alloy 2.4 was modified for industrial hot-dip galvanizing trials and laboratory TRIP

treatment and Q&P processing tests. The material was designated as IE1. The scientific objective of the line trials aimed at answering the second and fourth research questions.

3.5.1 Steel making and chemical composition

Reduced silicon content was one of the main priorities in order to ensure the galvanizability of the steel, which is why the main alloying component was aluminium. The manganese content was increased in order to utilize a lower carbon content. The industrial melt, IE1, was manufactured at SSAB Europe Raahe Works. The chemical alloying components measured by OES and maximum impurity level in wt.% are presented in Table 6.

Table 6. Alloying components and maximum levels of S, N and P (in wt.%) of IE1.

Alloy	C	Si	Al	Mn	Cr	Mo	Nb	V	S_{max}	N_{max}	P_{max}
IE1	0.10	0.5	0.8	2.7	0.30	0.15	0.015	0.010	0.0035	0.0060	0.0160

After casting and cutting, the steel slab was slowly cooled inside an induction-heated box for 72 hours in order to reduce the hydrogen content. Thereafter, the 220-mm-thick slab was reheated to 1280 °C before hot rolling with subsequent rolling passes in the roughing mill and finalizing into a 2.5 mm strip using 4-high 6-stand tandem hot-rolling mill.

The hot-rolled strip was pickled using hydrochloric acid and subsequently cold-rolled at SSAB Europe Hämeenlinna Works. Cold rolling was performed with 4-high 4-stand tandem cold rolling mill to produce a 1.5 mm strip to be used in the industrial hot-dip galvanizing and laboratory TRIP and Q&P processing experiments. The total cold rolling reduction of the strip was 40%.

3.5.2 TRIP heat treatment and Q&P processing

The cold-rolled, full hard specimens of IE1 were subjected to TRIP heat treatment and Q&P processing using the Gleeble 3800 thermomechanical simulator at CASR, Oulu, Finland. Schematic representations of the temperature profiles used in the experiments are given in Figure 34.

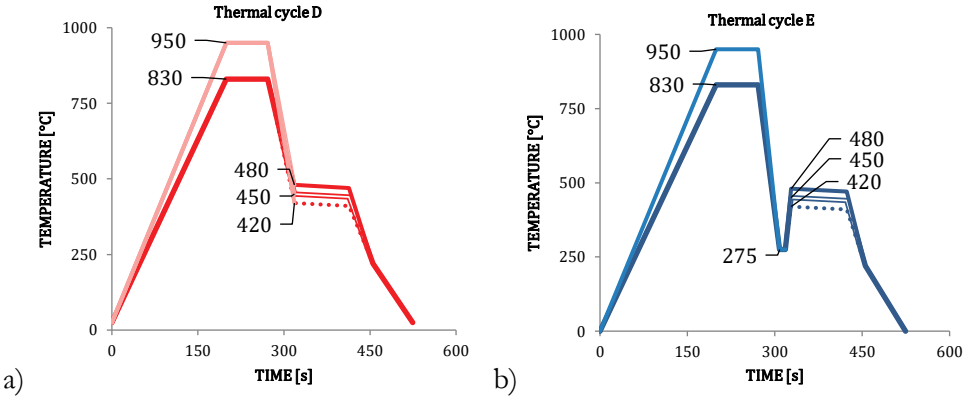

Figure 34. Temperature profiles of a) the TRIP type heat treatment and b) the Q&P processing of IE1.

Thermal cycle D represented TRIP treatment, while E was used to investigate the Q&P processing. Both were performed using intercritical annealing temperatures of 830 °C and 950 °C, where the austenite fraction was 56 vol.% at 830 °C and 100 vol.% at 950 °C. In thermal cycle D, the heating rate for IA 830 was 4 °C/s and 5 °C/s for IA 950 °C, after which the specimen was cooled to IBT at 9 – 10 °C/s. After 100 s at IBT, the final cooling to below M_s was performed at approximately 10 °C/s before slow cooling (2 °C/s) to ambient temperature. In thermal cycle E, the heating rate for IA 830 was 4 °C/s and 5 °C/s for IA 950 °C, after which the specimen was cooled to QT at 15 – 20 °C/s.

The calculated ideal quenching stop temperatures (QT) after intercritical annealing at 830 °C and after full austenitization at 950 °C were 275 °C and 315 °C, respectively. For comparison purposes, the lower temperature of 275 °C was utilized for both. These QT temperatures were obtained from JMatPro® by calculating the fraction of martensite in the final quench using the austenite composition at intercritical temperature.

After interrupted quenching, the heating rate for PT was 20 °C/s. After 100 s partitioning, the final cooling to below M_s was performed at approximately 10 °C/s before slow cooling (2 °C/s) to ambient temperature. The set temperature parameters and times are presented in Table 7.

Table 7. Temperature and time parameters of the TRIP and Q&P heat treatments of IE1.

Alloy	Thermal cycle	IA [°C]	t_{IA} [s]	QT [°C]	IBT / PT [°C]	t_{IBT} / t_{PT} [s]
IE1	D	830, 950	70		420, 450, 480	100
IE1	E	830, 950	70	275	420, 450, 480	100

The TRIP-treated and Q&P-processed specimens of IE1 were subjected to similar investigations using duplicate microstructural and mechanical properties testing. The specimen sizes were 10 mm · 60 mm for the microstructural investigations and 20 mm · 120 mm for the mechanical tests.

3.5.3 Hot-dip galvanizing trials

Continuous hot-dip galvanizing of the 1.5 mm cold-rolled IE1, which included intercritical annealing and subsequent dipping into a molten zinc bath, was performed at continuous galvanizing line (CGL) no. 3 of SSAB Europe Hämeenlinna Works. The steel strip was heated to 830 °C using a radiant tube furnace containing N_2 + H_2 atmosphere, where the steel was held for approximately 70 s. Thereafter, the strip was cooled rapidly using cooled high-pressure gas to the holding section, where it was austempered at 470 °C for 100 s before entering the zinc bath, where the strip was at 455 °C for approximately two seconds. The zinc coating thickness was adjusted to 100 g/m^2 using high-pressure air knives. The strip was cooled to room temperature using pressurized air and a water-containing quenching box. Before coiling, the strip was skin-pass milled using 0.2% reduction. A typical CGL layout is presented in Figure 35 [147].

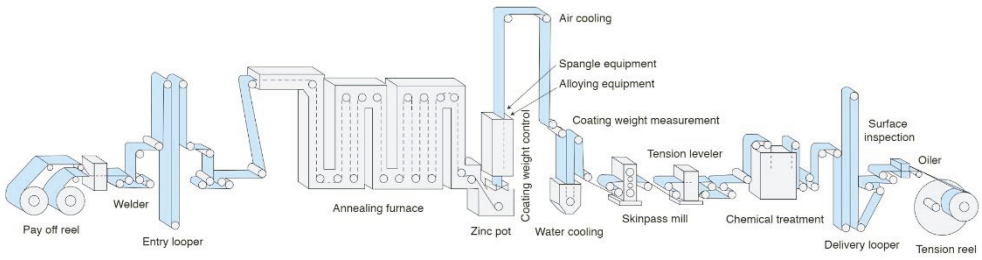

Figure 35. Layout of a typical CGL. Courtesy of WorldAutoSteel [147].

The galvanized specimens of IE1 were subjected to microstructural investigations and mechanical properties testing similarly to the other specimens in the present study. Duplicate heat treatment specimens were prepared for the microstructural investigations (10 mm · 60 mm) and for the mechanical tests (20 mm · 120 mm). Additionally, zinc coating and substrate adhesion properties of a galvanized specimen were investigated.

4 RESULTS

This chapter introduces the experimental results from the laboratory experiments and industrial hot-dip galvanizing trials. Alloys 1.1 – 1.4 were designated as TRIP-assisted Nb- and V-microalloyed DP steels, and their results were compared to alloy REF. Alloys 2.1 – 2.4, which were TRIP heat-treated, were designated as low-carbon Al-and Si-alloyed steels, of which alloy 2.4 was also utilized in the Q&P processing experiments. Industrial alloy IE1, namely Nb-microalloyed steel, was utilized both in the TRIP heat treatments and Q&P processing experiments on laboratory scale. Experiments were also performed on IE1 in the hot-dip galvanizing trials.

4.1 TRIP-assisted Nb- and V-microalloyed DP steels

The laboratory cold-rolled specimens of 1.1 – 1.4 were subjected to dilatometry, annealing experiments and material characterization including tensile tests as well as microstructural investigations using FESEM-EBSD and TEM. The retained austenite content was measured by performing XRD analysis.

4.1.1 Dilatometer tests and phase transformation temperatures

Phase transformation temperatures were determined from the dilatometer experiments and calculated using JMatPro® and Thermo-Calc. From the dilatometer data, the phase fractions against temperatures were first calculated using the lever rule. Next, the M_s temperatures were determined by fitting non-linear regression into the quenching curve, and A_{c1} and A_{c3} were determined by fitting the heating curve into the JMA equation.

The specimens of alloys REF and 1.1 were annealed at 900 °C and 1000 °C, whereas those of 1.2, 1.3 and 1.4 were annealed only at the higher temperature. Table 8 presents the phase transformation temperatures A_{c1}, A_{c3} and M_s from the dilatometer data and the austenite volume fractions at equilibrium temperatures A_1 and A_3 from JMatPro®.

Table 8. Phase transformation temperatures determined from the dilatometer data and austenite volume fractions, M_s temperatures and carbon content calculated using JMatPro®.

Alloy	Dilatometry				Calculated								
	A_{c1} [°C]	A_{c3} [°C]	M_s [°C] IA 900 °C	M_s [°C] IA 1000 °C	γ [vol.%] at 760 °C	γ [vol.%] at 830 °C	γ [vol.%] at 900 °C	γ [vol.%] at 1000 °C	A_1 [°C]	A_3 [°C]	M_s [°C]	γ carbon content [wt.%] at 830 °C	γ carbon content [wt.%] at 900 °C
REF*	740	870	374	-	31	100	100	-	682	806	365	0.13	0.14
1.1	750	985	158	193	25	50	77	100	727	946	411	0.37	0.24
1.2	735	980	-	394	21	43	69	100	741	968	411	0.36	0.25
1.3	740	980	-	389	24	51	81	100	740	939	399	0.35	0.25
1.4	720	940	-	384	28	54	84	100	728	933	404	0.38	0.25

* Dilatometer A_{c1} and A_{c3} results for REF after 900 °C annealing

The calculation of austenite volume fractions is presented in Figure 36 as a function of temperature in REF, 1.1 and 1.4 using JMatPro® (Fig. 36a) and Thermo-Calc (Fig. 36b). The experimentally determined values are presented in Figure 36c.

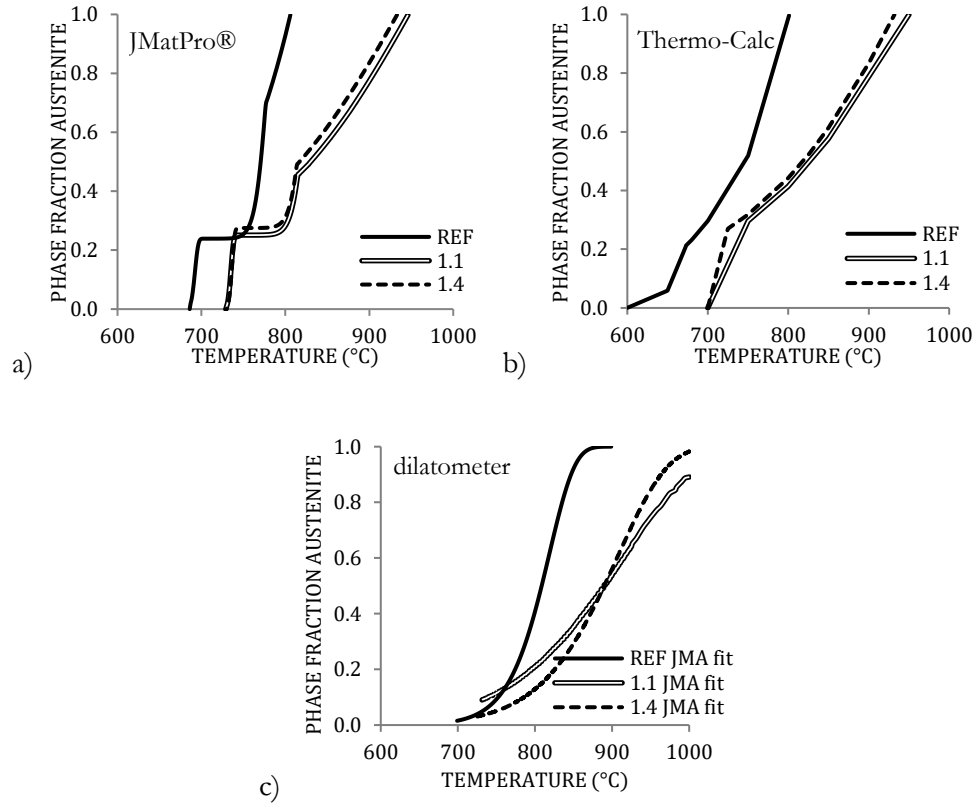

Figure 36. Austenite fraction of REF, 1.1 and 1.4 calculated by a) JMatPro® and b) Thermo-Calc compared to c) the dilatometer data fitted into the JMA equation.

The dilatometer results were in reasonable agreement with the calculations in Figure 36. It was apparent from the dilatometer experiments that the alloying additions had a significant effect on the A_{c3} temperatures of the alloys. Whereas REF clearly reached the fully austenitized state during annealing, 1.1 was still in the ferrite-austenite dual-phase region during holding at 900 °C. The specimens of alloys 1.1 – 1.4 were not fully austenitized until the temperature reached 1000 °C. The evolution of ferrite to austenite followed the JMA equation in the cases of REF and 1.4, but 1.1 did not fit the equation as finely. However, the relation to JMA was tested plotting $\ln\{\ln[1/(1-f_{\gamma IA})]\}$ versus ln(t), which yielded a straight line in the cases of REF, 1.1 and 1.4.

The effect of Si and Al alloying is also visible in the TTT diagram in Figure 37, which compares alloys 1.1 and REF. Alloy 1.1 had a pronounced ferrite transformation region compared to REF which means that a more rapid cooling speed is required in order to avoid the formation of ferrite during quenching.

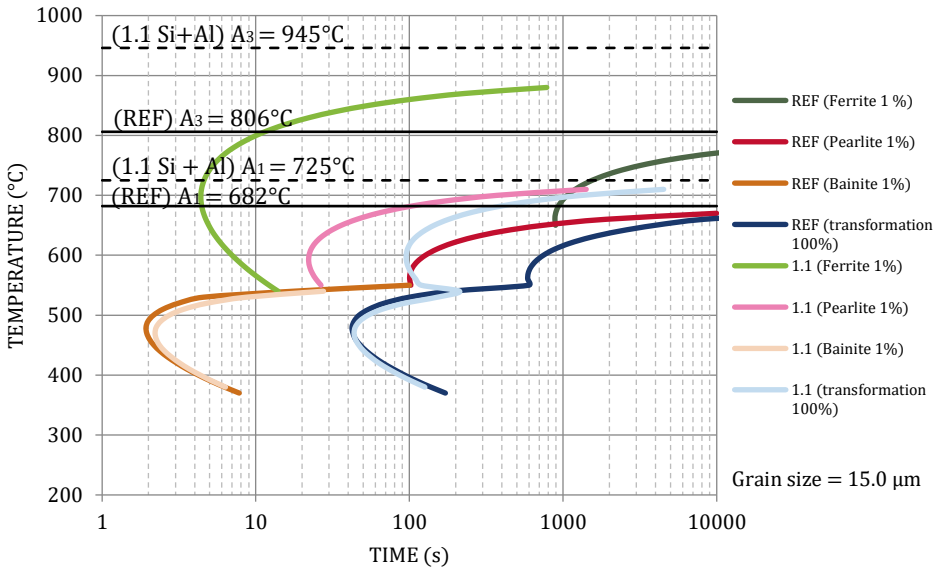

Figure 37. TTT diagrams and A_1 and A_3 temperatures of REF and 1.1.

As shown in the TTT diagrams in Figure 37, bainite transformation occurred at approximately the same time and in a temperature range of 370 – 540 °C in both steels. Due to the ferrite-stabilizing effect of Si and Al, however, the ferrite transformation range was more pronounced in 1.1 compared to REF. In these TTT diagrams according to JMatPro®, 1.1 was quenched from 1000 °C and REF from 900 °C, at which point they were both fully austenitic. Starting from the intercritical

annealing temperature of 1.1, such as 830 °C or 900 °C, the ferrite region was in the same time and temperature range as that of REF according to JMatPro®. See Appendix 1 for the TTT diagrams of the other investigated alloys.

4.1.2 XRD measurements

This section presents the volume fraction and carbon content of retained austenite after the final cooling of the specimens of REF and 1.1 – 1.4. The X-ray diffraction (XRD) studies utilized cobalt tube and Kα radiation. The XRD spectra of selected specimens of alloys 1.1, 1.3 and 1.4 are presented in Figure 38.

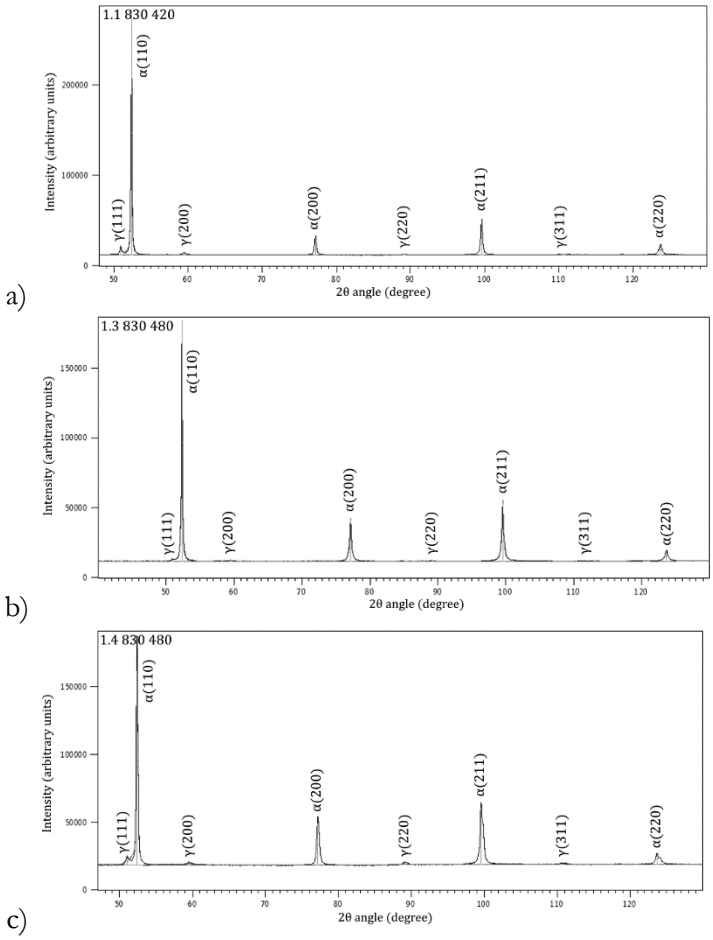

Figure 38. XRD spectra for a) 1.1 IA830 IBT420, b) 1.3 IA830 IBT480 and c) 1.4 IA830 IBT480.

The integrated intensities of the austenite peaks (111), (200), (220) and (311) were relatively low compared to those of the ferrite peaks. Some amount of retained austenite was, however, detected from the specimens of 1.1 and 1.4. Table 9 presents the retained austenite volume fractions from corresponding peaks using Equation 3.1 and the carbon content as calculated using Equation 3.2.

Table 9. Average volume fraction (vol.%) and carbon content (wt.%) of retained austenite in REF and 1.1 – 1.4.

Steel	IBT [°C]	IA (830 °C)		IA (900 °C)	
		average f_γ [vol.%]	average C_γ [wt.%]	average f_γ [vol.%]	average C_γ [wt.%]
REF	420	0.1	1.22		
REF	450	0.1	1.22		
REF	480	0.1	1.22		
1.1	420	8.5 ± 0.2	0.72	13.4 ± 0.1	0.73
1.1	450	4.6 ± 0.3	0.73	12.9 ± 0.6	0.73
1.1	480	1.2 ± 0.1	0.72	11.4 ± 0.2	0.74
1.2	420	0	-	0	-
1.2	450	0	-	0	-
1.2	480	0	-	0	-
1.3	420	0.3	1.19	0	-
1.3	450	1.1	0.70	0	-
1.3	480	1.2	0.73	0	-
1.4	420	5.4 ± 1.8	0.71	14.3 ± 0.7	0.71
1.4	450	12.0 ± 0.5	0.82	11.3 ± 0.6	0.74
1.4	480	8.7 ± 0.2	0.66	8.9 ± 0.4	0.65

According to the XRD measurements, the retained austenite content of 1.1 and 1.4 was between 4 and 14 vol.%. The carbon content of this retained austenite was at a level of approximately 0.7 wt.%. The lower IBT temperatures generally resulted in a higher retained austenite volume content, with the exception of the 1.4 specimen, which was intercritically annealed at 830 °C and austempered at 420 °C. As suspected, the REF specimens did not contain a significant amount of retained austenite. In addition to REF, the 1.2 and 1.3 specimens also did not contain any retained austenite or the fractions were below the detection limit (< 2.0 vol.%).

4.1.3 Mechanical properties

The mechanical properties were measured by performing tensile experiments on the heat-treated specimens. Table 10 presents the mechanical test results where strength,

elongation and n values were the results of engineering stress and strain. The work-hardening exponent, the n value, was calculated from the true strain-true stress from the strain range of 4% to 6% as well as between 10% and 20%, or between 10% and uniform elongation, A_g.

Table 10. Mechanical test results of REF and 1.1 – 1.4.

Steel	IBT [°C]	IA (830 °C)							IA (900 °C)						
		$R_{p0.2}$ [MPa]	R_m [MPa]	$R_{p0.2}/R_m$	A_g [%]	A_{25} [%]	n (4-6)	n (10-20/A_g)	$R_{p0.2}$ [MPa]	R_m [MPa]	$R_{p0.2}/R_m$	A_g [%]	A_{25} [%]	n (4-6)	n (10-20/A_g)
REF	420	614	910	0.67	14.0	23.2	0.21	0.18							
REF	450	550	956	0.58	12.3	24.3	0.25	0.10							
REF	480	600	1024	0.59	8.1	15.3	0.21	-							
1.1	420	417	937	0.45	18.4	18.7	0.34	0.25	381	827	0.46	12.8	18.5	0.29	0.16
1.1	450	451	999	0.45	18.5	24.9	0.34	0.22	393	843	0.47	15.0	26.0	0.30	0.19
1.1	480	503	1050	0.48	14.6	19.2	0.31	0.16	415	895	0.46	11.7	20.7	0.29	0.11
1.2	420	473	1006	0.47	12.6	16.5	0.29	0.15	435	932	0.47	13.5	20.7	0.28	0.17
1.2	450	493	1021	0.48	15.5	18.3	0.28	0.16	432	915	0.47	14.4	21.4	0.28	0.17
1.2	480	533	1053	0.51	8.1	10.3	0.25	-	479	971	0.49	10.7	20.0	0.26	0.09
1.3	420	456	956	0.48	11.8	18.2	0.28	0.13	434	862	0.50	11.4	21.2	0.28	0.12
1.3	450	493	975	0.51	13.1	19.9	0.29	0.16	425	894	0.48	12.2	23.2	0.28	0.16
1.3	480	538	1035	0.52	11.1	15.3	0.26	0.12	524	961	0.55	10.2	11.2	0.22	0.09
1.4	420	401	887	0.45	15.5	21.5	0.31	0.19	392	830	0.47	17.1	20.7	0.31	0.23
1.4	450	422	939	0.45	15.7	24.2	0.31	0.19	388	850	0.46	17.9	21.1	0.32	0.22
1.4	480	448	950	0.47	12.7	16.6	0.30	0.16	415	859	0.48	11.3	15.3	0.27	0.11

The highest ultimate tensile strength, 1053 MPa, was measured from the alloy 1.2 specimen, which was intercritically annealed at 830 °C and austempered at 480 °C. A similar strength level, approximately 1050 MPa, was also measured from the 1.1 and 1.3 specimens. The overall strength of 1.1, 1.2 and 1.3 was at the 1000 MPa level, whereas the 1.4 and REF specimens had an ultimate tensile strength of approx. 900 MPa. The most pronounced differences, however, were seen in the yield ratio (Rp0.2/Rm) and the elongations. The yield ratios of 1.1 – 1.4 were approximately 0.47, whereas that of REF was 0.61 on average. This indicated a higher elongation capability for 1.1 – 1.4 compared to REF. A similar trend was also noticed for the elongation values.

The elongation values were further investigated by determining the derivative of the true stress-true strain ($d\sigma/d\varepsilon$) and comparing it to the true stress-true strain curve. In addition, the incremental strain hardening n value was also plotted as a function of true strain. The necking onset point, and also the uniform elongation, were measured from the intersection of these curves. On the whole, higher elongation values led to an increased capacity to persist necking onset during the

straining of the material. Figures 39 and 40 present examples of the values after 830 °C and 900 °C annealing, respectively.

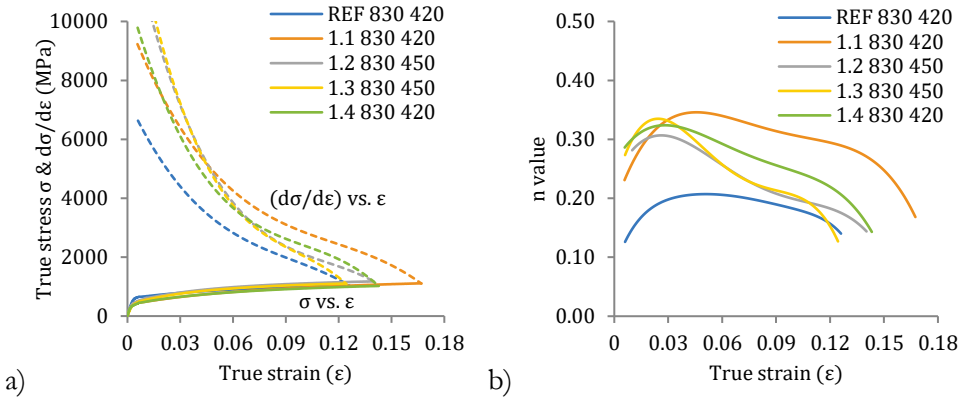

Figure 39. Examples of a) true strain-true stress curves and b) n values of REF and 1.1 – 1.4 after intercritical annealing at 830 °C.

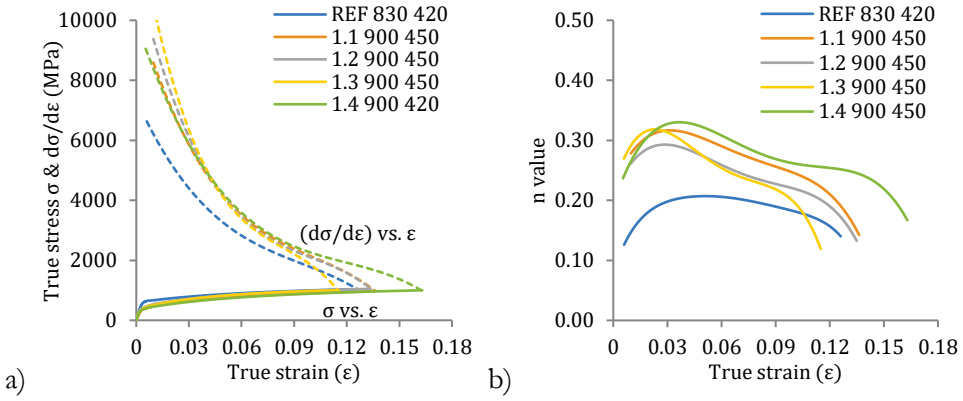

Figure 40. Examples of a) true strain-true stress curves and b) n values of REF after intercritical annealing at 830 °C and 1.1 – 1.4 after intercritical annealing at 900 °C.

The highest necking onset value of the 830 °C annealed specimens was measured from the alloy 1.1 specimen, which was austempered at 420 °C (Fig. 39a). After intercritical annealing at 900 °C, the highest necking onset value was measured from the 1.4 specimen austempered at 450 °C. It was also seen that after the higher intercritical annealing temperature, the austempering temperature of 450 °C resulted in better uniform elongations than austempering at 420 °C or 480 °C.

A similar trend was seen when the n values were investigated. The graphs in Figure 39b and 40b demonstrated that alloy 1.1 – 1.4 specimens had higher ductility compared to REF. The highest n values were found in the specimens which also had the highest A_g value.

The true fracture strain (TFS) and thickness strain at fracture (ε_{3f}) values were also measured from the fracture surfaces of the tensile testing specimens. These values depict the damage tolerance of the material during uniaxial strain. TFS takes into account the fracture surface area, whereas ε_{3f} is the third principal strain at fracture. When TFS ≈ ε_{3f}, the significance of cross-sectional area is low, because ε_{3f}, does not take the width of fracture surface into account.

Table 11 presents the measured ε_{3f} and TFS for the REF specimens after intercritical annealing at 830 °C and for 1.1 – 1.4 specimens after intercritical annealing at 830 °C and 900 °C. The measured values, together with other results in the present investigation, are also presented in Appendix 2.

Table 11. Thickness strain at fracture (ε_{3f}) and true fracture strain (TFS) values.

Steel	IBT	IA (830 °C)			IA (900 °)		
	[°C]	ε_u	ε_{3f}	TFS	ε_u	ε_{3f}	TFS
REF	420	0.13	0.77	0.80			
REF	450	0.11	0.72	0.73			
REF	480	0.08	0.50	0.50			
1.1	420	0.17	0.53	0.61	0.12	0.70	0.82
1.1	450	0.17	0.43	0.52	0.14	0.75	0.76
1.1	480	0.13	0.42	0.52	0.11	0.61	0.71
1.2	420	0.11	0.53	0.58	0.13	0.53	0.65
1.2	450	0.14	0.35	0.42	0.13	0.61	0.62
1.2 *	480	-	-	-	0.10	0.54	0.60
1.3	420	0.11	0.42	0.53	0.11	0.51	0.65
1.3	450	0.12	0.42	0.52	0.12	0.47	0.58
1.3	480	0.11	0.51	0.57	0.10	0.44	0.51
1.4	420	0.14	0.58	0.73	0.16	0.68	0.79
1.4	450	0.14	0.45	0.57	0.16	0.51	0.61
1.4	480	0.12	0.55	0.65	0.11	0.63	0.74

* Specimen fractured outside gauge length

After intercritical annealing at 830 °C, REF had the highest ε_{3f} and TFS values, but its elongation values, ε_u, were lower. Typically, the aim for balanced formability properties are as high as possible elongation values and ε_{3f} as well as high TFS values. In other words, the target is to reach the upper right corner of the diagram for the increased ductility, as shown in Figures 41a and 41b.

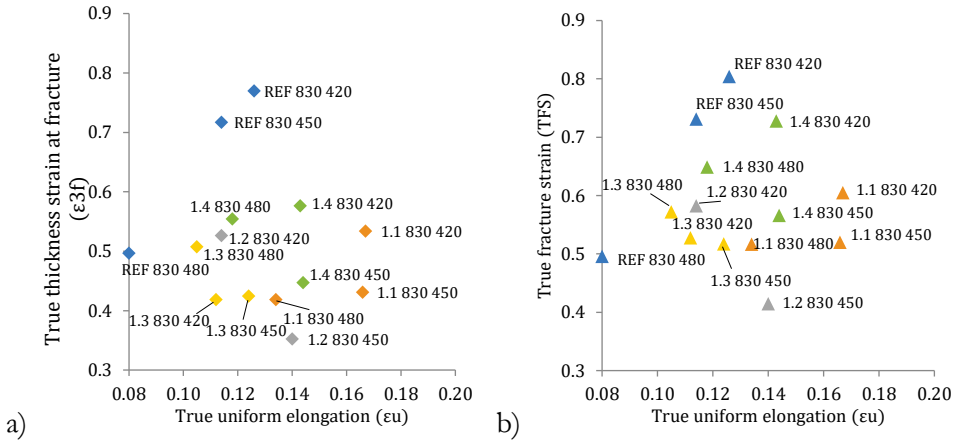

Figure 41. True thickness strain at fracture ε_{3f} (a) and TFS (b) values as a function of true uniform elongation of REF and 1.1 – 1.4 after intercritical annealing at 830 °C.

After IA at 900 °C, REF had the highest ε_{3f} and TFS values, but the ε_u values were lower compared to those of 1.1 – 1.4. A specimen of 1.4 achieved the highest combined elongation values in both ε_{3f} and TFS. The result of specimen 1.4 (IA900 °C IBT420 °C) indicates its balanced strength-ductility properties (Fig. 42a and 42b).

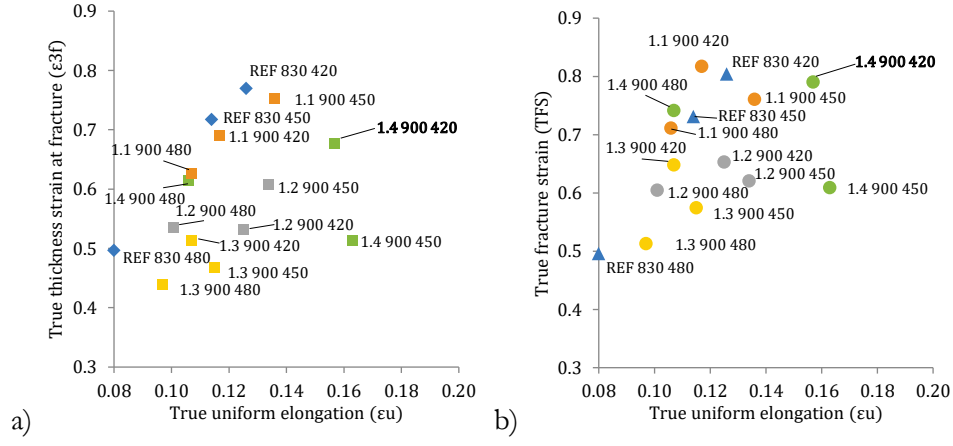

Figure 42. True thickness strain at fracture ε_{3f} (a) and TFS (b) values as a function of true uniform elongation of 1.1 - 1.4 after 900 °C annealing and REF after 830 °C annealing.

Annealing at higher temperature shifted the properties of 1.1 – 1.4 closer to those of REF (Fig. 42a and 42b). This could be seen as an effect of increased austenitization compared to the specimens annealed at 830 °C.

4.1.4 Microstructural analysis

Microstructural investigations were performed with Nital-etched specimens using secondary electron and back-scatter electron detectors in FESEM. Additionally, the selected microstructures were further analysed using EBSD. The precipitation properties were studied using the TEM carbon replica method.

Figure 43 presents micrographs of a typical microstructure for REF and 1.1 after austempering. The microstructure of 1.1 consisted of a ferrite matrix with martensite-austenite islands on the grain boundaries, whereas REF was predominately bainitic-ferritic with some amount of martensite constituents shown as distinct blocks of lighter grey.

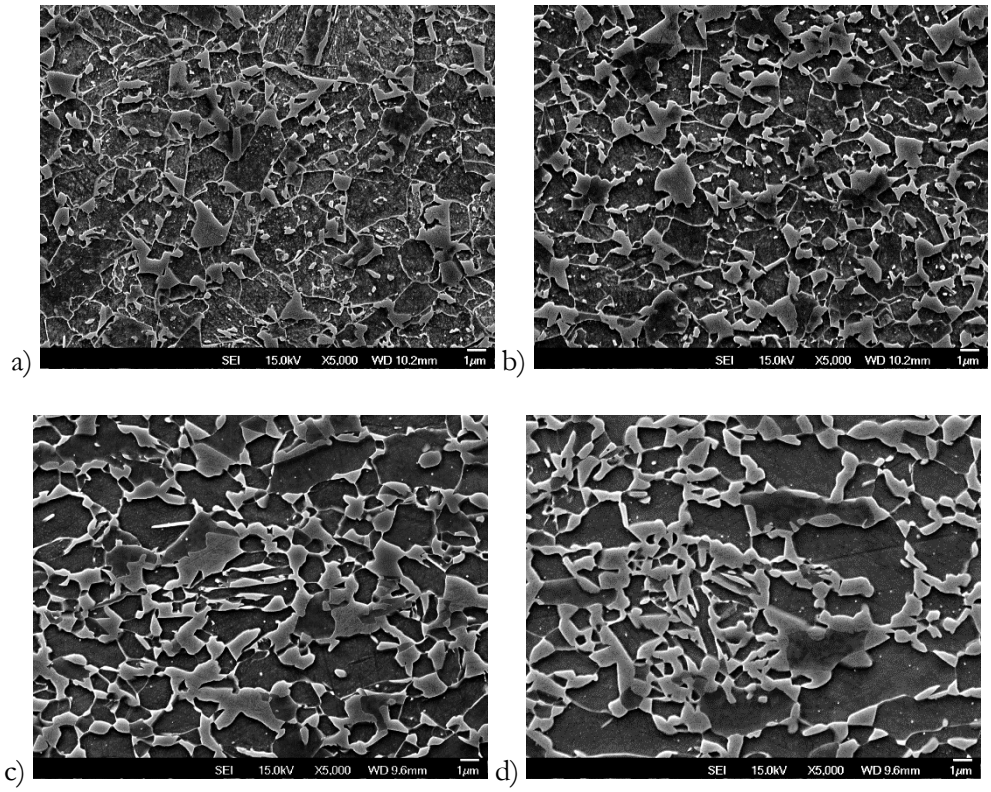

Figure 43. FESEM micrographs from the ¼ thickness of longitudinal cross-section samples of a) REF IA830 IBT420, b) REF IA830 IBT480, c) 1.1 IA830 IBT450 and d) 1.1 IA830 IBT480.

Figure 44 presents the EBSD PQM phase maps of the selected specimens of 1.1 and 1.4 after intercritical annealing at 830 °C and austempering at 420 °C and 480 °C.

Ferrite is presented in light red and austenite in dark blue. The islands in the ferrite grain boundaries in both 1.1 and 1.4 were analysed as austenite (dark blue) or martensite, which was unindexed (black).

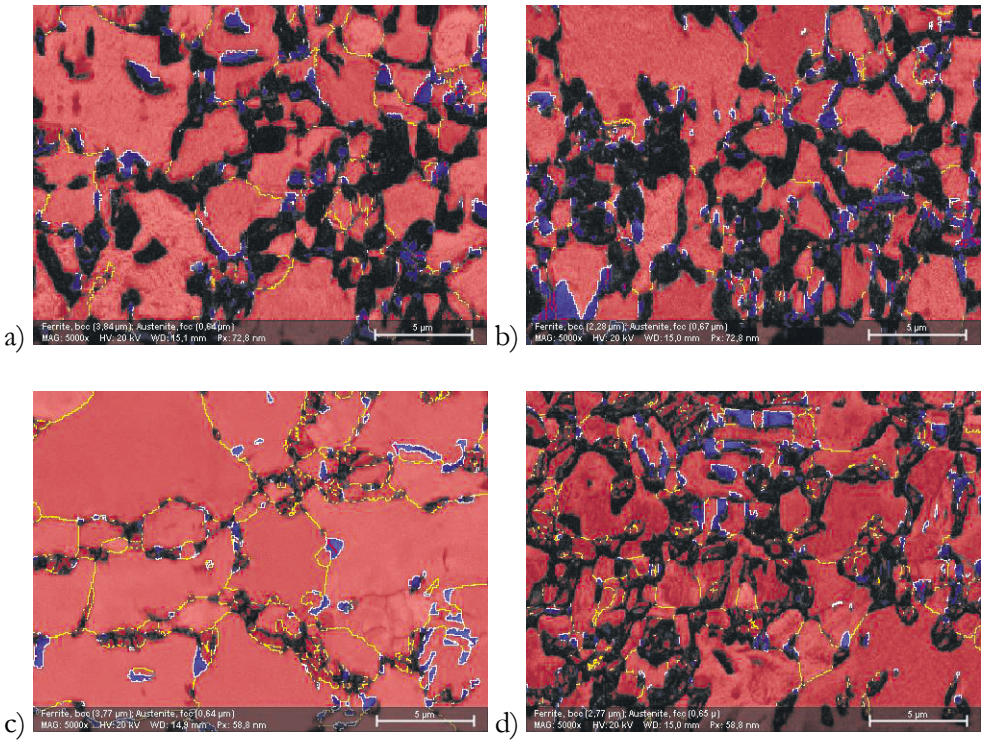

Figure 44. EBSD PQM phase maps of a) 1.1 IA830 IBT420, b) 1.1 IA830 IBT480, c) 1.4 IA830 IBT420 d) 1.4 IA830 IBT480.

The effect of the microalloying elements Nb and V on the grain sizes is visible in Figure 44. The composition without microalloying, 1.4, had the largest ferrite grain size (Fig. 44c), which is inherited in the intercritically annealed microstructure from previous heat treatment steps.

The amount of retained austenite increased with increasing annealing temperature. The effect was the most pronounced in 1.4 IA900 °C IBT450 °C. Figure 45 presents the EBSD phase maps of the austenite overlaid on the PQM of 1.1 and 1.4 specimens of IA 900 °C / IBT 420, 450 and 480 °C. The austenite phase is displayed with inverse pole figure (IPF) orientation colouring visible in the upper left corner. IPF colouring is displayed as the orientation difference on macroscopic x-axis. For example, grains oriented with <111> direction parallel to the x-axis will appear blue in the IPF X colouring. The rolling direction is parallel to the y-axis.

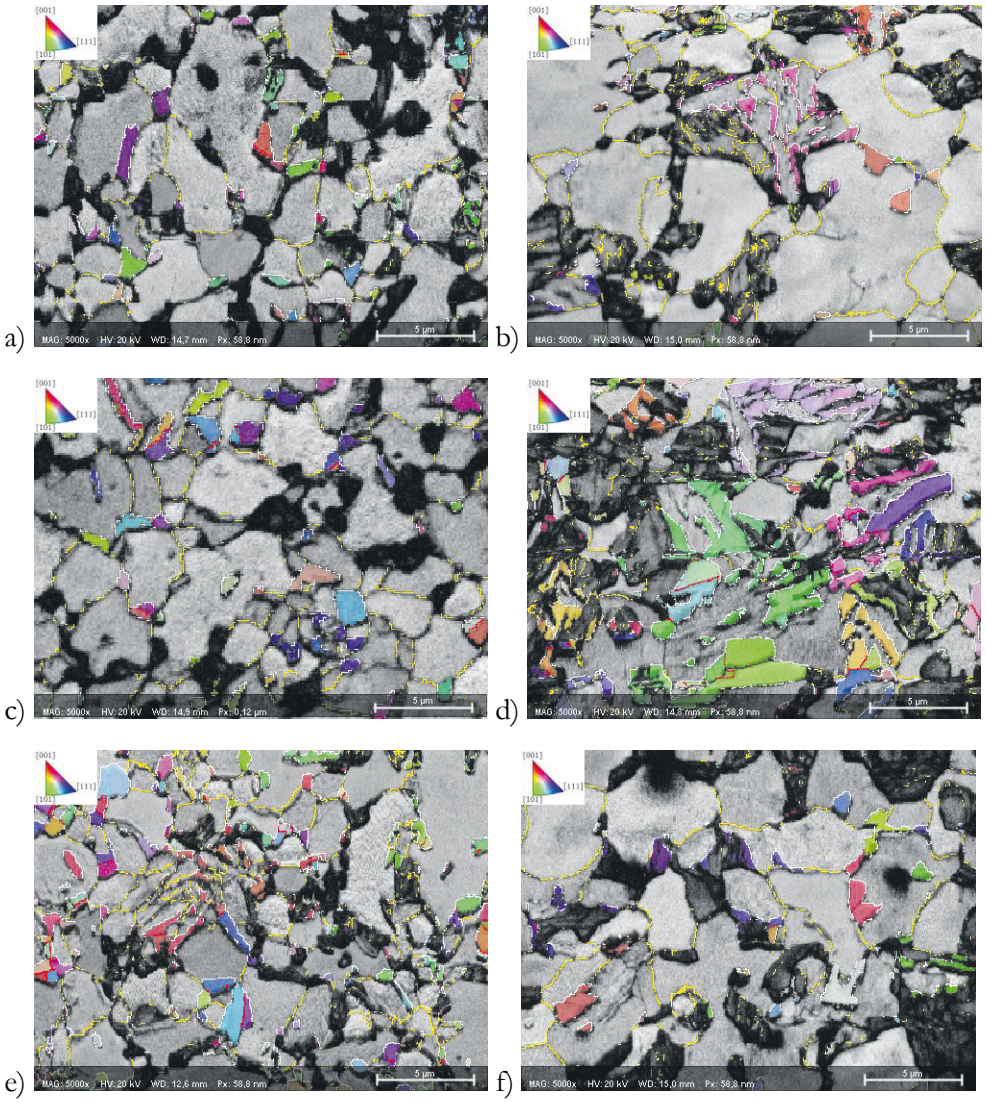

Figure 45. EBSD PQM phase maps of austenite in IPF X colouring. From top to bottom on the left (a, c, e): 1.1 IA 900 °C / IBT 420, 450, and 480 °C. From top to bottom on the right (b, d, f): 1.4 IA 900 °C / IBT 420, 450, and 480 °C.

The EBSD phase maps presented in Figure 45 show that the austenite phase appeared as individual retained austenite grains on the ferrite grain boundaries or film-like structures inside MA islands or sheaves in bainitic ferrite. The latter type of retained austenite mixed with bainite, for example, was found in the specimen of alloy 1.4 intercritically annealed at 900 °C and austempered at 450 °C.

The EBSD investigation of austenite in the microstructure of REF, 1.2 and 1.3 revealed minuscule amounts of retained austenite in the final microstructure. Figure 46 presents their EBSD PQM phase maps with austenite vol.% overlaid on the micrographs.

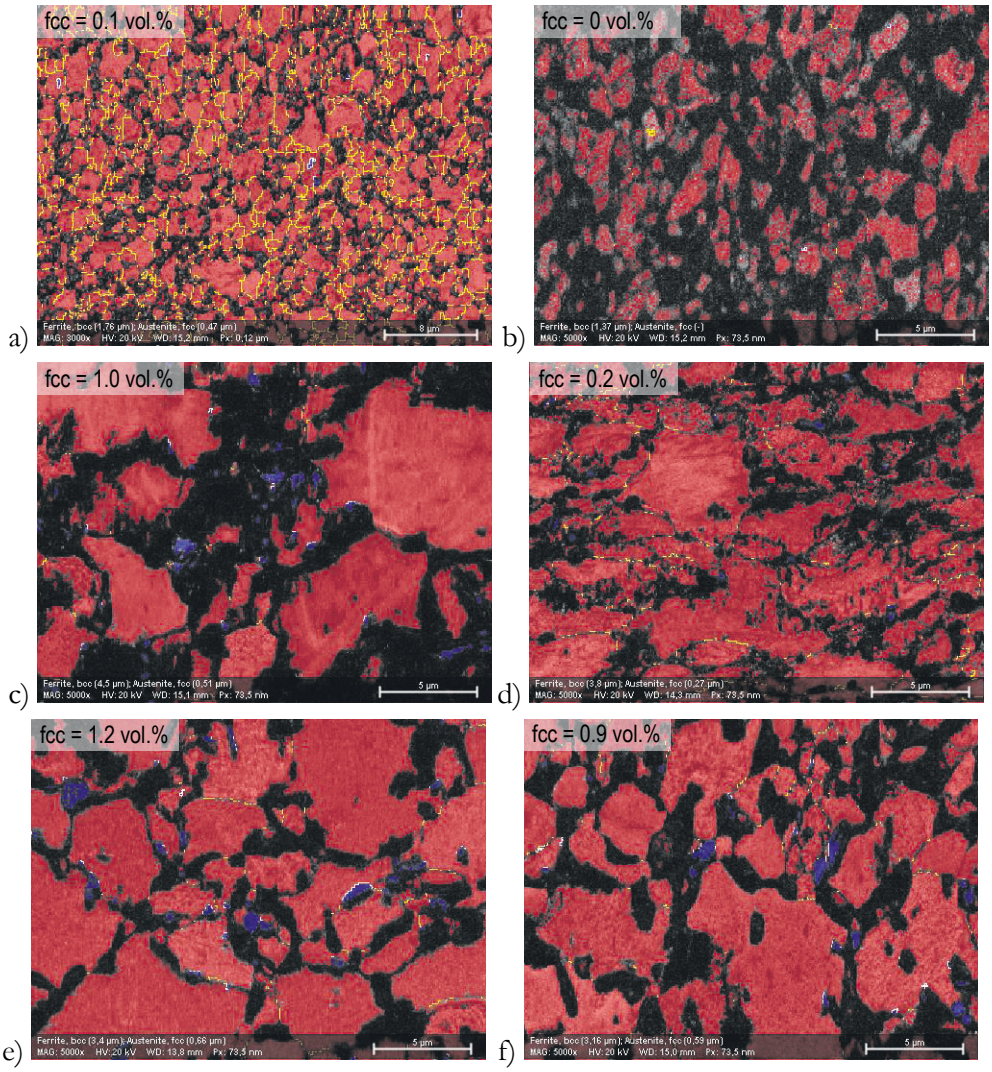

Figure 46. EBSD PQM maps overlaid with phase maps of ferrite and austenite of a) REF IA830 IBT480, b) REF IA830 IBT480 (with increased magnification), c) 1.2 IA830 IBT480, d) 1.2 IA900 IBT450, e) 1.3 IA830 IBT420 and f) 1.3 IA900 IBT450.

In the case of the microstructures shown in Figure 46, REF was predominately bainitic-ferritic with some amount of martensite and single retained austenite grains.

The microstructure of specimens of alloys 1.2 and 1.3, on the other hand, contained intercritical ferrite and martensite islands within the grain boundaries. A small amount of retained austenite was found in the phase maps of alloys 1.2 and 1.3. The phase determination results are presented in Appendix 3.

4.1.5 Stability of retained austenite

The retained austenite stability was investigated by performing EBSD analysis on the post-tensile test microstructure. Figure 47 presents the microstructure of the tensile specimen of alloy 1.1 IA830 °C IBT450 °C at zero strain and maximum strain.

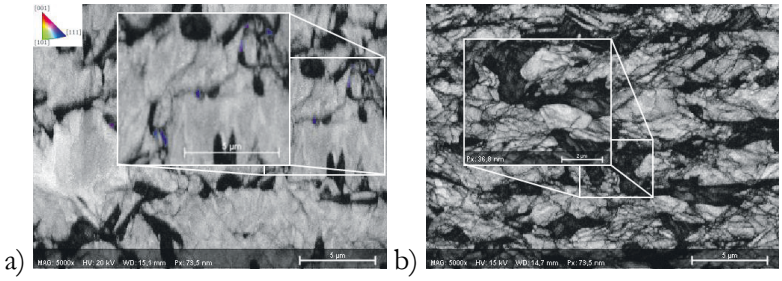

Figure 47. EBSD PQM phase map of 1.1 IA830 °C IBT450 °C at a) 0% and b) maximum strain.

The EBSD phase map of 1.1 IA830 °C IBT450 °C at zero strain (Fig. 47a) showed ferrite matrix with retained austenite on the ferrite grain boundaries adjacent to martensite islands. The same specimen at maximum strain (Fig. 47b) exhibited a highly deformed ferritic microstructure without retained austenite. A similar effect was seen in Figure 48 for the tensile specimen of 1.4 IA900 °C IBT420 °C, which shows that retained austenite was completely transformed into martensite at maximum strain.

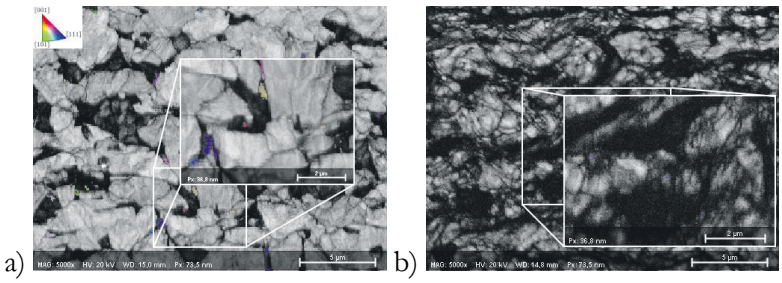

Figure 48. EBSD PQM phase map of 1.4 IA900 °C IBT420 °C at a) 0% and b) maximum strain.

The stability of retained austenite was also studied by fitting the retained austenite volume fractions from the strained tensile specimen (Fig. 33) XRD measurements into the Ludwigson & Berger relationship (Equation 2.4) and fitting the linear relationship of retained austenite transformation as a function of true strain. Figure 49a presents the retained austenite content as a function of true strain, and Figure 49b shows the linear fitting curves as a function of true strain.

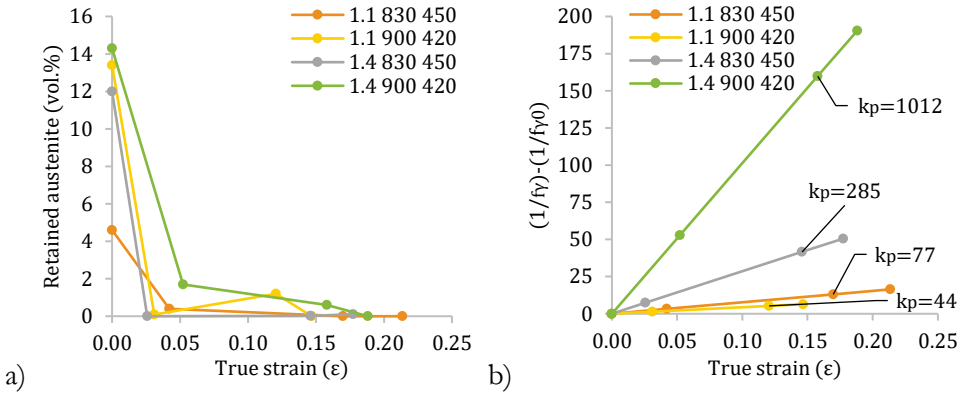

Figure 49. a) Retained austenite vol.% and b) the linear fitting curves of the Ludwigson & Berger relationship as function of true strain.

The values for k_p, which are presented overlaid on the graph in Figure 49b, showed that the 1.4 specimen intercritically annealed at 900 °C and austempered 420 °C had the highest value. It was considerably higher than those of other specimens in the present investigation, which was the result of the slightly higher retained austenite fractions measured from the strained microstructure. As shown in Figure 49a, the volume fractions of retained austenite in the strained locations were relatively low, which indicated low mechanical stability.

4.1.6 Precipitate analysis

Carbon replicas were prepared from the specimens of alloys REF and 1.1 – 1.4 and investigated using STEM-EDS. The heat treatment of specimens studied by STEM-EDS was intercritical annealing at 830 °C and austempering at 450 °C. The qualitative analysis of the precipitates in 1.1, 1.2 and 1.3 indicated they were mainly complex carbide and carbonitride precipitates Ti(Nb)N, Nb(Ti,V,Mo)C and

V(Ti,Nb,Mo)C. For example, the Nb-microalloyed 1.1 contained Ti(Nb)N and Nb(Mo)C with approximate diameters of 100 nm and 50 nm, respectively (Fig. 50a).

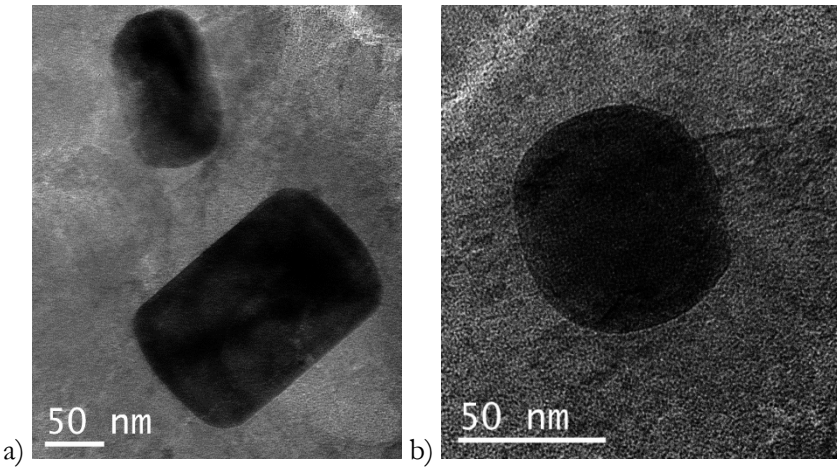

Figure 50. TEM micrographs of a) Ti(Nb)N and Nb(Mo)C precipitates in 1.1 and b) spherical Ti(Nb)N precipitate in 1.4.

STEM-EDS analysis also indicated the presence of Ti(Nb,Mo)C and Ti(Nb)N in the alloy 1.4 specimen, which demonstrates the powerful precipitation tendency of Nb even at low concentrations. A TEM micrograph of this type of precipitate, which had spherical morphology, is presented in Figure 50b.

Similarly to 1.1 and 1.4, the EDS analysis of 1.3 indicated the presence of Ti(Nb)N precipitates with average diameters of 50 – 100 nm, but in addition the sample contained vanadium carbides (VC), which were also found in 1.2. Compared to NbC, these spherical VC precipitates in 1.2 and 1.3 were smaller, their approximate diameter being below 30 nm.

Figure 51 presents STEM micrograph examples of the observed VC precipitates in the specimens of alloys 1.2 and 1.3 as well as the respective EDS spectra where the Cu peak is presumed to originate from the copper grid used to mount the carbon replicas. VC was identified from the Kα peak of vanadium and the presence of other carbide-forming elements, such as Mo and Ti, were also detected. The peaks of Al, Mn and Fe are presumed to originate from the steel matrix as residual elements in the carbon replica.

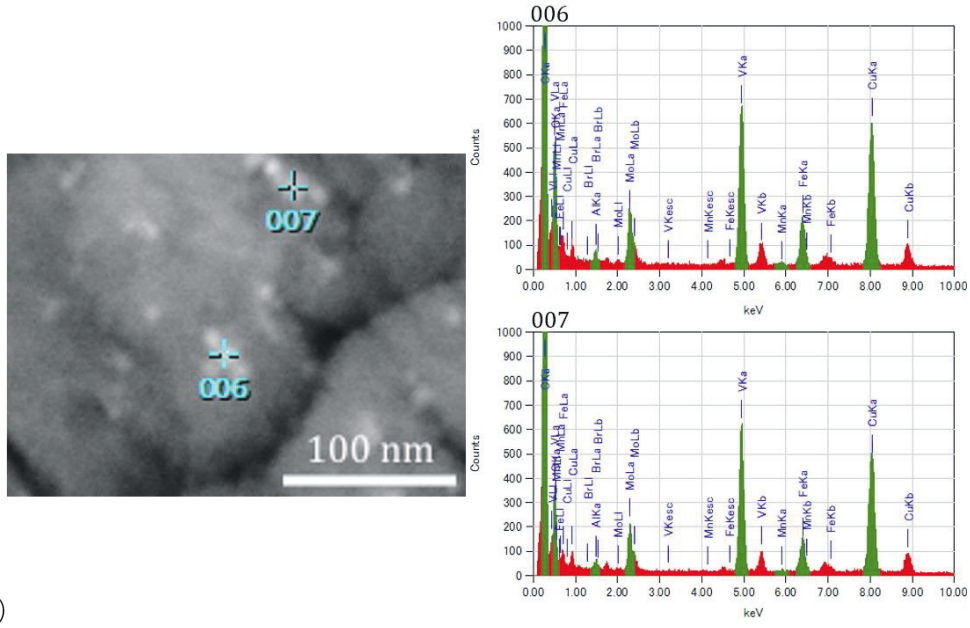

a)

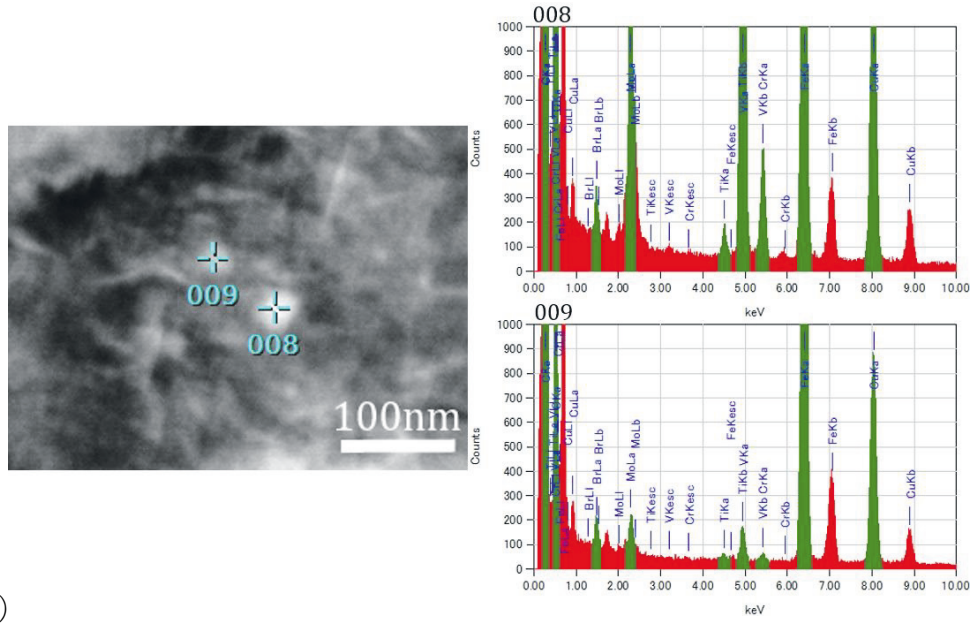

b)

Figure 51. Precipitates analysed using STEM-EDS from carbon replicas of a) 1.2 and b) 1.3.

NbC and most of the VC precipitates were probably formed during the hot-rolling process, whereas VC, due to its higher solubility, also included secondary precipitates formed during intercritical annealing.

Thermo-Calc was utilized to calculate the equilibrium phase content of phases other than ferrite and austenite. The mass fraction of phases on a logarithmic scale as a function of temperature in REF and 1.1 – 1.4 alloys is presented in Figure 52.

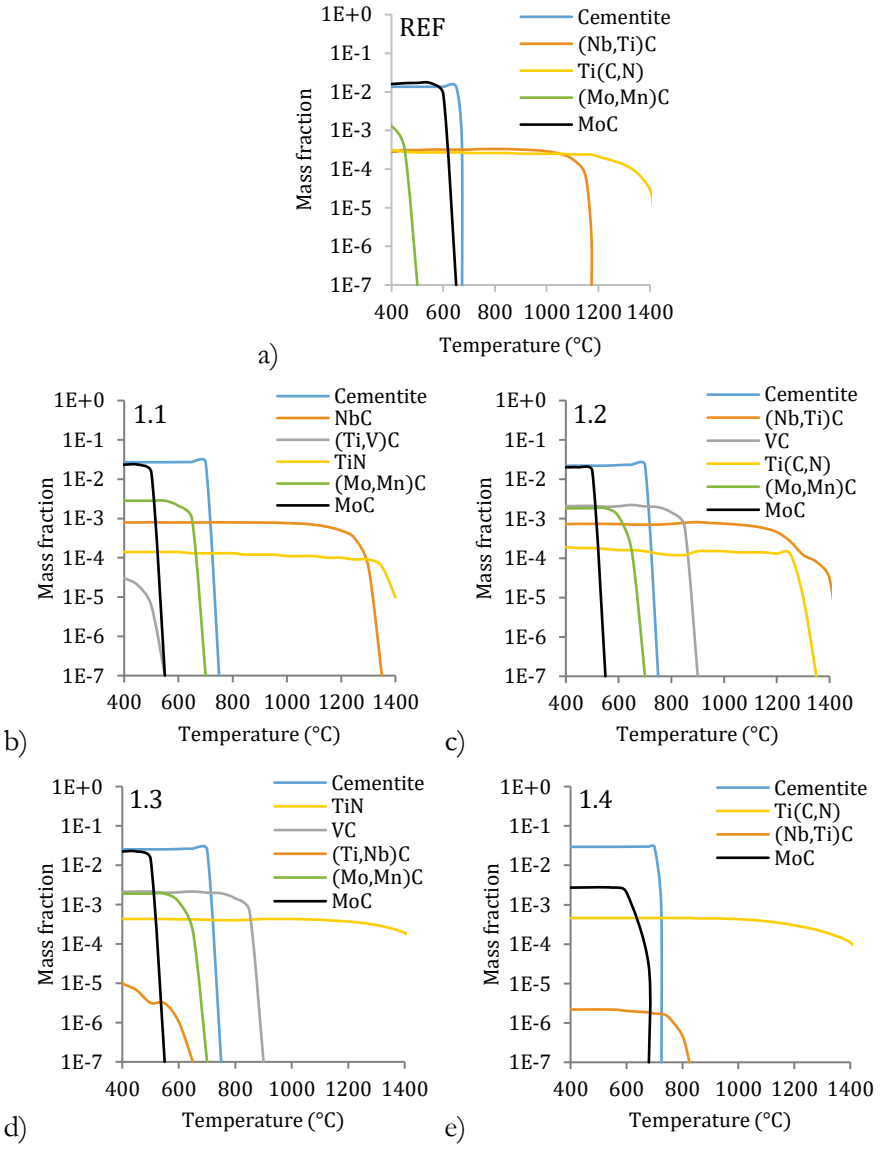

Figure 52. Mass fraction of equilibrium phases in a) REF, b) 1.1, c) 1.2, d) 1.3 and e) 1.4 alloys calculated using Thermo-Calc.

Figure 52 shows that the presence of cementite occurred in the REF alloy below 650 °C, whereas in alloys 1.1 – 1.4 it was stable until approx. 750 °C. Other phases, such as the hexagonal close-packed (HCP) $(Mo,Mn)_2C$ and Mo_7C_3 phase appeared below the cementite. Significant phases at higher temperatures were NbC, VC, TiN and Ti(Nb)C, depending on the alloying. For example, VC was present in alloys 1.2 and 1.3, while the only significant high temperature phase in alloy 1.4 was TiN.

4.2 Low-carbon Al- and Si-alloyed DH steels

The laboratory cold-rolled specimens of alloys 2.1 – 2.4 were subjected to dilatometry, annealing experiments and material characterization including tensile tests as well as microstructural investigations using FESEM-EBSD. XRD analysis was performed in order to measure the retained austenite content.

4.2.1 Dilatometer tests and phase transformation temperatures

Table 12 presents the phase transformation temperatures A_{c1}, A_{c3} and M_s of the investigated alloys. These temperatures were determined from the dilatometer data as well as calculated using JMatPro® software. From the dilatometer data, the M_s temperatures were determined by fitting the quenching curve into a non-linear regression curve with Minitab software. A_{c1} and A_{c3} were determined by fitting the heating curve into the JMA equation. The dilatometer specimens of alloys 2.1 and 2.4 were annealed at both temperatures, whereas those of 2.2 and 2.3 were only annealed at 1000 °C, at which temperature the alloys were expected to be fully austenitized.

Table 12. Experimental A_{c1}, A_{c3} and M_s temperatures from dilatometer tests and austenite volume fractions M_s temperatures and carbon contents calculated using JMatPro®.

Alloy	Dilatometry				Calculated								
	A_{c1} [°C]	A_{c3} [°C]	M_s [°C] IA 900 °C	M_s [°C] IA 1000 °C	γ [vol.%] at 760 °C	γ [vol.%] at 830 °C	γ [vol.%] at 900 °C	γ [vol.%] at 1000 °C	A_1 [°C]	A_3 [°C]	M_s [°C]	γ carbon content [wt.%] at 830 °C	γ carbon content [wt.%] at 900 °C
2.1	702	877	429	-	17	100	100	100	681	827	380	0.08	0.08
2.2	652	903	-	437	13	89	100	100	687	842	374	0.09	0.08
2.3	748	993	-	441	12	44	75	100	703	948	408	0.20	0.12
2.4	727	1000	330	430	11	36	61	100	712	988	404	0.22	0.14

Figure 53 presents the volume fraction of austenite during the annealing of alloys 2.1 – 2.4 calculated by JMatPro®, Thermo-Calc and from dilatometer data. The effect of Si and Al alloying on the A_1 and A_3 is visible in the experimental results. Whereas 2.1 and 2.2 were fully austenitic at 900 °C, the 1 wt.% Al-containing 2.3 and 2.4 did not reach fully austenitic state until 948 °C and 988 °C, respectively.

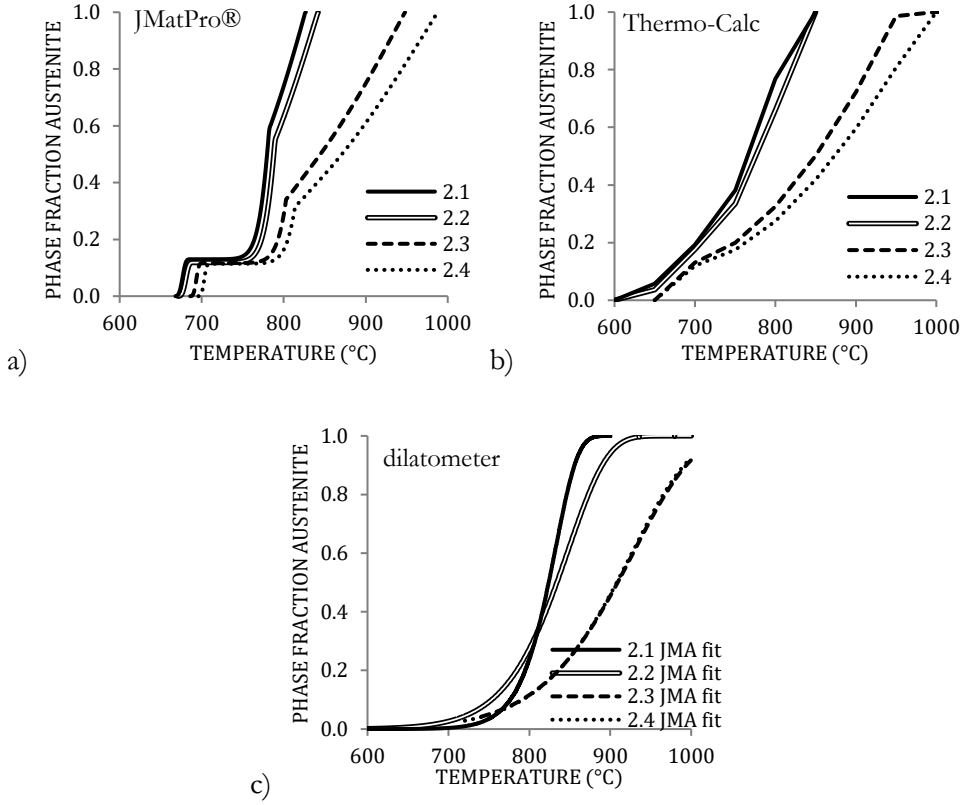

Figure 53. Austenite volume fractions of 2.1, 2.2, 2.3, and 2.4 calculated using a) JMatPro® and b) Thermo-Calc compared to c) dilatometer data fitted into JMA equation.

Data from the dilatometer experiments generally yielded higher austenite transformation temperatures than the JMatPro® and Thermo-Calc calculations, which were in good agreement with each other (Fig. 53). However, the JMA fit of 2.3 and 2.4 was not perfect compared to that of 2.1 and 2.2. This meant that the fitting curve did not reach 100% transformation for the Al-alloyed 2.3 and 2.4. The austenite transformation was near completion at 1000 °C, whereas as 2.1 and 2.2 were fully austenitic at lower temperatures and the data fits finely to the JMA equation. Clearly, the ferrite-stabilizing effect of Al was seen in these results.

The evolution of ferrite to austenite followed the JMA equation in the case of 2.1 and 2.2, but the Al-alloyed 2.3 and 2.4 did not fit the equation as well. However, the relation to JMA was tested by plotting $\ln\{\ln[1/(1-f_{\gamma IA})]\}$ versus $\ln(t)$, which yielded a straight line in all cases.

4.2.2 XRD measurements

This section presents the volume fraction of retained austenite after the final cooling of REF and 2.1 – 2.4 specimens. Table 13 presents the XRD measurements (using copper tube) of the investigated specimens. It was observed that the specimens of alloys 2.1 and 2.2 after annealing at 900 °C contained a detectable amount of retained austenite. The others were below the reliably detectable content of 2.0 vol.%. The volume fractions of retained austenite were calculated using Equation 3.1 and the carbon contents was calculated using Equation 3.2.

Table 13. Average volume fraction (vol.%) and carbon content (wt.%) of retained austenite in alloys 2.1 - 2.4.

Steel	IBT [°C]	IA 830 °C		IA 900 °C	
		average f_γ [vol.%]	average C_γ [wt.%]	average f_γ [vol.%]	average C_γ [wt.%]
REF	420	< 1	-		
REF	450	< 1	-		
REF	480	< 1	-		
2.1	420	< 2	-	3.5 ± 0.5	0.87
2.1	450	< 1	-	5.4 ± 0.2	0.70
2.1	480	< 1	-	< 1	-
2.2	420	< 1	-	3.8 ± 1.5	0.61
2.2	450	< 1	-	< 1	-
2.2	480	< 1	-	< 1	-
2.3	420	< 1	-	< 1	-
2.3	450	< 2	-	< 1	-
2.3	480	< 2	-	< 1	-
2.4	420	< 1	-	< 1	-
2.4	450	< 2	-	< 1	-
2.4	480	< 1	-	< 1	-

Surprisingly, the highest retained austenite content was measured from the specimen of alloy 2.1 which did not contain a significant amount of either Si or Al (0.32 wt.% and 0.10 wt.%, respectively). The second highest retained austenite content was detected from alloy 2.2, which had Si and Al alloying of 0.71 wt.% and 0.10 wt.%, respectively. These results were from the higher intercritical annealing temperature,

indicating that the higher annealing temperature may have led to retained austenite stabilization when the lower Al alloying was used. This effect could not have been due to the carbon content of austenite which was lower at the higher temperature. The low retained austenite fractions, which were < 2 vol.%, demonstrated that TRIP heat treatment did not stabilize the retained austenite in the present case. Retained austenite fractions below 2.0 vol.% were considered below the detection limit.

4.2.3 Mechanical properties

Tensile tests at constant strain rate were carried out on the specimens which had gone through similar heat treatments as the microstructural specimens. Table 14 presents the heat treatment parameters and the mechanical properties of REF and 2.1 – 2.4. Strength and elongation values were measured from the engineering strain, while n values were calculated from the true stress-true strain curves.

Table 14. Tensile test results of alloys 2.1 – 2.4 compared to REF.

Steel	IBT [°C]	IA (830 °C)							IA (900 °C)						
		$R_{p0.2}$ [MPa]	R_m [MPa]	$R_{p0.2}/R_m$	A_g [%]	A_{25} [%]	n (4-6)	n (10-20/A_g)	$R_{p0.2}$ [MPa]	R_m [MPa]	$R_{p0.2}/R_m$	A_g [%]	A_{25} [%]	n (4-6)	n (10-20/A_g)
REF	420	614	910	0.67	14.0	23.2	0.21	0.18							
REF	450	550	956	0.58	12.3	24.3	0.25	0.10							
REF	480	600	1024	0.59	8.1	15.3	0.21	-							
2.1	420	489	785	0.62	7.0	15.7	0.15	-	593	835	0.71	5.1	13.0	0.06	-
2.1	450	589	907	0.65	7.5	16.5	0.15	-	599	851	0.70	5.7	14.5	0.07	-
2.1	480	600	918	0.65	6.7	12.6	0.14	-	572	832	0.69	4.4	12.3	0.03	-
2.2	420	599	968	0.62	7.0	9.5	0.14	-	665	973	0.68	6.7	12.3	0.12	-
2.2	450	636	992	0.64	7.0	14.1	0.11	-	627	943	0.66	5.3	13.5	0.08	-
2.2	480	677	1019	0.66	6.7	18.2	0.10	-	677	1000	0.68	4.9	10.5	0.07	-
2.3	420	550	937	0.59	9.6	10.5	0.15	-	524	890	0.59	9.5	14.3	0.16	-
2.3	450	585	921	0.64	8.6	18.3	0.14	-	545	905	0.60	9.3	18.3	0.14	-
2.3	480	552	927	0.60	11.3	19.1	0.14	0.11	580	946	0.61	9.7	18.7	0.13	-
2.4	420	543	941	0.58	12.7	18.5	0.18	0.13	531	907	0.58	8.2	15.5	0.15	-
2.4	450	551	957	0.58	12.8	20.3	0.18	0.14	541	906	0.60	8.4	14.6	0.14	-
2.4	480	550	943	0.58	12.0	16.9	0.19	0.15	542	912	0.59	8.5	16.0	0.13	-

As can be seen in Table 14, the austempering temperature had an effect on the strength level. In general, the highest temperature provided the highest strength with the exceptions of 2.3 IA830 °C IBT480 °C, 2.4 IA830 °C IBT480 °C and 2.2 IA900 °C IBT480 °C. Ultimate tensile strength, R_m, after austempering at 480 °C averaged 966 MPa, whereas the R_m after austempering at 420 °C was 908 MPa. The effect of the annealing temperature, however, was two-fold: alloys 2.2, 2.3 and 2.4, which had

an A_{c3} temperature of over 830 °C, were less affected by the annealing temperature than 2.1, which had the lowest A_{c3} (833 °C).

The n values were lower in the specimens of alloys 2.1 – 2.4 compared to those of the REF alloy. In most cases, only the lower n value between a strain of 4% and 6% could be observed, because the uniform strain did not reach the 10%, which was the lower limit of the upper n value. The n values below 0.20 indicated lower work-hardening capacity in 2.1 – 2.4 compared to REF. The uniform and total elongations of 2.4 were, however, approximately on the same level as REF.

Elongations of the tensile specimens were further examined by determining the intersection of dσ/dε and true stress-true strain curves. Additionally, the incremental n values were plotted as a function of true strain. Figures 54 and 55 present the graphs of selected specimen after intercritical annealing at 830 °C and 900 °C, where it is visible that the lower intercritical temperature typically led to higher elongations and n values in 2.1 – 2.4. REF had both higher uniform elongation values, which were measured from the intersections of derivatives dσ/dε and true stress-true strain curves, and higher n values.

The mechanical test results indicated that 2.4 reached elongation values closest to REF but did not present an n value curve typical of TRIP-assisted steels. The curves in Figure 54b and 55b showed that the instantaneous n value of 2.4 was the highest at the beginning of the tensile test but decreased rapidly with increasing strain.

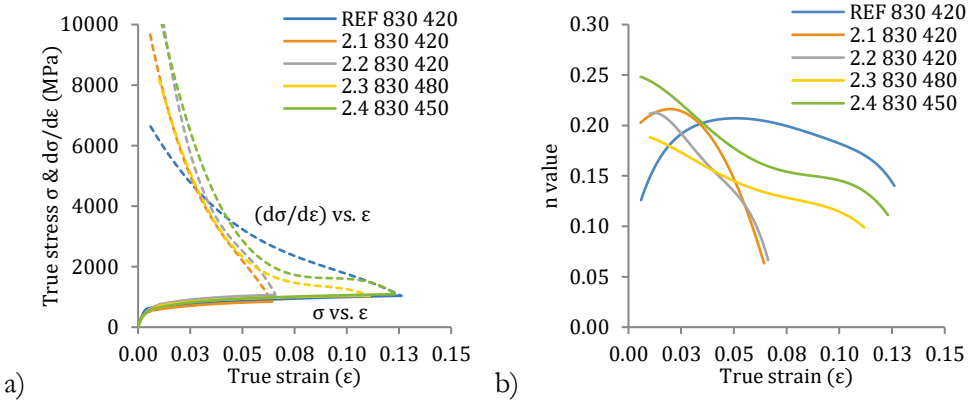

Figure 54. Examples of a) true strain-true stress and b) n values of REF and 2.1 – 2.4 after intercritical annealing at 830 °C.

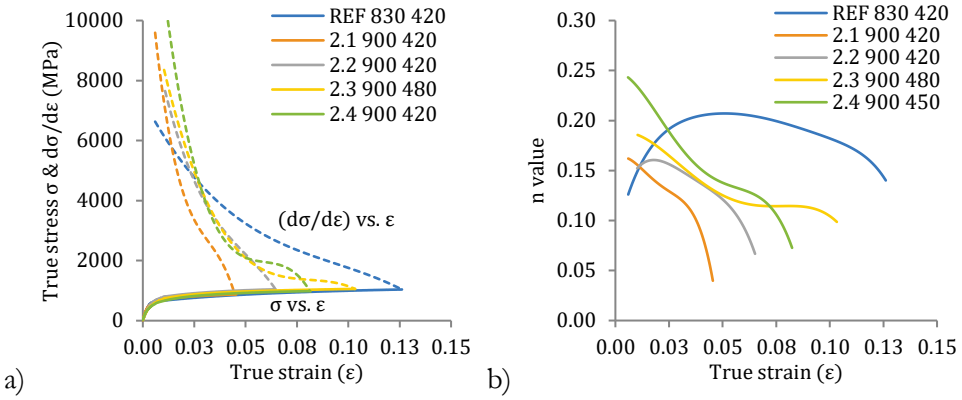

Figure 55. Examples of a) true strain-true stress and b) n values of REF after 830 °C and 2.1 – 2.4 after intercritical annealing at 900 °C.

In addition to the tensile results, true fracture strain (TFS) and thickness strain at fracture values (ε_{3f}) were also compared. The results of the specimens of the REF and 2.4 alloys were the closest in a comparison of the specimens possessing high-strength and high-ductility properties.

Figure 56 presents ε_{3f} and TFS measurements after intercritical annealing at 830 °C and Figure 57 presents the values after annealing at 900 °C. The highest ε_u and ε_{3f} or TFS combinations were found from specimens REF IA830 °C IBT420 °C and 2.4 IA830 °C IBT450 °C visible in Figure 56a and 56b.

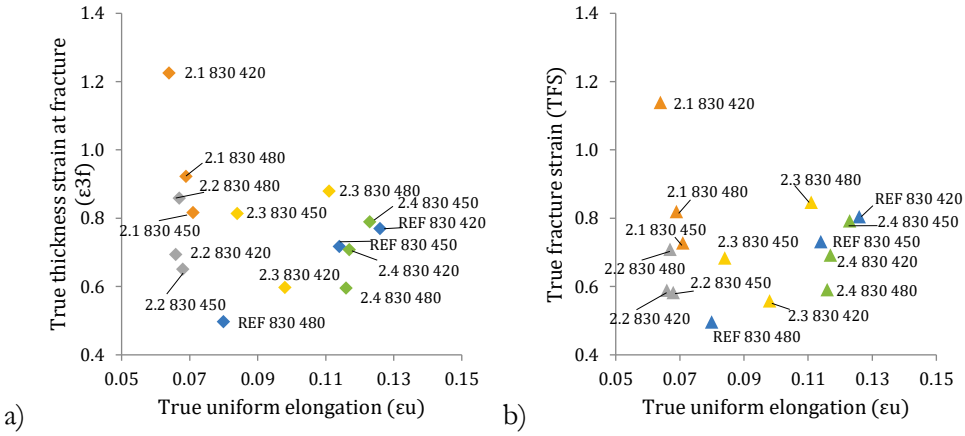

Figure 56. True thickness strain at fracture ε_{3f} (a) and TFS (b) values as a function of true uniform elongation of REF and 2.1 – 2.4 after IA 830 °C.

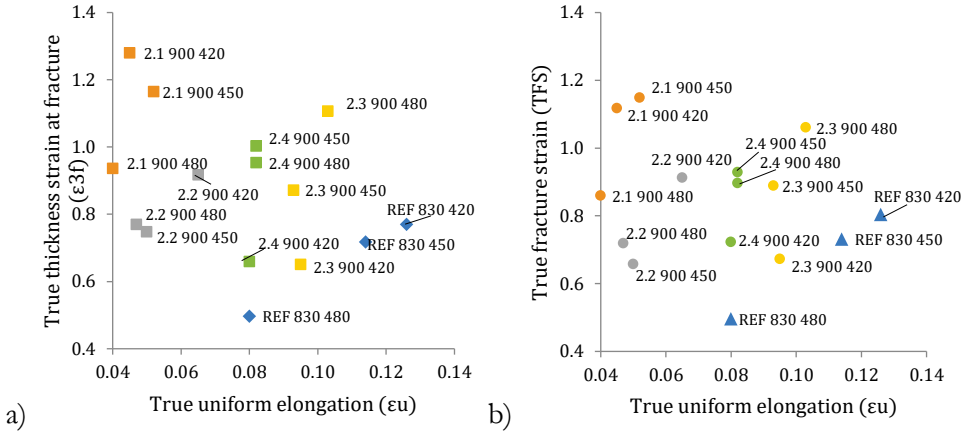

Figure 57. True thickness strain at fracture ε_{3f} (a) and TFS (b) values as a function of true uniform elongation of 2.1 - 2.4 samples after IA 900 °C and REF after IA 830 °C.

The above-mentioned results of the ε_{3f} and TFS measurements compared to other specimens in the present investigation are presented in Appendix 2.

4.2.4 Microstructural analysis

Microstructural analysis of the specimens intercritically annealed at 830 °C showed that the microstructure was either multi-phase or dual-phase. The multi-phase microstructure in 2.1, 2.2 and REF consisted of small amount of polygonal ferrite and varying amounts of granular bainite, bainitic ferrite, and MA islands (Fig. 58a, 58b, and 58e). The small amount of ferrite indicated that these alloys were almost fully or fully austenitized during annealing and new ferrite had not formed during subsequent cooling. The dual-phase microstructure in the specimens of alloys 2.3 and 2.4, on the other hand, indicated that the aluminium-alloyed 2.3 and 2.4 were only partly austenitized at this temperature. Figure 58c and 58d present a microstructure that consisted predominantly of martensite islands in a ferrite matrix. Some of the MA islands displayed the characteristics of retained austenite, but it was not detected in the XRD or EBSD measurements.

The microstructural investigations showed that the annealing temperature of 900 °C was not sufficient for full austenitization of alloys 2.3 and 2.4, which was supported by the calculations presented in Figure 53. A dual-phase microstructure was observed, because the aluminium alloying increased the A_{c3} temperature above 900 °C (Table 12). For example, the microstructure of 2.4 annealed at 900 °C and

austempered at 480 °C consists of similar martensite islands in the polygonal ferrite matrix as in the 2.4 specimen annealed at 830 °C, followed by austempering at 480 °C. In this context, the 2.2 specimens after annealing at 830 °C, which, according to dilatometry, had a austenite volume fraction of 95% during the annealing step, are also considered to be fully austenitized.

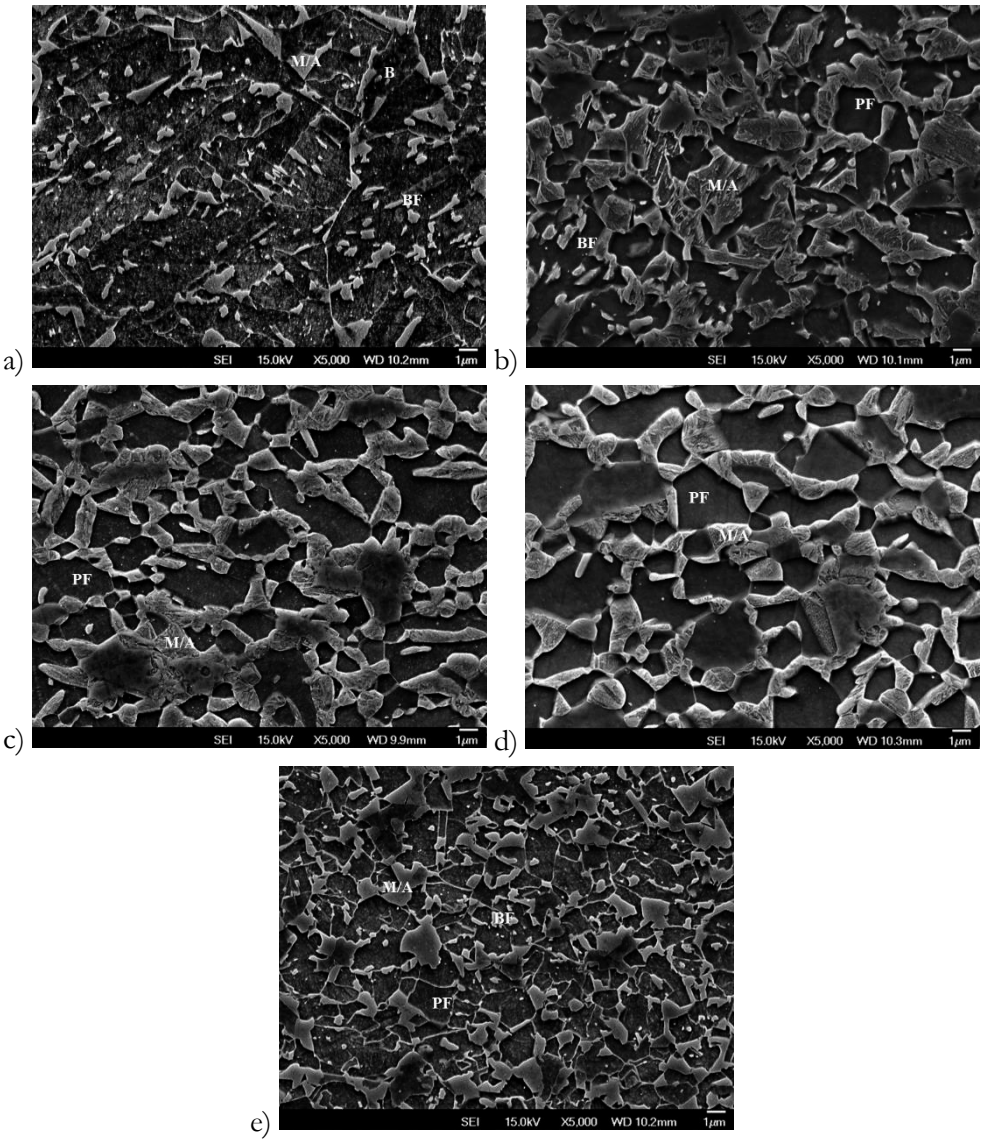

Figure 58. FESEM micrographs of a) 2.1 IA830 IBT480, b) 2.2 IA830 IBT480, c) 2.3 IA830 IBT480, d) 2.4 IA830 IBT480 and e) REF IA830 IBT480. The markings denote microstructural elements: polygonal ferrite = PF, granular bainite = B, bainitic ferrite = BF and martensite-austenite = M/A.

Silicon alloying did not increase the A_{c3} temperature as effectively as aluminium alloying did (Table 12). However, the comparison between the annealing temperatures of 830 °C and 900 °C followed by austempering at 480 °C of alloy 2.2 indicated that the amount of polygonal ferrite decreased with the higher annealing temperature and the volume fraction of bainitic ferrite increased. Austenite grain growth, which can be seen from the increase in the size of bainitic structures, also proceeded further when the annealing temperature was increased. Figure 59 presents the microstructure of specimens from alloys 2.2 and 2.4 after annealing at 900 °C and austempering at 480 °C.

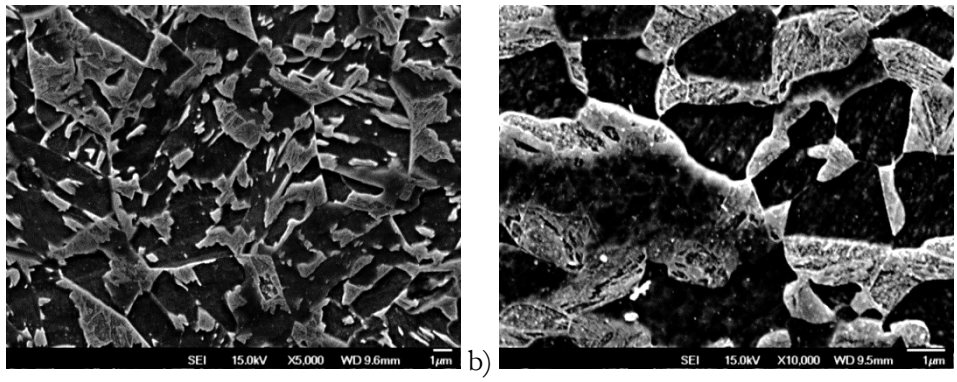

Figure 59. FESEM micrographs of a) 2.2 and b) 2.4 annealed at 900 °C and austempered at 480 °C.

The austempering temperature of 480 °C was also the nearest temperature to the calculated bainite transformation temperature in all the experimental steels. The TTT diagrams of the investigated steels are presented in Appendix 1. The list of phase contents is presented in Appendix 3.

4.2.5 EBSD analysis

EBSD analysis of the specimens of alloys 2.1 – 2.4 is presented using PQM phase maps of ferrite and austenite. Average grain sizes of the bcc and fcc phases were calculated from the phase maps and are presented overlaid on the micrographs. The areas that could not be indexed as either ferrite or austenite in the orientation maps show up as a dark colourless area in the phase map. They were composed of martensite, either as islands among the intercritical ferrite or as individual laths

among bainitic ferrite. It was also noted that the low-carbon regions inside the MA islands were usually indexed as bcc.

Figure 60 presents selected EBSD PQM phase maps of the specimens of alloys 2.1 – 2.4 after intercritical annealing at 830 °C. The yellow lines represent grain boundaries between the bcc grains. Grain boundaries between unindexed regions and austenite are uncoloured. Retained austenite was not detected or was represented as single pixels and was removed during post-processing, as it was beyond the relevant detection limit.

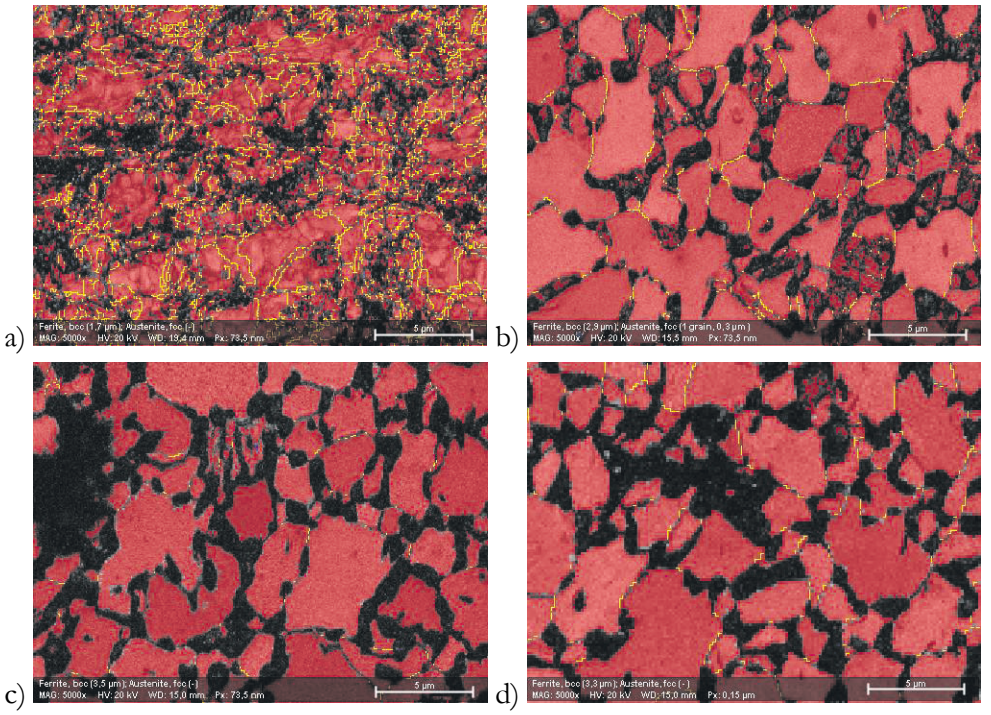

Figure 60. EBSD PQM phase maps of ferrite (bcc) and austenite (fcc): a) 2.1 IA830 IBT420, b) 2.2 IA830 IBT420, c) 2.3 IA830 IBT450 and d) 2.4 IA830 IBT450.

Figure 61 presents selected EBSD PQM phase maps of alloys 2.1 – 2.4 after intercritical annealing at 900 °C. As expected after the retained austenite measurements with XRD, specimens of 2.1 and 2.2 contained some amount of retained austenite (indicated in blue). The volume percentage detected via EBSD analysis, however, was significantly lower compared to the XRD results (Table 13) than that of 2.1 after intercritical annealing at 900 °C and austempering at 450 °C and 2.2 intercritically annealed at 900 °C and austempered at 420 °C: 0.1 vol.% and

0.4 vol.%, respectively. Even though the volume content of austenite was low, individual retained austenite grains were detected reliably.

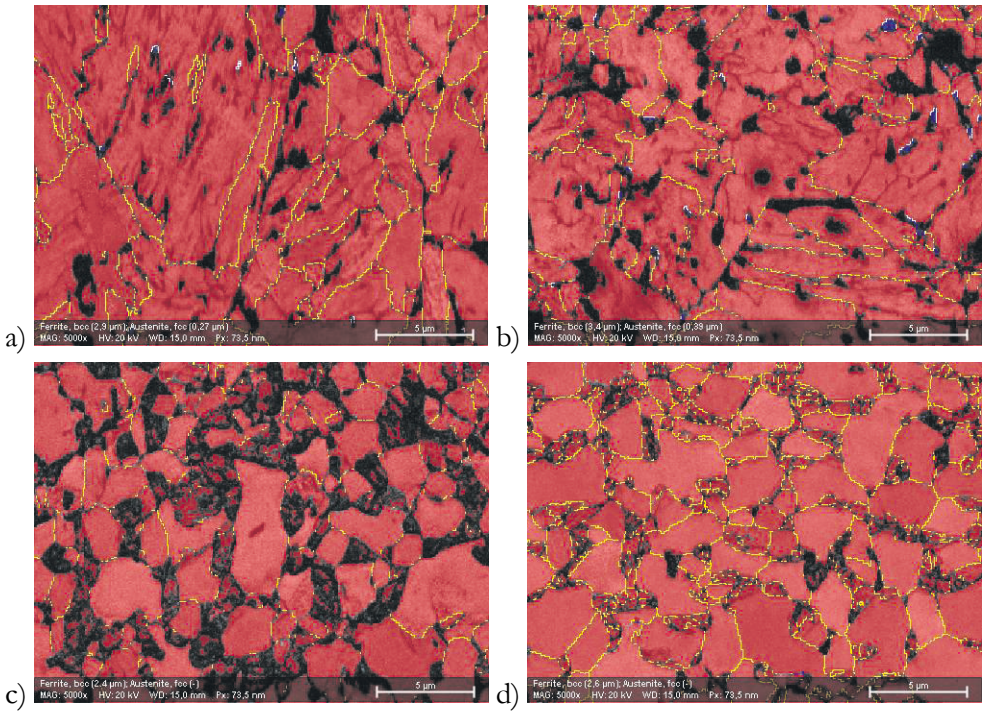

Figure 61. EBSD PQM phase maps of ferrite (bcc) and austenite (fcc): a) 2.1 IA900 IBT450, b) 2.2 IA900 IBT420, c) 2.3 IA900 IBT480 and d) 2.4 IA900 IBT450.

A comparison of the micrographs in Figure 58a and 58b with the EBSD PQM phase maps in Figure 61a and 61b) shows that the retained austenite was mainly located in bainitic ferrite in the microstructure of alloys 2.1 and 2.2. This bainitic structure was increased in size when the austenitizing temperature was increased from 830 °C to 900 °C. In the case of intercritical annealing at 900 °C, the subsequent austempering had stabilized the retained austenite.

In contrast, the microstructures of the specimens of alloys 2.3 and 2.4 mainly consisted of polygonal ferrite grains and martensite islands; retained austenite was not detected. The martensite islands were larger in size when the higher intercritical annealing temperature was used. Subsequently, this reduced the ferrite grain size.

4.2.6 Stability of retained austenite

The stability of retained austenite was investigated by performing EBSD phase mapping on the unstrained material and tensile specimen location at maximum strain. Figure 62 presents the microstructure of the 2.2 IA900 °C IBT420 °C tensile specimen at zero strain and maximum strain.

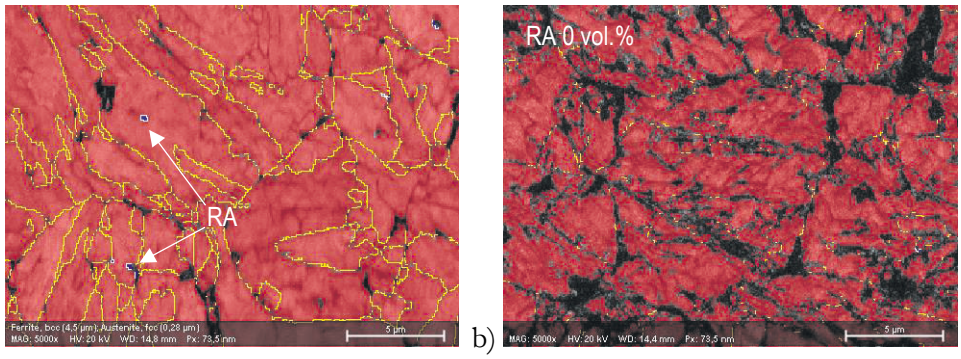

Figure 62. EBSD PQM maps representing a) phase map of tensile specimen at zero elongation and b) phase map of tensile specimen at maximum elongation.

The retained austenite content did not seem to increase the elongation of 2.2 IA900 °C IBT480 °C compared to 2.2 IA900 °C IBT420 °C or 2.2 IA900 °C IBT450 °C (Table 13). The stability of retained austenite in these sparsely located areas was low. In fact, the retained austenite content in the maximum strain specimen (Fig. 62b) was zero.

4.2.7 Precipitate analysis

Carbon replicas for STEM-EDS investigations were prepared from specimens of alloys 2.1 – 2.4 after intercritical annealing at 830 °C and austempering at 450 °C. Quantitative analysis using statistical methods was not performed, but the qualitative analysis of the precipitates indicated that they were mainly vanadium carbides (VC) in addition to complex carbonitrides containing Ti, V and Mo. The STEM bright field micrographs revealed VC inside the grains, which resembled bainitic ferrite in SEM micrographs (Figs. 58a and 58b) in 2.1 and 2.2; these are presented in Figure 63.

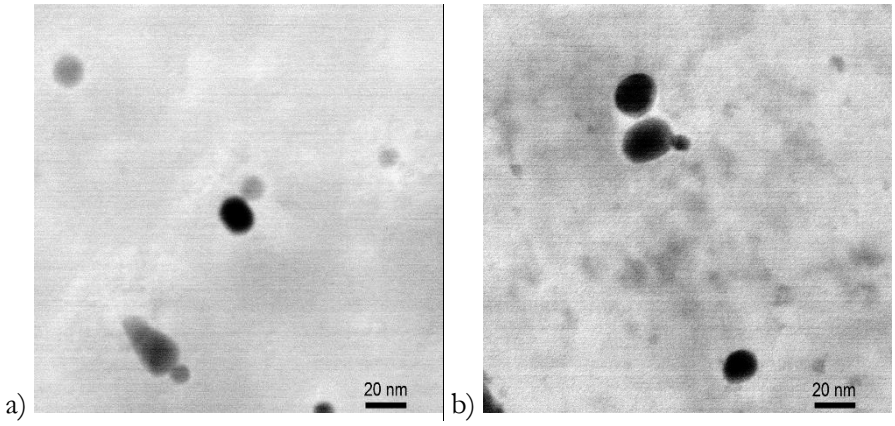

Figure 63. STEM micrographs of VC in a) 2.1 and b) 2.2.

In alloys 2.3 and 2.4, VC and Ti(C,N) precipitates were mainly observed adjacent to grains which resembled martensite grains. Large (diameter approximately 100 – 150 nm) iron carbides were also found in these areas, which are presented in STEM bright field micrographs in Figure 64.

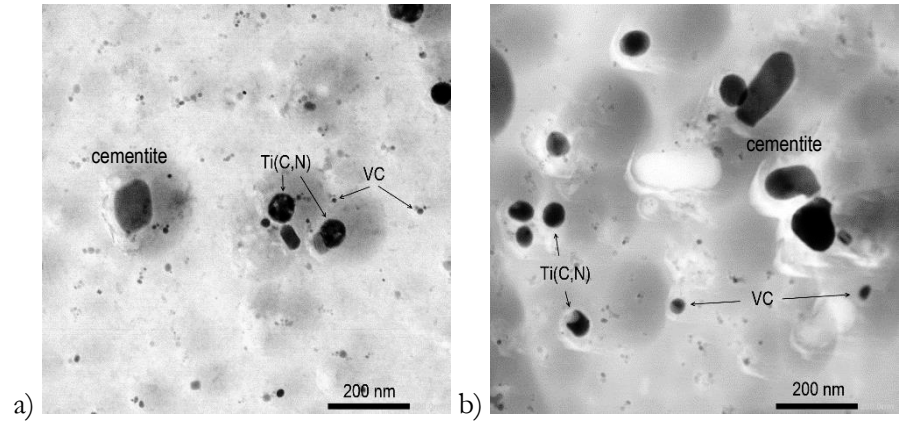

Figure 64. STEM micrographs of VC and cementite in a) 2.3 and b) 2.4.

The equilibrium phase contents at various temperatures were calculated using Thermo-Calc. The mass fractions of phases against temperature for alloys 2.1 – 2.4 are presented in Figure 65. The presence of cementite, Cr(C,N) and vanadium-containing MoC was shown under 700 °C. Other significant phases, such as VC and AlN, were stable at temperature higher than this.

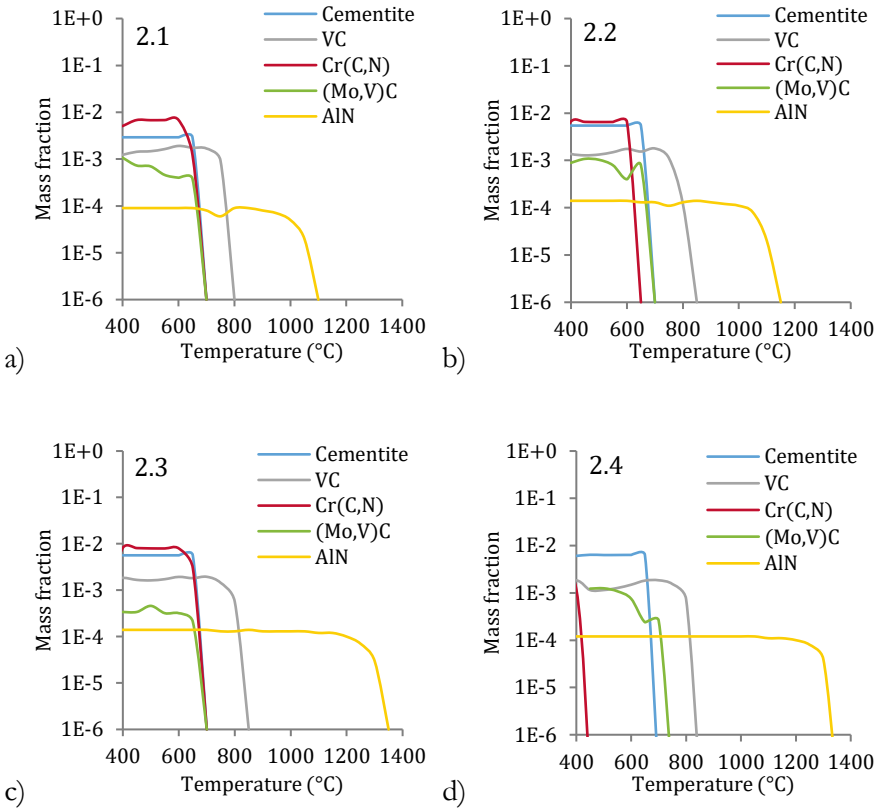

Figure 65. Thermo-Calc data showing mass fraction of equilibrium phases versus temperature of alloys a) 2.1, b) 2.2, c) 2.3 and d) 2.4.

The AlN precipitates proposed by Thermo-Calc were not observed using either SEM or STEM-EDS. Presumably, the nitrogen was in reality consumed by other nitrides and carbonitrides including TiN and Ti(C,N), which was observed in STEM-EDS analysis.

4.3 Low-carbon Q&P steel

The following section presents the experimental results of alloy 2.4 tested in Q&P processing. This instance of the alloy was designated as low-carbon Q&P steel. The cold-rolled sheet of alloy 2.4 was utilized to prepare specimens for intercritical Q&P experiments using thermal cycle C, as presented in Figure 27.

4.3.1 Dilatometry and phase transformation calculations

Figure 66 presents the dilatometer data from the quenching step after the intercritical annealing step for the investigated steel. Martensite transformation was calculated from the quenching curves (Fig. 66a) using the lever rule. The difference between the two intercritical temperatures was not significant; after both annealing temperatures the martensite transformation began at approximately 390 °C (Fig. 66b). The observation of the effect of annealing temperature was in line with the findings presented in Table 12, where it was shown that the lower annealing temperature yielded a lower M_s temperature.

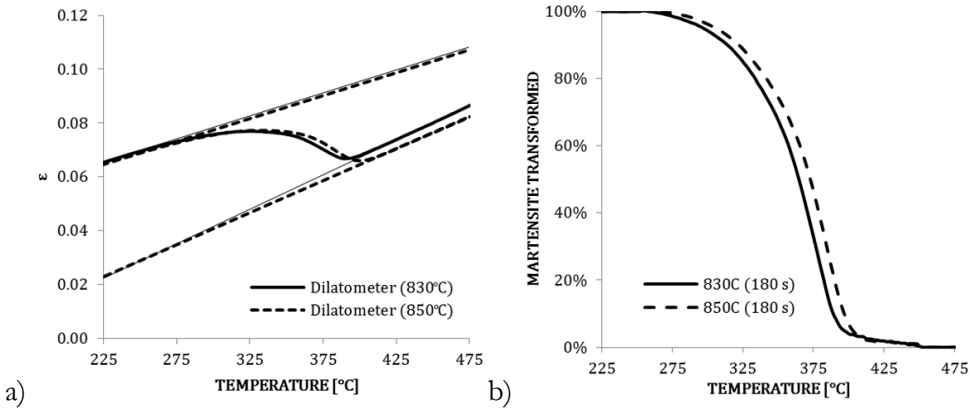

Figure 66. Transformations on the dilatometer specimen of 2.4 during cooling, where a) presents the dilatometer contraction curves during cooling from 830 °C and 850 °C, and b) presents martensite transformation calculated from the dilatometer data using the lever rule.

The dilatometer data was further processed using Minitab® software by fitting the curve into the K-M relation (Equation 2.7) from which the constant K and M_s temperature were calculated. The resulting non-linear regression curves with a 95% confidence interval for the M_s temperature are presented in Figure 67. The M_s temperatures after intercritical annealing at 830 °C and 850 °C and their corresponding austenite carbon contents in wt.% are presented in Table 15.

Table 15. M_s temperatures calculated from dilatometer data and austenite carbon content calculated using JMatPro®.

Alloy	γ carbon content [wt.%] at 830 °C	IA 830 °C M_s [°C]	γ carbon content [wt.%] at 850 °C	IA 850 °C M_s [°C]
2.4	0.22	396	0.20	400

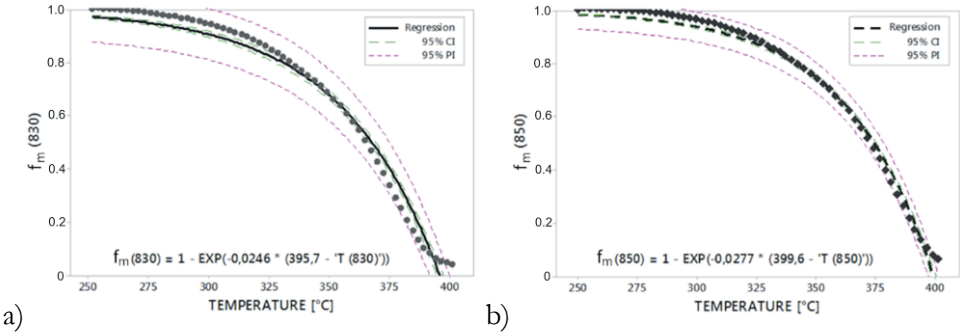

Figure 67. Fitting of dilatometer data of intercritical annealing at a) 830 °C and b) 850 °C into non-liner regression using the K-M equation.

According to the fit visible in Figure 67, martensite transformation occurs approximately between 400 °C and 250 °C. In the quenching and partitioning experiments, the quenching stop temperature (QT) temperature was varied between 200 °C and 350 °C (Table 5). The transformed martensite and untransformed austenite fraction calculated using the lever rule are presented in Table 16. The intercritical austenite vol.%, from which the martensite transformed, was calculated using JMatPro®.

Table 16. Experimentally determined martensite content and untransformed austenite contents at various quenching stop temperatures (QT).

	IA 830 °C		IA 850 °C	
QT [°C]	Martensite transformed	The untransformed fraction of austenite	Martensite transformed	The untransformed fraction of austenite
200	99%	0%	100%	0%
250	97%	0%	98%	0%
275	95%	0%	97%	0%
300	91%	4%	94%	3%
350	68%	15%	75%	12%

The interrupted quenching at a lower QT between 200 °C and 275 °C meant that basically all the intercritical austenite was transformed into martensite, because the percentage of martensite transformation was over 95%. Similarly at QT 300 °C the transformation was 91% and 94%. At QT 350 °C, however, 32% and 25% of intercritical austenite was untransformed, which means that the stabilization of the retained austenite would be possible. The actual vol.% of untransformed austenite, however, is smaller than this, because the annealing was performed in approximately the 50-50 ferrite-austenite region.

The calculated final retained austenite phase fraction against quenching temperature is presented in Figure 68, which shows the calculated ideal retained austenite content for the alloy. Reflecting the result in terms of experimentally determined martensite transformation (Table 16), the ideal amount of retained austenite, 10 vol.%, could not be achieved below 275 °C, because martensite transformation had already finished.

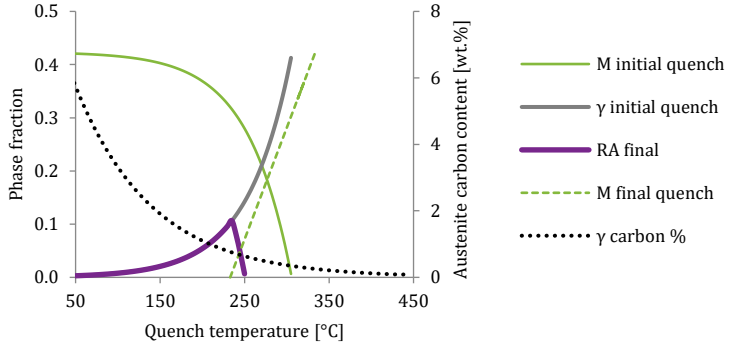

Figure 68. Ideal quenching temperature for 2.4 after intercritical annealing at 850 °C calculated using K-M relation and JMatPro®.

The data shown in Figure 68 was obtained using JMatPro® by calculating the martensite (M) final quench fraction using the austenite composition at the intercritical temperature. The austenite carbon content (γ carbon) was calculated using Equation 2.9.

4.3.2 XRD measurements

XRD investigations using a cobalt tube were performed in order to measure the volume fraction and calculate the carbon content of the retained austenite after Q&P processing. The volume fractions of the retained austenite were calculated using Equation 3.1 and the carbon contents was calculated using Equation 3.2. The XRD results of the 2.4QP specimens are presented in Table 17.

Table 17. Average volume fraction (vol.%) and carbon content (wt.%) of retained austenite in the 2.4QP specimens measured by XRD.

IA, [°C]	QT, [°C]	f_γ [vol.%]	C_γ [wt.%]
830	200	0.6	0.85
830	250	0.7	0.85
830	275	0.1	0.87
830	300	1.1	0.89
830	350	0.4	0.89
850	200	3.1 ± 0.4	0.89
850	250	3.8 ± 0.4	0.92
850	275	1.4	0.89
850	300	1.1	0.91
850	350	2.0	0.92

The retained austenite fractions were relatively low and the highest measurement of 3.8 vol.% was approximately 6 vol.% lower than the ideal fraction shown in Figure 68. Retained austenite fractions below 2.0 vol.% can be considered below the detection limit and could not be measured with any confidence.

4.3.3 Mechanical properties

The mechanical tensile tests were performed for the duplicate specimens of the 2.4QP heat treatment. Strength and elongation were found from engineering stress-strain curves, whereas n values were measured from the true stress-true strain curve. The results are presented in Table 18.

Table 18. Mechanical properties and retained austenite vol.% of 2.4QP experiments.

IA [°C]	QT [°C]	$R_{p0.2}$ [MPa]	R_m [MPa]	$R_{p0.2}/R_m$	A_g [%]	A_{25} [%]	n (4-6)	n (10-20/A_g)	RA [vol.%] XRD
830	200	913	1004	0.91	2.9	8.5	-	-	0.6
830	250	818	923	0.89	2.8	10.9	-	-	0.7
830	275	732	1010	0.72	8.0	13.7	0.13	-	0.1
830	300	706	999	0.71	7.2	16.1	0.14	-	1.1
830	350	764	1039	0.74	7.3	12.4	0.13	-	0.4
850	200	945	1028	0.92	4.7	10.8	0.04	-	3.1
850	250	893	998	0.89	4.9	10.1	0.04	-	3.8
850	275	920	1020	0.90	4.2	11.3	0.02	-	1.4
850	300	792	1013	0.78	6.1	11.4	0.08	-	1.1
850	350	780	1023	0.76	6.6	15.7	0.12	-	2.0

The lower QT of 200 °C and 250 °C led to lower elongations and a higher yield ratio than the QT of 275 °C and above. Compared to the TRIP treatment of 2.4 (Table 14), the yield strengths were higher, elongations were lower, but the overall tensile strength was at the same level. Figure 69 shows the true strains of the 2.4QP specimens as a function of true stress, where it is visible that elongations increased with the higher QT. Similarly, the peak incremental n value increased with the higher QT, which is visible in Figure 70.

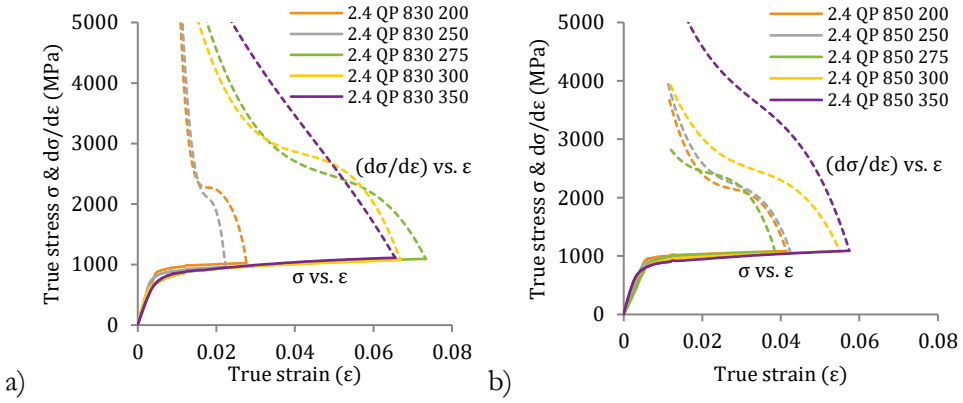

Figure 69. True strain-true stress and dσ/dε curves of 2.4QP after a) 830 °C and b) 850 °C annealing.

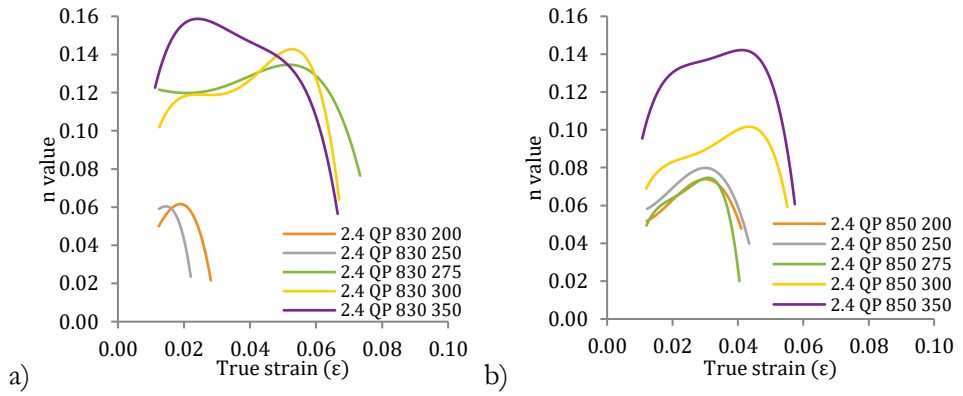

Figure 70. The n value curves of different quench stop temperatures as a function of true uniform elongation of 2.4QP after intercritical annealing at a) 830 °C and b) 850 °C.

The retained austenite fraction in the 2.4QP specimens, which were intercritically annealed at 850 °C and quenched to 200 – 250 °C, showed an increase in their n

values compared to that of IA at 830 °C. The highest overall strain hardening values, however, were achieved after intercritical annealing at 830 °C and quenching to 275 °C or above, even with a lower retained austenite fraction.

Similarly to the results of the TRIP heat treatment presented in Sections 4.1.3 and 4.2.3, the 2.4QP tensile specimens were also used to measure the local ductility values from the fracture surfaces. Two tensile specimens, which were intercritically annealed at 830 °C and quenched to 250 °C and 300 °C, broke outside the elongation gauge and were not utilized to measure the local ductility values from the fracture surfaces. The ε_{3f} and TFS values of the investigated specimen are presented in Figure 71 and the data is presented in table format in Appendix 2.

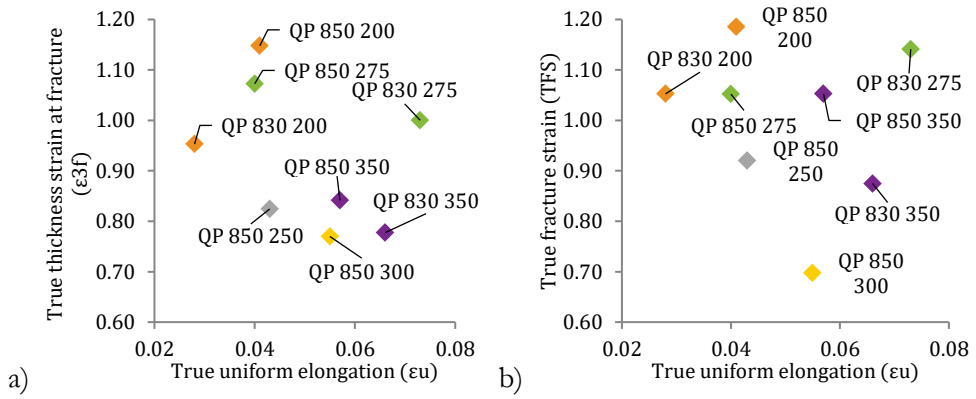

Figure 71. True thickness strain at fracture ε_{3f} (a) and TFS (b) values as a function of true uniform elongation of 2.4QP specimens.

Figure 71 shows that for both ε_{3f} and TFS, the value closest to the upper right corner came from the sample intercritically annealed at 830 °C and quenched to 275 °C. Clearly, the low quench temperatures lead to high thickness strain before fracture, but the necking onset and fracture occur at low elongation.

4.3.4 Microstructural analysis

The microstructural specimens of 2.4QP after heat treatment were subjected to EBSD analysis to determine the location of retained austenite grains. The EBSD PQM phase maps, where ferrite is coloured red and retained austenite blue, are presented in Figure 72. The retained austenite phase fractions of the respective phase maps are presented in Table 19.

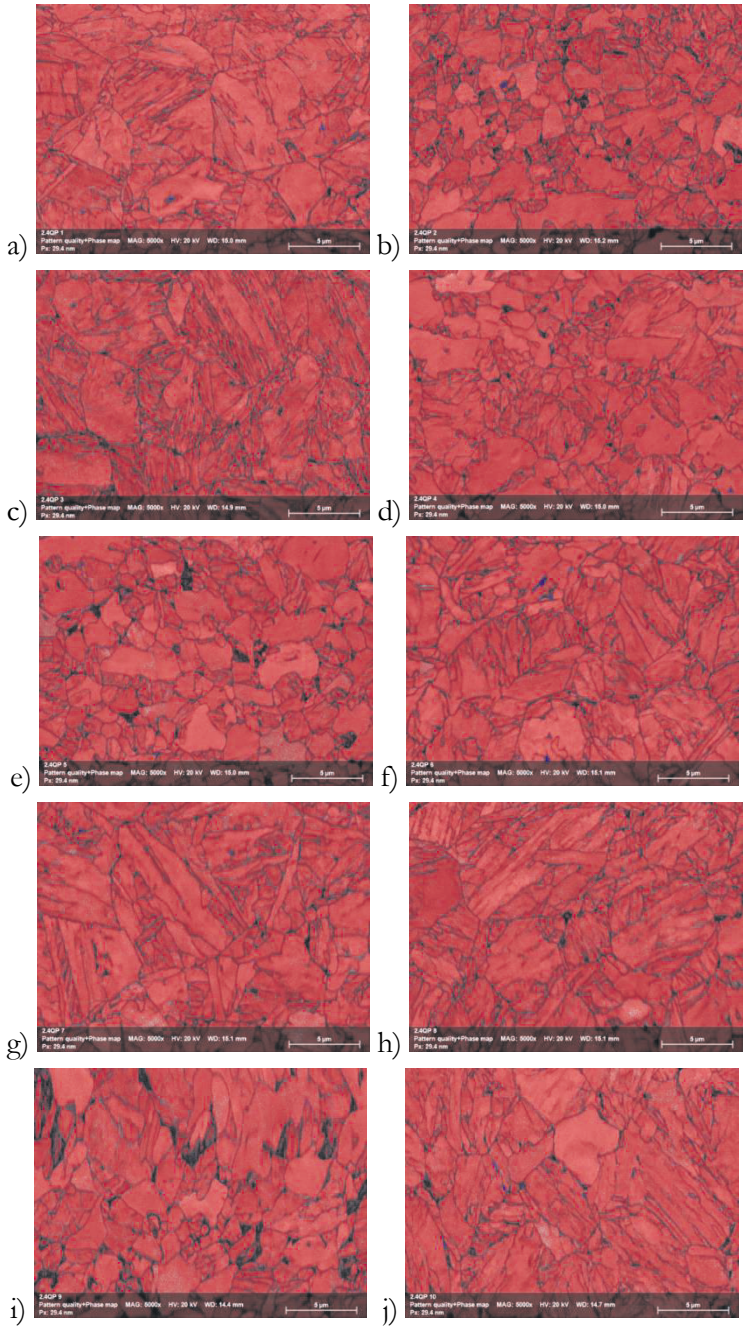

Figure 72. EBSD PQM phase maps of ferrite and retained austenite in 2.4QP specimens after (IA/QT °C) a) 830/200, b) 850/200, c) 830/250, d) 850/250, e) 830/275, f) 850/275, g) 830/300, h) 850/300, h) 830/350 and j) 850/350.

Table 19. Retained austenite fraction in 2.4QP specimens measured by EBSD.

IA, [°C]	QT, [°C]	RA [vol.%] EBSD
830	200	1.2
830	250	1.8
830	275	1.4
830	300	1.3
830	350	1.7
850	200	1.8
850	250	1.1
850	275	1.4
850	300	1.3
850	350	1.2

The EBSD analysis showed that single retained austenite blocks were detected in the ferrite grain boundaries in the IA 850 °C specimens, but also in the specimen which was intercritically annealed at 830 °C and quenched to 200 °C (Fig. 72). The retained austenite fraction (vol.%) measured either by XRD or EBSD did not present significant correlation against the Rm · A (MPa%) values of the 2.4QP specimens. The R^2 value of the linear regression was 0.02 in both cases. The Rm · A values against the retained austenite content are presented in Figure 73.

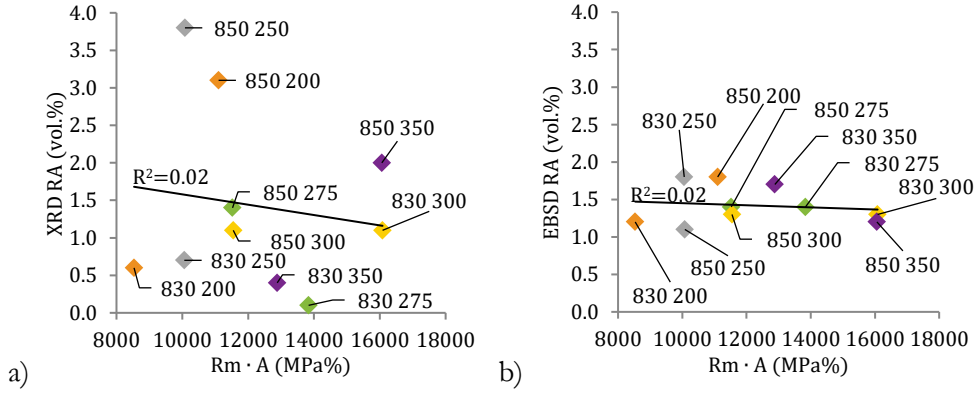

Figure 73. Linear regression analysis of ductility value Rm · A (MPa%) as a function of vol.% of retained austenite from a) XRD analysis and b) EBSD measurement.

The microstructures of the 2.4QP specimens were predominately tempered martensite with various amounts of polygonal ferrite and a minuscule amount of retained austenite. The indirect effect of the amount of ferrite and tempered martensite on the local ductility properties of the specimens was more significant

than the amount of retained austenite. Due to the fast cooling from intercritical annealing, the time in the ferrite transformation region was insufficient for the formation of pro-eutectoid ferrite (see Appendix 1 for JMatPro® calculated TTT diagrams). Thus, the ferrite was predominately inherited from the intercritical annealing. The FESEM micrographs in Figure 74 show the microstructural characteristics of the 2.4QP specimens.

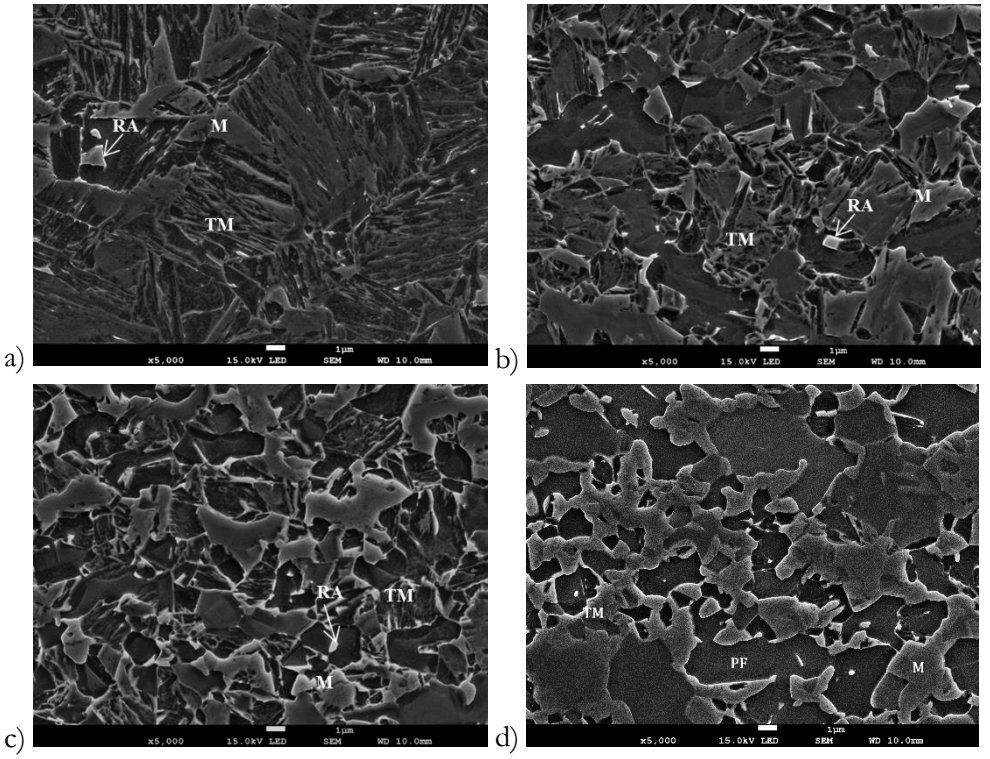

Figure 74. FESEM micrographs of 2.4QP specimens after a) IA830 QT200, b) IA830 QT275, c) IA850 QT300, and d) IA850 QT350 heat treatments. The markings denote polygonal ferrite = PF, martensite = M, tempered martensite = TM and retained austenite = RA.

Comparing the microstructures presented in Figures 74a and 74b, the amount of martensite decreased when the QT increased from 200 °C to 275 °C, leading to increased uniform elongation and slightly increased local ductility (ε_{3f}). The higher intercritical annealing temperature (Fig. 74c) led to similar characteristics in the tempered martensite, albeit with a smaller ferrite fraction. Thus, the uniform elongation and local ductility were at a lower level. The highest ferrite content was observed in Figure 74d, which showed characteristics of a DP steel microstructure, i.e. martensite islands within a ferrite matrix.

4.4 Nb-microalloyed industrially produced steel

This section presents the findings from the investigations on the industrial alloy IE1. Heat treatment experiments and line trials were performed on industrially cold-rolled sheets designated as Nb-microalloyed steel. The specimens were subjected to material characterization including tensile tests and microstructural investigations.

4.4.1 Laboratory TRIP heat treatment and Q&P processing

The properties of the industrially manufactured IE1 were studied by performing TRIP heat treatment and Q&P processing on cold-rolled, full hard sheets. Duplicate specimens of microstructural examinations and mechanical testing were studied.

As shown in Table 20, in respect of the n value and total elongation, the mechanical properties were enhanced by implementing Q&P processing. This effect was seen by comparing intercritical Q&P and TRIP treatments at 830 °C following the partitioning or austempering at 420 °C and 450 °C.

Table 20. Mechanical properties of IE1 after TRIP and Q&P annealing experiments.

IA [°C]	QT [°C]	IBT/PT [°C]	$R_{p0.2}$ [MPa]	R_m [MPa]	$R_{p0.2}/R_m$	A_g [%]	A_{25} [%]	n (4-6)	n (10-20/A_g)
830		420	754	1182	0.64	7.2	14.5	0.13	-
830		450	749	1189	0.63	8.9	14.9	0.13	-
830		480	740	1178	0.63	9.4	16.5	0.13	-
950		420	765	1078	0.71	7.1	14.2	0.13	-
950		450	744	1079	0.69	5.9	16.6	0.09	-
950		480	787	1123	0.70	5.0	14.9	0.07	-
830	275	420	670	1120	0.60	6.7	16.2	0.16	-
830	275	450	768	1040	0.74	8.7	20.5	0.16	-
830	275	480	717	1151	0.62	6.7	14.9	0.14	-
950	275	420	928	1048	0.89	3.1	11.8	-	-
950	275	450	913	1026	0.89	2.8	13.8	-	-
950	275	480	848	984	0.86	2.9	14.8	-	-

IA at 950 °C generally decreased the properties, especially in the Q&P processing. The decreasing effect was also found in TRIP heat treatments, but in that case the margin between annealing temperatures was narrower. Selected examples of the true stress-true strain curves from TRIP and Q&P specimens are presented in Figure 75. The intersection of the true stress-true strain and $d\sigma/d\varepsilon$ curves demonstrate (Fig. 75a) that the TRIP specimen intercritically annealed at 830 °C and austempered at 480 °C had a higher necking onset than the Q&P specimens. The n values curve

(Fig. 75b), on the other hand, implies that Q&P heat treatment after intercritical annealing at 830 °C had increased the work-hardening capacity.

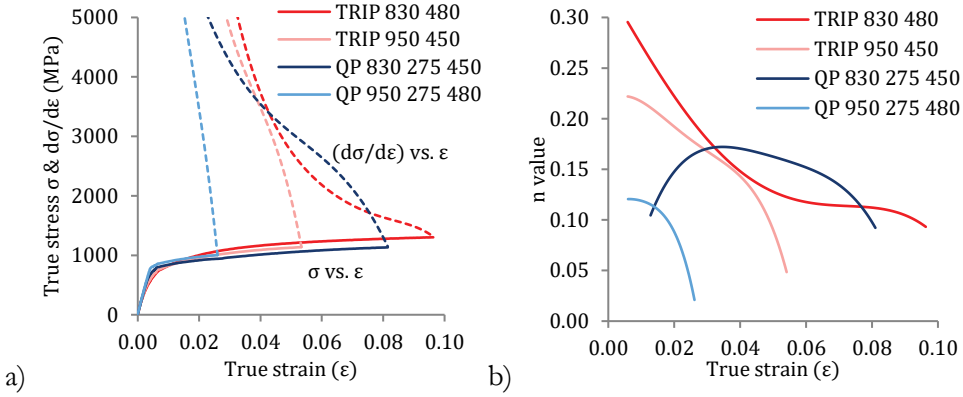

Figure 75. Examples of a) true stress-true strain and b) n value curves of IE1 after intercritical annealing and TRIP treatment or Q&P processing.

A similar effect was observed regarding the local ductility measurements. Clearly, the QP 950 °C specimen had lower elongations compared to those of the TRIP and QP 830 °C specimens. Figure 76 presents the ε_{3f} and TFS values against the true uniform elongation and shows the effect of the annealing temperature (see Appendix 2 for data in table format).

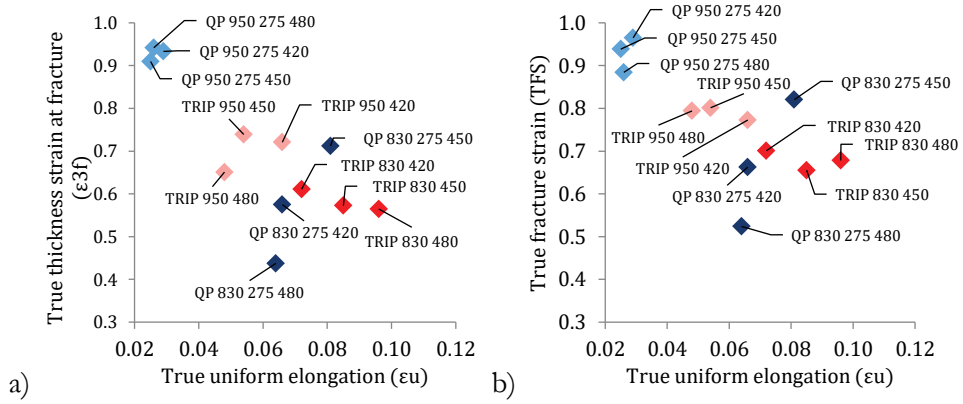

Figure 76. True thickness strain at fracture ε_{3f} (a) and TFS (b) values as a function of true uniform elongation of TRIP-treated or Q&P-processed IE1.

The microstructure of the TRIP-treated and Q&P-processed specimens of IE1 reflected their mechanical properties. The specimens with enhanced elongations were ferritic-martensitic or they consisted of tempered martensite within the ferrite matrix, the latter being the case for Q&P processed specimens. The increased martensite content seemed to have a positive effect on the elongations in the TRIP IA830 °C treatment. Overall, in both cases, there were no significant differences in the observed microstructures. The SEM micrographs of IA 830 °C TRIP and QP specimens are presented in Figure 77.

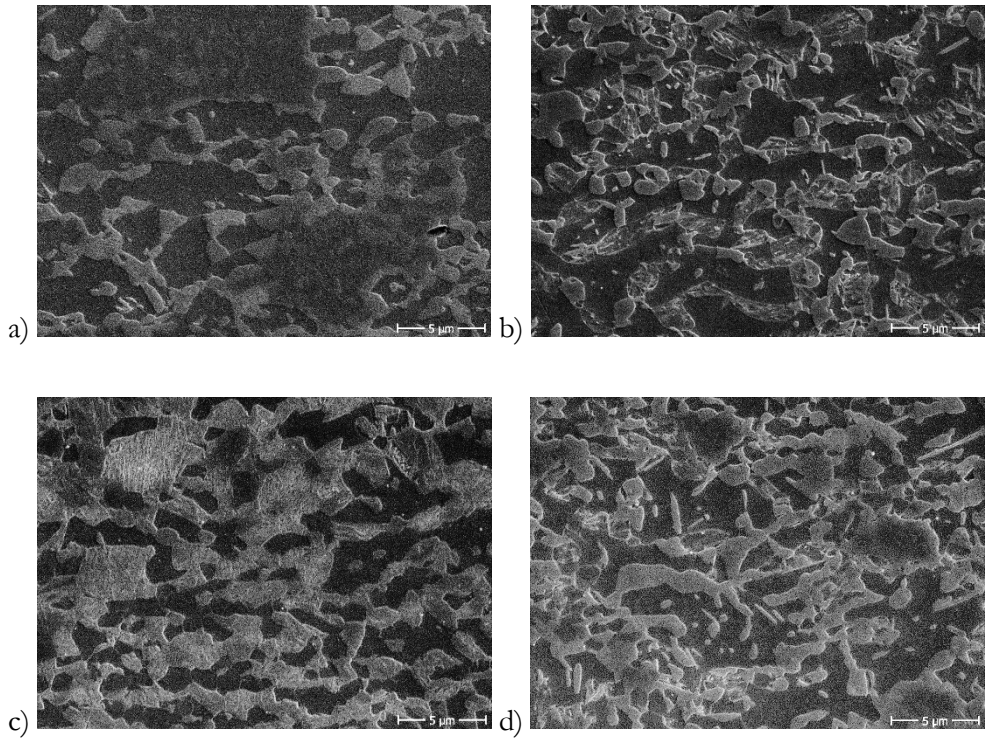

Figure 77. SEM micrographs of IA830 TRIP and Q&P samples of a) TRIP IA830 IBT420, b) QP IA830 QT275 PT420, c) TRIP IA830 IBT480 and d) QP IA830 QT275 PT480.

As expected, observations of TRIP and Q&P specimens annealed at 950 °C indicated that they were fully austenitic during annealing, which was confirmed from the microstructure of the dilatometry specimen. The observed microstructures did not contain any intercritical ferrite; rather the ferrite observed was bainitic ferrite. Other types of bainite were also observed. For example, the TRIP specimen intercritically annealed at 950 °C and austempered at 480 °C contained upper bainite. The Q&P specimens annealed at 950 °C, on the other hand, were fully or almost

fully martensitic, containing both tempered martensite formed during QT or fresh martensite transformed during the final cooling step. The SEM micrographs of IA 950 °C TRIP and QP specimens are presented in Figure 78.

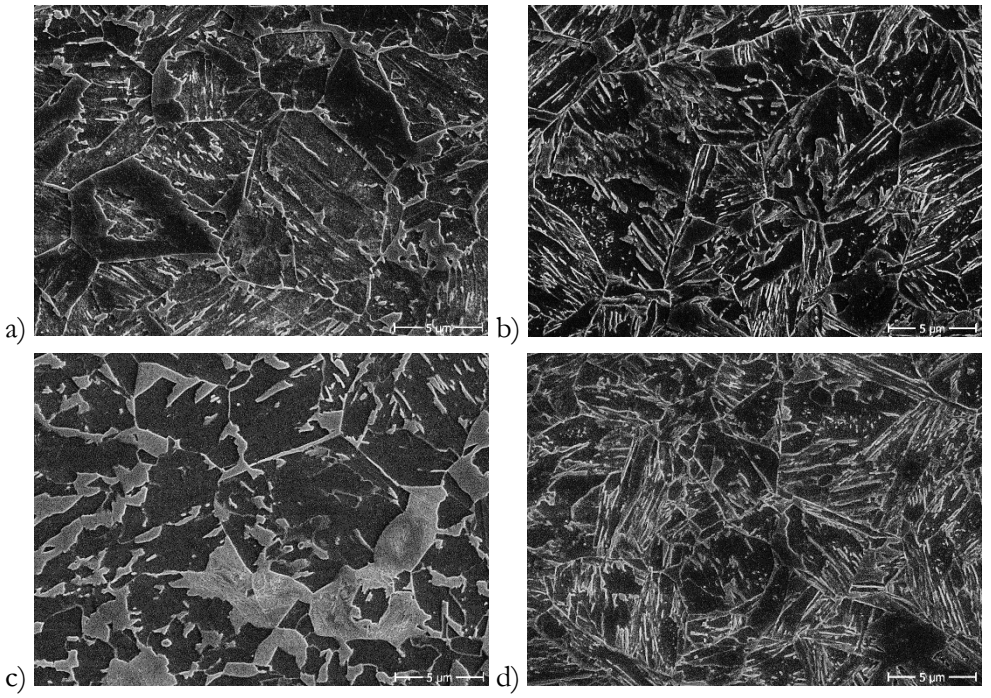

Figure 78. SEM micrographs of IA950 TRIP and Q&P samples of a) TRIP IA950 IBT420, b) QP IA950 QT275 PT420, c) TRIP IA950 IBT480 and d) QP IA950 QT275 PT480.

The microstructural observations of the Q&P specimens intercritically annealed at 950 °C offered explanations for the elongation of the tensile samples. It is plausible that the increased martensite amount in the microstructure had resulted in decreased elongation and local ductility capacity compared to the specimens intercritically annealed at 830 °C.

Retained austenite investigations by EBSD analysis were carried out for samples from both experimental series. The selected EBSD PQM phase maps of ferrite and austenite are presented in Figure 79.

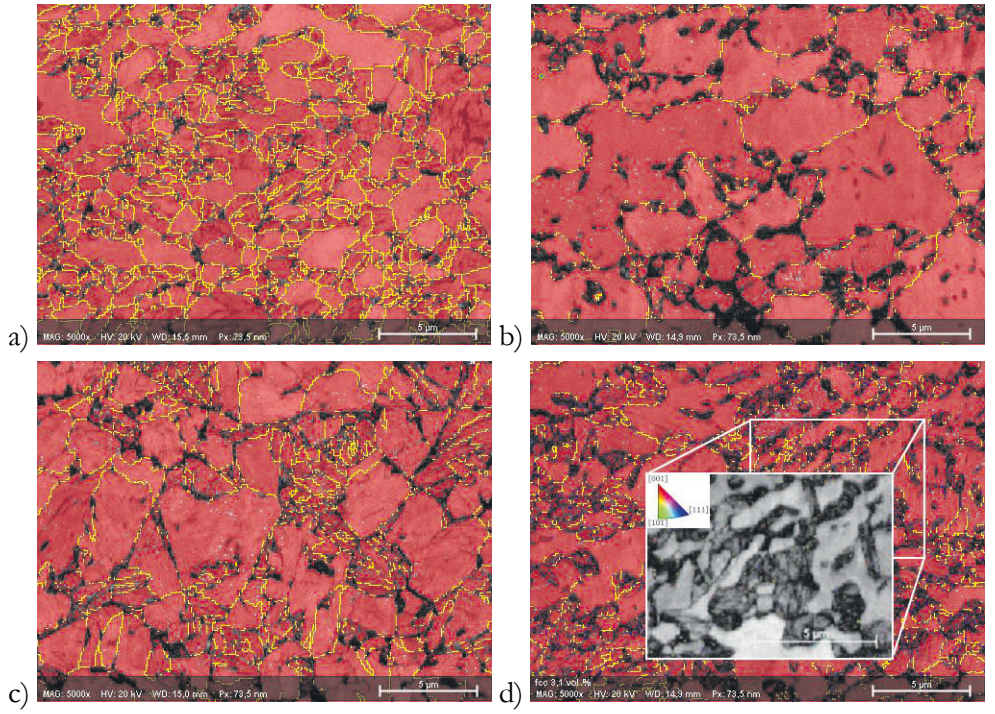

Figure 79. EBSD PQM phase maps of selected IE1 specimens after TRIP treatment and Q&P processing: a) TRIP IA830 IBT480, b) Q&P IA830 PT450, c) TRIP IA950 IBT450 and d) Q&P IA830 PT480.

Small amounts of retained austenite were observed in the Q&P specimen which was intercritically annealed at 830 °C and partitioned at 480 °C (Fig. 79d). It was probable that retained austenite laths resided adjacent martensite laths (approximately 3 vol.% according to EBSD phase mapping). Otherwise, the investigated specimens did not contain any retained austenite that would have been reliably detected using the present methods.

4.4.2 Hot-dip galvanizing line trials

IE1 was continuously annealed and hot-dip galvanized in the CGL production line (Fig. 35) using an average process speed of 75 m/min. The furnace atmosphere (dew point) in the annealing section was approximately -25 °C. The annealing and austempering temperatures, IA at 830 °C and IBT 470 °C, were well within the target as was the zinc coating of 100 g/m².

The mechanical properties of the industrially galvanized material were measured from a similar sample size (120 mm · 20 mm) as in the laboratory experiments. The mechanical properties are presented in Table 21. The average tensile strength (Rm, 1161 MPa) of the three samples was close to the target of 1180 MPa. The results of the line trials were in agreement with the laboratory TRIP 830 °C results, which were shown earlier in Table 20.

Table 21. Mechanical properties of industrially produced hot-dip galvanized IE1.

Sample no.	IA [°C]	IBT [°C]	$R_{p0.2}$ [MPa]	R_m [MPa]	$R_{p0.2}/R_m$	A_g [%]	A_{25} [%]	n (4-6)	n (10-20/A_g)
1	830	470	726	1152	0.63	7.4	15.1	0.11	-
2	830	470	738	1173	0.63	7.5	13.3	0.11	-
3	830	470	724	1160	0.62	7.4	13.1	0.11	-

The true stress-true strain curves and incremental n values of the three specimens from the line trial are presented in Figure 80. The first test specimen yielded a slightly (approximately 2%) higher total elongation compared to the other two. Otherwise, the deviation between samples was negligible. For instance, the uniform elongation and n values were in good agreement with each other.

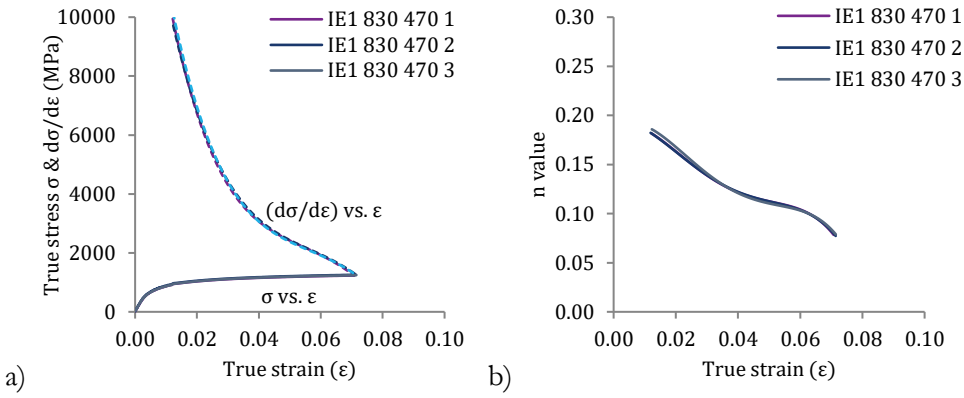

Figure 80. True stress-true strain with dσ/dε derivative curves (a) and b) incremental n values of hot-dip galvanized IE1 as a function of true strain.

Figure 81 presents the local ductility measurements of the IE1 specimens. The deviation between samples was negligible. The results of ε_{3f} were between the CH1000 (complex-phase high-formability steel) and DH1000 (dual-phase high-formability steel) results previously reported by Heibel et al. [15], which shows similar properties to typical CP800.

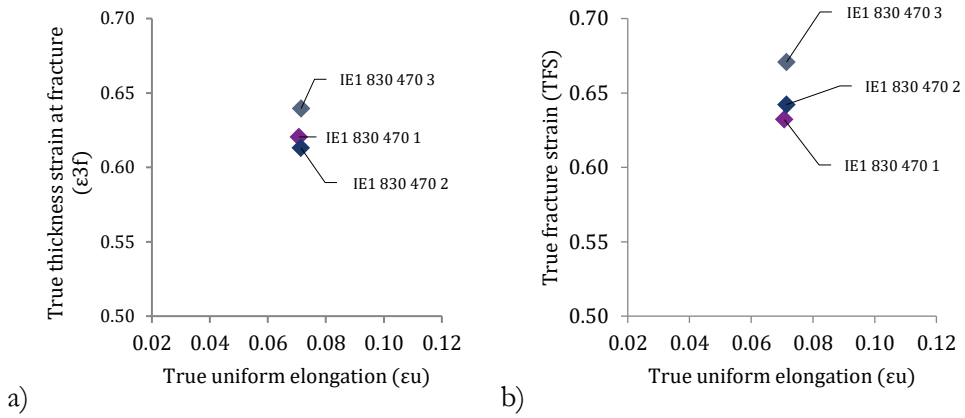

Figure 81. True thickness strain at fracture ε_{3f} (a) and TFS (b) values as a function of true uniform elongation of hot-dip galvanized IE1.

The microstructure of industrially produced IE1 was predominately ferritic-martensitic (Fig. 82a). This was similar to that of the specimen of alloy 2.4 (Fig. 58d), which was intercritically annealed at 830 °C and austempered at 480 °C.

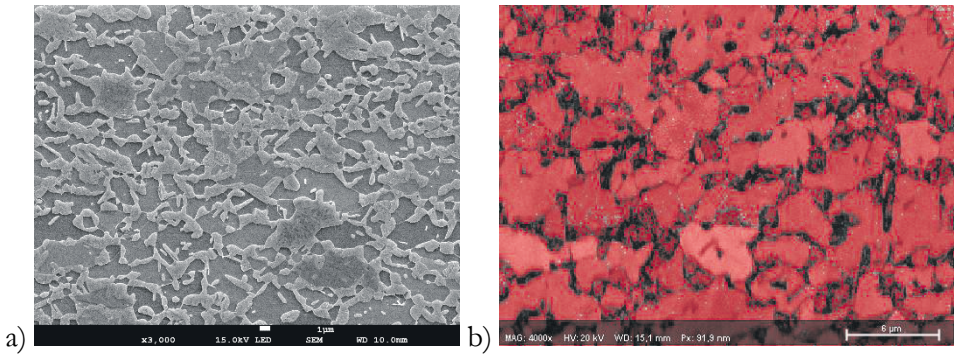

Figure 82. Microstructure of IE1 by a) scanning electron micrograph and b) EBSD phase map.

The retained austenite fraction in the specimen of IE1 was measured using similar XRD practices to other samples (see Section 3.4.2). The average retained austenite volume fraction was below 2 vol.%, which means that the content was below detection. The result was comparable to the EBSD measurement presented in Figure 82b, where ferrite is presented red and austenite (blue), which was not detected.

The intermetallic bond between the steel substrate and the hot-dip galvanized zinc coating was studied by preparing a cross-section specimen using ion-milling. Investigations included the EDS elemental mapping of the region in order to study

the inhibition layer at the interface. Figure 83 presents the coating cross-section and an elemental map of the steel substrate (top) and the zinc coating (below).

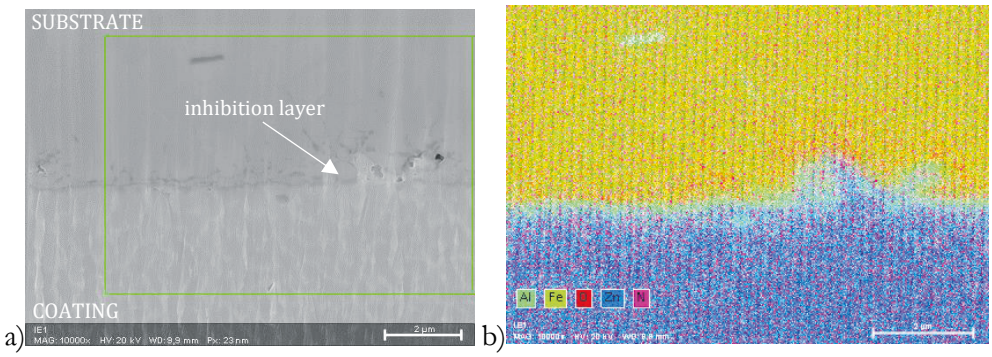

Figure 83. Surface cross-section of the intermetallic bond between steel substrate and zinc coating in the bottom surface of IE1 specimen presented by a) SEM micrograph and b) EDS elemental map of selected elements.

Elemental maps of the selected elements Fe, Zn, Mn, Al, O and N, are presented in Figure 84. The elemental maps of Al and O in Figure 84 show the inhibition layer between the substrate and coating. Thickness of the inhibition layer was below 1 µm.

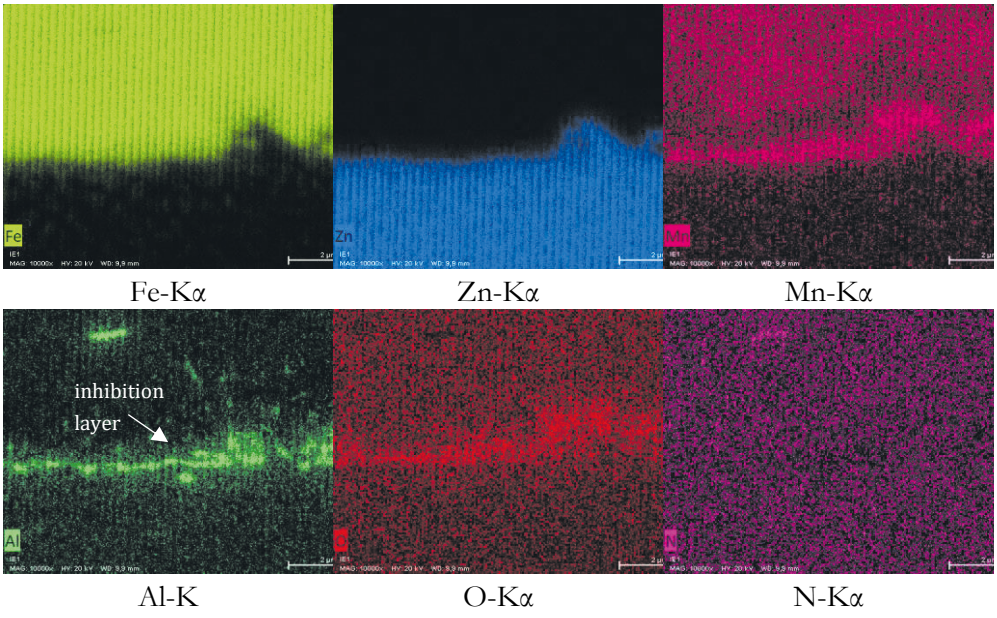

Figure 84. EDS elemental maps of Fe, Zn, Al, O, N and Mn in the inhibition layer.

5 DISCUSSION

This chapter discusses the results in terms of the tested hypothesis of the varying rate of bainitic reaction at different isothermal temperatures during TRIP heat treatment, which thus affects the stabilization of retained austenite, its volume fraction and subsequently its morphology. In addition, it was hypothesized that the morphology and the varying content of phases other than retained austenite also affect the properties of the investigated steels, which was tested by varying the alloying and heat treatment. Thus, the discussion is divided into sub-sections concentrating on the effects of the alloying elements, the effect of TRIP heat treatment and Q&P processing on the morphology and mechanical properties, the quenching & partitioning response and the stability of the retained austenite.

As expected based on the literature presented in Chapter 2, the stabilization of retained austenite in room-temperature microstructures was achieved by implementing Si and Al alloying. The alloying prevented cementite precipitation when austempering or partitioning treatments were in use. In some cases, however, microalloying with Nb and V interfered with the stabilization of retained austenite by forming alloy carbides. It was clear that the main alloying as well as microalloying elements affected the morphology and the properties of the investigated alloys.

5.1 Role of alloying

5.1.1 Main alloying elements

Carbon had the most pronounced effect on the mechanical properties and morphology of the experimental specimens. It is well known that carbon, as an interstitial element, has a significant effect on the strengthening of steels [61]. Although the tensile strengths were between 900 and 1100 MPa, the difference in carbon content had a powerful effect on the phase morphology and mechanical properties of the specimens. The comparison between low (0.08 – 0.10 wt.%) and typical (0.15 – 0.20 wt.%) carbon content demonstrated the effect of carbon on the

elongation and local ductility of different microstructure types. In the present work, the "typical carbon" content meant the conventional carbon upper limit of 0.20 wt.% due to welding requirements (REF and 1.1 – 1.4), whereas "low" indicates the carbon content in alloys 2.1 – 2.4 and IE1. Compared to "low-carbon", "typical carbon" resulted in enhanced uniform elongation, as shown in Figure 85, where the true fracture strain is presented as a function of true uniform elongation.

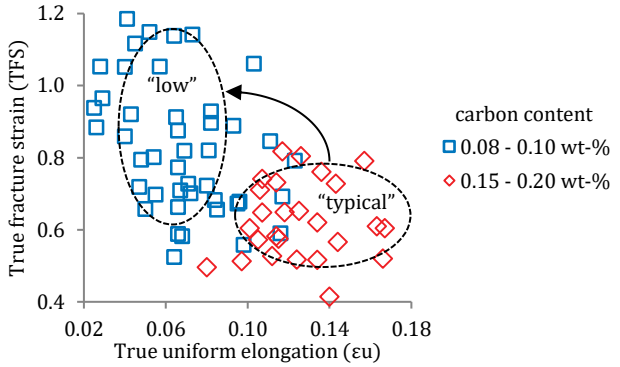

Figure 85. Effect of carbon on mechanical properties.

"Typical carbon" resulted in high uniform elongation values and relatively low TFS, which was most probably related to the fractions of martensite and retained austenite. Retained austenite stabilization relies on the partitioning of carbon into retained austenite, because without a sufficiently high carbon level, the remaining austenite transforms to martensite in final cooling [80]. The stabilization of retained austenite was intermixed with other factors, such as the annealing temperature and alloying elements, but the clear trend was that the higher carbon level enhanced the austenite retention capacity, which is in line with earlier findings [72]. The effect of carbon was seen by comparing the retained austenite measurements of the specimens of alloys 1.1 – 1.4 and 2.1 – 2.4 (Tables 9 and 13). The highest retained austenite content, 5 – 14 vol.%, was found in the specimens of alloy 1.4, which was the Ti-microalloyed composition without Nb or V.

Manganese acted as a strengthener in alloys 2.1 – 2.4, in which lower carbon alloying was utilized, but no increase in the fraction of retained austenite was detected after TRIP heat treatment. In the present study, Mn controlled the carbon content in the austenite and the M_s temperatures. The latter was shown in dilatometry where lowering the carbon level, compared to alloy 1.4 for example, increased the M_s temperature of specimens of alloys 2.1 – 2.4. This effect was,

however, counteracted by manganese which decreased the M_s temperature. The M_s temperatures of alloys 2.1 – 2.4 were 30 – 40 °C higher compared (Table 12) to alloys 1.2, 1.3 and 1.4 (Table 8). This was in line with the results by Sugimoto et al. [59], who suggested this phenomenon was related to the ability of manganese to lower both the A_{c3} as well as the T_0. In addition, Takahaski and Bhadeshia [121] have proposed that carbon concentration in retained austenite decreases with increased Mn content. These effects were seen as a reason for the lower retained austenite content in TRIP heat-treated alloys 2.1 – 2.4 compared to alloys 1.1 – 1.4.

It is known that both silicon and aluminium are ferrite stabilizers, since they partition into ferrite, thus increasing the A_{c3} temperature during intercritical annealing [111], [122] by delaying nucleation and the growth of austenite [123]. As shown in Tables 8 and 12, there was a strong increase in A_{c3} when varying amounts of Si and Al were used in alloys 2.1 – 2.4. The ferrite stabilization is also visible in the time-temperature transformation (TTT) diagram where the ferrite region moves to the shorter transformation times. This can be seen in Figure 86, where a part of the TTT diagrams of alloys 2.1 (Al 0.15 wt.%) and 2.4 (Si 0.7 wt.% and Al 1.1 wt.%) are presented.

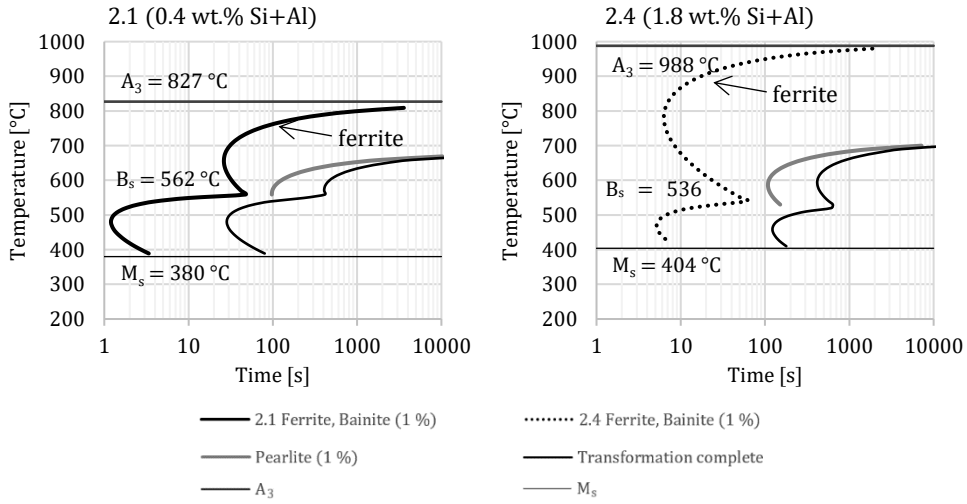

Figure 86. Effect of silicon and aluminium on the times and temperatures of phase transformations after full austenitization.

Silicon and aluminium enhanced the uniform elongation of alloys 1.1 – 1.4 compared to those of REF (Figs. 39 and 40). In alloys 1.1 and 1.4 Si and Al suppressed the precipitation of cementite which led to the stabilization of retained austenite and

enhanced uniform elongation. The findings regarding alloy 1.1 were in line with those of Wang et al. [20], who have proposed Nb microalloying in Si- and Al-containing TRIP steels. The present investigation complemented those results by implementing a similar concept without microalloying. The new information, shown in Table 9, is that, without Nb, the retained austenite contents was increased. This was not considered to be the effect of Si or Al nor heat treatment, but the effect of the microalloying elements which are discussed in Section 5.1.2

Retained austenite was not observed in the Si- and Al-alloyed, TRIP heat-treated alloys 2.2 and 2.4, because the austempering did not efficiently stabilize the retained austenite. Compared to alloy 1.4, for example, the lower carbon content of the austenite in alloy 2.4 was not enriched enough to hinder the transformation of martensite during final cooling. These effects were seen in the microstructure of the TRIP-treated specimen (Fig. 58d) and in the XRD measurements in which retained austenite was not detected (Table 13). The increased ferrite content due to Al-alloying in 2.4 together with the small grain size yielded high n values and elongations. The effect of Si and Al is presented in Figure 87, where alloying with these elements is seen to increase the uniform elongation.

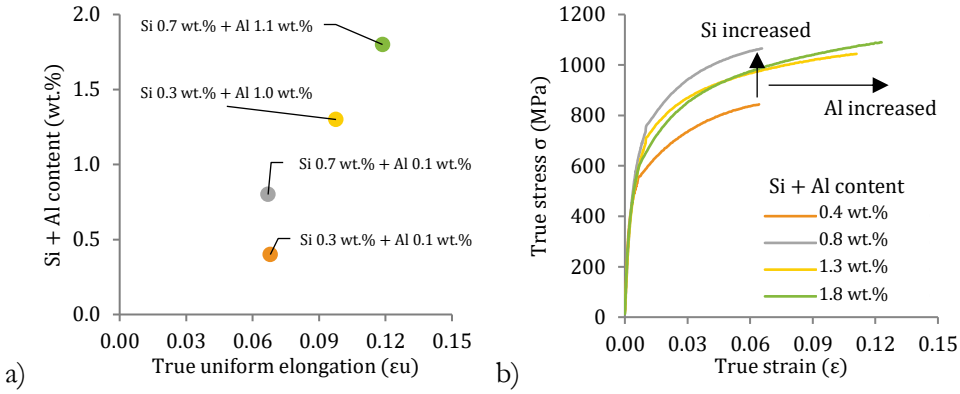

Figure 87. Effect of silicon and aluminium on mechanical properties presented by a) n value and b) true stress as a function of true strain.

Compared to the stress-strain curves reported by Girault et al. [21] (Fig. 24a), the present results showed similar effects where Si alloying increased the highest measured true stress Fig. 87b). Also visible in Figure 87b, the Al alloying led to similar true stress, but the uniform elongation was pronounced.

Interestingly, the uniform elongation increasing effect was found in the specimens of alloys 2.3 and 2.4, which did not contain any significant amount of

retained austenite after TRIP heat treatment. Whereas Girault et al. [21] attributed the increase to the TRIP effect of retained austenite, the present results showed that it was not required for increased uniform elongations.

The difference between the retained austenite contents of alloys 2.3 and 2.4 and those of Girault et al. [21] is probably due to the difference in the carbon content of the alloy, which was 0.08 wt.% in the present study and 0.12 wt.% in the comparison study. In addition to the lower carbon, the alloys used in the present study had a higher Mn content, which lowers the T_o temperature implying that during austempering the carbon content of retained austenite decreases making it more unstable [59].

5.1.2 Microalloying elements

The grain size decreasing effects of microalloying elements are well known [22], [24]-[27]. Microalloying additions of Nb and V both had a noticeable effect on the microstructure and strength of the investigated specimens. The Nb-containing alloy 1.1 had a higher uniform elongation and n value compared to those of REF and V-containing alloys 1.2 and 1.3. The XRD results of these alloys showed the effect of microalloying elements on the fraction of retained austenite after TRIP heat treatment.

The above-mentioned results suggest that Nb predominately inhibits grain growth, leading to smaller grain sizes compared to those in which V and Ti microalloying was utilized. A minor effect due to precipitation hardening by V was also identified.

The composition of the precipitates in the specimens of alloys 1.1 – 1.4 and 2.1 – 2.4 was determined from carbon extraction replicas using STEM-EDS. Specimens from alloys 1.1 – 1.3 showed fine precipitates that were mainly complex carbides and carbonitrides Ti(Nb)N, Nb(Ti,V,Mo)C and V(Ti,Nb,Mo)C. Due to differences in the dissolving temperatures, Nb- and V-containing carbides and carbonitrides are formed at different stages of heat treatment. It is probable that Nb-containing precipitates of alloy 1.1 were mostly inherited from the reheating step of the hot rolling stage, because of their higher dissolving temperature (Fig. 52). V-containing precipitates in alloys 1.2 and 1.3, on the other hand, were in solution during reheating and before hot rolling due to their lower dissolving temperature, thus V was available for the precipitation strengthening of ferrite during intercritical annealing.

The STEM-EDS findings supported the above-mentioned conclusion, since relatively large V carbonitrides and Nb containing carbides were detected in both alloys 1.2 and 1.3, which also contained 50 – 100 nm Ti and Nb carbides (Section 4.1.6). However, both of them also contained a smaller amount of vanadium carbides (VC) with an approximate size of 30 nm, similar to findings by Perrard et al. [29]. They have proposed that the smaller VC were nucleated during the heating step of intercritical annealing, while the coarse VC were inherited from the hot strip. In the present study, relatively large precipitates were frequently seen, which suggests coarsening of the precipitates during annealing [20], [29].

The Ti-microalloyed 1.4 specimen also contained fine carbides and carbonitrides. Similarly to alloys 1.1 – 1.3, Ti(Nb,Mo)C complex carbides were detected, but Nb containing precipitates were also seen (Fig. 50b). Alloy 1.4 was deliberately not microalloyed with Nb or V, so this indicates the strong precipitation tendency of Nb, which was a trace element in this case, and its coring effect [117]. As a result, the typical precipitates had a TiN core and NbC case. This suggests that the nitride had acted as a nucleation site for the carbide case.

The qualitative precipitation analysis of specimens of 2.1 – 2.4 showed that the precipitates were mainly VC in addition to complex carbonitrides containing Ti, V and Mo. These were found both inside the ferrite and bainitic ferrite as well as on the martensite block boundaries or primary austenite grain boundaries, which suggests they were formed at different stages of the heat treatment. However, due to the slow kinetics of V(C,N) formation in austenite [117], most of the vanadium-containing precipitates were found in ferrite. Also, the alloying content of nitrogen was not adjusted to complement the driving force for V(C,N) formation. Zajac et al. [148] have proposed that the increase in nitrogen content, up to the stoichiometric ratio of V:N (3.65:1), increases the volume fraction of strengthening precipitates.

In addition to V(C,N), the specimens of 2.3 and 2.4 also contained Ti(C,N), which were mainly observed adjacent to areas which consisted of martensite laths and prior austenite grain boundaries. This assumption was made by comparing the respective SEM and TEM micrographs. The observation of precipitates on the grain boundaries demonstrates the grain boundary pinning effect, which led to the smaller grain size and higher elongation found in 2.3 and 2.4 specimens compared to those of 2.1 and 2.2. However, large (approximately 100 – 150 nm in diameter) iron carbides, presumably cementite, were also found in these areas which explains the reduced retained austenite content. The number density of precipitates, however, was not quantified nor any statistical analysis performed, so further STEM-EDS studies using additional replicas would be helpful.

The specimens containing vanadium had the lowest retained austenite fractions, which raised the question of whether the carbides, especially VC, had consumed carbon, lowering the free carbon in solution before the stabilization of the retained austenite was possible. The carbon (in solution) during the intercritical annealing of alloys 1.2 and 1.4 was simulated using Thermo-Calc. Figure 88 presents the mass fraction of carbon in phases of alloy 1.4, which did not contain Nb or V, compared to 1.2, which was alloyed with both Nb and V. This comparison shows that the mass fraction of carbon in the austenite of alloy 1.4 was 0.02 mass% higher at 900 °C (Fig 88a) than that of alloy 1.2 (Fig. 88b). The difference can be explained by the carbon bound in the carbides and carbonitrides. The higher austenite carbon mass fraction of alloy 1.4 was beneficial in increasing the final retained austenite fraction, because it increased the stability of austenite against martensite transformation during final cooling.

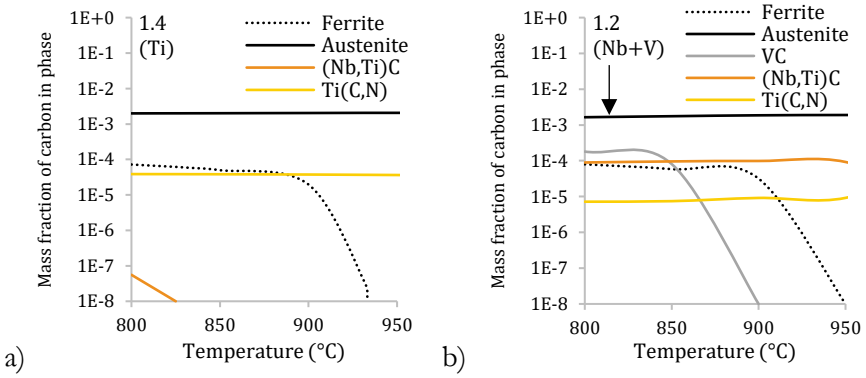

Figure 88. Mass fractions of carbon in phases of alloys a) 1.4 and b) 1.2 as a function of temperature calculated using Thermo-Calc.

More accurate free carbon calculation would require the modelling of the diffusion of carbon, for example by using DICTRA. However, the present approach explains why the retained austenite content was lower in alloy 1.2 than in alloy 1.4. This estimation does not take cementite into account, which might have also reduced the retained austenite content in alloy 2.4 (Fig. 64), so further investigations would be useful to clarify these observations.

Another microalloying effect mentioned in the literature, which would require further research, is the increase of retained austenite with the microalloying additions of Nb proposed by Hausmann et al. [27]. There may be some controversy, because the effect was the reverse in the present study, and the exact reason for the observed effect was not explained in their previous work.

5.2 Process parameters and microstructure

5.2.1 TRIP heat treatment

The intercritical TRIP heat treatment utilized in the present investigation was sufficient to stabilize the retained austenite in the final microstructures of alloys 1.1 and 1.4 (Table 9). The carbon content in the austenite phases at the intercritical temperature 830 °C of alloys 1.1 and 1.4 was 0.37 wt.% and 0.38 wt.%, respectively (Table 8). This carbon content was the starting point of the carbon concentration in the retained austenite during austempering. The carbon content of retained austenite increased to approx. 0.70 – 0.80 wt.%, which was sufficient to stabilize 5 – 14 vol.% of the retained austenite to be measured from the room-temperature microstructure.

Microstructural characterization showed that the highest austempering temperature of 480 °C led to an increased amount of martensite and bainitic ferrite, whereas the retained austenite content was the highest after austempering at 450 °C. The higher annealing temperature of 900 °C led to an increased prior austenite grain size, thus also increasing the volume fraction of retained austenite as well as its grain size. The changes observed in the morphology of Al- and Si-alloyed TRIP-assisted steels after different IA and austempering (IBT) temperatures are summarised in Figure 89.

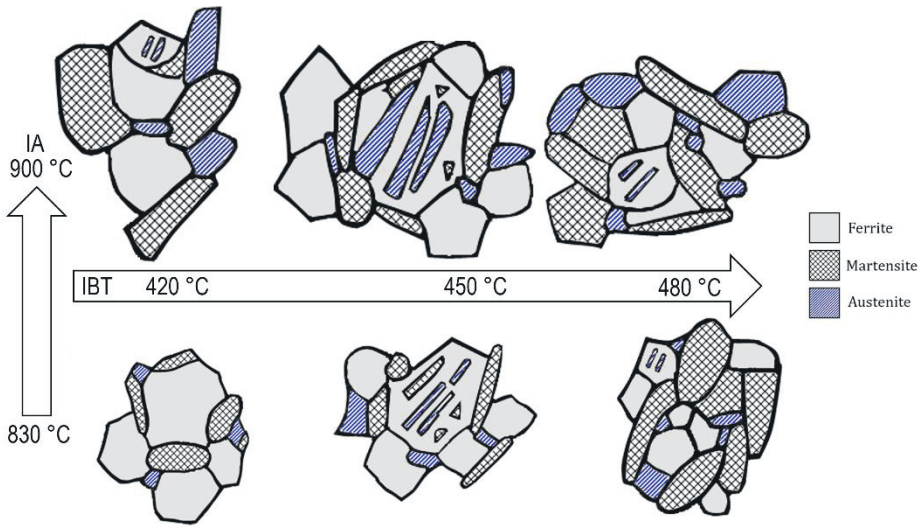

Figure 89. Morphology of Si- and Al-alloyed TRIP-assisted microstructure as a function of intercritical annealing (IA) and austempering (IBT) temperatures.

A schematic presentation (Fig. 89) is based on EBSD analysis and microstructural investigations presented in Section 4.1.4. The schematic presentation as such is suitable for the experimental material with a carbon content of 0.20 wt.% in alloys 1.1 – 1.4, because the effect of TRIP heat treatment on 0.08 – 0.10 wt.% carbon-containing alloys 2.2 – 2.4 and IE1 was different. They were mostly ferritic-martensitic containing and did not contain any retained austenite or the volume fraction of retained austenite was negligible.

In the specimens with the highest retained austenite content, i.e. 1.1 IA830 IBT450 °C, 1.1 IA900 IBT450 °C, 1.4 IA830 IBT420 °C and 1.4 IA900 IBT420 °C, the average retained austenite grain sizes were 0.40 μm, 1.1 μm, 0.64 μm and 0.78 μm, respectively. Figure 90 shows their micrographs where the retained austenite is visible in the IPFX orientation colouring.

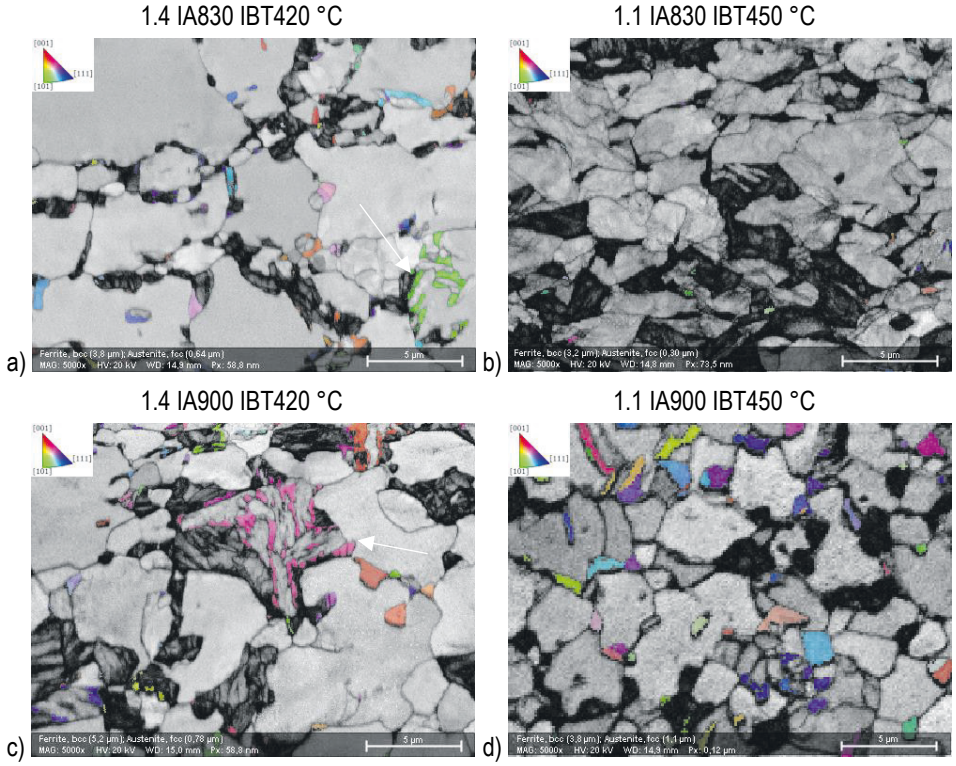

Figure 90. Retained austenite sheaves and blocks in Ti-microalloyed 1.4 and Nb-microalloyed 1.1.

Several retained austenite morphologies can be seen, which indicates that heat treatment significantly altered the final microstructures (Figs. 44 – 46, 61b). The variations are noticeable, but certain similarities can also be seen. For example,

austempering at 420 °C resulted in to finer islands of retained austenite (0.3 – 0.6 μm) inside the bainitic ferrite grains. In contrast, austempering at 480 °C, which led to higher martensite content, contained even smaller grains of austenite (0.01 μm) scattered adjacent to the martensite islands.

Bainitic ferrite was distinguished from ferrite by its morphology, similarly to how Bellhouse et al. [85] had proposed. Ferrite is polygonal and typically equiaxed, while bainitic ferrite is in a form of lamellae-containing sheaves, which are formed from prior austenite during cooling. These lamellae-containing sheaves are the result of decomposed austenite and they exhibit the same orientation inside the prior austenite grain boundaries. In the present study, these sheaves were indeed in the same orientation and are indicated by arrows in Figures 90a and 90c. As a result of the larger prior austenite grain size after intercritical annealing at 900 °C, the bainitic ferrite that contained these sheaves had also increased in size.

The retained austenite volume fraction of the vanadium-microalloyed TRIP-assisted DP alloys, 1.2 and 1.3, was negligible or below the reliable detection limit of XRD, but EBSD analysis showed small retained austenite blocks adjacent to martensite islands (Figs. 46e and 46f). This was supported by the lower uniform elongation of specimens 1.3 IA830 °C and IBT420 °C (Fig. 46e) compared to the other investigated alloys. These observations were not entirely in line with the literature [22] where a significant retained austenite volume fraction of 15.2 vol.% was reported in similar steel although the mechanical properties were comparable.

5.2.2 Q&P processing

In the majority of the TRIP heat treatments performed on the specimens of alloys 2.1 – 2.4, the treatments was ineffective in stabilizing retained austenite to room temperature. The intercritical Q&P processing, on the other hand, produced retained austenite fraction of 3 – 4 vol.% on the specimens of alloys 2.4 and IE1. As expected, martensite, in tempered and untempered form, was the dominant phase along with polygonal ferrite, but some retained austenite was found as blocks adjacent to ferrite grain boundaries or as thin laths adjacent to martensite laths.

Q&P processing for alloys 2.4 and IE1 led to microstructures that resembled those previously reported [77], [90]. In the present study, microstructures after intercritical Q&P consisted of polygonal intercritical ferrite as well as martensite islands formed from prior austenite grains, and contained retained austenite. The measured volume fractions of retained austenite were relatively low but indicated

that the "low-carbon" and Si- and Al-alloyed concept produced metastable retained austenite intermixed in a dual-phase microstructure.

Concerning the above-mentioned alloys, the specimens that were intercritically annealed at 830 °C, quenched to 275 °C and subsequently partitioned at 450 °C had the morphology of intercritical Q&P steel that contained retained austenite. These parameters were, however, not in line with the calculations using K-M and the composition of austenite (Fig. 68). In the Q&P experiments of alloys 2.4 and IE1, the calculated ideal quenching stop temperatures (QT) after intercritical annealing at 830 °C was 230 °C and 275 °C, respectively. The QT of IE1 for producing maximum retained austenite content in ideal conditions after full austenitizing at 950 °C was slightly higher (315 °C). In other words, the ideal final austenite fraction did not correlate with the results. The low carbon content in alloys 2.4 and IE1 offers one explanation, but most probably carbon was partitioned into other phases, such as carbides and carbonitrides and was not free to stabilize the retained austenite.

As a summary, the quenching and partitioning conditions were not optimal for alloys 2.4 and IE1 (Table 2 and 6), but a small amount of retained austenite was found in certain specimens. Figure 91 illustrates the idealized combination of TRIP-assisted DP and Q&P type microstructural morphologies, where increased yield strength is attributed to tempered martensite, which is discussed in Section 5.4.

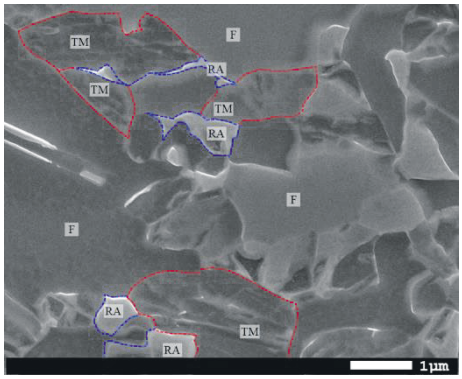

Figure 91. Idealized combination of TRIP-assisted DP and Q&P type morphology in the present work. TM = tempered martensite, F = ferrite, RA = retained austenite.

The idealized combination of DP and Q&P morphologies visible in Figure 91 was isolated, percolating ferrite grains intermixed with tempered martensite and small blocks or laths of retained austenite (< 1 µm). The microstructure that surrounded the retained austenite had a significant effect on the local ductility, which is discussed in Section 5.3.2.

5.3 Microstructure and mechanical properties

Regarding mechanical properties, investigations showed that all of the alloys could readily produce tensile strength levels of 980 MPa, but with different microstructural morphologies, e.g. TRIP microstructures containing retained austenite as well as DP microstructures containing ferrite-martensite. In terms of the usability of the materials, it is important to examine the effects of morphology on the work-hardening characteristics and local ductility. Local ductility is essential when the formability types of the materials are connected to the heat treatments of the materials.

The effect of retained austenite on the work hardening of the investigated TRIP-assisted and DH steels is shown in Figure 92, which presents the true stress-true strain curves and incremental n values of selected specimens after intercritical annealing at 830 °C.

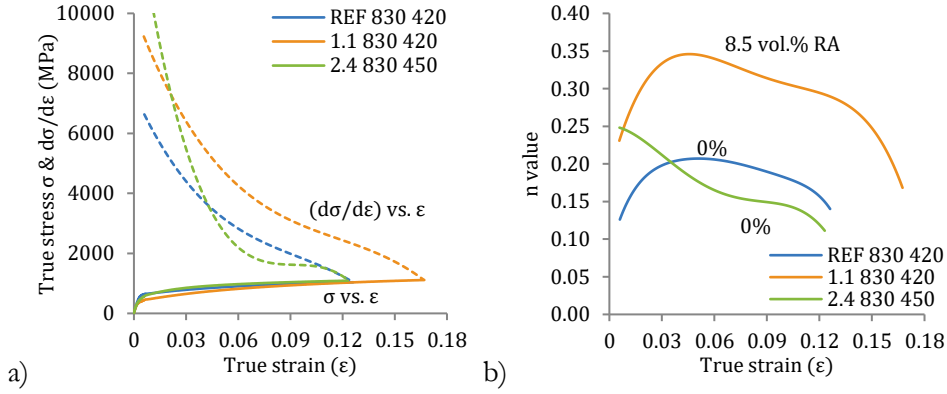

Figure 92. Mechanical properties of REF, 1.1 and 2.4 after intercritical annealing at 830 °C presenting a) true stress & dσ/dε and b) n value as a function of true strain. The latter includes the corresponding retained austenite fraction in vol.%.

Figure 92b shows that alloy 1.1, which was intercritically annealed at 830 °C and austempered at 420 °C, had a significantly higher n value compared to that of REF after similar heat treatment to alloy 2.4, i.e. intercritically annealed at 830 °C and austempered at 450 °C. The difference can be explained by the higher retained austenite content of alloy 1.1 (Table 9) and its subsequent transformation-induced plasticity effect. The sharp increase in the n value to maximum at the beginning of the curve suggests the rapid transformation of retained austenite into martensite as Bellhouse et al. [85] have reported. This indicates that less retained austenite is later available to increase the resistance to necking and, thus, to enhance uniform

elongation. Even with the decreased mechanical stability of retained austenite, the results show that the effect of retained austenite to increase the work-hardening capacity was clearly present when comparing alloy 1.1 and REF specimens (Fig. 92a).

The alloy 2.4, on the other hand, displays work-hardening behaviour typical of DP steels [115], in which the incremental n value decreases after an initial spike at the maximum, which is clearly visible in Figure 92b. This can be mainly seen as the effect of the polygonal ferrite and martensite islands in the microstructure.

In alloys 1.1 and 2.4, which contained polygonal ferrite, the important aspect is the balance between ferrite and martensite/retained austenite. Both alloys have approximately 50% of polygonal ferrite and the rest is divided between martensite and retained austenite. Uniform elongation increases when retained austenite is present, but the degree of work-hardening and the TRIP effect depend on the stability of austenite.

The effect of retained austenite on the combination of the n value and uniform elongation is also clearly seen with the highest measured retained austenite content (14.3 vol.%), as shown in Figure 93. The graph summarizes the selected tensile results of alloys 1.4, 2.2 and 2.3 after intercritical annealing at 900 °C compared to REF after intercritical annealing at 830 °C. Although the incremental n values of alloys 1.1 – 1.4 were higher compared to REF (Fig 39b and 40b), the work-hardening behaviour of conventional Al-alloyed TRIP steel cannot be observed even in the tensile test of the specimen with the highest retained austenite fraction (Fig. 93b).

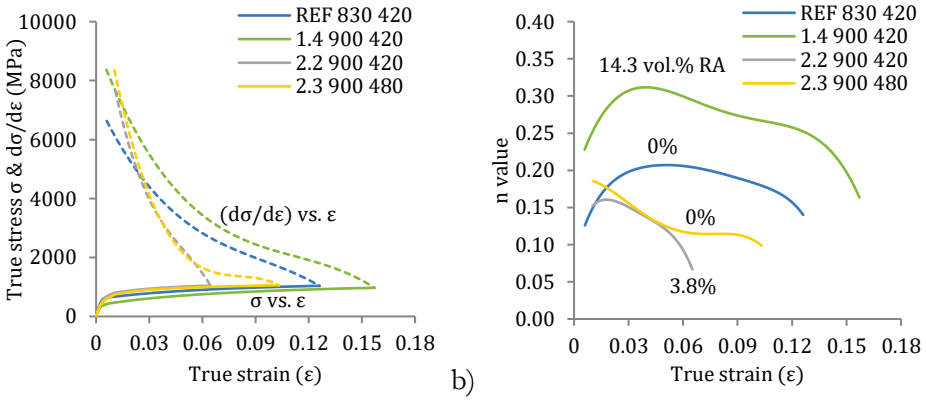

Figure 93. Mechanical properties of REF after intercritical annealing at 830 °C and of alloys 1.4, 2.2 and 2.3 after 900 °C presenting a) true stress & dσ/dε and b) n value as a function of true strain. The latter includes the corresponding retained austenite fraction in vol.%.

Conventional behaviour [33] would be seen as uniformly distributed strain hardening as the progressive transformation of retained austenite takes place. The TRIP heat-treated specimens of alloys 1.4, 2.2 and 2.3 shown in Figure 93b present pronounced or DP-type work hardening resulting in higher n values in the early stage of deformation (between 4% to 6% strain) and lower in the end stage (between 10% strain to uniform elongation).

The true stress-true strain and work-hardening behaviour (Fig. 93) is similar to that of the Si-alloyed steel studied by De Meyer et al. [33] and TRIP-Si and TRIP-Al steels presented by Yakubovsky et al. [115]. The differences in the location of the peak n value are most probably due to the mechanical stability of retained austenite. The n value peak at lower strains in the present investigation as well as that in the study of Yakubovsky et al. [115] indicates lower stability compared to the case reported by De Meyer et al. [33].

The main finding when comparing the different intercritical annealing temperatures was that intercritical annealing at 900 °C led to an increased amount of retained austenite without enhancement of the work-hardening behaviour. At the same time, work-hardening was lower, which was seen in lower n values before the necking onset point. The higher intercritical annealing temperature led to a larger austenite grain size, but the stability of retained austenite was lower. This was mainly seen as the effect of the lower carbon content of austenite at the higher temperature.

The presumed effect of lower retained austenite stability was not clearly seen in the local ductility measurements (Fig. 41), because the higher annealing temperature led to increased true fracture strain and true thickness strain at fracture values in the specimens of alloys 1.1 and 1.4. Therefore, it is proposed that the increase in local ductility is the result of the distribution of MA islands in contrast to polygonal ferrite rather than the strain hardening induced by the retained austenite.

The mechanical properties test results of the alloys containing retained austenite suggest that that the overall stability was affected more by mechanical than chemical stability. The former is affected by the grain morphology including the surrounding phases, whereas the latter is affected by the chemical composition of the retained austenite, mainly the carbon content. For instance, the low and presumably unstable content of retained austenite in alloy 2.2, intercritically annealed at 900 °C and austempered at 420 °C (Fig. 61b), had only a minuscule increasing effect on strain hardening. The ferrite in the microstructure increased the true fracture strain (Fig. 57) rather than the above-mentioned low retained austenite content.

5.3.1 True fracture strain

In addition to strain hardening curves and incremental n values, the true fracture strain (TFS) values were measured and utilized to investigate the mechanical properties. The TFS value is useful for establishing the relation between local morphology and the formability of the material.

When local ductility is introduced into a set of various specimens or steel types, the effect of the microstructure and alloying on local and global formability is seen by looking at different segments of the graphs shown in Figures 22a and 22b. A true fracture strain on the y-axis represents local formability, which correlates to the hole expansion ratio [15], [16], while uniform elongation on the x-axis represents the global formability that correlates with the n value [15]. The latter is also the case in the present study, but balanced properties were also found combining the increased uniform elongation of the global formability into the fracture toughness of local formability. This is presented in Figure 94, which shows a summary of TFS measurements as a function of true uniform elongation and connects the formability type to the morphology.

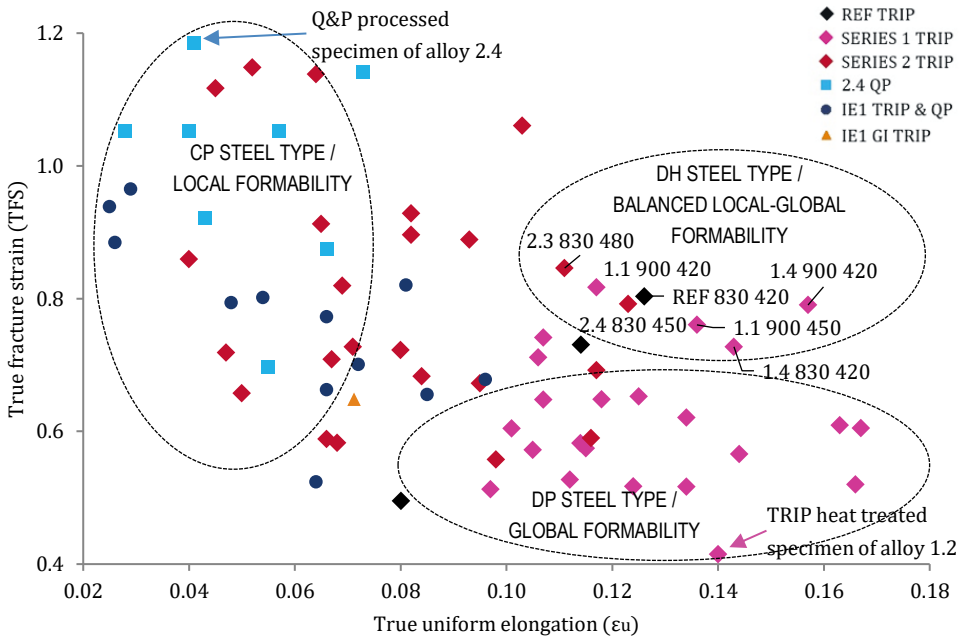

Figure 94. Summary of TFS measurements as a function of true uniform elongation.

There are three main aspects to discuss based on the TFS measurements shown in Figure 94. Firstly, balanced local and global formability are found in the following specimens: 1.1 IA900 IBT450 °C, 1.4 IA830 IBT420 °C, 1.4 IA900 IBT420 °C, 2.3 IA830 IBT480 °C, 2.4 IA830 IBT450 °C, and REF IA830 IBT420 °C. Of these, the first, second and third contained a significant amount of retained austenite which assisted with strain hardening and ductility. Secondly, the Q&P processed alloy 2.4 and TRIP heat-treated alloy 1.2, which are indicated by an arrow, are seen at the opposite ends of the graph. Alloy 2.4 has the highest TFS value with the lowest elongation, indicating the introduction of necking rapidly after the start of plastic deformation with high true stress. Thirdly, CP and fully austenitized specimens are mostly found in the upper left corner, whereas the intercritically annealed dual-phase specimens, which contained retained austenite, reside in the lower right region.

The retained austenite did not present a direct correlation with local ductility or, for example, with the strength-elongation of low-carbon Q&P steel (Fig. 73). Balanced formability and strength properties were observed from both specimens that contained retained austenite as well as specimens that did not. This shows that the overall microstructure and local morphology of MA islands is a more definitive factor for formability than the retained austenite fraction. However, the highest uniform elongation values were measured from specimens containing retained austenite.

The microstructure of CP type steel may contain some retained austenite, but the morphology leads to increased local formability, whereas a ferrite-containing DP type of microstructure, which may contain retained austenite, leads to increased global formability [15]. The TRIP effect increases global formability due to increased elongation before necking. At the same time, the increased retained austenite content in CP or DP steel results in balanced global-local properties, seen as a DH type of morphology. In the present study, the last-mentioned type contained retained austenite as blocks on the ferrite grain boundaries or sheaves inside lamellae-containing bainitic ferrite.

When examining the microstructures of the specimens with balanced local-global formability presented in Figures 41 and 42, EBSD analysis revealed that the microstructure contained blocky-type retained austenite with average grain sizes below 1 μm. In the specimens of alloys 2.3 and 2.4, however, retained austenite was not detected. In their case, the enhanced true uniform elongation was most probably the result of polygonal ferrite and tensile strength due to martensite islands [68].

In the TRIP heat-treated specimens of alloys 1.1 – 1.4 and 2.1 – 2.4, austempering at 480 °C led to the highest amount of hard secondary phase, which were MA islands.

Due to the intercritical annealing, however, the final microstructure was predominately polygonal ferrite, which means that the tensile specimens mostly had increased global formability and were located in the DP steel type region of the TFS map (Fig. 94), despite their TRIP treatment.

The lower IBT temperatures, 420 and 450 °C, led to the best combination of uniform elongation and true fracture strains meaning the highest TFS, elongation and n value as a function of tensile strength. Isothermal holding in this temperature range led to the most rapid bainitic transformation, shown in the TTT diagrams (Fig. 37 and Appendix 1), resulting in the highest retained austenite content, thus increasing work-hardening. The heat treatment and ferrite-stabilizing alloying elements aided the formation of bainitic ferrite, which in turn enhanced the stabilization of the retained austenite.

When the TRIP heat-treated and Q&P-processed specimens were compared from the perspective of retained austenite morphology, the retained austenite within the lamellae inside bainitic ferrite (Figs. 45b and 45e) was seen as more important for enhanced elongation than the retained austenite inside martensite islands (Fig. 79d). Regarding the latter, it has been speculated that the occurrence of diffuse necking at relatively low strain [87] is the reason for high TFS at low uniform elongation. The limitation of the present study was that TEM investigations of the retained austenite inside martensite islands were not performed and therefore this is suggested as further research.

5.3.2 Stress distribution between phases

It has been proposed that the phases in the microstructure contribute differently to the stress during cold forming [68]. Thus, it is important to discuss the origin of ductility and the stress distribution between the microstructural constituents. The results shown in Figure 92 and Figure 93 indicated that the contribution to yield stress from ferrite and martensite was pronounced when no significant amount of retained austenite was present.

Martensite has been seen to contribute much more to the phase stress compared to austenite or ferrite [68]. In this respect, it was deliberated whether ferrite in the microstructure of the TRIP heat-treated specimens enhanced the elongation, while the MA islands acted as strengthening constituents. The retained austenite and its morphology modified the balance of yield strength and uniform elongation as well as the n value.

Retained austenite as sheaves inside lamellae-containing bainitic ferrite was seen after the austempering temperature that led to enhanced uniform elongation (Fig. 95d). In the case of alloy 1.4, with an austenite fraction of approx. 60 vol.% during intercritical annealing at 900 °C, the rapid quenching and subsequent austempering introduced two types of morphologies: (Type I) retained austenite mainly as sheaves inside lamellae-containing bainitic ferrite, and (Type II) blocks on the ferrite grain boundaries.

As shown in the EBSD phase maps of the retained austenite in Figure 95a, 95b and 95c, the retained austenite in both types, I and II, is mostly surrounded by ferrite. This does not cause hydrostatic pressure [73] which would increase the stability of retained austenite by decreasing the M_s temperature. Thus, the stability of retained austenite is similar in Type I and Type II until the most unstable retained austenite is transformed to martensite by the TRIP effect (Fig 95e). After that point, uniform elongation is affected by the morphology and by the microconstituents present, e.g. fresh martensite, in the surrounding microstructure.

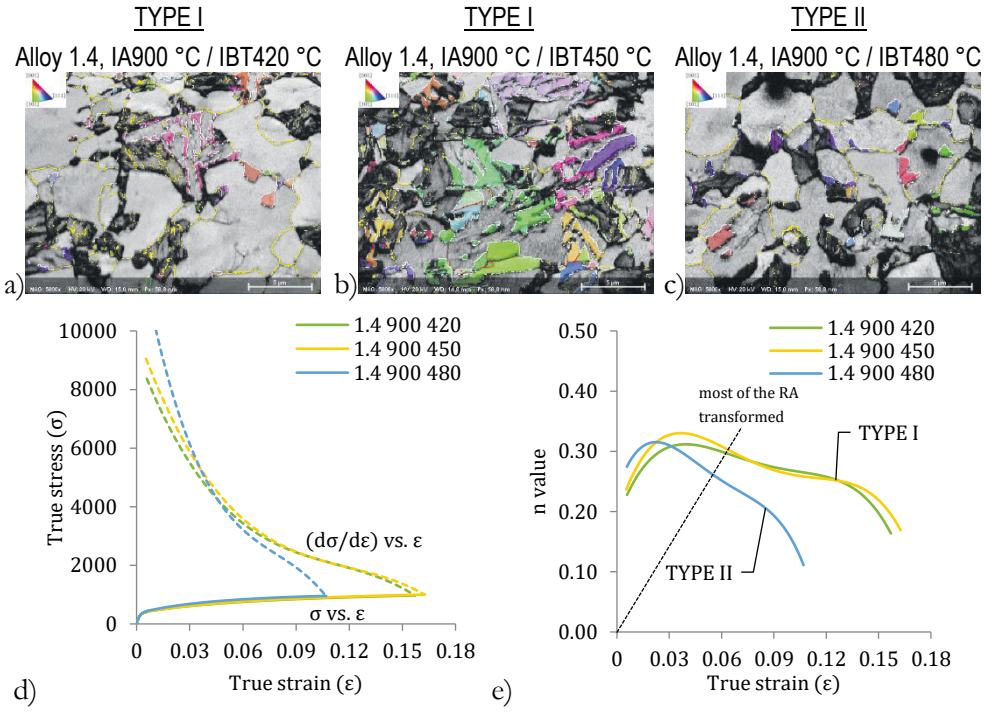

Figure 95. Retained austenite morphology (a-c), strain hardening curve (d) and n value (e) of the specimens of alloy 1.4 austempered at three temperatures: 420, 450 and 480 °C.

In the low-carbon Q&P processed specimens, however, tempered martensite increased strain hardening more than fresh martensite in the TRIP-treated specimens. This is shown in Figure 96 where Q&P processing of alloy 2.4 modified the location of the n value peak and changed the work-hardening curve to an increasing trend compared to the decreasing trend of the TRIP-treated specimen. It should be noted that the retained austenite fraction was 0 vol.% after TRIP heat treatment and 3 – 5 vol.% after the Q&P processing.

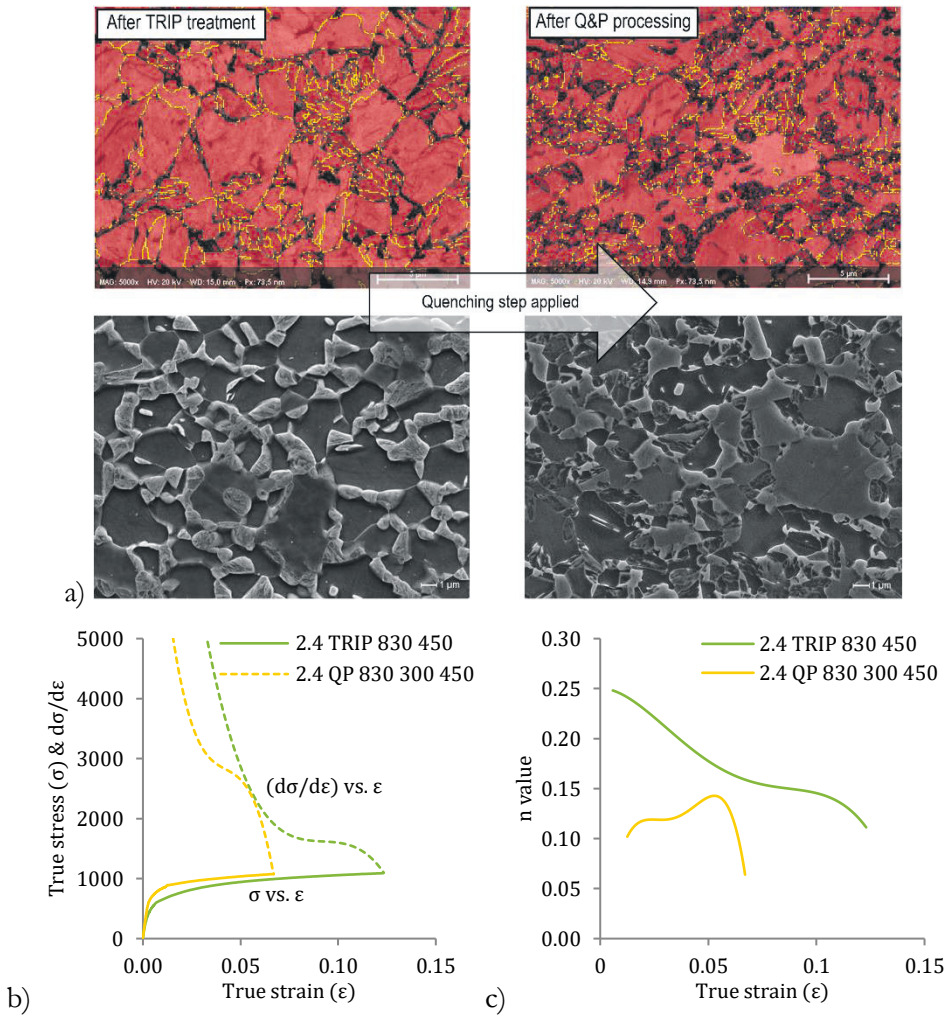

Figure 96. Comparison between TRIP heat-treated and Q&P processed alloy 2.4. The effect of applying the quenching step of Q&P on a) the microstructure as EBSD phase maps and scanning electron micrographs, b) strain hardening curve and c) n value curve.

The results indicate that there is a possibility to increase the yield strength and modify the strain hardening properties of low-carbon steel via Q&P processing. Most probably, the observed yield strength increase was partly due to the increased martensite fraction in the microstructure. The results suggest that, for the stabilization of retained austenite in alloy 2.4, the target quenching stop temperature must be lower (e.g. 250 °C, Table 17), but in order to increase both the yield strength and work hardening without retained austenite, a higher quench stop temperature should be targeted (e.g. 350 °C, Figures 69b and 70b). Austenite stabilization with carbon would be seen as a restriction of fresh martensite formation in the final cooling to room temperatures.

5.4 Quenching and partitioning response

In the present investigation, the volume fractions of ferrite and austenite during intercritical annealing were varied by selecting different annealing temperatures within the dual-phase region. After intercritical annealing, austenite would be partially transformed into martensite during the quenching step. Subsequently, the retained austenite was stabilized due to carbon enrichment during the partitioning step. The key finding was the stabilization of a small fraction of retained austenite in the room-temperature microstructures of alloys 2.4 and IE1. The Q&P process parameters are summarized in Figure 97.

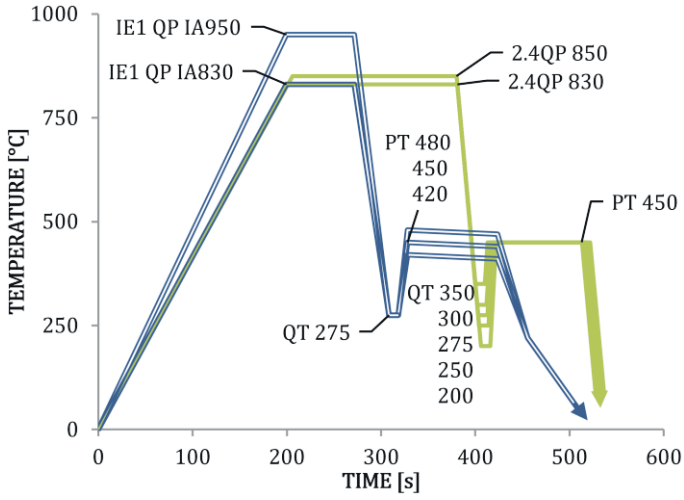

Figure 97. Summary of Q&P parameters.

According to the microstructural investigations, the intercritical annealing of IE1 at 950 °C led to almost full austenitization during the intercritical annealing step. The microstructures in Figure 78 are predominately martensitic, indicating a high strength level. This was confirmed by the mechanical test results and local ductility measurements. Intercritical annealing at 950 °C led to low elongations with a similar tensile strength level compared to the same alloy intercritically annealed at 830 °C. The increased volume fraction of martensite after the higher intercritical annealing temperature resulted in reduced ductility.

Intercritical annealing at 830 °C produced an equal amount of ferrite and martensite (72i and 74b). In contrast to TRIP heat treatment, however, the Q&P process led to an increased volume fraction of tempered martensite, which was to be expected due to the partitioning step that tempers the already transformed martensite. Part of the retained austenite transformed into martensite during the final cooling. In certain specimens, the Q&P processing increased the work hardening n value, which was observed especially with the higher quench stop temperature (e.g. 2.4 IA850 °C with QT 350 °C in Fig. 70b).

The volume fractions of retained austenite were relatively low, which was the result of several factors: (1) isothermal martensite formation during quenching may have interfered with carbon partitioning; (2) carbon was precipitated into carbides instead of partitioning into austenite; (3) the quench stop temperatures were not optimal; (4) the carbon content of the retained austenite was insufficient to decrease the M_s temperature below the ambient temperature; and (5) there was insufficient time for carbon partitioning between martensite laths and austenite during the partitioning step.

The microstructures of 2.4QP QT275 °C after intercritical annealing at 830 °C and 850 °C contained isolated ferrite regions and a tempered martensite fraction of approx. 50%. This results in a situation where martensite carries most of the load at the beginning of the deformation stage and subsequently leads to the delay of strain build-up on the ferrite-martensite interface. This was seen as increased elongation as a function of increased QT temperature (Fig. 69a and 69b). In the present study, these Q&P parameters resulted in a large prior austenite grain size and blocky retained austenite islands (Fig. 91). This behaviour has previously been reported by Tan et al. [77] who proposed that it was related to microstructures consisting of martensite islands with convex shape and finely dispersed retained austenite.

It is probable that martensitic transformation was not homogeneous, which means that the transformation degree varied within the austenite grains due to differences in carbon content, leading to heterogeneous grain transformation. This

was seen as an intermixed microstructure containing MA islands, which may or may not contain retained austenite films within martensite laths (Figs. 72, 74 and 79).

In addition to the amount of retained austenite, the second and probably the more important factor is morphology. As mentioned earlier, the microstructures were heterogeneous, meaning that the phase transformation of austenite had proceeded gradually, producing several microstructural constituents. This means, in practice, that when the specimens are quenched to an interrupted quenching temperature, the less stable large austenite grains, which typically have lower carbon content compared to smaller grains [104], undergo transformation, while the more stable small grains remain unchanged. For example, 2.4QP at QT300 °C, which had an approximate MA island size above 3 μm, transformed completely into martensite, and subsequently into tempered martensite, while the smaller austenite grains remained untransformed and were stabilized into metastable retained austenite.

In ideal Q&P processing, the carbon-enriched retained austenite would be dispersed between the laths of tempered martensite. In the case of IA Q&P, however, the retained austenite was present as films or laths and blocks within the ferrite grain boundaries and tempered martensite. During partitioning, carbon leaves the martensite laths and moves to austenite laths and films. However, regarding the partitioning process after intercritical annealing, the behaviour varies greatly from grain to grain [104].

In the intercritically Q&P processed microstructures, ferrite provided ductility while the strengthening and work hardenability were due to martensite and retained austenite, similarly to TRIP heat treatment. The yield strength difference between these two types was one of the clearest differences. It was shown in the mechanical tests that Q&P alloys had a higher yield strength than that of TRIP-treated alloys. Interestingly, the latter also had higher total elongations even without any retained austenite.

5.4.1 Work hardening and local ductility

The estimation of formability is possible using TFS and ε_{3f} as a function of true uniform elongation, and the measurements showed that TRIP treatment yielded more of a global formability type, whereas the Q&P process led to the local formability type of mechanical properties (Fig. 94).

Concerning the Q&P processed specimens, the partitioning of strain between the soft and hard phases proposed by Tan et al. [77] was seen as one of the characteristics

of the microstructure. They hypothesized that strain localizes mainly into ferrite during deformation and a smaller fraction of the strain is partitioned into martensite or retained austenite laths.

In the case of alloy IE1, Figure 98a shows that the partitioning temperature of 480 °C led to a steadily decreasing incremental n value, whereas the lower partitioning temperature of 450 °C resulted in a lower n value at low strain, but enhanced uniform elongation.

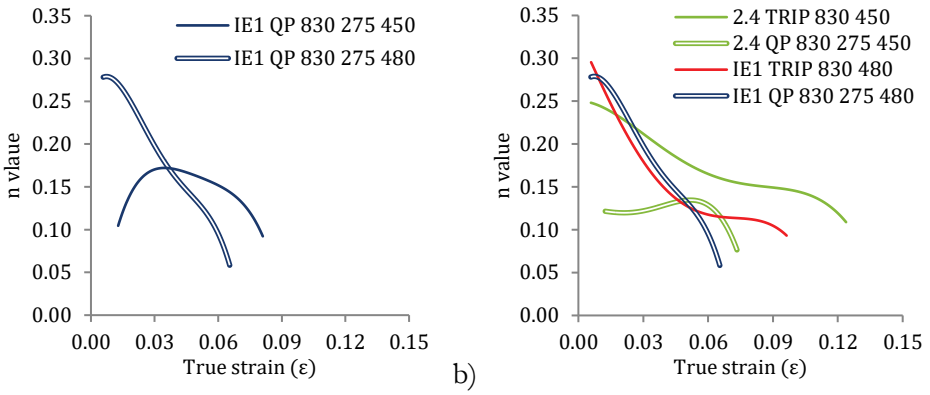

Figure 98. Comparison of n value after TRIP treatment and Q&P processing.

The reason for this behaviour is seen in the difference between the respective microstructure after partitioning at different temperatures. The microstructure of the specimen partitioned at 450 °C contained more ferrite (Fig. 79b) compared to the more martensitic specimen (Fig. 79d), which was partitioned at 480 °C. It seems that strain localization in the ferrite increased the uniform elongation of the former specimen, and its n value curve was similar to that of TRIP IBT 400 °C reported in an earlier study [63]. A similar difference in the work-hardening behaviour between TRIP and QP specimens can be seen between 2.4 TRIP IA830 IBT450 °C and 2.4 QP IA830 PT450 °C (Fig. 98b), albeit the n value and uniform elongations were slightly lower.

The n value curves of the IE1 specimen of IA830 QT275 PT450 °C shown in Figure 98 demonstrate an early-stage work-hardening effect where the incremental n value reached its maximum at relatively low strain. After the same heat treatment, there was approximately 3 vol.% of retained austenite according to EBSD phase mapping. In contrast, Zhang et al. [72] have obtained lower n values with gradual work-hardening and proposed that the retained austenite fraction, which was 6.5 vol.% in their case, transforms gradually with a weak TRIP effect due to its low

mechanical stability. In the present study, the above-mentioned behaviour was seen as the result of local microstructure rather than the TRIP effect, because of the lower retained austenite fraction.

On the other hand, the n value curves in Figure 98 resemble those of the DP or Q&P steels obtained in earlier investigations [63], [115]. De Moor et al. [63] have associated the continuously decreasing n value curve, which was similar to that of IE1 QP 830 275 450 °C, with an increased strength level. In the present study, the n value curve type of IE1 QP 830 changed when the partitioning temperature was altered (Fig. 98a).

In the present investigation, the lowest measured retained austenite fractions of 2.4QP, 3 – 4 vol.% as shown in Table 17, were at the lower end of those measured by De Moor et al. [63] and Yakubovsky et al. [115], which were 4 – 10 vol.% and 4.5 – 7 vol.%, respectively. The important aspect shown here was the alternating work-hardening behaviour with and without retained austenite as an effect of the processing parameters.

5.4.2 Influence of processing parameters on ductility

The quenching and partitioning response is highly dependent on the quenching stop temperature, but the partitioning temperature also affects the positions of the results on the true fracture strain diagram. As shown in Figure 94, the results of Q&P processed specimens were found in the local formability region. For more clarity, it is important to discuss the individual results.

The true fracture strain measurements after Q&P processing are revisited in Figure 99, where the highest combined uniform elongations and true fracture strains are found in the upper right corner of the diagram. In comparison with the TRIP-treated specimens (Fig. 94), these values were all in the local formability region, which indicates the capability for a high hole expansion ratio [15]. Concerning the results of certain other steels of 980 MPa and above strength class [15], a quenching stop temperature of 275 °C produced the highest strength-elongation combination.

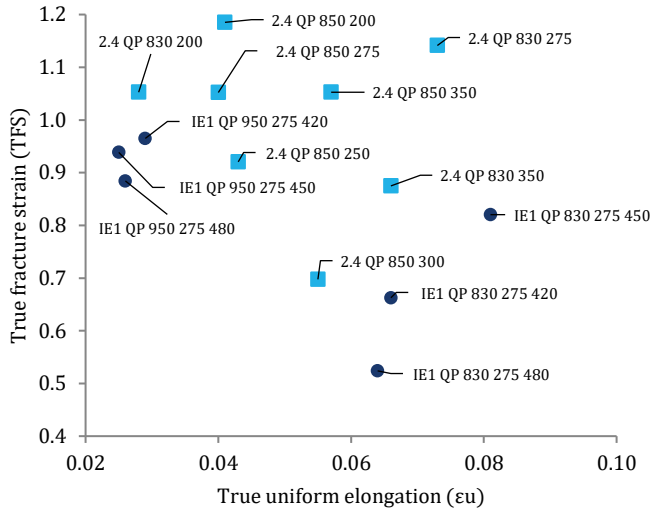

Figure 99. True fracture strains of Q&P processed alloys as a function of true uniform elongation.

Regarding 2.4QP alloy, the significance of the quench stop temperature was seen in the retained austenite morphology as well as the surrounding morphology and the amount of martensite. Before quenching, all the samples had approximately the same amount of intercritical austenite, 40 vol.%. Based on the dilatometry, all the intercritical austenite had transformed into martensite at QT 200 °C and 250 °C, while QT 275, 300 and 350 °C still contained 5, 10 and 30 vol.% of untransformed austenite corresponding to 2, 4 and 12 vol.% of the retained austenite of the whole volume.

In the context of Q&P processing, the balanced properties between elongation and ductility are seen in alloy 2.4, which was intercritically annealed at 830 °C and quenched to 275 °C, where the microstructure contained isolated, percolating ferrite grains, tempered martensite and blocky-type retained austenite, as shown in Figure 74b. The ductility is attributed to the delayed crack initiation at the ferrite-tempered martensite interface, where retained austenite also enhances fracture toughness. Film-like retained austenite was not found in the present study, and the suggestion [77] that the carbon concentration in blocky-type austenite islands is smaller and stability lower compared to film-like austenite inside MA islands could not be verified.

Only a few percent of the retained austenite, 3 – 4 vol.%, was found in the Q&P processed 2.4QP (Fig. 72d and f) and IE1 (Fig. 79d), but in alloy 2.4 the volume fractions were lower than those predicted by the calculations (Fig. 68). The ideal

situation was not achieved, although higher volume fractions of retained austenite were found in Q&P processed alloy 2.4 compared to those that had undergone TRIP heat treatment. A possible reason for the difference is the higher cooling rate after intercritical annealing to the quench stop temperature compared to that of TRIP heat treatment. The lower cooling rate during TRIP treatment gives time for the formation of new ferrite, which may decrease the fraction of martensite and retained austenite.

With the respect of the formation of new ferrite, Santofimia et al. [94] have proposed that epitaxial ferrite can reduce the amount of martensite formed during initial quenching by introducing a carbon gradient in the remaining austenite. The carbon gradient leads to situation where carbon enrichment is more likely to happen at grain boundaries rather than inside austenite islands. Consequently, this will decrease the retained austenite fraction after final cooling and making martensite formation more likely. Epitaxial ferrite, or new ferrite, had formed in initial cooling during both TRIP and Q&P processes. In the case of TRIP treated 2.4 the new ferrite decreased the retained austenite fraction to practically non-existent, whereas the carbon gradient in the Q&P case led to formation of thin laths or small blocks of retained austenite.

As a summary of the present investigations on alloy 2.4, it is proposed that higher carbon alloying would have expanded the martensite transformation range, thus enhancing the robustness of austenite stabilization at a wider range of quenching stop temperatures.

5.5 Stability of retained austenite

The stability of retained austenite during straining is indicated by three primary parameters: 1) the carbon content, 2) the size of grains within the microstructure, and 3) the morphology and distribution of the retained austenite in the microstructure [65], [68], [74]. The secondary parameters, which have an indirect yet important effect, are the properties of the surrounding microstructure and the presence of other phases and microconstituents.

The occurrence of the TRIP effect was confirmed by investigating the post-tensile test microstructure of a selected specimen via EBSD and XRD. The chemical composition and heat treatment had significant effects on the stabilization of the retained austenite in the final microstructure. Retained austenite, when present, transforms by stress- and strain-induced mechanisms into martensite during

deformation. The mechanical stability was studied by investigating the strain hardening curves and the microstructures of selected specimens. The chemical stability, in which the most important factor is the carbon content, was evaluated by calculating the carbon concentration from XRD results according to the equation by Holmes and Dyson [145].

In some cases the TRIP effect was seen, but utilizing the Ludwigson & Berger relation and calculating the k_p values was difficult after the entire tensile test had been performed (Fig. 49). Additional research on the experimental alloys of the present study is a relevant topic for future research.

The retained austenite carbon content of alloys 1.1 and 1.4 was at the same level after 830 °C, at approximately 0.70 wt.%, with the exception of 1.4 intercritically annealed at 830 °C and austempered at 450 °C, which had a carbon content of 0.82 wt.% (Table 9). Apart from this exception, the carbon content of the retained austenite was insensitive to the austempering temperature. This led to the conclusion that the stability of retained austenite during straining is probably the result of mechanical stability rather than chemical stability. The former is the effect of morphology, while the latter is the effect of carbon content. Additionally, the surrounding microstructure plays an important role in the mechanical stability. The martensite content in the surrounding microstructure increased when austempering at 480 °C was utilized instead of 420 °C, which is visible in Figure 44. The martensite fractions in the specimens of 1.1 and 1.4 austempered at 420 °C were 32 vol.% and 21 vol.% respectively, while after austempering at 480 °C the volume fractions were 38 vol.% and 37 vol.% respectively (Appendix 3, Table 1).

The specimen of alloy 2.2, which was intercritically annealed at 900 °C and austempered at 420 °C (Fig. 61b), was compared to the findings reported by Tan et al. [77]. The EBSD analysis of the microstructure of the tensile test samples revealed that the location and morphology of the retained austenite had a significant influence on the martensite transformation during straining and the onset of the TRIP effect. Similarly to observations by Tan et al. [77], the small amount of retained austenite (below 3 μm in the case of 2.4QP) located intergranularly remained untransformed, whereas the larger grains located adjacent to martensite islands were transformed at lower strain.

6 CONCLUSIONS

The present work investigated 3rd generation Advanced High-Strength Steels designed for a strength class of 980 MPa and above. The technological target was 1180 MPa tensile strength with improved ductility and formability compared to the current AHSS concepts. The influence of Si- and Al-alloying with Nb, V and Ti microalloying was studied using ten alloying concepts and 74 annealing cycles. The scientific contributions in terms of the research questions are summarized as follows.

1. **How does the isothermal bainitic transformation holding temperature affect the stabilization of retained austenite in silicon- and aluminium-alloyed steels in the case of intercritical TRIP heat treatment?**

   The isothermal bainitic transformation temperature for the highest possible austenite retention and balanced strength-ductility properties was between 420 °C and 450 °C, depending on the chemical composition of the steel and the intercritical annealing temperature used, which adjusts the volume fraction and carbon content of austenite. The retained austenite stabilizing effect of austempering at 480 °C was lower, which was seen in increased martensite formation. The TRIP heat treatments that led to the highest retained austenite fractions in the 0.20 wt.% carbon-containing alloys were as follows: IA900 °C & IBT420 °C for Nb-microalloyed and IA830 °C & IBT420 °C for Ti-microalloyed sheets.

2. **Can lower carbon containing steels (0.08 – 0.10 wt.%) be utilized to produce TRIP-assisted or Q&P steels with metastable retained austenite intermixed in a dual-phase or multi-phase microstructure which is predominately ferritic and has a tensile strength of 980 MPa and above?**

   Experimental results on the low-carbon (0.08 – 0.10 wt.%) containing steels raised the possibility of retaining austenite using Si and Al alloying. The procedure required an intercritical two-step Q&P processing instead of the conventional TRIP heat treatment schedules or annealing close to the fully austenitic state followed by austempering. The tensile strength level target of

980 MPa was obtained with a modest elongation, which points to local formability capacity. Retained austenite contents were low, which was considered to be partly due to insufficient carbon partitioning times in both TRIP and Q&P heat treatments and partly due to the V microalloying concept.

3. **How does vanadium compare to the more commonly utilized niobium microalloying in the metallurgical response of TRIP and Q&P processed silicon- and aluminium-alloyed steels?**

   In the investigated alloys, vanadium-microalloying demonstrated ineffective qualities which were due to its greater precipitation tendency compared to niobium. The carbon in solution, which would otherwise have been utilized for the carbon partitioning of retained austenite, was bound in vanadium carbides and carbonitrides. Vanadium-microalloying was not effective in assisting carbon diffusion to austenite without carbide formation in both typical and low-carbon alloys when TRIP heat treatment was used. Equilibrium calculations and microstructural studies offered an explanation for the low retained austenite content of vanadium-microalloyed steels. However, the low amount of retained austenite could be counteracted by performing Q&P processing, which led to increased yield strength through the increased tempered martensite fraction. In contrast to vanadium microalloying, it was demonstrated that TRIP-assisted DP steel with an addition of 1.0 wt.% aluminium, with and without niobium microalloying, prevented cementite precipitation during isothermal bainitic transformation, thus stabilizing the retained austenite at room temperature.

4. **What is the main origin of ductility and the effectiveness of the TRIP effect in multi-phase TRIP heat treated and Q&P processed steels?**

   The ductility origin and effectiveness of the TRIP effect were investigated by performing local ductility measurements to obtain the values of true fracture strain and true thickness strain at fracture. These values showed that the intercritical quenching and partitioning of low-carbon alloys led to increased local formability, whereas intercritical TRIP heat treatment led to a global formability type of morphology. Balanced local-global formability was achieved with and without a retained austenite fraction in the final microstructure, but the retained austenite increased the true uniform

elongations. On the other hand, the overall ductility was the combination of small ferrite grain size and martensite-austenite islands. The TRIP-treated or Q&P-processed 0.08 wt.% carbon-containing alloys displayed these balanced properties even though retained austenite stabilization was only partly successful.

Other remarks:

- The industrial processing of hot-dip galvanized Si- and Al-alloyed steel was successful in terms of galvanizability. The tensile strength class of 1180 MPa was not reached although the margin to the target was narrow.
- The quenching & partitioning process can be utilized to enhance the properties of a TRIP-assisted DP/DH type microstructure by introducing additional secondary phases for a strengthening effect, which was attributed to partitioned martensite.
- Even without the retained austenite content, the low-carbon concept that was introduced, increased the strain-hardening capacity and uniform elongation. It is envisioned that this property could be utilized in the energy absorption components of the automotive body-in-white crumple zone. The novel steel would then replace certain other 980 MPa tensile strength class steels.
- The balanced global and local formability properties were connected to the 'dual-phase with improved formability' type of morphology. In the present study, this type contained retained austenite as blocks on ferrite grain boundaries or sheaves inside lamellae-containing bainitic ferrite.
- Industrial alloy IE1, which was experimented on laboratory TRIP treatment and Q&P processing, resulted in tensile strength levels of 980 – 1180 MPa. The characteristics of TRIP and Q&P processed specimens was idealized as follows: (1) rapid quenching after intercritical annealing led to higher yield strength as a result of the increased volume fraction of martensite and bainitic ferrite, and (2) stabilization of the retained austenite was achieved by implementing intercritical annealing at 830 °C, quenching stop temperature at 275 °C and partitioning at 480 °C.

7 FUTURE RESEARCH

The present work showed the effect of heat treatment parameters on the properties of Si- and Al-alloyed TRIP-assisted steels. Heat treatment parameters for retained austenite containing microstructures were introduced. However, open questions still remain on the areas of isothermal processing as well as the stability of retained austenite, and the usability of this type of steels. Further studies are suggested as follows:

- TRIP heat treatment and Q&P processing experiments on low-carbon Al- and Si-alloyed steel without V microalloying are recommended. In Q&P processing tests, it advisable to target the quenching stop temperatures where a sufficient fraction of untransformed austenite is present. In TRIP heat treatment, the effect of increased austempering time for increased retained austenite stabilization should be investigated.
- Interrupted tensile tests for the investigation of retained austenite stability were not performed in the present study. Tests using interrupted tensile tests in combination with XRD measurements of retained austenite fraction are proposed.
- TEM investigations of the retained austenite films inside MA islands were not performed in the present investigation and are suggested as further research.
- Additional TEM investigations on precipitates (statistical analysis) would be useful. In the present study, the precipitation of microalloying elements was studied using STEM-EDS from approximately 20 particles / specimen. Statistical analysis would require a larger number of measurements.
- Hydrogen embrittlement induced by retained austenite was not investigated in the present study. The effect of hydrogen on steels with a strength class of above 1000 MPa should be in the scope of future research.

BIBLIOGRAPHY

[1] S. Keeler, M. Kimchi, and P. J. Mooney. Advanced High-Strength Steels Application Guidelines. Version 6.0, WorldAutoSteel, 2017.

[2] B. K. Zuidema. Bridging the Design–Manufacturing–Materials Data Gap: Material Properties for Optimum Design and Manufacturing Performance in Light Vehicle Steel-Intensive Body Structures. *JOM,* vol. 64, *(9),* pp. 1039-1047, 2012.

[3] D. K. Matlock, J. Speer, E. De Moor, and P. Gibbs. Recent Developments in Advanced High Strength Sheet Steels for Automotive Applications: An Overview. *JESTECH, Engineering Science and Technology, an International Journal,* vol. 15, *(1),* pp. 1-12, 2012.

[4] O. Bouaziz, H. Zurob, and M. Huang. Driving Force and Logic of Development of Advanced High Strength Steels for Automotive Applications. *Steel Research International,* vol. 84, *(10),* pp. 937-947, 2013.

[5] Web page. European Commission. Reducing CO2 emissions from passenger cars. Available: https://ec.europa.eu/clima/policies/transport/vehicles/cars_en. Accessed: November 25th, 2021.

[6] Web document. WorldAutoSteel. FutureSteelVehicle (FSV) Executive Summary. Available: http://www.worldautosteel.org/download_files/FutureSteelVehicle%20Results%20and%20Reports/FSV_Phase1_ExecutiveSummary.pdf. Accessed: November 25th, 2021.

[7] D. Krizan, K. Steineder, S. Kaar, T. Hebesberger. *Development of Third Generation Advanced High Strength Steels for Automotive Applications. Int. Conf. Transfer 2018, Trencianske Teplice, Slovakia* 2018.

[8] D. K. Matlock, J. G. Speer. Third Generation of AHSS: Microstructure Design Concepts. In: Haldar A., Suwas S., Bhattacharjee D. (eds) Microstructure and Texture in Steels. Springer, London. pp. 185-205. 2009.

[9] VDA 239-100 Werkstoffblatt/VDA 239-100 Material specification, *Sheet Steel for Cold Forming,* German Association of the Automotive Industry - Verband der Automobilindustrie, 2016.

[10] B. C. De Cooman. Structure-properties relationship in TRIP steels containing carbide-free bainite. *Curr. Opin. Solid State Mater. Sci.,* vol. 8, *(3-4),* pp. 285-303, 2004.

[11] J. Mahieu, S. Ciaessens, B. C. De Cooman, and F. Goodwin. Galvanizing of AHSS: Influence of the surface and sub-surface of Si-, Al- and P-alloyed TRIP-aided steel after intercritical annealing. *Materials Science and Technology, MS and T 2004; Volume 1: AIST Process Metallurgy, Product Quality and Applications Proceedings,* New Orleans, LA, 2004, pp. 847-857.

[12] G. N. Haidemenopoulos, A.T. Kermanidis, C. Malliaros, H.H. Dickert, P. Kucharzyk, and W. Bleck. On the effect of austenite stability on high cycle fatigue of TRIP 700 steel. *Materials Science and Engineering: A,* vol. 573, pp. 7-11, 2013.

[13] W. Bleck, X. Guo, and Y. Ma. The TRIP Effect and Its Application in Cold Formable Sheet Steels. *Steel Res. Int.,* vol. 88, *(10),* 2017.

[14] B. Hance. *Advanced High Strength Steel: Deciphering Local and Global Formability. Conference. IABC 2016 Dearborn, Michigan, USA,* 2016.

[15] S. Heibel, T. Dettinger, W. Nester, T. Clausmeyer, and A. E. Tekkaya. Damage Mechanisms and Mechanical Properties of High-Strength Multi-phase Steels. *Materials,* vol. 11, *(5),* pp. 761, 2018.

[16] M. Gruenbaum, G. Aydin, T. Dettinger, S. Heibel. Local formability of AHSS: Measurement technique, specimen types and robustness. *IOP Conference Series.Materials Science and Engineering; IOP Conf.Ser.: Mater.Sci.Eng,* vol. 651, *(1),* pp. 12056, 2019.

[17] P. Jacques, X. Cornet, Ph. Harlet, J. Ladrière, and F. Delannay. Enhancement of the mechanical properties of a low-carbon, low-silicon steel by formation of a multi-phased microstructure containing retained austenite. *Metall. Mater. Trans. A Phys. Metall. Mater. Sci.,* vol. 29, *(9),* pp. 2383-2393, 1998.

[18] P. J. Jacques, E. Girault, A. Mertens, B. Verlinden, J. Van Humbeeck, and F. Delannay. The developments of cold-rolled TRIP-assisted multi-phase steels. Al-alloyed TRIP-assisted multi-phase steels. *ISIJ Int.,* vol. 41, *(9),* pp. 1068-1074, 2001.

[19] O. Matsumura, Y. Sakuma, and H. Takechi. Enhancement of elongation by retained austenite in intercritical annealed 0.4C-1.5Si-0.8Mn Steel. *Trans. Iron Steel Inst. Jpn.,* vol. 27, *(7),* pp. 570-579, 1987.

[20] C. Wang, H. Ding, Z. Y. Tang and J. Zhang. Effect of isothermal bainitic processing on microstructures and mechanical properties of novel Mo and Nb microalloyed TRIP steel. *Ironmaking Steelmaking,* vol. 42, *(1),* pp. 9-16, 2015.

[21] E. Girault, A. Mertens, P. Jacques, Y. Houbaert, B. Verlinden, and J. Van Humbeeck. Comparison of the effects of silicon and aluminium on the tensile behaviour of multi-phase TRIP-assisted steels. *Scripta Mater,* vol. 44, *(6),* pp. 885-892, 2001.

[22] D. Krizan, K. Spiradek-Hahn, and A. Pichler. Relationship between microstructure and mechanical properties in Nb-V microalloyed TRIP steel. *Mater. Sci. Technol.,* vol. 31, *(6),* pp. 661-668, 2015.

[23] T. Bhattacharyya, S. B. Singh, D. Sourav, H. Arunansu, and D. Bhattacharjee. Development and characterisation of C–Mn–Al–Si–Nb TRIP aided steel. *Materials Science and Engineering: A,* vol. 528, *(6),* pp. 2394-2400, 2011.

[24] W. Bleck, A. Frehn, J. Ohlert. Niobium in dual phase and trip steels. *Niobium, Science and Technology*, 2001.

[25] D. Krizan and B. C. De Cooman. Mechanical properties of TRIP steel microalloyed with Ti. *Metall. Mater. Trans. A Phys. Metall. Mater. Sci.,* vol. 45, *(8),* pp. 3481-3492, 2014.

[26] Z. Tang, H. Ding, L. Du, and L. Li. Microstructures and mechanical properties of Si-Al-Mn trip steel with niobium. *J Mater Sci Technol,* vol. 23, *(6),* pp. 790-794, 2007.

[27] K. Hausmann, D. Krizan, K. Spiradek-Hahn, A. Pichler and E. Werner. The influence of Nb on transformation behavior and mechanical properties of TRIP-assisted bainitic-ferritic sheet steels. *Mater. Sci. Eng. A,* vol. 588, pp. 142-150, 2013.

[28] K. Hausmann. TRIP-Assisted Thin Sheet Steel with a Bainitic and/Or Martensitic Matrix. Doctoral thesis, Technical University of Munich, 2015.

[29] F. Perrard and C. Scott. Vanadium precipitation during intercritical annealing in cold rolled TRIP steels. *ISIJ Int,* vol. 47, *(8),* pp. 1168-1177, 2007.

[30] C. Scott, P. Maugis, P. Barges and M. Gouné. Microalloying with vanadium in TRIP steels. *International Conference on Advanced High Strength Sheet Steels for Automotive Applications - Proceedings,* 2004, pp. 181-193.

[31] L. Rothleutner, R. Cryderman, and C. Van Tyne. Influence of Temperature and Holding Time on the Interaction of V, Al, and N in Microalloyed Forging Steels. *Metallurgical and Materials Transactions,* vol. 45, *(10),* pp. 4594-4609, 2014.

[32] J. Benz. The Effect of Vanadium and Other Microalloying Elements on the Microstructure and Properties of Bainitic HSLA Steels. Doctoral thesis, Colorado School of Mines, 2019.

[33] M. De Meyer, D. Vanderschueren, and B. C. De Cooman. The Influence of the Substitution of Si by Al on the Properties of Cold Rolled C-Mn-Si TRIP Steels. *ISIJ International,* vol. 39, *(8),* pp. 813, 1999.

[34] M. Hori, T. Nakamori, N. Usuki, T. Toki and M. Arai. Effect of Si in steel on hot-dip galvanizing and galvannealing. *Proceedings of the International Conference on Zinc and Zinc Alloy Coated Steel Sheet (GALVATECH),* 1998, pp. 221.

[35] E. Scheil. Über die Umwandlung des Austenits in Martensit in Eisen-Nickellegierungen unter Belastung. *Z. Anorg. Allg. Chem.,* vol. 207, *(1),* pp. 21-40, 1932.

[36] E. Scheil. Über die Umwandlung des Austenits in Martensit in gehärtetem Stahl. *Z. Anorg. Allg. Chem.,* vol. 183, *(1),* pp. 98-120, 1929.

[37] V. F. Zackay, E. R. Parker, D. Fahr, and R. Busch. The enhancement of ductility in high-strength steels. *ASM Trans. Quart.,* vol. 60, pp. 252, 1967.

[38] D. Bhandarkar, V. F. Zackay, and E. R. Parker. Stability and mechanical properties of some metastable austenitic steels. *Metallurgical Transactions B,* vol. 3, *(10),* pp. 2619, 1972.

[39] C. D. Horvath and J. R. Fekete. Opportunities and challenges for increased usage of advanced high strength steels in automotive applications. *International Conference on Advanced High Strength Sheet Steels for Automotive Applications,* Winter Park, CO, 2004, pp. 3-10.

[40] B. K. Jha, R. Avtar, and S. V. Dwivedi. Retained austenite and its effect on properties of a commercially produced dual phase steel. *Trans. Iron Steel Inst. Jpn.,* vol. 28, *(2),* pp. 125-128, 1987.

[41] Y. Sakuma, O. Matsumura, and H. Takechi. Mechanical properties and retained austenite in intercritically heat-treated bainite-transformed steel and their variation with Si and Mn additions. *Metall Trans. A,* vol. 22, *(2),* pp. 489-498, 1991.

[42] Y. Sakuma, O. Matsumura, and O. Akisue. Influence of C content and annealing temperature on microstructure and mechanical properties of 400°C transformed steel containing retained austenite. *ISIJ Int,* vol. 31, *(11),* pp. 1348-1353, 1991.

[43] I. Tsukatani, S. Hashimoto, and T. Inoue. Effects of silicon and manganese addition on mechanical properties of high-strength hot-rolled sheet steel containing retained austenite. *ISIJ Int,* vol. 31, *(9),* pp. 992-1000, 1991.

[44] O. Matsumura, Y. Sakuma, Y. Ishii, and J. Zhao. Effect of retained austenite on formability of high strength sheet steels. *ISIJ Int.,* vol. 32, *(10),* pp. 1110-1116, 1992.

[45] A. Itami, M. Takahashi, and K. Ushioda. Cold-rolled high-strength TRIP sheet steels and plastic stability of their retained austenite. *High-Strength Steels for Automotive Symposium,* 1994, pp. 245.

[46] A. Kujanpää, E. Anelli, and B. Wade. Ferritic-Bainitic and TRIP Steels for Improved Combinations of Strength and Ductility. ECSC Report, 2002.

[47] C. Scott, L. Gavard, A. DeRo, T. Evertz, and T. Maiwald. New metallurgy for microalloyed TRIP steels. RFCS Report 2007.

[48] D. Lindell, P. Jussila, A. Rüskamp, A. Haglund, and F. Winkelhofer. Advanced High Strength Cold Rolled Sheet Steels (AHSS) with Optimised Profiling Properties Produced through Different Lines (AHSS-PROFILE). RFCS Report, 2015.

[49] J. A. Ronevich, J. G. Speer and D. K. Matlock. Hydrogen Embrittlement of Commercially Produced Advanced High Strength Sheet Steels. *SAE International Journal of Materials and Manufacturing,* vol. 3, *(1),* pp. 255-267, 2010.

[50] T. Hickel, R. Nazarov, E. McEniry, Z. Zermout, Y. Yagodzinsky, H. Hänninen, O. Rott, R. Thiessen, K. Mraczek. *Hydrogen Sensitivity of Different Advanced High Strength Microstructures (HYDRAMICROS).* ECSC Report, 2015.

[51] M. Nagumo. Function of hydrogen in embrittlement of high-strength steels. *ISIJ Int.,* vol. 41, *(6),* pp. 590-598, 2001.

[52] S. Takagi, Y. Toji, M. Yoshino, and K. Hasegawa. Hydrogen embrittlement resistance evaluation of ultra high strength steel sheets for automobiles. *ISIJ Int.,* vol. 52, *(2),* pp. 316-322, 2012.

[53] A. Laureys, T. Depover, R. Petrov, K. Verbeken. Characterization of hydrogen induced cracking in TRIP-assisted steels. *Int. J. Hydrogen Energy,* vol. 40, *(47),* pp. 16901-16912, 2015.

[54] A. Laureys, T. Depover, R. Petrov, and K. Verbeken. Microstructural characterization of hydrogen induced cracking in TRIP-assisted steel by EBSD. *Mater. Charact.,* vol. 112, pp. 169-179, 2016.

[55] T. Hojo, R. Kikuchi, H. Waki, F. Nishimura, Y. Ukai, and E. Akiyama. Effect of strain rate on the hydrogen embrittlement property of ultra high-strength low alloy TRIP-aided steel. *ISIJ Int,* vol. 58, *(4),* pp. 751-759, 2018.

[56] J. R. Patel and M. Cohen. Criterion for the action of applied stress in the martensitic transformation. *Acta Metallurgica,* vol. 1, *(5),* pp. 531-538, 1953.

[57] G. B. Olson and M. Cohen. A mechanism for the strain-induced nucleation of martensitic transformations. *Journal of the Less-Common Metals,* vol. 28, *(1),* pp. 107-118, 1972.

[58] G. B. Olson and M. Cohen. Kinetics of strain-induced martensitic nucleation. *Metallurgical Transactions A,* vol. 6, *(3),* pp. 791-795, 1975.

[59] K. Sugimoto, N. Usui, M. Kobayashi, and S-I. Hashimoto. Effects of Volume Fraction and Stability of Retained Austenite on Ductility of TRIP-aided Dual-phase Steels. *ISIJ International,* vol. 32, *(12),* pp. 1311, 1992.

[60] M. Y. Sherif, C. G. Mateo, T. Sourmail and H. K. D. H. Bhadeshia. Stability of retained austenite in TRIP-assisted steels. *Mater. Sci. Technol.,* vol. 20, *(3),* pp. 319-322, 2004.

[61] H. K. D. H. Bhadeshia and R. W. K. Honeycombe. Steels: Microstructure and properties: Fourth edition. pp. 1-461, 2017.

[62] D. C. Ludwigson and J. A. Berger. Plastic behaviour of metastable austenitic stainless steels. *Journal of the Iron and Steel Institute,* vol. 207, pp. 63, 1969.

[63] E. De Moor, S. Lacroix, A. J. Clarke, J. Penning, and J. G. Speer. Effect of Retained Austenite Stabilized via Quench and Partitioning on the Strain Hardening of Martensitic Steels. *Metallurgical and Materials Transactions A,* vol. 39, *(11),* pp. 2586-2595, 2008.

[64] H. K. D. H. Bhadeshia. TRIP-assisted steels? *ISIJ Int.,* vol. 42, *(9),* pp. 1059-1060, 2002.

[65] P. J. Jacques, J. Ladrière, and F. Delannay. On the influence of interactions between phases on the mechanical stability of retained austenite in transformation-induced plasticity multi-phase steels. *Metall. Mat. Trans. A Phys. Metall. Mat. Sci.,* vol. 32, *(11),* pp. 2759-2768, 2001.

[66] P. J. Jacques. Transformation-induced plasticity for high strength formable steels. *Current Opinion in Solid State and Materials Science,* vol. 8, *(3–4),* pp. 259-265, 2004.

[67] J.-S. Kim, J. B. Jeon, J. E. Jung, K.-K. Um, and Y. W. Chang. Effect of deformation induced transformation of e-martensite on ductility enhancement in a Fe-12 Mn steel at cryogenic temperatures. *Met. Mater. Int.,* vol. 20, *(1),* pp. 41-47, 2014.

[68] S. Harjo, N. Tsuchida, J. Abe, and W. Gong. Martensite phase stress and the strengthening mechanism in TRIP steel by neutron diffraction. *Sci. Rep.,* vol. 7, *(1),* 2017.

[69] A. Ma and A. Hartmaier. A study of deformation and phase transformation coupling for TRIP-assisted steels. *Int. J. Plast.,* vol. 64, pp. 40-55, 2015.

[70] E. J. Seo, L. Cho, Y. Estrin, B. C. De Cooman. Microstructure-mechanical properties relationships for quenching and partitioning (Q&P) processed steel. *Acta Materialia,* vol. 113, pp. 124-139, 2016.

[71] K. Zhang, M. Zhang, Z. Guo, N. Chen and Y. Rong. A new effect of retained austenite on ductility enhancement in high-strength quenching-partitioning-tempering martensitic steel. *Mater. Sci. Eng. A,* vol. 528, *(29-30),* pp. 8486-8491, 2011.

[72] K. Zhang, P. Liu, W. Li, Z. Guo and Y. Rong. Ultrahigh strength-ductility steel treated by a novel quenching-partitioning-tempering process. *Mater. Sci. Eng. A,* vol. 619, pp. 205-211, 2014.

[73] K. Sugimoto, M. Misu, M. Kobayashi, H. Shirasawa. Effects of Second Phase Morphology on Retained Austenite Morphology and Tensile Properties in a TRIP-aided Dual-phase Steel Sheet, *ISIJ Int,* vol. 33, *(7),* pp. 775-782, 1993.

[74] J. Wang and S. Van Der Zwaag. Stabilization mechanisms of retained austenite in transformation-induced plasticity steel. *Metallurgical and Materials Transactions A,* vol. 32, *(6),* pp. 1527-1539, 2001.

[75] K. K. Park, S. T. Oh, S. M. Baeck, D. -I. Kim, J. H. Han, H. N. Han, Park, S.-H., Lee, C.G., S. -J. Kim and K. H. Oh. In-situ deformation behavior of Retained Austenite on TRIP steel. *Materials Science Forum,* vol. Volume 408-412, *(Issue I),* pp. 571-576, 2002.

[76] A. Varshney, S. Sangal, S. Kundu, and K. Mondal. Superior work hardening behavior of moderately high carbon low alloy super strong and ductile multi-phase steels with dispersed retained austenite. *Mater. Des.,* vol. 99, pp. 439-448, 2016.

[77] X. Tan, D. Ponge, W. Lu, Y. Xu, X. Yang, X. Rao, D. Wu, and D. Raabe. Carbon and strain partitioning in a quenched and partitioned steel containing ferrite. *Acta Mater.,* vol. 165, pp. 561-576, 2019.

[78] G. K. Tirumalasetty, M. A. Van Huis, C. Kwakernaak, J. Sietsma, W. G. Sloof and H. W. Zandbergen. Deformation-induced austenite grain rotation and transformation in TRIP-assisted steel. *Acta Mater,* vol. 60, *(3),* pp. 1311-1321, 2012.

[79] M. Avrami. Kinetics of Phase Change. I General Theory. *Journal of Chemical Physics,* vol. 12, *(1),* pp. 1103, 1939.

[80] M. De Meyer, J. Mahieu, and B. C. De Cooman. Empirical microstructure prediction method for combined intercritical annealing and bainitic transformation of TRIP steel. *Materials Science and Technology,* vol. 18, *(10),* pp. 1121-1132, 2002.

[81] C. Oh, H. N. Han, C. G. Lee, T.-H. Lee, and S.-J. Kim. Dilatometric analysis on phase transformations of intercritical annealing of Fe−Mn−Si and Fe−Mn−Si−Cu low carbon TRIP steels. *Metals and Materials International,* vol. 10, *(5),* pp. 399-406, 2004.

[82] E. Pereloma and D. V. Edmonds. *Phase Transformations in Steels, Vol 2: Diffusionless Transformations, High Strength Steels, Modelling and Advanced Analytical Techniques.* Woodhead Publishing Limited, 2012.

[83] H. K. D. H. Bhadeshia. *Bainite in Steels: Transformations, Microstructure and Properties (Second Edition).* 2001.

[84] J. Mahieu, S. Claessens, and B. C. De Cooman. Galvanizability of high-strength steels for automotive applications. *Metall Mat Trans A Phys. Metall. Mater. Sci.,* vol. 32, *(11),* pp. 2905-2908, 2001.

[85] E. M. Bellhouse and J. R. McDermid. Effect of continuous galvanizing heat treatments on the microstructure and mechanical properties of high Al-low Si transformation induced plasticity steels. *Metall. Mater. Trans. A Phys. Metall. Mat. Sci.,* vol. 41, *(6),* pp. 1460-1473, 2010.

[86] K.-I. Sugimoto, J. Sakaguchi, T. Iida, and T. Kashima. Stretch-flangeability of a high-strength TRIP type bainitic sheet steel. *ISIJ Int.,* vol. 40, *(9),* pp. 920-926, 2000.

[87] K.-I. Sugimoto, K. Nakano, S. -M. Song, and T. Kashima. Retained austenite characteristics and tensile properties in a TRIP type bainitic sheet steel. *ISIJ Int.,* vol. 40, *(9),* pp. 902-908, 2000.

[88] K. Hausmann, D. Krizan, A. Pichler, and E. Werner. Trip-aided bainitic-ferritic sheet steel: A critical assessment of alloy design and heat treatment. *Materials Science and Technology Conference and Exhibition 2013, MS and T 2013,* Montreal, QC, 2013, pp. 209-218.

[89] J. Speer, D. K. Matlock, B. C. De Cooman, and J. G. Schroth. Carbon partitioning into austenite after martensite transformation. *Acta Mater.,* vol. 51, *(9),* pp. 2611-2622, 2003.

[90] A. M. Streicher, J. G. Speer, D. K. Matlock, and B. C. De Cooman. Quenching and partitioning response of a si-added TRIP sheet steel. *International Conference on Advanced High Strength Sheet Steels for Automotive Applications - Proceedings,* 2004, pp. 51-62.

[91] J. Kähkönen. Quenching and Partitioning Response of Carbon-Manganese-Silicon Sheet Steels Containing Nickel, Molybdenum, Aluminum and Copper Additions. Masters' thesis, Colorado School of Mines, 2016.

[92] T. Nyyssönen. Quenching and Partitioning of High-Aluminum Steels. Doctoral thesis, Tampere University of Technology, 2017.

[93] T. Nyyssönen, M. Somani, P. Peura, and V. -T. Kuokkala. Microstructural response of high aluminum steels to quenching and partitioning treatment. *ASME International Mechanical Engineering Congress and Exposition, Proceedings (IMECE),* 2013.

[94] M. J. Santofimia, L. Zhao, J. Sietsma. Microstructural Evolution of a Low-Carbon Steel during Application of Quenching and Partitioning Heat Treatments after Partial Austenitization. *Metall. and Mat. Trans. A,* vol. 40, *(1),* pp. 46-57, 2009.

[95] J. G. Speer, E. De Moor, K. O. Findley, D. K. Matlock, B. C. De Cooman, and D. V. Edmonds. Analysis of microstructure evolution in quenching and partitioning automotive sheet steel. *Metall. Mater. Trans. A Phys. Metall. Mater. Sci.,* vol. 42, *(12),* pp. 3591-3601, 2011.

[96] J. G. Speer, E. De Moor, and A. J. Clarke. Critical assessment 7: Quenching and partitioning. *Mater. Sci. Technol.,* vol. 31, *(1),* pp. 3-9, 2015.

[97] D. V. Edmonds, K. He, F. C. Rizzo, B. C. De Cooman, D. K. Matlock, and J. G. Speer. Quenching and partitioning martensite-A novel steel heat treatment. *Mater. Sci. Eng. A,* vol. 438-440, *(SPEC. ISS.),* pp. 25-34, 2006.

[98] D. P. Koistinen and R. E. Marburger. A general equation prescribing the extent of the austenite-martensite transformation in pure iron-carbon alloys and plain carbon steels. *Acta Metallurgica,* vol. 7, *(1),* pp. 59-60, 1959.

[99] W. Stuhlmann. *Härterei Tech. Mitteilungen,* vol. 31, *(6),* 1954.

[100] F. Forouzan. Increasing phase transformation rate in advanced high strength steel applications. Doctoral thesis. (2019) Luleå University of Technology. ISBN 9789177903246; and Universität des Saarlandes, Germany.

[101] J. G. Speer, F. C. Rizzo Assunção, D. K. Matlock, and D. V. Edmonds. The "quenching and partitioning" process: Background and recent progress. *Mater. Res.,* vol. 8, *(4),* pp. 417-423, 2005.

[102] N. Saunders, U. K. Z. Guo, X. Li, A. P. Miodownik and J. -Ph Schillé. Using JMatPro to model materials properties and behavior. *JOM,* vol. 55, *(12),* pp. 60-65, 2003.

[103] J. Andersson, T. Helander, L. Höglund, P. Shi, and B. Sundman. Thermo-Calc & DICTRA, computational tools for materials science. *Calphad,* vol. 26, *(2),* pp. 273-312, 2002.

[104] T. Nyyssönen, O. Oja, P. Jussila, A. Saastamoinen, M. Somani, and P. Peura. Quenching and Partitioning of Multi-phase Aluminum-Added Steels. *Metals,* vol. 9, *(3),* pp. 373, 2019.

[105] T. Nyyssönen, P. Peura, E. De Moor, D. Williamson, and V. -T. Kuokkala. Crystallography and mechanical properties of intercritically annealed quench and partitioned high-aluminum steel. *Mater. Charact.,* vol. 148, pp. 71-80, 2019.

[106] Q. Furnemont, P. J. Jacques, and T. Pardoen. The macro- and micromechanics of TRIP-assisted multi-phase steels, experiments and modelling. *5th European Mechanics of Materials Conference on Scale Transitions from Atomistics to Continuum Plasticity EUROMECH-MECAMAT'2001,* Delft, 2001, pp. Pr5325-Pr5332.

[107] E. Girault, P. Jacques, Ph. Harlet, K. Mols, J. Van Humbeeck, E. Aernoudt, and F. Delannay. Metallographic Methods for Revealing the Multi-phase Microstructure of TRIP-Assisted Steels. *Mater. Charact.,* vol. 40, (2), pp. 111-118, 1998.

[108] R. Pradham and J. P. Wise. Aluminum-rich, TRIP-aided steels: Effects of alloying additions & processing. *45th MWSP Conference Proceedings, Vol. XLI,* 2003, pp. 153.

[109] S.-J. Kim, C. G. Lee, T.-H. Lee, and C.-S. Oh. Effect of Cu, Cr and Ni on mechanical properties of 0.15 wt.% C TRIP-aided cold rolled steels. *Scripta Mater.,* vol. 48, *(5),* pp. 539-544, 2003.

[110] A. Pichler, P. Stiaszny, R. Potzinger, R. Tikal, and E. Werner. TRIP steels with reduced Si content. *40th MWSP Conference Proceedings,* 1998, pp. 259.

[111] J. Mahieu, J. Maki, B. C. De Cooman, and S. Claessens. Phase transformation and mechanical properties of Si-free CMnAl transformation-induced plasticity-aided steel. *Metall. Mater. Trans. A Phys. Metall. Mater. Sci.,* vol. 33, *(8),* pp. 2573-2580, 2002.

[112] S. Traint, A. Pichler, K. Hauzenberger, P. Stiaszny and E. Werner. Influence of silicon, aluminium, phosphorus and copper on the phase transformations of low alloyed TRIP-steels. *International Conference on TRIP-Aided Ferrous Alloys,* 2002, pp. 121.

[113] J. Maki, J. Mahieu, B. C. De Cooman, and S. Claessens. Galvanisability of silicon free CMnAl TRIP steels. *Mater. Sci. Technol.,* vol. 19, *(1),* pp. 125-131, 2003.

[114] E. M. Bellhouse and J. R. Mcdermid. Selective oxidation and reactive wetting during hot-dip galvanizing of a 1.0 pct Al-0.5 pct Si TRIP-assisted steel. *Metall. Mater. Trans. A Phys. Metall. Mater. Sci.,* vol. 43, *(7),* pp. 2426-2441, 2012.

[115] O. Yakubovsky, N. Fonstein and D. Bhattacharya. Effect of composition and microstructure on the stress-strain behavior of TRIP and dual-phase steels in *AHSSS Conference,* pp. 295-306, 2004.

[116] I. B. Timokhina, P. D. Hodgson, and E. V. Pereloma. Effect of alloying elements on the microstructure-property relationship in thermomechanically processed C-Mn-Si TRIP steels. *Steel Res.,* vol. 73, *(6-7),* pp. 274-279, 2002.

[117] R. Lagneborg, T. Siwecki, S. Zajac, and B. Hutchinson. The Role Of Vanadium In Microalloyed Steels. *The Scandinavian Journal of Metallurgy,* 1999.

[118] W. Bleck. Using the TRIP effect - the dawn of a promising group of cold formable steels. *International Conference of TRIP-Aided High Strength Ferrous Alloys,* 2002, pp. 13.

[119] R. Eric. Production of Ferroalloys. *Treatise on Process Metallurgy,* vol. 3, pp. 477-532, 2014.

[120] R. Ruismäki. Metallurgy and Heat Treatment of Medium Manganese Quenching & Partitioning Steels. Masters' thesis, Aalto University, 2018.

[121] M. Takahashi and H. K. D. H. Bhadeshia. Model for the microstructure of some advanced bainitic steels. *Mater. Trans. JIM,* vol. 32, *(8),* pp. 689-696, 1991.

[122] M.-H. Cai, H. Ding, Y.-K. Lee, Z.-Y. Tang, and J.-S. Zhang. Effects of Si on microstructural evolution and mechanical properties of hot-rolled ferrite and bainite dual-phase steels. *ISIJ Int,* vol. 51, *(3),* pp. 476-481, 2011.

[123] S. Serajzadeh and A. Karimi Taheri. An investigation of the silicon role on austenite recrystallization. *Mater. Lett.,* vol. 56, *(6),* pp. 984-989, 2002.

[124] R. Zhu, S. Li, M. Song, I. Karaman, and R. Arroyave. Phase constitution effect on the ductility transformation induced plasticity steels. *Mater. Sci. Eng. A,* vol. 569, pp. 137-143, 2013.

[125] D. Bhattacharya, N. Fonstein, O. Girina, I. Gupta, and O. Yakubovsky. A family of 590 MPa, advanced high strength steels with various microstructures. *45th Mechanical Working and Steel Processing Conference Proceedings,* 2003, pp. 173-186.

[126] B. Y. Navarrete Pino, A. A. Torres Castillo, E.J. Gutiérrez Castañeda, L. A. Espinosa Zúñiga, L. Hernández Hernández, A. Salinas Rodríguez, R. Deaquino Lara, R. Saldaña Garcés, I. A. Reyes Domínguez, J. Aguilar Carrillo. Using Intercritical CCT Diagrams and Multiple Linear Regression for the Development of Low-Alloyed Advanced High-Strength Steels, *Metals,* vol. 11, *(11),* 2021.

[127] J. H. Jang, I. G. Kim and H. K. D. H. Bhadeshia. e-Carbide in alloy steels: First-principles assessment. *Scripta Mater.,* vol. 63, *(1),* pp. 121-123, 2010.

[128] Y. Kimura and S. Takaki. Phase transformation mechanism of Fe-Cu alloys. *ISIJ Int.,* vol. 37, *(3),* pp. 290-295, 1997.

[129] K. E. Daehn, A. Cabrera Serrenho, and J. M. Allwood. How Will Copper Contamination Constrain Future Global Steel Recycling? *Environ. Sci. Technol.,* vol. 51, *(11),* pp. 6599-6606, 2017.

[130] J. Zhang, H. Matsuura and F. Tsukihashi. Chapter 4.4 - Processes for Recycling. *Treatise on Process Metallurgy,* pp. 1507-1561, 2014.

[131] S. Traint, A. Pichler, M. Blaimschein, B. Röthler, C. Krempaszky, and E. Werner. Alloy design, processing and properties of TRIP steels: A critical comparison. *International Conference on Advanced High Strength Sheet Steels for Automotive Applications,* Winter Park, CO, 2004, pp. 79-98.

[132] N. Fonstein. Advanced high strength sheet steels: Physical metallurgy, design, processing, and properties. pp. 1-396, 2015.

[133] J. Mahieu, D. Van Dooren, L. Barbé, and B. C. De Cooman. Influence of Al, Si and P on the kinetics of intercritical annealing of TRIP-aided steels: thermodynamical prediction and experimental verification. *Steel Research,* vol. 73, *(6-7),* pp. 267-273, 2002.

[134] B. Mintz. Hot dip galvanising of transformation induced plasticity and other intercritically annealed steels. *International Materials Reviews,* vol. 46, *(4),* pp. 169-197, 2001.

[135] H. C. Chen, H. Era, and M. Shimizu. Effect of phosphorus on the formation of retained austenite and mechanical properties in Si-containing low-carbon steel sheet. *Metall. Trans. A,* vol. 20, *(3),* pp. 437-445, 1989.

[136] C. M. Parish. Fundamental Study of Phase Transformations in Si-Al TRIP Steels. Masters' thesis, University of Pittsburgh, 2003.

[137] S. Dionne, B. Voyzelle, E. Essadiqi, O. Dremailova, E. Baril, J. R. McDermid, and F. Goodwin. Galvanizing of a hot rolled C-mn-si TRIP steel. *International Conference on Advanced High Strength Sheet Steels for Automotive Applications,* Winter Park, CO, 2004, pp. 405-415.

[138] L. Bordignon, J. Paavilainen, and X. Vanden Eynde. Enhanced Hot Dip Galvanising by Controlled Oxidation in the Annealing Furnace. ECSC report, 2002.

[139] J. Dearden and H. A. O'Neill. A guide to the selection and welding of low-alloy structural steels. *Trans. Inst. Weld.,* vol. 3, pp. 203-214, 1940.

[140] Y. Ito and K. Bessyo. Weldability formula of high strength steels related to heat-affected zone cracking. *Journal of Japan Welding Society,* vol. 37, pp. 683-991, 1968.

[141] M. I. Khan, M. L. Kuntz, E. Biro, and Y. Zhou. Microstructure and mechanical properties of resistance spot welded advanced high strength steels. *Mater. Trans.,* vol. 49, *(7),* pp. 1629-1637, 2008.

[142] H. Brandis. Rechnerische Bestimmung der Umwandlungstemperaturen von niedriglegierten Stählen. *TEW – Technische Berichte,* vol. 1, *(1),* pp. 8-10, 1975.

[143] S. H. Park. Development of Ductile Ultra-High Strength Hot Rolled Steels. POSCO Technical report, pp 50-128, 1996.

[144] C. F. Jatczak, J. A. Larsen, and S. W. Shin. Retained Austenite and its Measurements by X-Ray Diffraction, SP-453. *Society of Automotive Engineers,* 1980.

[145] D. J. Dyson and B. Holmes. Effect of alloying additions on the lattice parameter of austenite. *J Iron Steel Inst (London),* vol. 208, *(5),* pp. 469-474, 1970.

[146] L. Wagner and P. Larour. Influence of specimen geometry on measures of local fracture strain obtained from uniaxial tensile tests of AHSS sheets. *IOP Conference Series: Materials Science and Engineering,* 2018.

[147] Web page. *Coatings - AHSS Guidelines*. Available: https://ahssinsights.org/coatings/coatings/. Accessed: November 25th, 2021.

[148] S. Zajac, R. Lagneborg and T. Siwecki. The role of nitrogen in microalloyed steels in *International Conference Microalloying '95,* 11-14 June, 1995, pp. 321-338.

[149] Web document. *Gleeble 3800-GTC Brochure*. Available: http://dsi.gleeble.com/3800. Accessed: April 10th, 2022.

APPENDIX 1: TIME-TEMPERATURE TRANSFORMATION DIAGRAMS

Time temperature transformation (TTT) curves for each composition were calculated using a suitable thermodynamic database available in JMatPro® software, version 11 (Sente Software Ltd., UK). The calculations in Appendix 1 are based on the chemical analysis of alloys presented in Table 2 of Section 3.2.1 and Table 6 of Section 3.5.

Figure 1 presents TTT diagram for alloy REF starting from 900 °C, which represents full austenitizing temperature for this alloy. A_3 temperature of this alloy is 806 °C.

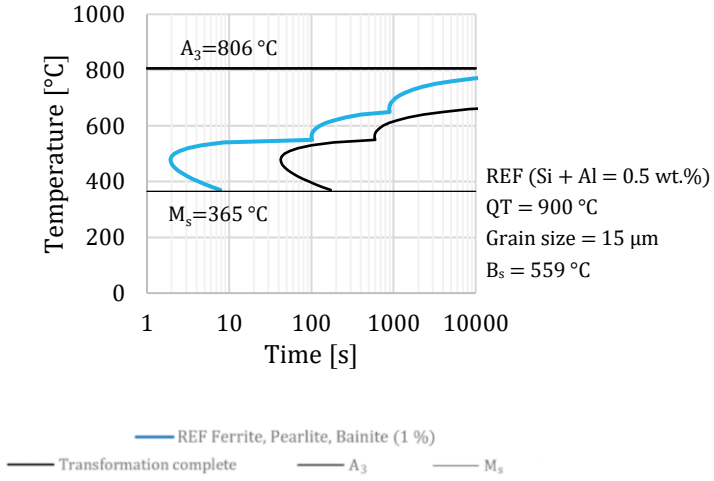

Figure 1. TTT diagram of alloy REF.

According to JMatPro® software, alloys 1.1, 1.2, 1.3 and 1.4 have higher A_3 temperature compared to alloy REF. Figure 2 presents their TTT diagrams starting from 1000 °C, which for these alloys is required for full austenitizing.

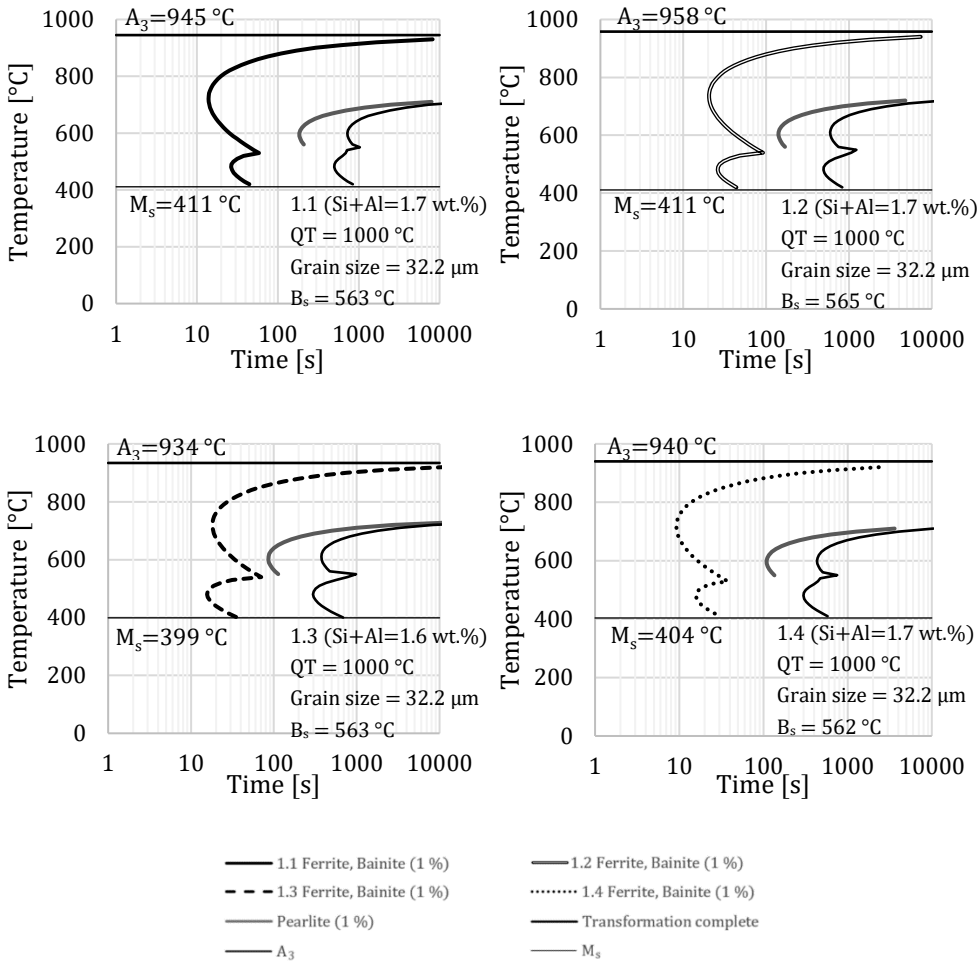

Figure 2. TTT diagram of alloys 1.1, 1.2, 1.3 and 1.4.

According to the diagrams visible in Figure 2, the A_3 temperatures of 1.1, 1.2, 1.3 and 1.4 are around 930 °C to 950 °C, which means that considerably higher annealing temperature is required for full austenitizing compared to REF. The higher required austenitizing temperature is mainly due to increased Si and Al alloying.

The highest A_3 temperature of the investigated alloys, according to JMatPro® software, was in alloy 2.4 and was 988 °C. Figure 3 presents TTT diagrams of alloys 2.1 and 2.2 starting from 900 °C and those of alloys 2.3 and 2.4 starting from 1000 °C. The A_3-increasing effect of Si and Al is visible the diagrams. TTT diagram of alloy IE1 is presented in Figure 4, which shows A_3 temperature of 914 °C which is slightly lower compared to alloy 2.3 that has similar Si and Al content.

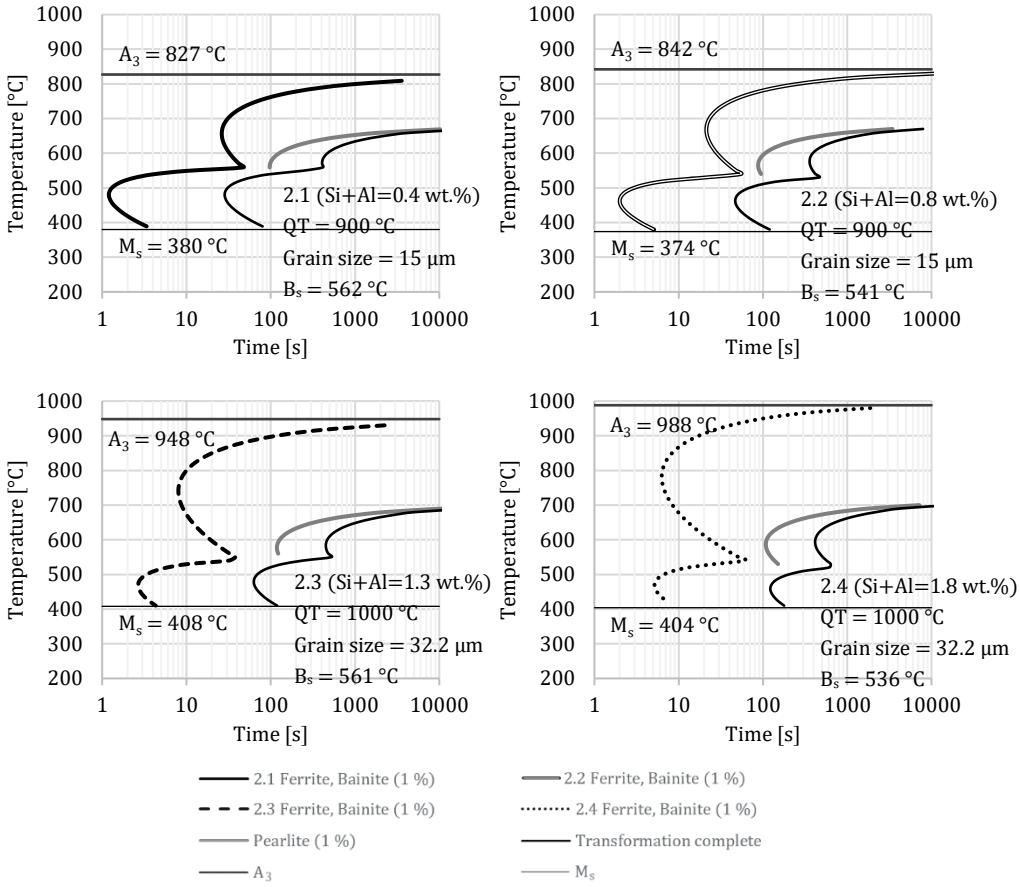

Figure 3. TTT diagram of alloys 2.1, 2.2, 2.3 and 2.4.

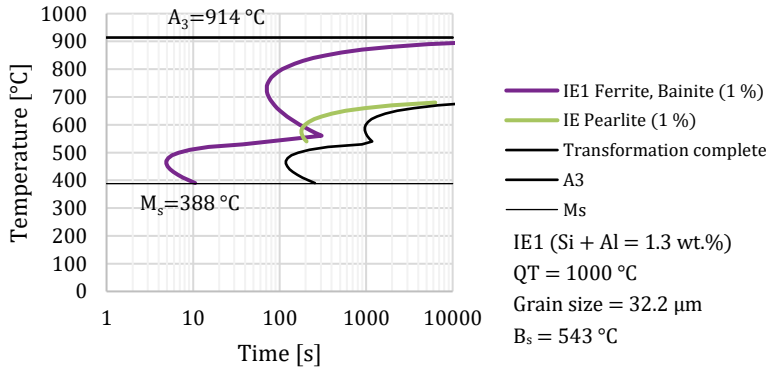

Figure 4. TTT diagram of alloy IE1.

APPENDIX 2: LIST OF EXPERIMENTAL CONDITIONS AND RESULTS

Appendix 2 summarizes the mechanical test results and retained austenite measurements of the present study. Table 1 presents the list of heat treatment conditions and their corresponding test results.

Table 1. Summary of the test results and experimental conditions.

#	Alloy	Thermal cycle	IA [°C]	t_{IA} [s]	QT [°C]	IBT / PT [°C]	t_{IBT} / t_{PT} [s]	$R_{p0.2}$ [MPa]	R_m [MPa]	$R_{p0.2}/R_m$	A_g [%]	A_{25} [%]	n [4-6]	n [10- 20/A_g]	ε_u	ε_{3f}	TFS	RA vol.% (XRD)	RA carbon wt.%
1	REF	A	830	70		420	100	614	910	0.67	14.0	23.2	0.21	0.18	0.13	0.77	0.80	0.1	1.22
2	REF	A	830	70		450	100	550	956	0.58	12.3	24.3	0.25	0.10	0.11	0.72	0.73	0.1	1.22
3	REF	A	830	70		480	100	600	1024	0.59	8.1	15.3	0.21	-	0.08	0.50	0.50	0.1	1.22
4	1.1	A	830	70		420	100	417	937	0.45	18.4	18.7	0.34	0.25	0.17	0.53	0.61	8.5	0.72
5	1.1	A	830	70		450	100	451	999	0.45	18.5	24.9	0.34	0.22	0.17	0.43	0.52	4.6	0.73
6	1.1	A	830	70		480	100	503	1050	0.48	14.6	19.2	0.31	0.16	0.13	0.42	0.52	1.2	0.72
7	1.2	A	830	70		420	100	473	1006	0.47	12.6	16.5	0.29	0.15	0.11	0.53	0.58	0	-
8	1.2	A	830	70		450	100	493	1021	0.48	15.5	18.3	0.28	0.16	0.14	0.35	0.42	0	-
9*	1.2	A	830	70		480	100	533	1053	0.51	8.1	10.3	0.25	-	-	-	-	0	-
10	1.3	A	830	70		420	100	456	956	0.48	11.8	18.2	0.28	0.13	0.11	0.42	0.53	0.3	1.19
11	1.3	A	830	70		450	100	493	975	0.51	13.1	19.9	0.29	0.16	0.12	0.42	0.52	1.1	0.70
12	1.3	A	830	70		480	100	538	1035	0.52	11.1	15.3	0.26	0.12	0.11	0.51	0.57	1.2	0.73
13	1.4	A	830	70		420	100	401	887	0.45	15.5	21.5	0.31	0.19	0.14	0.58	0.73	5.4	0.71
14	1.4	A	830	70		450	100	422	939	0.45	15.7	24.2	0.31	0.19	0.14	0.45	0.57	12.0	0.82
15	1.4	A	830	70		480	100	448	950	0.47	12.7	16.6	0.30	0.16	0.12	0.55	0.65	8.7	0.66
16	2.1	A	830	70		420	100	489	785	0.62	7.0	15.7	0.15	-	0.06	1.23	1.14	< 1	-
17	2.1	A	830	70		450	100	589	907	0.65	7.5	16.5	0.15	-	0.07	0.82	0.73	< 1	-
18	2.1	A	830	70		480	100	600	918	0.65	6.7	12.6	0.14	-	0.07	0.92	0.82	< 1	-
19	2.2	A	830	70		420	100	599	968	0.62	7.0	9.5	0.14	-	0.07	0.69	0.59	< 2	-
20	2.2	A	830	70		450	100	636	992	0.64	7.0	14.1	0.11	-	0.07	0.65	0.58	< 1	-
21	2.2	A	830	70		480	100	677	1019	0.66	6.7	18.2	0.10	-	0.07	0.86	0.71	< 1	-
22	2.3	A	830	70		420	100	550	937	0.59	9.6	10.5	0.15	-	0.10	0.60	0.56	< 1	-
23	2.3	A	830	70		450	100	585	921	0.64	8.6	18.3	0.14	-	0.08	0.81	0.68	< 1	-
24	2.3	A	830	70		480	100	552	927	0.60	11.3	19.1	0.14	0.11	0.11	0.88	0.85	< 1	-
25	2.4	A	830	70		420	100	543	941	0.58	12.7	18.5	0.18	0.13	0.12	0.71	0.69	< 1	-
26	2.4	A	830	70		450	100	551	957	0.58	12.8	20.3	0.18	0.14	0.12	0.79	0.79	< 2	-
27	2.4	A	830	70		480	100	550	943	0.58	12.0	16.9	0.19	0.15	0.12	0.60	0.59	< 2	-
28	1.1	B	900	70		420	100	381	827	0.46	12.8	18.5	0.29	0.16	0.12	0.70	0.82	13.4	0.73

29	1.1	B	900	70		450	100	393	843	0.47	15.0	26.0	0.30	0.19	0.14	0.75	0.76	12.9	0.73
30	1.1	B	900	70		480	100	415	895	0.46	11.7	20.7	0.29	0.11	0.11	0.61	0.71	11.4	0.74
31	1.2	B	900	70		420	100	435	932	0.47	13.5	20.7	0.28	0.17	0.13	0.53	0.65	0	-
32	1.2	B	900	70		450	100	432	915	0.47	14.4	21.4	0.28	0.17	0.13	0.61	0.62	0	-
33	1.2	B	900	70		480	100	479	971	0.49	10.7	20.0	0.26	0.09	0.10	0.54	0.60	0	-
34	1.3	B	900	70		420	100	434	862	0.50	11.4	21.2	0.28	0.12	0.11	0.51	0.65	0	-
35	1.3	B	900	70		450	100	425	894	0.48	12.2	23.2	0.28	0.16	0.12	0.47	0.58	0	-
36	1.3	B	900	70		480	100	524	961	0.55	10.2	11.2	0.22	0.09	0.10	0.44	0.51	0	-
37	1.4	B	900	70		420	100	392	830	0.47	17.1	20.7	0.31	0.23	0.16	0.68	0.79	14.3	0.71
38	1.4	B	900	70		450	100	388	850	0.46	17.9	21.1	0.32	0.22	0.16	0.51	0.61	11.3	0.74
39	1.4	B	900	70		480	100	415	859	0.48	11.3	15.3	0.27	0.11	0.11	0.63	0.74	8.9	0.65
40	2.1	B	900	70		420	100	593	835	0.71	5.1	13.0	0.06	-	0.05	1.29	1.12	3.5	0.87
41	2.1	B	900	70		450	100	599	851	0.70	5.7	14.5	0.07	-	0.05	1.17	1.15	5.4	0.70
42	2.1	B	900	70		480	100	572	832	0.69	4.4	12.3	0.03	-	0.04	0.94	0.86	< 1	-
43	2.2	B	900	70		420	100	665	973	0.68	6.7	12.3	0.12	-	0.07	0.92	0.91	3.8	0.61
44	2.2	B	900	70		450	100	627	943	0.66	5.3	13.5	0.08	-	0.05	0.75	0.66	< 1	-
45	2.2	B	900	70		480	100	677	1000	0.68	4.9	10.5	0.07	-	0.05	0.77	0.72	< 1	-
46	2.3	B	900	70		420	100	524	890	0.59	9.5	14.3	0.16	-	0.10	0.65	0.67	< 1	-
47	2.3	B	900	70		450	100	545	905	0.60	9.3	18.3	0.14	-	0.09	0.87	0.89	< 1	-
48	2.3	B	900	70		480	100	580	946	0.61	9.7	18.7	0.13	-	0.10	1.11	1.06	< 1	-
49	2.4	B	900	70		420	100	531	907	0.58	8.2	15.5	0.15	-	0.08	0.66	0.72	< 1	-
50	2.4	B	900	70		450	100	541	906	0.60	8.4	14.6	0.14	-	0.08	1.00	0.93	< 1	-
51	2.4	B	900	70		480	100	542	912	0.59	8.5	16.0	0.13	-	0.08	0.95	0.90	< 1	-
52	2.4	C	830	180	200	450	100	913	1004	0.91	2.9	8.5	-	-	0.03	0.95	1.05	0.6	0.85
53*	2.4	C	830	180	250	450	100	818	923	0.89	2.8	10.9	-	-	-	-	-	0.7	0.85
54	2.4	C	830	180	275	450	100	732	1010	0.72	8.0	13.7	0.13	-	0.07	1.00	1.14	0.1	0.87
55*	2.4	C	830	180	300	450	100	706	999	0.71	7.2	16.1	0.14	-	-	-	-	1.1	0.89
56	2.4	C	830	180	350	450	100	764	1039	0.74	7.3	12.4	0.13	-	0.07	0.78	0.88	0.4	0.89
57	2.4	C	850	180	200	450	100	945	1028	0.92	4.7	10.8	0.04	-	0.04	1.15	1.19	3.1	0.89
58	2.4	C	850	180	250	450	100	893	998	0.89	4.9	10.1	0.04	-	0.04	0.82	0.92	3.8	0.92
59	2.4	C	850	180	275	450	100	920	1020	0.90	4.2	11.3	0.02	-	0.04	1.07	1.05	1.4	0.89
60	2.4	C	850	180	300	450	100	792	1013	0.78	6.1	11.4	0.08	-	0.06	0.77	0.70	1.1	0.91
61	2.4	C	850	180	350	450	100	780	1023	0.76	6.6	15.7	0.12	-	0.07	0.78	0.88	2.0	0.92
62**	IE1	CGL	830	70		470	100	729	1162	0.63	7.4	13.8	0.11	-	0.07	0.62	0.65	< 2	-
63	IE1	D	830	70		420	100	754	1182	0.64	7.2	14.5	0.13	-	0.07	0.61	0.70	0	***
64	IE1	D	830	70		450	100	749	1189	0.63	8.9	14.9	0.13	-	0.09	0.57	0.66	0	***
65	IE1	D	830	70		480	100	740	1178	0.63	9.4	16.5	0.13	-	0.10	0.57	0.68	0	***
66	IE1	D	950	70		420	100	765	1078	0.71	7.1	14.2	0.13	-	0.07	0.72	0.77	0	***
67	IE1	D	950	70		450	100	744	1079	0.69	5.9	16.6	0.09	-	0.05	0.74	0.80	0	***
68	IE1	D	950	70		480	100	787	1123	0.70	5.0	14.9	0.07	-	0.05	0.65	0.79	0	***
69	IE1	E	830	70	275	420	100	670	1120	0.60	6.7	16.2	0.16	-	0.07	0.58	0.66	0	***
70	IE1	E	830	70	275	450	100	768	1040	0.74	8.7	20.5	0.16	-	0.08	0.71	0.82	0	***
71	IE1	E	830	70	275	480	100	717	1151	0.62	6.7	14.9	0.14	-	0.06	0.44	0.52	3.1	***
72	IE1	E	950	70	275	420	100	928	1048	0.89	3.1	11.8	-	-	0.03	0.93	0.97	0	***
73	IE1	E	950	70	275	450	100	913	1026	0.89	2.8	13.8	-	-	0.03	0.91	0.94	0	***
74	IE1	E	950	70	275	480	100	848	984	0.86	2.9	14.8	-	-	0.03	0.94	0.88	0	***

* Tensile specimen fractured outside the elongation gauge

** Average of three measurements

*** Retained austenite vol.% of specimens 63 - 74 was measured using EBSD

APPENDIX 3: LIST OF PHASE CONTENTS AND THERMAL CYCLES

Appendix 3 summarizes the heat treatment conditions and the corresponding phase contents in the specimens of the present study. Table 1 presents the summary of the heat treatment conditions and results.

Table 1. Summary of the experimental conditions and phase contents of the specimens.

#	Alloy	Thermal cycle type	IA [°C]	t_A [s]	QT [°C]	IBT / PT [°C]	t_{IBT} / t_{PT} [s]	Ferrite [vol.%]	Bainite / Bainitic ferrite [vol.%]	Martensite [vol.%]	Retained austenite [vol.%]	RA measurement type
1	REF	A	830	70		420	100	7	64	29	0	XRD
2	REF	A	830	70		450	100	7	61	32	0	XRD
3	REF	A	830	70		480	100	6	48	46	0	XRD
4	1.1	A	830	70		420	100	42	17	32	9	XRD
5	1.1	A	830	70		450	100	40	21	34	5	XRD
6	1.1	A	830	70		480	100	38	23	38	1	XRD
7	1.2	A	830	70		420	100	44	8	48	0	XRD
8	1.2	A	830	70		450	100	43	10	48	0	XRD
9*	1.2	A	830	70		480	100	45	7	48	0	XRD
10	1.3	A	830	70		420	100	49	10	42	0	XRD
11	1.3	A	830	70		450	100	48	18	33	1	XRD
12	1.3	A	830	70		480	100	39	15	45	1	XRD
13	1.4	A	830	70		420	100	43	31	21	5	XRD
14	1.4	A	830	70		450	100	43	23	22	12	XRD
15	1.4	A	830	70		480	100	40	14	37	9	XRD
16	2.1	A	830	70		420	100	12	79	10	0	XRD
17	2.1	A	830	70		450	100	6	77	17	0	XRD
18	2.1	A	830	70		480	100	14	57	29	0	XRD
19	2.2	A	830	70		420	100	15	57	28	0	XRD
20	2.2	A	830	70		450	100	22	40	38	0	XRD
21	2.2	A	830	70		480	100	19	33	48	0	XRD
22	2.3	A	830	70		420	100	46	0	54	0	XRD
23	2.3	A	830	70		450	100	48	7	45	0	XRD
24	2.3	A	830	70		480	100	40	2	57	0	XRD
25	2.4	A	830	70		420	100	55	0	45	0	XRD

26	2.4	A	830	70		450	100	39	0	61	0	XRD
27	2.4	A	830	70		480	100	52	0	48	0	XRD
28	1.1	B	900	70		420	100	27	31	29	13	XRD
29	1.1	B	900	70		450	100	21	43	23	13	XRD
30	1.1	B	900	70		480	100	24	38	27	11	XRD
31	1.2	B	900	70		420	100	35	7	58	0	XRD
32	1.2	B	900	70		450	100	42	12	46	0	XRD
33	1.2	B	900	70		480	100	44	11	45	0	XRD
34	1.3	B	900	70		420	100	39	23	38	0	XRD
35	1.3	B	900	70		450	100	30	26	44	0	XRD
36	1.3	B	900	70		480	100	35	26	39	0	XRD
37	1.4	B	900	70		420	100	32	26	28	14	XRD
38	1.4	B	900	70		450	100	21	29	39	11	XRD
39	1.4	B	900	70		480	100	32	18	41	9	XRD
40	2.1	B	900	70		420	100	4	77	19	4	XRD
41	2.1	B	900	70		450	100	5	74	16	5	XRD
42	2.1	B	900	70		480	100	10	42	49	0	XRD
43	2.2	B	900	70		420	100	2	76	18	4	XRD
44	2.2	B	900	70		450	100	8	68	24	0	XRD
45	2.2	B	900	70		480	100	6	67	28	0	XRD
46	2.3	B	900	70		420	100	38	30	32	0	XRD
47	2.3	B	900	70		450	100	14	63	22	0	XRD
48	2.3	B	900	70		480	100	31	21	48	0	XRD
49	2.4	B	900	70		420	100	25	19	56	0	XRD
50	2.4	B	900	70		450	100	36	6	58	0	XRD
51	2.4	B	900	70		480	100	26	0	74	0	XRD
52	2.4	C	830	180	200	450	100	57	0	43	0	XRD
53	2.4	C	830	180	250	450	100	67	0	33	0	XRD
54	2.4	C	830	180	275	450	100	62	0	38	0	XRD
55	2.4	C	830	180	300	450	100	52	0	48	0	XRD
56	2.4	C	830	180	350	450	100	62	0	38	0	XRD
57	2.4	C	850	180	200	450	100	53	0	44	3	XRD
58	2.4	C	850	180	250	450	100	43	0	53	4	XRD
59	2.4	C	850	180	275	450	100	40	0	60	0	XRD
60	2.4	C	850	180	300	450	100	42	0	58	0	XRD
61	2.4	C	850	180	350	450	100	48	0	50	2	XRD
62	IE1	CGL	830	70		470	100	41	0	59	0	XRD
63	IE1	D	830	70		420	100	52	0	48	0	EBSD
64	IE1	D	830	70		450	100	25	21	54	0	EBSD
65	IE1	D	830	70		480	100	31	15	54	0	EBSD
66	IE1	D	950	70		420	100	0	0	100	0	EBSD
67	IE1	D	950	70		450	100	19	51	30	0	EBSD
68	IE1	D	950	70		480	100	2	61	37	0	EBSD
69	IE1	E	830	70	275	420	100	46	0	54	0	EBSD
70	IE1	E	830	70	275	450	100	35	0	65	0	EBSD
71	IE1	E	830	70	275	480	100	38	0	59	3	EBSD
72	IE1	E	950	70	275	420	100	0	0	100	0	EBSD
73	IE1	E	950	70	275	450	100	10	0	90	0	EBSD
74	IE1	E	950	70	275	480	100	0	0	100	0	EBSD

Schematic representations of thermal cycle types A, B, C, D and E are presented in Figure 1. The diagrams show that the total length of thermal cycles was under 600 s in all thermal cycles utilized in the present study.

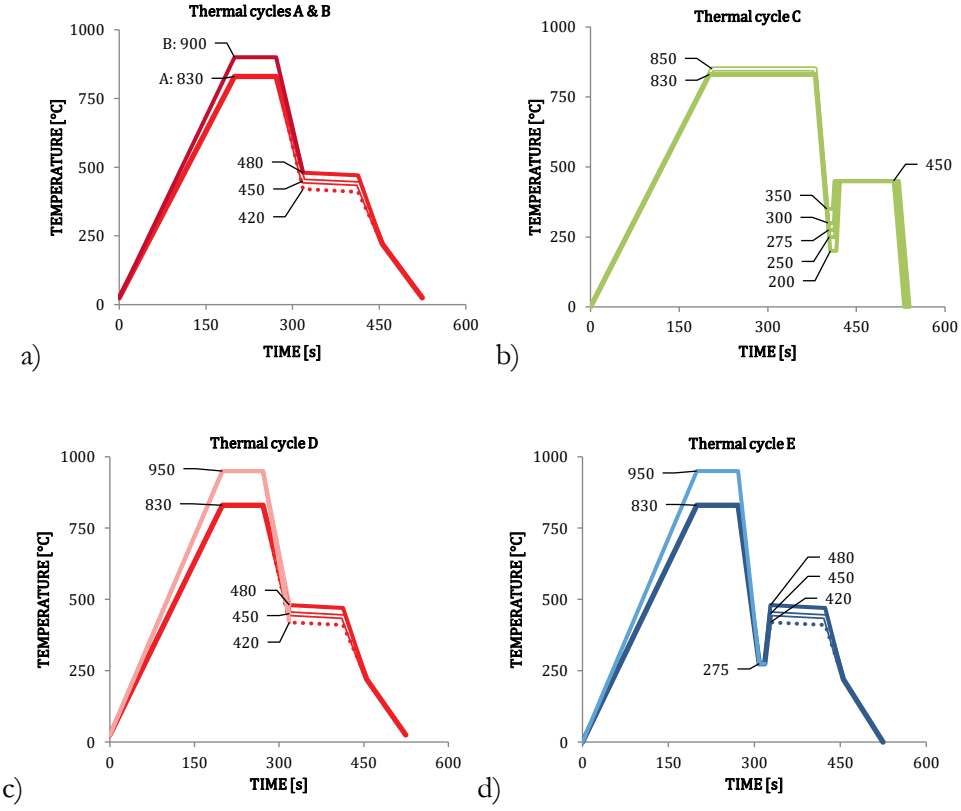

Figure 1. Schematic presentations of thermal cycle types A, B (a), C (b), D (c) and E (d).

Gleeble 3800 simulator available at the University of Oulu, Centre for Advanced Steel Research was utilized to perform the heat treatments. Gleeble thermomechanical physical simulation system is a trademark of Dynamic Systems Inc., Poestenkill, NY, USA. Figure 2 presents a photograph of the system and Figure 3 shows close-up of the copper grip setup utilized in the heat treatment simulations of metals.

Figure 2. Gleeble 3800 thermomechanical physical simulation system. Courtesy of Dynamic Systems Inc. [149]

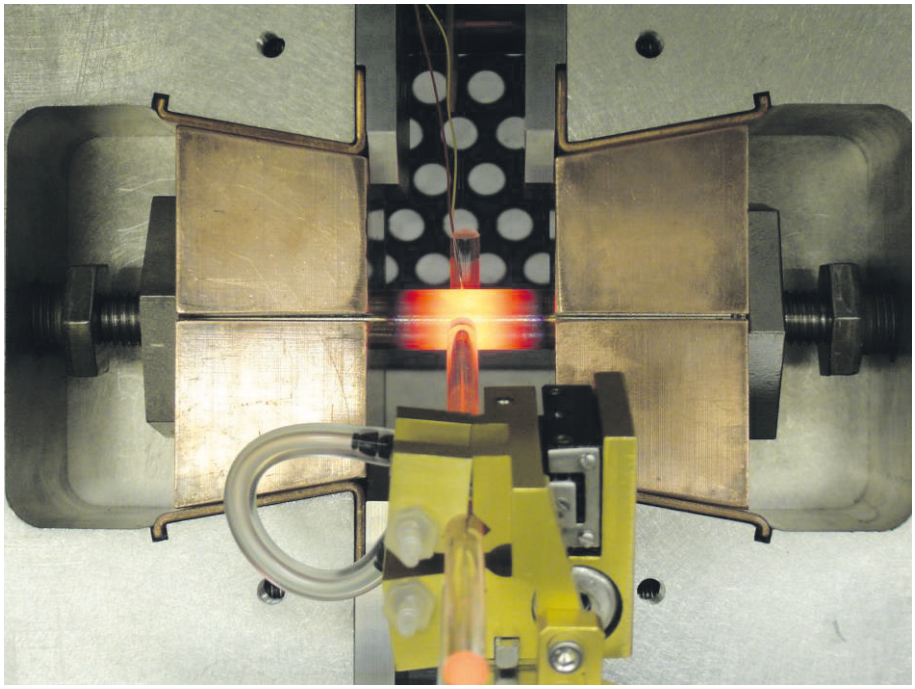

Figure 3. Grip system utilized for thermal cycles and heat treatments of metal specimens in Gleeble 3800 system. Courtesy of Dynamic Systems Inc. [149]